Doctoral theses at NTNU, 2023:439

Bjørn Andreas Kristiansen

Energy and Time Optimal Spacecraft Attitude Control and Operations

Doctoral thesis

NTNU
Norwegian University of Science and Technology
Thesis for the Degree of Philosophiae Doctor
Faculty of Information Technology and Electrical Engineering
Department of Engineering Cybernetics

NTNU
Norwegian University of Science and Technology

Bjørn Andreas Kristiansen

Energy and Time Optimal Spacecraft Attitude Control and Operations

Thesis for the Degree of Philosophiae Doctor

Trondheim, December 2023

Norwegian University of Science and Technology
Faculty of Information Technology and Electrical Engineering
Department of Engineering Cybernetics

NTNU
Norwegian University of Science and Technology

Thesis for the Degree of Philosophiae Doctor

Faculty of Information Technology and Electrical Engineering
Department of Engineering Cybernetics

ISBN 978-82-326-7580-7 (printed ver.)
ISBN 978-82-326-7579-1 (electronic ver.)
ISSN 1503-8181 (printed ver.)
ISSN 2703-8084 (online ver.)

ITK-nr.: 2023-24 -W

Doctoral theses at NTNU, 2023:439

Printed by NTNU Grafisk senter

Abstract

In this thesis, we present a cost function based on net power as a way to make attitude control maneuvers energy optimal for solar-powered spacecraft. Previous work has defined energy optimality in terms of input norms or, in some cases, actuator-based power models. The net power solution presented here is a cost function defined by the difference between the solar power the spacecraft gains at a given time minus the power it spends on actuation. Our solution is investigated both when the attitude control system is isolated and for a case where the full operations of a satellite are considered, displaying the benefits of this strategy in holistic satellite operations. The primary benefit of this method is that the time the satellite spends pointing towards the optimal solar attitude is maximized. This is evident from the smaller, isolated simulation study, which is performed solely based on the attitude control system, but the impact of this improvement becomes evident when the full operations of an agile satellite are considered, as the extra energy gained from the attitude control system could potentially increase the number of observations the satellite can perform per orbit. This net power concept is also investigated for a satellite actuated by magnetorquers, combined with a minimum time objective.

The second part of this thesis looks into maximum hands-off control for attitude control. Maximum hands-off control is a type of optimal control where the zeroth norm of the input is minimized, making the control signal as sparse as possible. Due to the zeroth norm being discontinuous, the L_1- and L_2-norm are common approximations to solve the maximum hands-off control problem. Having nice differentiation properties is particularly important due to the method we want to use to solve the problem: a Newton-type solver named IPOPT. We choose a different relaxation of the problem than the L_1- and L_2-norm to solve the maximum hands-off problem. From the results, we demonstrate the feasibility of this control method for attitude control, both for satellites actuated by reaction wheels and by on/off thrusters producing pure torque and a method of moving the sparsity around to where the operator desires.

The final part of this thesis is devoted to the slew maneuver that HYPSO-1 satellite, a 6U CubeSat from NTNU SmallSat lab used as the basis for several case studies in this thesis, performs. The slew maneuver has constant angular velocity in LVLH, a local frame that follows the satellite's orbit. In the first chapter of this part, we investigate whether a second-order sliding mode controller named generalized super-twisting algorithm improves the attitude control system's performance when the satellite points and performs the slewing maneuver in a simulation en-

vironment. In the final chapter, we analyze the connection between the attitude control telemetry from the satellite's operations and its data products, looking at how well the satellite performs with respect to its science requirements and otherwise theorized performance.

Sammendrag

I denne avhandlingen presenterer vi en kostfunksjon basert på nettoeffekt som en måte å gjøre orienteringsreguleringsmanøver energioptimal for solcelledrevne romfartøyer. Tidligere arbeid har definert energioptimalitet i form av normer for input eller i noen tilfeller aktuatorbaserte kraftmodeller. Nettoeffektløsningen som presenteres her er en kostfunksjon definert av forskjellen mellom solenergien romfartøyet får på et gitt tidspunkt minus kraften det bruker på aktuering. Løsningen vår blir undersøkt både når orienteringsreguleringssystemet er isolert og for et tilfelle der full drift av en satellitt vurderes, og med det vises fordelene med denne strategien i holistiske satellittoperasjoner. Hovedfordelen med denne metoden er at tiden satellitten bruker på å peke mot den optimale solorienteringen maksimeres. Dette er mulig å tyde fra den kortere, isolerte simuleringsstudien som er utført utelukkende basert på orienteringsreguleringssystemet, men virkningen av denne forbedringen blir tydelig når man tar de fulle operasjonene til en smidig satellitt i betraktning, siden den ekstra energien som oppnås fra orienteringsreguleringssystemet kan potensielt øke antallet observasjoner satellitten kan utføre. Dette nettoeffektkonseptet er også undersøkt for en satellitt aktuert av magnetorquere, kombinert med et mål om minimering av tid.

Den andre delen av avhandlingen ser på maksimal hands-off regulering for orienteringsregulering. Maksimal hands-off-regulering er en type optimalregulering hvor den nulte normen til pådraget er minimert, noe som gjør pådragssignalet så sparsomt som mulig. På grunn av at den nulte normen er diskontinuerlig, er L_1- og L_2-normen vanlige tilnærminger for å løse det maksimale hands-off reguleringsproblemet. Å ha fine differensieringsegenskaper er spesielt viktig på grunn av metoden vi ønsker å bruke for å løse problemet: en løser som baserer seg på informasjon fra de deriverte av systemet, kalt IPOPT. Vi velger en annen løsning på problemet enn L_1- og L_2-normen for å løse maksimale hands-off-problemet. Fra resultatene demonstrerer vi gjennomførbarheten av denne reguleringsmetoden for orienteringsregulering, både for satellitter aktuert av reaksjonshjul og av på/av thrustere som produserer et rent dreiemoment, og en metode for å flytte sparsomheten i pådragssignalet dit operatøren ønsker.

Den siste delen av avhandlingen er viet svingmanøveren som HYPSO-1 satellitten, en 6U CubeSat fra NTNU SmallSat lab som er brukt som grunnlag for flere casestudier i denne oppgaven, utfører. Selve svingmanøveren er en manøver med konstant vinkelhastighet i LVLH, en lokal referanseramme som følger satellittens bane. I det første kapittelet av denne delen undersøker vi om en andre-ordens regulator av typen "sliding mode controller" kalt "generalized super-twisting algorithm"

forbedrer orienteringsreguleringssystemets ytelse når satellitten peker og utfører svingmanøveren i simulering. I det siste kapittelet analyserer vi sammenhengen mellom telemetri fra orienteringsreguleringssystemet under operasjonene til satellitten og satellittens dataprodukter, og ser på hvor godt satellitten presterer med hensyn til tidligere spesifiserte vitenskapelige krav og ellers teoretisert ytelse.

Contents

Preface

This thesis is submitted in partial fulfillment of the requirements for the degree of philosophiae doctor (PhD) at the Norwegian University of Science and Technology (NTNU), Trondheim. The work presented in this thesis has been carried out from August 2019 to August 2023 at the Centre for Autonomous Marine Operations and Systems (NTNU AMOS) and the Department of Engineering Cybernetics under the supervision of Professor Jan Tommy Gravdahl and co-supervision of Professor Tor Arne Johansen, both with the Department of Engineering Cybernetics. The work has been tied to the NTNU SmallSat Lab, a multi-department lab hosted by the Department of Electronic Systems. The work has been supported by the Research Council of Norway through the Centre of Excellence funding scheme, project number 223254, NTNU AMOS.

Acknowledgments

First, I would like to thank my supervisor, Professor Jan Tommy Gravdahl. I have had a lot of questions over the years, but you have always made time to answer them, which I appreciate. We have been working together on both my research for my PhD and the TTK4100 course, and I feel like the collaboration has been going well, even as the meetings have changed from being scheduled to me just knocking on the door to talking about the most recent problem. Secondly, I want to thank my co-supervisor, Professor Tor Arne Johansen. I am still unsure how you can find the main points in the wall of text I spend days writing, only to reply with solutions and improvements five minutes later. I would also like to thank Professor Sébastien Gros, who always seems to have time to discuss the strange issues that show up.

I cannot get around mentioning Mariusz Eivind Grøtte. His research topic was the closest to mine in the department, and for a while, we made up a small group where we discussed similar research and ideas, which was nice. I have supervised two master's students for their theses, Sigrid Kjønnø Schaanning and Carl Martin Krokeide (and the current students, Olve Skurdal Skagen and Henning Granne Andresen), which were positive experiences. I would also like to mention the others who were part of the discussion group at some point, Jørgen Anker Olsen and Frieda Franke, who helped make it a good research environment.

While I cannot name everyone, I would like to mention some people[1]:

[1] This section could have been longer, as there are many people I have worked with, talked to, and would have liked to thank or mention somehow. The people who read these theses all read them differently. Some are interested in the content of the thesis for professional (academic)

- The people I have shared an office with. At the beginning of my PhD, I shared an office with Andreas Moltumyr, Andreas Våge, and Trym (Tengesdal) for a few weeks. We were then split into two rooms, and Erlend Andreas Basso and Vilde Benoni Gjærum joined Andreas Moltumyr and me in room D444. As we were all named Andreas in one way or another, apart from Vilde, we made Vilde an honorary Andreas by giving her Andreas as a middle name. Basso left our office to work with Henrik Schmidt-Didlaukies at Tyholt, an event sometimes jokingly referred to locally at D444 as "The Betrayal". Sindre Benjamin Remman took Basso's place. When Moltumyr left (read: deserted) the group for a job in the private sector sometime later, Thomas Nakken Larsen joined our group at D444. Vilde's graduation led to Glen Hjelmerud Mørkbak Sørensen joining our office. I want to say that I have appreciated sharing an office with all of you over the past four years.
- I have been part of the NTNU SmallSat Lab for my PhD. I should to mention Sivert, Evelyn, Simen, Marie, Gara, Dennis, Joe, Roger, Amund, Martine, Tord, Elizabeth, Corrado, Samuel, Cameron, Esmée, Daniel, Jon, Alberto, Milica, Fernando, Alvaro, Torbjørn, Håkon, and all the other students who have been part of the project.
- For the past four years, I have been the research assistant in TTK4100. I have worked closely with Tommy, the teacher in the subject, but I also want to mention the others I have worked with over the years: Jo Arve, Knut, and Morten. I would also like to thank Linn, who was the teaching assistant before me and who helped me get an easy start on the job by sharing her experiences from the year before. I would also like to mention others I came into contact with owing to my work as a TA, which would be Stefano, Glenn, Terje, Rune, Kristian, Åsmund, and Anders, who all helped me with problems I encountered during my time where the deadlines for fixing them were usually way too short, and somehow all the people on the first floor, although Janne joked that we only spoke when I had lost something.
- Katrine, Akhil, Erlend (Lundby), Amer, Mariusz, Linn, and Mathias were part of the group of people Tommy supervised during my PhD, which made for a good working environment. This good environment can also be attributed to the rest of the people at the department, during work at the department itself, or other activities such as trips for conferences. Examples beyond those mentioned include (but are not limited to[1]) Dordije, Marianna, Torleiv, Pål, Irja, Sverre, Eirik, Simon, and Trym (Gabrielsen).

At the end of this long list of people, I would like to thank my family: my mom, dad, brother, aunt, and finally, my grandma, who always wanted to hear what I was working on, even at the beginning of the PhD when I was unable to present my ideas in a coherent way to anyone.

Bjørn Andreas Kristiansen
Trondheim, November 2023

reasons, while others would only read this very section. In choosing what names to include, I have gambled on who would read this section and who would not. If you expected to see your name here but don't, it is not because I have forgotten about you; it is simply because I guessed wrong.

Publications

The results presented in this thesis are based on the following papers, listed in chronological order. The author of this thesis' name is highlighted in bold text.

Papers

[1] **B. A. Kristiansen**, M. E. Grøtte, and J. T. Gravdahl, "Quaternion-Based Generalized Super-Twisting Algorithm for Spacecraft Attitude Control", in *Proceedings of the 21st IFAC World Congress*, Berlin (Virtual), Germany, July 2020.

[2] **B. A. Kristiansen**, J. T. Gravdahl, and T. A. Johansen, "Energy optimal attitude control for a solar-powered spacecraft," *European Journal of Control*, 2021 European Control Conference Special Issue, vol. 62, pp. 192–197, Nov. 2021.

[3] S. K. Schaanning, **B. A. Kristiansen**, and J. T. Gravdahl, "Maximum Hands-Off Attitude Control,", in *2022 American Control Conference (ACC)*, pp. 4003–4010, Atlanta, Georgia, USA, Jun. 2022.

[4] **B. A. Kristiansen** and J. T. Gravdahl, "Maximum Hands-Off Attitude Control of a Spacecraft Actuated by Thrusters," in *Proceedings of the 22nd IFAC World Congress*, Yokohama, Japan, Jul. 2023.

[5] **B. A. Kristiansen**, J. T. Gravdahl, S. Gros, and T. A. Johansen, "Energy optimal attitude control of a satellite actuated by magnetorquers in minimum time", in *Proceedings of the 7th IEEE Conference on Control Technology and Applications (CCTA)*, Bridgetown, Barbados, Aug. 2023.

[6] **B. A. Kristiansen***, D. D. Langer*, J. L. Garrett, S. Berg, J. T. Gravdahl, and T. A. Johansen, "Accuracy of a slew maneuver for the HYPSO-1 satellite — in-orbit results," in *13th Workshop on Hyperspectral Image and Signal Processing Evolution in Remote Sensing (IEEE-WHISPERS)*, Athens, Greece, Oct. 2023.

[7] **B. A. Kristiansen**, J. T. Gravdahl, S. Gros, and T. A. Johansen, "Energy Optimal Attitude Control and Task Execution for a Solar-Powered Spacecraft", *IEEE Transactions on Control Systems Technology*, 2023, *conditionally accepted for publication.*

Note that both B. A. Kristiansen and D. D. Langer are considered first authors of **B. A. Kristiansen***, D. D. Langer*, J. L. Garrett, S. Berg, J. T. Gravdahl, and T. A. Johansen, "Accuracy of a slew maneuver for the HYPSO-1 satellite —

in-orbit results," in *13th Workshop on Hyperspectral Image and Signal Processing Evolution in Remote Sensing (IEEE-WHISPERS)*, Athens, Greece, Oct. 2023.

Other publications

The following publications were written during the PhD, but are not included in this thesis.

Papers

[8] S. Bakken, M. B. Henriksen, R. Birkeland, D. D. Langer, A. E. Oudijk, S. Berg, Y. Pursley, J. L. Garrett, F. Gran-Jansen, E. Honoré-Livermore, M. E. Grøtte, **B. A. Kristiansen**, M. Orlandic, P. Gader, A. J. Sørensen, F. Sigernes, G. Johnsen, and T. A. Johansen, "HYPSO-1 CubeSat: First Images and In-Orbit Characterization,", *Remote Sensing*, vol. 15, no. 3, p. 755, Jan. 2023.

Chapter 1

Introduction

1.1 Introduction

Attitude control is a common problem for spacecraft, particularly satellites [9], and has been studied for decades. The motivation for attitude control in space vehicles is simple: payloads and other spacecraft parts need to point toward given objects for collecting data, transmitting data, or other purposes. For satellites orbiting the Earth, examples of these purposes could be pointing an imaging payload to take an image of the ground, an antenna to downlink an image, or solar panels toward the Sun. An alternative solution to actively pointing would be for the spacecraft to be made such that any instrument that is supposed to point out in any given direction does in the default attitude configuration. Then, the satellite would just wait for the interesting area to appear. However, this alternative solution significantly limits the time a payload can be helpful in many missions. Therefore, having agile attitude control could increase the frequency and quality of the data products the satellite can create.

Changing a satellite's orbit is expensive as it would require spending fuel. While these same fuel-based actuators that can raise an orbit can be used for attitude control, it is not strictly necessary: the attitude of a spacecraft can be controlled by actuators that only require electricity to work, such as reaction wheels and magnetorquers. Magnetorquers require the orbiting body to have a magnetic field to control against, which the Earth does have. While electricity is not a perishable resource for most spacecraft like fuel, it is still limited as the other onboard systems of the spacecraft would draw power for various purposes. For this reason, it is desirable to keep the attitude control maneuvers as efficient as possible with respect to energy. As spacecraft missions commonly have a purpose beyond staying alive, there may be other objectives critical to the mission operations that are at some point valued as high as energy, such as minimizing time.

Attitude maneuvers have been studied for various purposes and with various controllers, and optimal controllers have been investigated for the problem for a while. For example, time optimal attitude control was investigated in [10–13]. When it comes to energy optimal attitude control, the cost function has typically been constructed based on the first ([14]) or the second ([15]) norm of the input.

Minimizing the first norm of the input has been referred to as fuel optimal, while minimizing with respect to the second norm has been referred to as energy optimal. The idea behind both these strategies is to use as little energy on actuation as possible. There are some alternative approaches to using these norms to minimize actuation. An example of this can be seen in [16], where the authors use a power model of the actuators as the basis for the cost function rather than the previously mentioned norm-based solution.

1.2 Research questions

Based on this brief introduction, the following research questions are formulated:

RQ-1: How can attitude control maneuvers be made more time and energy-efficient?
The main idea behind this research question is to see if there are any potential improvements to previous optimization strategies. As mentioned, previous research has been done into cost functions based on norms of the control input and some actuator-based power models, but the current objective is to look for strategies that are more energy-efficient in some sense or another. Time relates to energy efficiency in that maneuvers cannot simply be put off indefinitely for the energy expenditure to be as small as possible, so there are bound to be some trade-offs.

RQ-2: How can alternative approaches for attitude control be used for satellites with payloads that are not continuously operated?
With payloads that are not continuously operated, such as a camera that only takes pictures every thirty minutes, there is much room and time for the satellite to perform attitude maneuvers. This freedom can be used to move the payload into position for a new operation sequence or some other satellite subsystem. Examples include communication with a ground station or controlling the satellite towards an attitude that maximizes solar harvesting or minimizes drag. The goal of this research question is to look into attitude control approaches that can improve the performance of the attitude control system, even in specialized cases.

RQ-3: How can the results in research questions 1 and 2 be taken advantage of in agile and holistic satellite operations?
While the results from research questions 1 and 2 are interesting in and of themselves, they make more sense in the context of the overall satellite operations. As mentioned in the introduction, the agility that attitude control brings to satellite operations is important for many missions. This research question looks, therefore, to address the connection between the attitude control schemes and agile satellite operations, looking at the impact the results from research question 1 and research question 2 have on the operations of the satellite.

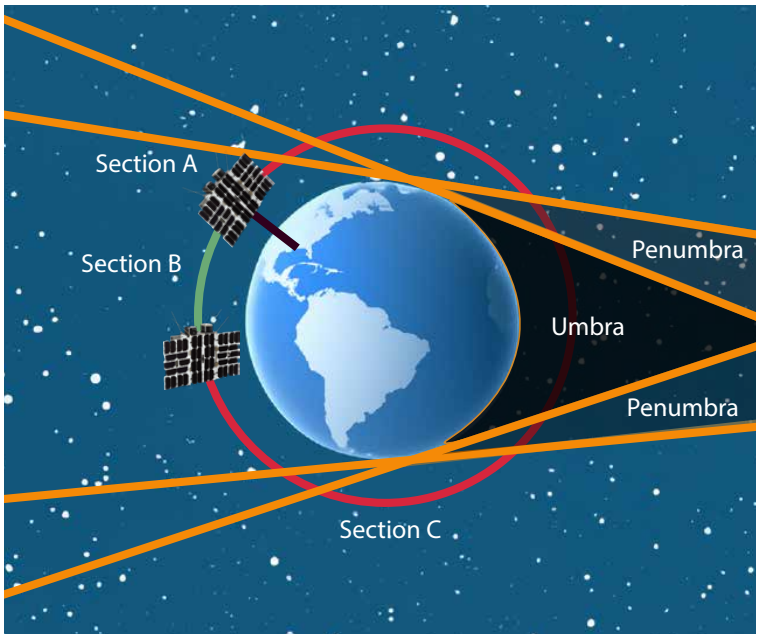

Figure 1.1: Thesis outline based on an orbiting satellite. The dimensions of the figure have been exaggerated.

1.3 Outline and contributions

The results in this thesis are divided into three parts: Energy optimal attitude control, maximum hands-off attitude control, and slewing maneuver results. Figure 1.1 shows the thesis outline on top of a satellite orbiting the Earth. The orbit is divided into three sections to illustrate the content of each chapter, covering different aspects of what the satellite does. In the context of Figure 1.1, the three sections are

- Section A: Where the satellite takes images based on the imaging modes for the HYPSO satellites. This phase is relatively short and contains the slew maneuver the satellite requires to achieve its scientific objectives. Section A is marked by the purple line, indicating that the satellite is taking images of the Earth.
- Section B: A section between two pointing maneuvers close in time. The pointing maneuvers can be either for imaging or contact with a ground station. The green section of the orbit in the figure marks section B.
- Section C: Between two pointing maneuvers far apart in time. The duration of the full maneuver spans the orbit's eclipse, in the figure marked by the penumbra (partially shaded region) and umbra (fully shaded region). Section C is marked in the figure by the red part of the orbit.

Chapter 2 introduces the background material common to all the papers and subsequent chapters, including the dynamical model of the satellite, shared as-

sumptions, and the HYPSO satellite mission. Each part also briefly introduces the material common to the papers.

1.3.1 Part I: Energy Optimal Attitude Control

This part consists of three chapters made up of material from [2], [7], and [5]. The shared background material, primarily based on the formulations first introduced in the following publication,

[2] **B. A. Kristiansen**, J. T. Gravdahl, and T. A. Johansen, "Energy optimal attitude control for a solar-powered spacecraft," *European Journal of Control*, 2021 European Control Conference Special Issue, vol. 62, pp. 192–197, Nov. 2021,

is found in Chapter 3.

Energy Optimal Attitude Control for a Solar-Powered Spacecraft (Chapter 4)

In this chapter, we aim to maximize the net energy a solar-powered spacecraft gains when performing a maneuver. The net energy can be defined as the integral of the power supplied by the solar panels minus the power used by the attitude control system and is a key quality since energy is a scarce resource in space. Previous research on optimal attitude control has focused on optimization with respect to other costs, such as time-optimal control and optimal attitude control with respect to the integral of the square of the input. The energy flow depends on both the power spent on actuation and the power received from the solar panels. Thus, the optimal attitude control problem should be formulated so that the spacecraft's attitude relative to the Sun during the maneuver is included in the calculations. In this chapter, we propose a cost function based on net power to address this problem. This new cost function incorporates the incoming energy from the solar irradiance and the outgoing energy due to actuation. A simulation study comparing an optimal control solution of the proposed net power cost function using IPOPT in CasADi is presented for a 6U CubeSat equipped with solar cell arrays, where the net power-based optimal control maneuver is shown to compare favorably to a sun-pointing PD controller.

This chapter is based on the following publication:

[2] **B. A. Kristiansen**, J. T. Gravdahl, and T. A. Johansen, "Energy optimal attitude control for a solar-powered spacecraft," *European Journal of Control*, 2021 European Control Conference Special Issue, vol. 62, pp. 192–197, Nov. 2021.

Energy Optimal Attitude Control and Task Execution for a Solar-Powered Spacecraft (Chapter 5)

In this chapter, we aim to maximize the net energy a solar-powered spacecraft gains when performing a sequence of tasks leading to attitude maneuvers over the spacecraft orbit, including eclipse. The net energy can be defined as the integral

of the power supplied by the solar panels minus the power used by the payload and satellite systems, including the attitude control system. The energy flow depends on both the power spent on the satellite electronic systems and the power received from the solar panels. Thus, the optimal attitude control problem should be formulated to include the spacecraft's attitude relative to the Sun during the maneuver in the calculations and the actuation cost. In this chapter, we propose a cost function based on net energy to address this problem. This function extends the net power cost function we introduce in Chapter 4. Compared to Chapter 4, this chapter introduces a function that differentiates between the fully and partially shaded regions of the eclipse and is added to simulate the solar irradiance in the eclipse. The formulation of the cost function is refined on several points. One of these points is the solar power function, which is changed so that the formulation works for satellites with deployable solar panels. Our approach is demonstrated in a simulation study where the HYPSO-2 Earth observation satellite executes a sequence of imaging, communication, and energy-harvesting tasks. HYPSO-2 is a 6U CubeSat equipped with deployable solar cell arrays, and the optimal control problem is solved using IPOPT in CasADi.

This chapter is based on the following publication:

[7] **B. A. Kristiansen**, J. T. Gravdahl, S. Gros, and T. A. Johansen, "Energy Optimal Attitude Control and Task Execution for a Solar-Powered Spacecraft", *IEEE Transactions on Control Systems Technology*, 2023, *conditionally accepted for publication.*

Energy Optimal Attitude Control of a Satellite Actuated by Magnetorquers in Minimum Time (Chapter 6)

In this chapter, we combine a previously introduced energy optimal cost function based on net power with a time-based cost for attitude control of a spacecraft. The benefit of such an approach over the previous optimization scheme, which used a fixed control horizon, is that the control horizon does not have to be set in advance, which can be desirable if it is challenging to know the final time of the optimization. This time optimal objective is combined with a cost function based on net energy, which is the integral of the difference between the power the satellite gains from solar power and the power it spends performing the attitude maneuvers. The weighting between these two objectives can be exploited to let the optimal solver choose the final time in cases where the exact final time of the maneuver is not critical. Magnetorquers produce a magnetic torque that can be used to control the attitude of a spacecraft. However, due to their physical limitation, it is not trivial to tell when the spacecraft will reach its reference value. For this reason, an approach where the optimal solver sets the final time can be beneficial. The difficulties related to using two terms in the cost function for the distance from the reference attitude and angular velocity, together with the net power cost function and time, are discussed.

This chapter is based on the following publication:

[5] **B. A. Kristiansen**, J. T. Gravdahl, S. Gros, and T. A. Johansen, "Energy optimal attitude control of a satellite actuated by magnetorquers in minimum

time", in *Proceedings of the 7th IEEE Conference on Control Technology and Applications (CCTA)*, Bridgetown, Barbados, Aug. 2023.

1.3.2 Part II: Maximum Hands-Off Control

The part contains material from two publications, and the background chapter, Chapter 7, contains the material used in both of the following publications to produce the results:

[3] S. K. Schaanning, **B. A. Kristiansen**, and J. T. Gravdahl, "Maximum Hands-Off Attitude Control,", in *2022 American Control Conference (ACC)*, pp. 4003–4010, Atlanta, Georgia, USA, Jun. 2022.

[4] **B. A. Kristiansen** and J. T. Gravdahl, "Maximum Hands-Off Attitude Control of a Spacecraft Actuated by Thrusters," in *Proceedings of the 22nd IFAC World Congress*, July 2023, Yokohama, Japan.

Maximum Hands-Off Attitude Control with Reaction Wheels (Chapter 8)

In this chapter, we explore the use of maximum hands-off control for attitude control of a spacecraft actuated by reaction wheels. The maximum hands-off, or L_0-optimal, controller aims to find the sparsest control signal among all admissible control signals. L_0-optimal problems are generally complex to solve as L_0-cost functions are discontinuous and non-convex. Previous research has investigated methods to approximate the L_0-norm in the cost function, for instance, using an L_1-norm. We propose an approach to the maximum hands-off control problem for spacecraft attitude control involving an L_0-cost function relaxed through complementarity constraints. The controller is applied to the spacecraft attitude control problem, and the performance of the maximum hands-off controller is compared to that of the L_1-optimal controller. Simulations of a 6U CubeSat were conducted using CasADi as the primary optimization tool, and the L_1- and L_0-optimal control problems were discretized using direct multiple-shooting and solved using the IPOPT solver. In addition to these results, we propose a new control scheme, called *moving* maximum hands-off control, which lets the user specify in which time interval the control should occur and then aims to find the sparsest control among all admissible controls based on this information. The moving maximum hands-off controller is demonstrated to be as sparse as the maximum hands-off controller for some spacecraft maneuvers.

This chapter is based on the following publication:

[3] S. K. Schaanning, **B. A. Kristiansen**, and J. T. Gravdahl, "Maximum Hands-Off Attitude Control,", in *2022 American Control Conference (ACC)*, pp. 4003–4010, Atlanta, Georgia, USA, Jun. 2022.

Maximum Hands-Off Attitude Control of a Spacecraft Actuated by Thrusters (Chapter 9)

In this chapter, we investigate the use of maximum hands-off control for spacecraft attitude control of a spacecraft equipped with thrusters. Other than a more natural

choice of actuators than in our previous paper, the definition of the L_0-norm for a vector of continuous-time signals most suited for this optimal control problem is refined. An extra term is introduced to the cost function to handle the actuator change. We introduce relative sparsity, a concept where sparsity is defined as a function of the control horizon. With this definition, comparing the sparsity of any given signal is easier. Finally, we show how the relative sparsity of an optimized state trajectory changes with the resolution and constraints of the optimal control problem.

This chapter is based on the following publication:

[4] **B. A. Kristiansen** and J. T. Gravdahl, "Maximum Hands-Off Attitude Control of a Spacecraft Actuated by Thrusters," in *Proceedings of the 22nd IFAC World Congress*, July 2023, Yokohama, Japan.

1.3.3 Part III: Slewing Maneuver Results

Chapter 10 details the slewing maneuver used in this part.

Quaternion-Based Generalized Super-Twisting Algorithm for Spacecraft Attitude Control (Chapter 11)

A second-order sliding mode control, the generalized super-twisting algorithm (GSTA), is used for attitude control of a spacecraft actuated by reaction wheels for pointing and a slewing maneuver. Magnetorquers are used for reaction wheel momentum dumping. Simulation results are based on a typical CubeSat. The GSTA results are compared to sliding mode control (SMC) and a proportional–derivative (PD) controller. The simulation shows that the GSTA performs better than the SMC for the pointing and slewing maneuvers when it comes to settling time and accuracy due to reduced chattering. Compared to the PD controller, the GSTA performs similarly under the chosen conditions, with a shorter settling time for pointing and a longer settling time for slewing. The GSTA applies torque to the reaction wheels with lower spikes and less chattering than the PD controller.

This chapter is based on the following publication:

[1] **B. A. Kristiansen**, M. E. Grøtte, and J. T. Gravdahl, "Quaternion-Based Generalized Super-Twisting Algorithm for Spacecraft Attitude Control", in *Proceedings of the 21st IFAC World Congress*, Berlin (Virtual), Germany, July 2020.

Accuracy of a Slew Maneuver for the HYPSO-1 Satellite – in-orbit results (Chapter 12)

This chapter analyzes the accuracy of a slew maneuver performed by the HYPSO-1 satellite based on the data received during the satellite's first months in orbit. The slew maneuver, during which the satellite turns with a constant angular velocity over a given target area, is meant to decrease the ground sampling distance of pixels recorded by the push-broom hyperspectral imager. We compare the pointing accuracy when pointing nadir with the accuracy the satellite achieves when the satellite slews, and also the impact the slew maneuver has on the resulting data

products, namely the decreased ground sampling distance and the increased signal per area. The selected slew maneuver shows a root-mean-square accuracy of 0.675 mrad/s about the axis of rotation. Analysis of the images shows that the slew maneuver provides 2.80 times as many samples per area and a decrease in ground sampling distance of 63.6% along track.

This chapter is based on the following publication:

[6] **B. A. Kristiansen**, D. D. Langer, J. L. Garrett, S. Berg, J. T. Gravdahl, and T. A. Johansen, "Accuracy of a slew maneuver for the HYPSO-1 satellite — in-orbit results," in *13th Workshop on Hyperspectral Image and Signal Processing Evolution in Remote Sensing (IEEE-WHISPERS)*, Athens, Greece, Oct. 2023.

Chapter 2

Background

2.1 General attitude control information

Attitude control of a spacecraft, or more specifically, satellites, concerns various maneuvers related to the spacecraft's attitude. Common maneuvers include pointing, meaning the movement from one attitude to another relative to a chosen coordinate frame, and slewing, a maneuver where the attitude is time-varying.

The attitude control usually forms a subsystem with the estimation system. What this system is called varies: attitude determination and control system (ADCS) and attitude and orbit control system (AOCS) are common designations. This system commonly estimates and controls the pose of the satellite, which includes both attitude and position. The satellites associated with the HYPSO missions are actuated with reaction wheels and magnetorquers, meaning that no forces act on the orbit beyond the external forces that push the satellite towards the Earth, such as aerodynamic drag and solar radiation pressure. As the time horizons investigated in this thesis are generally shorter than the horizon these forces would work on, arguments based on the pure attitude maneuvers are preferred throughout the thesis, although the formulations are often adapted so that other actuator choices with orbit-changing capabilities can be used in the same framework.

2.2 Frames

In the articles in this thesis, we use four different reference frames: the Earth-centered inertial frame (ECI), the Earth-centered Earth-fixed frame (ECEF), the orbit frame or local vertical local horizontal (LVLH), and the body frame. The following sections, Section 2.2 and Section 2.3, are primarily based on

[1] **B. A. Kristiansen**, M. E. Grøtte, and J. T. Gravdahl, "Quaternion-Based Generalized Super-Twisting Algorithm for Spacecraft Attitude Control", in *Proceedings of the 21st IFAC World Congress*, Berlin (Virtual), Germany, July 2020.

Earth-centered inertial (ECI)

The earth-centered inertial frame $\{i\}$ has origin at the Earth's center of mass, with the z-axis pointing through the North Pole, the x-axis pointing towards vernal equinox, and the y-axis completing the right-handed system. Vectors and derivatives with respect to the ECI frame are denoted with a superscript i. The motivation for using an inertial reference frame is that Newton's laws hold in such frames. There are several types of inertial reference frames, or, more correctly stated, there are frames that seem inertial for various tasks. If the accuracy requirements are higher than the accuracy at which the Earth-centered inertial frame can be considered inertial, or if the time scale of the maneuvers significantly increases beyond what is investigated here, it would be natural to choose a different inertial reference frame. Regarding the tasks investigated here, the ECI frame is deemed sufficiently inertial. Several inertial reference frames are placed in the center of the Earth, such as J2000. Whenever possible, implementation details of the choice of inertial reference frame have been omitted as the methods are not dependent on a given implementation.

Orbit frame

The Local Horizontal, Local Vertical (LVLH) frame, or the orbit frame $\{o\}$, has superscript o for vectors represented in the frame. The orbit frame is centered in the center of mass of the spacecraft. The z-, x-, and y-axis point in the direction of the Earth's center of mass, the orbit velocity vector, and in a direction that completes the right-handed coordinate system, respectively. The unit vectors of the frame are given by

$$\hat{\mathbf{z}}^o = -\frac{\mathbf{r}^i}{\|\mathbf{r}^i\|_2}, \ \hat{\mathbf{x}}^o = \frac{\mathbf{v}^i}{\|\mathbf{v}^i\|_2}, \ \hat{\mathbf{y}}^o = \frac{\hat{\mathbf{z}}^o \times \hat{\mathbf{x}}^o}{\|\hat{\mathbf{z}}^o \times \hat{\mathbf{x}}^o\|_2}, \tag{2.1}$$

where $\mathbf{r}^i$ is the distance between the spacecraft and the center of the Earth, and $\mathbf{v}^i$ is the spacecraft's velocity, both represented in the inertial reference frame. The purpose of this frame is primarily to control the satellite's attitude relative to its orbit. A common situation where this is useful would be pointing the satellite nadir, which is simply controlling the satellite relative to the z-component of the attitude in LVLH.

Body frame

The axes of the body frame $\{b\}$ follow the spacecraft structure, and its origin is centered in the spacecraft's center of mass. Vectors represented in this frame have superscript b. Commonly, the reference frame follows the HYPSO spacecraft, which has the camera pointed towards the positive body frame z-axis.

Wheel frame

The wheel frame $\{w\}$ specifies vectors directly related to the reaction wheels. The two vectors that are represented in this frame are the wheel angular velocity, $\boldsymbol{\omega}_{\text{RW}}^w$,

and the torque applied to each wheel, $\boldsymbol{\tau}_{\text{RW}}^{w}$. The dimension of these vectors equals the number of reaction wheels, where each channel of the vectors specifies the angular velocity or torque applied about each wheel's axis of rotation. The mapping of the wheel frames to the body frame is represented by the matrix $\mathbf{A} \in \mathbb{R}^{3\text{x}n_{rw}}$, as

$$\boldsymbol{\tau}_{\text{RW}}^{b} = \mathbf{A}\boldsymbol{\tau}_{\text{RW}}^{w}, \tag{2.2}$$

where n_{rw} is the number of reaction wheels. Note that $\mathbf{A}$ is a constant mapping between the wheel and body frames due to a fixed reaction wheel configuration. This frame is only used when there are reaction wheels present. Note also that the reaction wheels, when present on the satellite, store momentum, meaning that they change the system's dynamics. This is pointed out in the various chapters depending on what type of satellite is in use.

2.3 Attitude representation

There are several ways to represent attitude. The attitude of a spacecraft can be represented as a rotation from one frame to another. The four types of representation we will briefly look at here are the rotation matrix, Euler angles, angle-axis, and unit quaternions.

In general terms, rotations evolve on SO(3), which is the special orthogonal group in three dimensions. The rotation of a vector $\mathbf{v}$ from an arbitrary frame $\{a\}$ to another frame $\{b\}$ can be written as

$$\mathbf{v}^{b} = \mathbf{R}_{a}^{b}\mathbf{v}^{a} \tag{2.3}$$

where $\mathbf{R}_{a}^{b} \in SO(3)$ is the rotation matrix between frames $\{a\}$ and $\{b\}$. The benefit of the rotation matrix representation is that it represents the attitude globally and uniquely. The drawback is that you need nine parameters to represent the attitude. The rotation matrix can be constructed directly from the basis of one frame represented in another frame.

Euler angles is an alternative to rotation matrices. The idea with Euler angles is that you can use three sequential rotations about different axes to represent (almost) any attitude. The drawback with Euler angles is that they have singularities in the angle that gets rotated about the second axis in the sequence. For some applications, this can be a non-issue due to design choices. Using boats or surface vessels as an example, the singularity can be placed such that it occurs when the bow is pointed straight up, which rarely occurs. Using the nature of the system in this way to design around the Euler angle deficiencies is more difficult for vehicles that are agile in all three attitude dimensions.

The concept behind the angle-axis is one of Euler's: any rotation can be represented by an axis and a rotation around it. This representation also introduces singularities, so it does not overcome the issues we can get with Euler angles. Quaternions, or unit quaternions, are based on the angle-axis representation. Unit quaternions are a global representation of SO(3) with its four parameters, unlike Euler angles, which cannot represent the full SO(3) since they only use three parameters. Quaternions map SO(3) twice, which means that the quaternion $\mathbf{q}$ and $-\mathbf{q}$

represent the same attitude, which potentially leads to some issues. Quaternions are the primary choice for attitude representation in this thesis, although some rotations are taken directly as rotation matrices due to their ease of construction.

For more on the differences between different attitude representations, see for example [17].

Unit quaternions, represented as $\mathbf{q} = \begin{bmatrix}\eta & \boldsymbol{\epsilon}\end{bmatrix}^\intercal = \begin{bmatrix}\eta & \epsilon_1 & \epsilon_2 & \epsilon_3\end{bmatrix}^\intercal$, are used to describe the attitude of the spacecraft, where η is the scalar part of the quaternion, $\boldsymbol{\epsilon}$ is the vector part of the quaternion and satisfies the condition $\eta^2 + \boldsymbol{\epsilon}^\intercal\boldsymbol{\epsilon} = 1$. $\mathbf{q}_b^o$ is denoted as the attitude of the body frame relative to the orbit frame. The rotation matrix between the two frames is given in terms of the quaternion as [18]

$$\mathbf{R}_b^o = \mathbf{I}_{3\times 3} + 2\eta_b^o\mathbf{S}(\boldsymbol{\epsilon}_b^o) + 2\mathbf{S}^2(\boldsymbol{\epsilon}_b^o), \tag{2.4}$$

where $\mathbf{I}_{3\times 3}$ is the three-dimensional identity matrix, and $\mathbf{S}(\cdot)$ is a skew-symmetric matrix that is equivalent to the cross product in three dimensions. In other words, $\mathbf{S}(\cdot)$ is given as

$$\mathbf{S}(\mathbf{x}) = \begin{bmatrix} 0 & -x_3 & x_2 \\ x_3 & 0 & -x_1 \\ -x_2 & x_1 & 0 \end{bmatrix}. \tag{2.5}$$

The time derivative of a rotation matrix $\mathbf{R}_o^b$ is $\dot{\mathbf{R}}_o^b = -\mathbf{S}(\boldsymbol{\omega}_{ob}^b)\mathbf{R}_o^b$, where $\boldsymbol{\omega}_{ob}^b$ denotes the angular velocity of $\{b\}$ relative to $\{o\}$.

The kinematic differential equation for $\mathbf{q}_b^o$ is given by

$$\dot{\mathbf{q}}_b^o = \begin{bmatrix}\dot{\eta}_b^o \\ \dot{\boldsymbol{\epsilon}}_b^o\end{bmatrix} = \frac{1}{2}\begin{bmatrix} -(\boldsymbol{\epsilon}_b^o)^\intercal \\ \eta_b^o\mathbf{I}_{3x3} + \mathbf{S}(\boldsymbol{\epsilon}_b^o)\end{bmatrix}\boldsymbol{\omega}_{ob}^b = \frac{1}{2}\mathbf{T}(\mathbf{q}_b^o)\boldsymbol{\omega}_{ob}^b, \tag{2.6}$$

where $\mathbf{T}(\cdot)$ is the angular velocity transformation matrix. Identically, the kinematic equation for the attitude of the body frame relative to the inertial frame is given by

$$\dot{\mathbf{q}}_b^i = \begin{bmatrix}\dot{\eta}_b^i \\ \dot{\boldsymbol{\epsilon}}_b^i\end{bmatrix} = \frac{1}{2}\begin{bmatrix} -\left(\boldsymbol{\epsilon}_b^i\right)^\intercal \\ \eta_b^i\mathbf{I}_{3x3} + \mathbf{S}(\boldsymbol{\epsilon}_b^i)\end{bmatrix}\boldsymbol{\omega}_{ib}^b = \frac{1}{2}\mathbf{T}(\mathbf{q}_b^i)\boldsymbol{\omega}_{ib}^b, \tag{2.7}$$

where all the previously introduced variables are defined similarly for the body frame relative to inertial frame attitude $\mathbf{q}_b^i$.

2.3.1 Angular velocity of LVLH relative to ECI

The angular velocity of the spacecraft's body frame relative to the orbit frame is given as

$$\boldsymbol{\omega}_{ob}^b = \boldsymbol{\omega}_{ib}^b - \boldsymbol{\omega}_{io}^b = \boldsymbol{\omega}_{ib}^b - \mathbf{R}_o^b\boldsymbol{\omega}_{io}^o, \tag{2.8}$$

where $\boldsymbol{\omega}_{io}^b$ is the angular velocity of the $\{o\}$ relative to the $\{i\}$, and $\boldsymbol{\omega}_{ib}^b$ is the angular velocity of the $\{b\}$ relative to the $\{i\}$.

The angular velocity of the $\{o\}$ frame relative to $\{i\}$, denoted $\boldsymbol{\omega}_{io}^o$, is defined in [19] as

$$\boldsymbol{\omega}_{io}^o = \mathbf{R}_i^o\frac{\mathbf{S}(\mathbf{r}^i)\mathbf{v}^i}{(\mathbf{r}^i)^\intercal\mathbf{r}^i}. \tag{2.9}$$

2.4 Optimization

2.4.1 General formulation

A general optimal control problem can be formulated as

$$\min_{\mathbf{x}} \ f(\mathbf{x}) \tag{2.10a}$$

$$\text{s.t. } \mathbf{h}(\mathbf{x}) = 0 \tag{2.10b}$$

$$\mathbf{g}(\mathbf{x}) \leq 0, \tag{2.10c}$$

where $\mathbf{h}(\mathbf{x})$ and $\mathbf{g}(\mathbf{x})$ are equality and inequality constraints, respectively. $f(\mathbf{x})$ is the cost function or objective function that is to be minimized. Common choices for $f(\mathbf{x})$ for control of vehicles include the first and second norm of the input, $|\mathbf{u}|$ and $\|\mathbf{u}\|$, sometimes called L_1 and L_2 optimization, respectively. Both these input norm minimization problems return optimal trajectories: For the L_1 case, the problem is often referred to as fuel minimization. With L_2 minimization, the problems get referred to as minimization of the energy, albeit this is energy in a different sense than what is discussed further in this thesis.

The constraints can take several different forms. Commonly, there are some upper and lower bounds on the input and potentially some state constraints. The formulation normally includes a constraint on the initial variables as the starting point of the optimization needs to be specified, sometimes referred to as an initial value problem. For a dynamical system, as we will investigate in this thesis, the system is also constrained by the dynamics of the system.

2.4.2 Direct optimization

There are two branches of methods to find solutions to optimal control problems: direct and indirect methods, which are separated by at which point in the process the system is discretized. With direct methods, the discretization occurs before the optimization. With indirect methods, the optimal solution is found before discretization. Indirect methods are based on analytical solutions based on theories such as Pontryagin's maximum principle. The main benefit direct methods have over indirect methods is that they always work numerically, whereas indirect methods require the existence of an analytical solution to work. In this thesis, the sole focus will be on direct optimal control whenever optimal control is discussed. As for the discretization method, all the problems are solved using direct multiple-shooting, a discretization method where the control horizon is partitioned into several smaller intervals.

Several types of solvers can be used for direct optimal control problems. Some methods take advantage of the problem being defined in a way that is easier for the computer to solve, primarily because the problem is convex. As the cost functions considered in this thesis are not convex, these methods are not investigated here. Instead, the optimal control problems here are solved as nonlinear programs. A common issue with direct optimization is that the optimization is local, which means that the optimizer might reach a local minimum. Newton-based methods use the information about the function's derivatives to find the optimal solution.

IPOPT is in this thesis chosen as it is preferable to other alternatives when the number of states becomes high, which it will when the time horizon increases [20].

For Newton-type methods, the cost function must be continuously two times differentiable. In this thesis, there are two expressions that need to be part of the objective function but are discontinuous. The function in question is a function that is only supposed to return a positive value or zero and an absolute value function. Such discontinuous functions can be expressed in terms of a max function. The max function is then implemented as the smooth max function given in (2.11),

$$\max(x_1, x_2) = \frac{1}{2}\left(x_1 + x_2 + \sqrt{(x_1 - x_2)^2 + \alpha}\right), \tag{2.11}$$

where α is a small positive constant. x_1 and x_2 are the first and the second arguments for the max function, so the max function returns approximately the argument with the highest value. For the two behaviors this thesis calls for: If you want the function to only return values of x if the argument is positive, it is possible to use $\max(0, x)$. The absolute value of x, $|x|$, can be implemented using the max function as $\max(-x, x)$.

2.4.3 Multi-objective optimization

The idea of multi-objective optimization is simple: the objective function can contain several variables that must be minimized. Sometimes, this might not be possible, of course: minimizing one variable may come at the cost of another variable. When one variable cannot improve without it coming at the cost of another variable, the solution is Pareto optimal.

There are two ways to move the optimized variables to their desired values. One way is to include the variables, for example, the final states, as constraints in the optimal control problem formulation. This is referred to as hard constraints. In this case, the solver must find a way to optimize the cost function while satisfying the constraints to the accuracy set by the solver's preferences. The alternative is what is called soft constraints. With soft constraints, the desired constraints are moved to the objective function. Using soft constraints, the solver does not have to fully satisfy the constraints anymore. Instead, the weight of the cost function determines how much the solver values get close to the constraints. This gives rise to a multi-objective optimization. A potential motivation for including the variables in the cost function instead of as constraints could be that the problem is hard for the computer to solve otherwise.

2.5 HYPSO

HYPSO is a multi-satellite mission at the NTNU SmallSat Lab. The purpose of the HYPSO mission is to monitor ocean color, particularly harmful algal blooms in coastal areas. The satellites, at the time this thesis is written, include the satellites HYPSO-1 and HYPSO-2. Both of the satellites are 6U CubeSats equipped with hyperspectral imagers. The hyperspectral imagers are push-broom hyperspectral imagers, which limits both the direction the imager needs to be when the images are

to be taken and the velocity of the scan. An analysis was performed for the HYPSO-1 satellite before launch [21], determining that a slew maneuver with a fixed angular velocity was required to get the desired resolution from the hyperspectral images.

2.5.1 HYPSO-1

The HYPSO-1 satellite is a 6U CubeSat with a pushbroom hyperspectral imager. The satellite bus was made by Kongsberg NanoAvionics, and the payload, meaning the hyperspectral imager itself, was constructed at NTNU. HYPSO-1 communicates with the ground through UHF and S-band. The satellite was launched in January 2022. A picture of the satellite undergoing testing before launch is shown in Figure 2.1.

Figure 2.1: The HYPSO-1 satellite before launch. Credit: Evelyn Honoré-Livermore.

2.5.2 HYPSO-2

HYPSO-2 is a 6U CubeSat, like HYPSO-1, and is similar in that the payload is the same. For the work in this thesis, there are two main differences between HYPSO-1 and HYPSO-2: HYPSO-2 will have deployable solar panels that will increase the energy the satellite gains, and HYPSO-2 will feature an X-band antenna in addition to the communication capabilities that HYPSO-1 already has. The X-band antenna will increase the satellite's communication capabilities and draw more power when in use. The satellite will launch in 2024. A picture showing the satellite bus, with the solar panels deployed, can be seen in Figure 2.2.

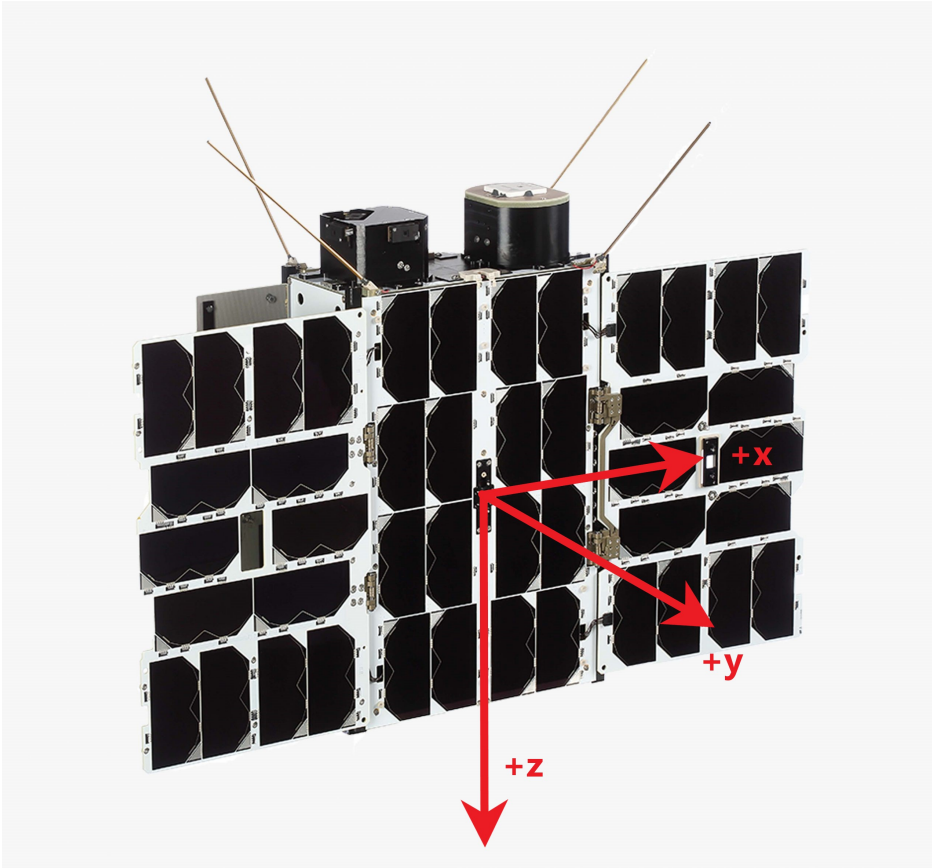

Figure 2.2: The HYPSO-2 satellite bus, image courtesy of Kongsberg NanoAvionics. Reference frame as is used in [7].

Part I

Energy Optimal Attitude Control

Chapter 3

Introduction

In the articles this part is based on, we have redefined energy optimal attitude control. In the literature, whatever is considered energy optimal has usually been defined as the minimum of the first or the second norm of the control input, meaning that previous authors generally have worked to minimize fuel or to minimize the square of the input, which has often been considered the energy of the signal. Our formulation is simple in that we aim to maximize the satellite's net power through actions taken by the attitude control system. What this means, in essence, is that we maximize the difference between the power the satellite manages to gain from exposure to the Sun and what it spends on actuation. Using this formulation, we find the optimal attitude trajectory between two points with respect to energy. In the context of a traditional satellite setup, this net power framework merges two control modes, sun pointing and target pointing, into a single optimization-based maneuver.

This part has three chapters: Chapter 4 is based on

[2] **B. A. Kristiansen**, J. T. Gravdahl, and T. A. Johansen, "Energy optimal attitude control for a solar-powered spacecraft," *European Journal of Control*, 2021 European Control Conference Special Issue, vol. 62, pp. 192–197, Nov. 2021,

which is the article where we first introduced the net power concept. The simulation setup is based on the HYPSO-1 satellite, and the final time of the optimization is set very short relative to a complete orbit. From Figure 3.1, the short time horizon places the paper in section B, meaning the shorter maneuvers, such as maneuvers between image captures or between image capture and downlink.

Chapter 5 is based on

[7] **B. A. Kristiansen**, J. T. Gravdahl, S. Gros, and T. A. Johansen, "Energy Optimal Attitude Control and Task Execution for a Solar-Powered Spacecraft", *IEEE Transactions on Control Systems Technology*, 2023, *conditionally accepted for publication*,

which is an extension to the work in Chapter 4. The final time is extended to cover several longer maneuvers over a full orbit. The scenario itself is based on HYPSO-2 and shows more of how the net power framework creates value by showing the

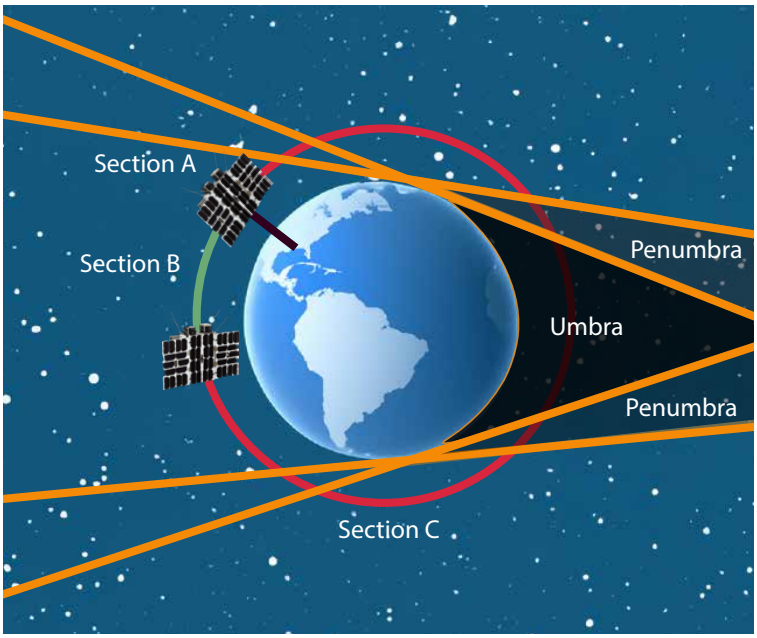

Figure 3.1: Thesis outline.

energy gain on the margins when the utilization of the satellite increases throughout section C in Figure 3.1. The paper also shows how to include a second set of actuators into the framework.

And finally, Chapter 6 is based on

[5] **B. A. Kristiansen**, J. T. Gravdahl, S. Gros, and T. A. Johansen, "Energy optimal attitude control of a satellite actuated by magnetorquers in minimum time", in *Proceedings of the 7th IEEE Conference on Control Technology and Applications (CCTA)*, Bridgetown, Barbados, Aug. 2023,

which also includes minimization over time. In this paper, and subsequently, in Chapter 6, we investigate using a satellite equipped with only magnetic actuators. While many satellites have other actuators besides magnetorquers, magnetorquers are still popular for tiny satellites due to their size and for all satellites owing to their reliability, a property the other actuators do not share. Their functioning principle and weak torque make them one of the more difficult actuators to use, making them an interesting case study for combining the net power framework with minimum time. This chapter is also in the section marked "Section C" in Figure 3.1.

Larger satellites often have a range of actuators, if not an assembly of all the actuators. The framework presented here works for all types of solar-powered satellites or spacecraft as the formulation only requires a general formulation based on geometry for the function describing the solar power the spacecraft gains and some models that represent the power lost from using a given actuator. A possible issue arises when the spacecraft is equipped with thrusters, which are not solely electricity-based actuators. Thrusters are usually included for specific maneuvers,

but as fuel is a perishable resource, their use does not translate well to the net power framework. So far, the framework has not been extended to allow for thrusters.

The two sections, Section 3.1 and Section 3.2, contain the common themes between the three articles on which this part is based. In Section 3.1, the shared state of the art on the topic is presented in all the articles mentioned above. The general version of the energy optimal control framework, as first shown in [2], is given in Section 3.2. This general formulation is in use in all three chapters in this part.

3.1 Introduction

Attitude control for spacecraft is a well-known problem [9]. Regarding optimal attitude control, research has been conducted on various cost functions. Optimization with respect to time is common; see for example [10–13]. Others have proposed optimal attitude control schemes with generalized cost functions [22, 23]. Optimization with respect to cost functions based on angular velocities has been studied in [24]. The authors in [16] and [25] used power models for optimization. In [16], the authors exploited a power model based on the energy lost due to the system's mechanics. In contrast, [25] uses a power model based on the power available in a control moment gyroscope. Minimizing with respect to energy functions based on the input, for example, by using a performance index [26] or an input-related norm [27], is a popular approach. Another name for the minimization of the input is minimal effort [13]. Minimizing the norm of the input has often been considered energy optimal. The authors in [15] define the optimal control problem of minimizing the input square as the optimal energy approach. The contribution of this paper is to show that solar power harvesting should be included in the optimization alongside the power consumption term to achieve energy-optimal control. This influences how the cost function is designed: in this part, we propose a physics-based cost function based on net electric power that we then use to achieve the minimal-energy cost control objective.

3.2 Energy optimal attitude control

The goal of the net energy optimization problem is to maximize the difference between the energy generated by the solar panels and the energy used to control the spacecraft's attitude. The net power function this objective is based on will have the general form

$$P(\mathbf{x}, \mathbf{u}) = s(\mathbf{x}) - m(\mathbf{x}, \mathbf{u}), \tag{3.1}$$

where the $s(\mathbf{x})$ is a function describing the power produced by the solar panels, and $m(\mathbf{x}, \mathbf{u})$ is the power consumed by the actuators. $\mathbf{x}$ is the state of the system, whereas $\mathbf{u}$ is the input. The power produced by the solar panels, $s(\mathbf{x})$, will, for non-symmetrical spacecraft, depend on the spacecraft's attitude and the position of the Sun relative to the spacecraft. The function can be seen as the product of three terms,

$$s(\mathbf{x}) = \eta_{\text{in}} \kappa(\mathbf{R}_b^i, \mathbf{r}_{\text{Sun}}) \delta(\mathbf{r}_{\text{Sun}}, \mathbf{r}_{\text{Earth}}), \tag{3.2}$$

where $\kappa(\cdot,\cdot)$ is the solar power the satellite would get with its current attitude relative to the position of the Sun, $\delta(\cdot,\cdot)$ is a function which returns the one when the satellite is irradiated by the Sun, zero when it is not. η_{in} is an efficiency parameter that will be introduced in Chapter 5.

The net energy objective function follows from integrating the net power in (4.1),

$$E = \int_0^T P(\mathbf{x},\mathbf{u})\ dt = \int_0^T \left(s(\mathbf{x}) - m(\mathbf{x},\mathbf{u})\right)\ dt. \tag{3.3}$$

When optimizing net energy, the goal will be to maximize (4.2), which is the equivalent of minimizing its negative. In addition to the net energy terms, an extra term J_{F} is added to reflect the cost of any other objective that merits its own cost, typically the final state. In total, the cost function that is to be minimized is

$$J = J_{\text{F}} - E - E_{\text{other}} = J_{\text{F}} - \int_0^T P(\mathbf{x},\mathbf{u})\,dt - E_{\text{other}}(\mathbf{x},t). \tag{3.4}$$

where E_{other} is the energy used by other subsystems. This term is first introduced in Chapter 5.

In the following chapters, the J_{F} term is made up of a term for the angular velocity and another for the attitude; in equation form, this becomes

$$\begin{aligned} J_{\text{F}} &= k_2 J_{\text{path}} + k_3 J_{\text{velocity}} \\ &= k_2\left(1 - |(\mathbf{q}(T))^\intercal\,\mathbf{q}_{\text{ref}}|\right) + k_3\left(\left(\boldsymbol{\omega}_e^b\right)^\intercal\,\boldsymbol{\omega}_e^b\right), \end{aligned} \tag{3.5}$$

where k_2 and k_3 are constants and $\boldsymbol{\omega}_e^b = \boldsymbol{\omega}_{\text{ref}}^b - \boldsymbol{\omega}_{ib}^b$. $|(\mathbf{q}(T))^\intercal\,\mathbf{q}_{\text{ref}}|$ is implemented using the smooth max function defined in (2.11) to ensure that the cost is differentiable.

Choosing to put the final states of the attitude and the angular velocity in the cost function as opposed to having them as hard constraints in the optimal control problem formulation is a choice, which in this case, makes sense since the cost function is difficult for the solver to solve, particularly the $\kappa(\cdot,\cdot)$ term in (4.3). The differences between soft and hard constraints are discussed in Section 2.4.1.

3.2.1 PD Sun pointing controller

In the following chapters, a PD controller is used as a comparison to show the usefulness of the energy optimal control formulation. It is also used to produce initial guesses for the solver. The PD controller used for benchmarking is given by [9]

$$\boldsymbol{\tau}_u^b = \mathbf{K}_p\boldsymbol{\epsilon}_e - \mathbf{K}_d\left(\boldsymbol{\omega}_{ib,\text{ref}}^b - \boldsymbol{\omega}_{ib}^b\right), \tag{3.6}$$

where $\mathbf{K}_d > 0,\ \mathbf{K}_p > 0$ are constant controller gain matrices, $\boldsymbol{\omega}_{ib,\text{ref}}^b$ is the reference angular velocity, and $\boldsymbol{\epsilon}_e$ is the error in the vector part of the quaternion, given as the final three elements of $\mathbf{q}_e$, which in turn is given as

$$\mathbf{q}_e = \mathbf{q}_d^{-1} \otimes \mathbf{q}, \tag{3.7}$$

where $\mathbf{q}_d$ is the desired quaternion, and $\otimes$ is the Hamilton product.

The quaternion references for the PD controller are set to the attitude with the maximal incoming solar energy at the beginning of the time horizon, then to the final reference quaternion towards the end. The attitude with the maximal incoming solar power is found by minimizing the solar power function $\kappa(\cdot)$ from (3.2) with respect to the attitude, here represented by the attitude unit quaternion $\mathbf{q}$,

$$\min_{\mathbf{q}} \; -\kappa(\mathbf{q}, \mathbf{r}_{\text{Sun}})^2 + k_1 J_{\text{path}} \tag{3.8a}$$

$$\text{s.t. } \mathbf{q}^\intercal \mathbf{q} = 1, \tag{3.8b}$$

where k_1 is a positive constant, J_{path} is a cost introduced to ensure that only one attitude would be optimal. J_{path} is defined as [28]

$$J_{\text{path}} = 1 - |\mathbf{q}^\intercal \mathbf{q}_{\text{ref}}|, \tag{3.9}$$

where $\mathbf{q}_{\text{ref}}$ is the reference quaternion. The absolute value is implemented using the smooth max function defined in (2.11), so that $|\mathbf{q}^\intercal \mathbf{q}_{\text{ref}}| = \max(\mathbf{q}^\intercal \mathbf{q}_{\text{ref}}, -\mathbf{q}^\intercal \mathbf{q}_{\text{ref}})$. Note that the metric used in J_{path} does not differentiate between the positive and negative inner product. Thus, the distance between the reference quaternion and the positive and the negative quaternion will be the same. The J_{path} term is only meant to differentiate between attitudes if several attitudes would otherwise be optimal, and for that reason, k_1 should be small. The scenario of several optimal attitudes is not unlikely: Using a CubeSat with only one solar panel on one side as an example, it is trivial to see that it would be optimal to point the axis with the solar panel towards the sun vector, but any rotation about this axis would result in the same optimal solar power.

Chapter 4

Energy optimal attitude control for a solar-powered spacecraft

This chapter is based on

[2] **B. A. Kristiansen**, J. T. Gravdahl, and T. A. Johansen, "Energy optimal attitude control for a solar-powered spacecraft," European Journal of Control, 2021 European Control Conference Special Issue, vol. 62, pp. 192–197, Nov. 2021.

4.1 Introduction

This chapter is organized as follows: Section 4.2 introduces the novel cost function based on net power, defined as the sum of the incoming solar power and the actuation power consumption of the system. In Section 4.3, the optimal attitude control problem is stated, both in the general case and for a reaction wheel actuated spacecraft with attitude represented with unit quaternions. Section 4.4 contains the formulation for the sun-pointing PD controller and the optimal control problem defining its references. The setup for a numerical example using the developed control algorithm is shown in Section 4.5. The results from the simulation, where the optimal energy cost function introduced in Section 4.2 is compared to the sun-pointing PD controller introduced in Section 4.4, are shown in Section 4.6. A discussion of the results is included in Section 4.7, while Section 4.8 concludes the chapter.

4.2 Objective function design

The goal of the net energy optimization problem is to maximize the difference between the energy generated by the solar panels and the energy used to control the spacecraft's attitude. The net power function this objective is based on will have the general form

$$P(\mathbf{x}, \mathbf{u}) = s(\mathbf{x}) - m(\mathbf{x}, \mathbf{u}), \tag{4.1}$$

where the $s(\mathbf{x})$ is a function describing the power produced by the solar panels, and $m(\mathbf{x}, \mathbf{u})$ is the power consumed by the actuators. $\mathbf{x}$ is the state of the system, whereas $\mathbf{u}$ is the input. The power produced from the solar panels will, for non-symmetrical spacecraft, depend on the spacecraft's attitude and the position of the Sun relative to the spacecraft.

The net energy objective function follows from integrating the net power in (4.1),

$$E = \int_0^T P(\mathbf{x}, \mathbf{u}) \, \mathrm{d}t = \int_0^T \left(s(\mathbf{x}) - m(\mathbf{x}, \mathbf{u}) \right) \, \mathrm{d}t. \tag{4.2}$$

The solar power $s(\mathbf{x})$ can be described as

$$s(\mathbf{x}) = \kappa(\mathbf{R}_b^i, \mathbf{r}_{\text{Sun}}) \delta(\mathbf{r}_{\text{Sun}}, \mathbf{r}_{\text{Earth}}), \tag{4.3}$$

where the current solar power $\kappa(\cdot)$ is the sum of incoming power from all the solar panels currently exposed to solar irradiance. $\mathbf{r}_{\text{Sun}}$ and $\mathbf{r}_{\text{Earth}}$ are the vectors from the center of the Sun to the spacecraft and from the center of the Earth to the spacecraft, respectively. $\kappa(\cdot)$ is a function of the attitude rotation matrix representation $\mathbf{R}_b^i$, which represents the attitude of the body frame b with respect to the inertial frame i. The $\delta(\cdot)$ function is a function that returns the solar irradiance that reaches the satellite: the function returns 0 when no part of the body is exposed to the Sun, and 1 when there is no occluding body. This function would indicate when the spacecraft is in eclipse for a spacecraft orbiting the Earth. For satellites where the solar panels are flat and not occluded, $\kappa(\cdot)$ can be defined as

$$\kappa(\mathbf{R}_b^i, \mathbf{r}_{\text{Sun}}) = \sum_{j=1}^{n_s} \max\left(\left(\hat{\mathbf{s}}^b\right)^\intercal \hat{\mathbf{n}}_j^b, 0 \right) \left(\left(\hat{\mathbf{s}}^b\right)^\intercal \hat{\mathbf{n}}_j^b \right) c_{s,j} A_j, \tag{4.4}$$

where n_s is the number of surfaces with solar panels, $\hat{\mathbf{s}}^b$ is the normalized solar vector, and $\hat{\mathbf{n}}_j^b$ is the normal vector of the jth solar panel pointing out of the surface. Both the aforementioned vectors are represented in the body frame, which explains how $s(\mathbf{x})$ depends on the spacecraft attitude, as the sun vector is originally represented in an inertial reference frame. $c_{s,j}$ is a constant that is the product of the solar irradiance and the efficiency of the jth solar panel with surface area A_j.

To ensure that the objective function (4.2) is differentiable, the max function is implemented as the smooth max function given in (4.5),

$$\max(x_1, x_2) = \frac{1}{2} \left(x_1 + x_2 + \sqrt{(x_1 - x_2)^2 + \alpha} \right), \tag{4.5}$$

where α is a small positive constant.

This work is motivated by HYPSO-1 [21], a satellite mission at NTNU with a 6U CubeSat actuated by reaction wheels. For a spacecraft actuated by reaction wheels, the power consumed by the actuators $m(\mathbf{x}, \mathbf{u})$ is given by

$$m(\mathbf{x}, \mathbf{u}) = -\frac{1}{\eta_{rw}} \left(\boldsymbol{\tau}_u^b \right)^\intercal \boldsymbol{\omega}_{\text{RW}}^b, \tag{4.6}$$

where η_{rw} is the energy conversion efficiency of the reaction wheels, $\boldsymbol{\tau}_u^b$ is the torque from the reaction wheels, and $\boldsymbol{\omega}_{\mathrm{RW}}^b$ is the angular velocity of the reaction wheels in the body frame.

When optimizing net energy, the goal will be to maximize (4.2), which is the equivalent to minimizing its negative. In addition to the net energy terms, an extra term J_{F} is added to reflect the cost of any other objective that merits its own cost, typically the final state. In total, the cost function that is to be minimized is

$$J = J_{\mathrm{F}} - E = J_{\mathrm{F}} - \int_0^T P(\mathbf{x}, \mathbf{u})\,\mathrm{d}t. \tag{4.7}$$

4.3 Optimal control problem statement

The optimal control problem can be stated the following way:

$$\min_{\mathbf{x},\mathbf{u}} \; J_{\mathrm{F}} - \int_0^T P(\mathbf{x}, \mathbf{u})\,\mathrm{d}t \tag{4.8a}$$
$$\text{s.t. } \dot{\mathbf{x}} = \mathbf{f}(\mathbf{x}, \mathbf{u}) \tag{4.8b}$$
$$\mathbf{g}(\mathbf{x}) \leq 0 \tag{4.8c}$$
$$\mathbf{u}_{\mathrm{lb}} \leq \mathbf{u} \leq \mathbf{u}_{\mathrm{ub}} \tag{4.8d}$$
$$\mathbf{x}(0) = \mathbf{x}_0, \tag{4.8e}$$

where the objective function defined in (4.7) in Section 4.2 is constrained by the system dynamics $\mathbf{f}(\mathbf{x}, \mathbf{u})$ in (4.8b) and the initial state $\mathbf{x}_0$. T is the length of the control horizon. $\mathbf{g}(\mathbf{x})$ is a vector constraining the state vector to some bounds, such as upper and lower bounds on reaction wheel angular velocities.

For the simulation example of this chapter, we will investigate the optimal control problem for a solar-powered spacecraft actuated by reaction wheels with attitude represented by unit quaternions. Defining the state variable $\mathbf{x} = \left[\mathbf{q}^\intercal \;\; \left(\boldsymbol{\omega}_{ib}^b\right)^\intercal \;\; \left(\boldsymbol{\omega}_{\mathrm{RW}}^b\right)^\intercal\right]^\intercal$ and the input $\mathbf{u} = \boldsymbol{\tau}_u^b$, the optimal control problem is defined by

$$\min_{\mathbf{x},\mathbf{u}} \; J_{\mathrm{F}} - \int_0^T P(\mathbf{x}, \mathbf{u})\,\mathrm{d}t \tag{4.9a}$$
$$\text{s.t. } \dot{\mathbf{q}} = \frac{1}{2}\mathbf{T}(\mathbf{q})\boldsymbol{\omega}_{ib}^b + \frac{1}{2}\rho\mathbf{q}\left((\mathbf{q}^\intercal\mathbf{q})^{-1} - 1\right) \tag{4.9b}$$
$$\dot{\boldsymbol{\omega}}_{ib}^b = \mathbf{J}_s^{-1}\left(-\boldsymbol{\omega}_{ib}^b \times \left(\mathbf{J}\boldsymbol{\omega}_{ib}^b + \mathbf{J}_w\boldsymbol{\omega}_{\mathrm{RW}}^b\right) - \boldsymbol{\tau}_u^b\right) \tag{4.9c}$$
$$\dot{\boldsymbol{\omega}}_{\mathrm{RW}}^b = \mathbf{J}_w^{-1}\boldsymbol{\tau}_u^b - \dot{\boldsymbol{\omega}}_{ib}^b \tag{4.9d}$$
$$\boldsymbol{\tau}_{u,\mathrm{lb}}^b \leq \boldsymbol{\tau}_u^b \leq \boldsymbol{\tau}_{u,\mathrm{ub}}^b \tag{4.9e}$$
$$\mathbf{x}(0) = \mathbf{x}_0, \tag{4.9f}$$

where (4.9b) describe the kinematics of the system, while (4.9c) and (4.9e) describe the dynamics for the spacecraft and for the reaction wheels, respectively [1]. $\mathbf{q} = [\eta \;\; \boldsymbol{\epsilon}^\intercal]^\intercal$ is the attitude unit quaternion, and $\boldsymbol{\omega}_{ib}^b$ is the angular velocity of the body frame about the inertial reference frame represented in the body frame. For this

scenario, one reaction wheel exists on each body frame axis. The inertia matrices $\mathbf{J}_s$, $\mathbf{J}_w$, and $\mathbf{J} = \mathbf{J}_s + \mathbf{J}_w$ represent the inertia of the spacecraft without the reaction wheels about their rotational axes, the reaction wheels about their rotational axes, and the total inertia of the spacecraft, respectively. $\boldsymbol{\tau}_{u,\text{lb}}^b$ and $\boldsymbol{\tau}_{u,\text{ub}}^b$ are the lower and upper bound on the reaction wheel torques, respectively. The $\mathbf{T}(\mathbf{q})$ matrix is given by [18]

$$\mathbf{T}(\mathbf{q}) = \begin{bmatrix} -\boldsymbol{\epsilon}^\intercal \\ \eta \mathbf{I}_{3\text{x}3} + \boldsymbol{\epsilon}\times \end{bmatrix}, \tag{4.10}$$

where $\mathbf{I}_{3\text{x}3}$ is the three-dimensional identity matrix, and $\times$ denotes the vector cross product. η is the scalar part and $\boldsymbol{\epsilon}$ is the vector part of the quaternion.

The unit quaternion is not constrained by a normalization constraint other than that the initial attitude should be a unit quaternion. The norm of the unit quaternion is preserved through the accuracy of the numerical integrator and the Baumgarte stabilization term $\frac{1}{2}\rho\mathbf{q}\left((\mathbf{q}^\intercal\mathbf{q})^{-1} - 1\right)$ with a small positive constant ρ [29].

4.4 PD controller

The PD controller used for benchmarking and creating initial guesses is defined in Section 3.2.

4.5 Simulation setup

The optimal control action is calculated using the IPOPT solver [20] in CasADi [30], where the optimal control problem in (4.9) is discretized as a multiple-shooting problem. The dynamics are discretized and integrated using CasADi's built-in Runge-Kutta integrator.

The energy generated by the optimal attitude control strategy given by the problem formulated in (4.9) is compared to a sun-pointing PD controller, which uses a setpoint for sun-pointing given by the optimal attitude for the problem in (3.8), which is also solved with IPOPT using CasADi. The energy-optimal control trajectory, based on (4.9), is calculated only once and compared to the sun-pointing PD in each time step. The simulation runs for 40 seconds, where the sun-pointing PD controller is fed the optimal attitude from (3.8) as reference for the first 20 seconds, and then the PD controller points towards the final reference attitude. The optimal net energy control strategy is only given the simulation's desired start and end states. This example takes place entirely in the part of the orbit that is in the sun, so $\delta(\cdot)$ as defined in (4.3) is set to 1. The torque from the PD controller is constrained in the same way as it is for the optimal control problem in (4.9). The step size used for the integrator was calculated by dividing the length of the time horizon by the number of control intervals. With 80 control intervals for the multiple-shooting method applied to (4.9), this gave a step size h of 0.5 s. The constants used in the simulation can be seen in Table 4.1. Note that the constant $c_{s,j}$ from (4.4), given by the solar irradiance times the given solar panel's efficiency, is equal to c_s in this simulation as all the solar panels are identical.

Table 4.1: Optimization constants

Variable	Value	Unit
Simulation time (T)	40	s
Control intervals (N)	80	-
Step size (h)	0.5	s
Solar irradiance	1361	$\mathrm{W/m^2}$
Solar panel efficiency	20	%
c_s	272.2	$\mathrm{W/m^2}$
η_{rw}	85	%
α	10^{-7}	-
k_1	1	$\mathrm{W^2}$
k_2	$3.75 \cdot 10^4$	W
k_3	$3.75 \cdot 10^6$	$\mathrm{W \cdot s^2}$
ρ	10^{-2}	-
$\boldsymbol{\tau}^b_{u,\mathrm{lb}}$	$-3.2 \cdot 10^{-3}$	N·m
$\boldsymbol{\tau}^b_{u,\mathrm{ub}}$	$3.2 \cdot 10^{-3}$	N·m

The inertia matrices are given by [1]

$$\mathbf{J} = \begin{bmatrix} 0.0775 & 0.0002 & -0.0002 \\ 0.0002 & 0.1067 & 0.0005 \\ -0.0002 & 0.0005 & 0.0389 \end{bmatrix} \mathrm{kg \cdot m^2}, \quad \mathbf{J}_w = I_w \mathbf{I}_{3\mathrm{x}3}, \tag{4.11}$$

where $I_w = 2.1 \cdot 10^{-4}$ kg·m^2, and $\mathbf{J}_s$ is given by the relation $\mathbf{J}_s = \mathbf{J} - \mathbf{J}_w$. In this simulation, all the sides of the 6U satellite are covered in solar panels. The areas of the solar cell covered surfaces A_j are then entries in the vector A in (4.12),

$$A = [0.03, 0.06, 0.02, 0.03, 0.06, 0.02]\mathrm{m^2}. \tag{4.12}$$

The sun vector is given in the inertial frame as $\hat{\mathbf{s}}^i = [0.2673, 0.5345, 0.8018]^\intercal$ and is constant throughout the simulation due to the simulation's relatively short duration. The initial conditions are $\mathbf{x}_0 = \left[\mathbf{q}(0); \boldsymbol{\omega}^b_{ib}(0); \boldsymbol{\omega}^b_{\mathrm{RW}}(0)\right] = [0, 0, 1, 0, 0, 0, 0, 0, 0, 0]^\intercal$. Both control algorithms attempt to control the system toward the same quaternion reference $\mathbf{q}_{\mathrm{ref}} = [0, 1, 0, 0]^\intercal$, as well as the angular velocity reference $\boldsymbol{\omega}^b_{ib,\mathrm{ref}} = [0, 0, 0]^\intercal$. The final cost for (4.9), J_{F}, is defined as

$$\begin{aligned} J_{\mathrm{F}} &= k_2 J_{\mathrm{path}} + k_3 J_{\mathrm{velocity}} \\ &= k_2 \left(1 - |(\mathbf{q}(T))^\intercal \mathbf{q}_{\mathrm{ref}}|\right) + k_3 \left(\left(\boldsymbol{\omega}^b_e\right)^\intercal \boldsymbol{\omega}^b_e \right), \end{aligned} \tag{4.13}$$

where k_2 and k_3 are constants with values given in Table 4.1 and $\boldsymbol{\omega}^b_e = \boldsymbol{\omega}^b_{\mathrm{ref}} - \boldsymbol{\omega}^b_{ib}$. $|(\mathbf{q}(T))^\intercal \mathbf{q}_{\mathrm{ref}}|$ is implemented with the smooth max function the same way as it is for (3.9) to ensure that the cost is differentiable. The torque from the sun-pointing PD controller is constrained by the same bounds as the optimal control torque. The PD controller gains $\mathbf{K}_p$ and $\mathbf{K}_d$ with the constant values $8 \cdot 10^{-2}$ and $1.08 \cdot 10^{-1}$, respectively, are found through tuning.

4.6 Results

Figure 4.1 shows the optimal quaternion trajectory. The trajectory for the sun-pointing PD controller is shown in Figure 4.2, where it is shown with the quaternion references. The angular velocity trajectories of the two controllers are plotted in Figure 4.3. In Figure 4.4, the input torques of both control schemes are plotted, where it is clearly shown that all torques are bounded by $\pm 3.2 \cdot 10^{-3}$.

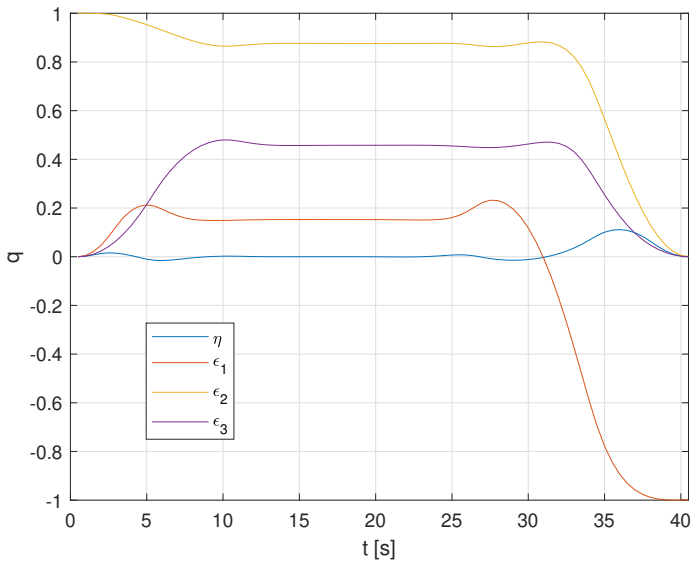

Figure 4.1: Optimal quaternion trajectory.

The individual parts of the net energy cost function can be plotted as functions of the quaternion and torque histories. The power function $P(\mathbf{x}, \mathbf{u})$, as defined in (4.1), is plotted in Figure 4.5. Its components $s(\mathbf{x})$ and $m(\mathbf{x}, \mathbf{u})$ are plotted in Figure 4.6 and Figure 4.7, respectively.

Figure 4.8 shows how the optimal control derived from (4.9) compares to the sun-pointing PD controller for the net energy objective described in (4.2) over the simulated time horizon. The difference between the net energy score of the optimal response and the PD controller is divided by the PD controller's net energy score to give Figure 4.9, which shows the increase in energy gained up until a point in time t, given as a percentage, calculated as $100\% \cdot \frac{E_{t,\mathrm{opt}} - E_{t,\mathrm{PD}}}{E_{t,\mathrm{PD}}}$, where E_t is given by (4.2) with $T = t$.

The net energy results for both the optimal solution and the sun-pointing PD controller are showcased in Table 4.2, which shows that the optimal solution improves on the score from the sun-pointing PD controller by about 13% for the given example.

The computation time of the given control scenario is shown in Table 4.3. The optimization was performed with a 2.4 GHz 8-core processor.

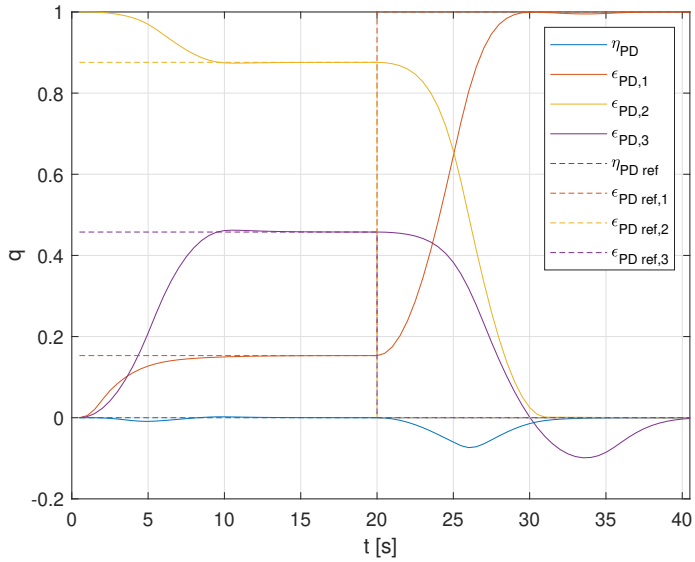

Figure 4.2: Sun-pointing trajectory with PD control, and references.

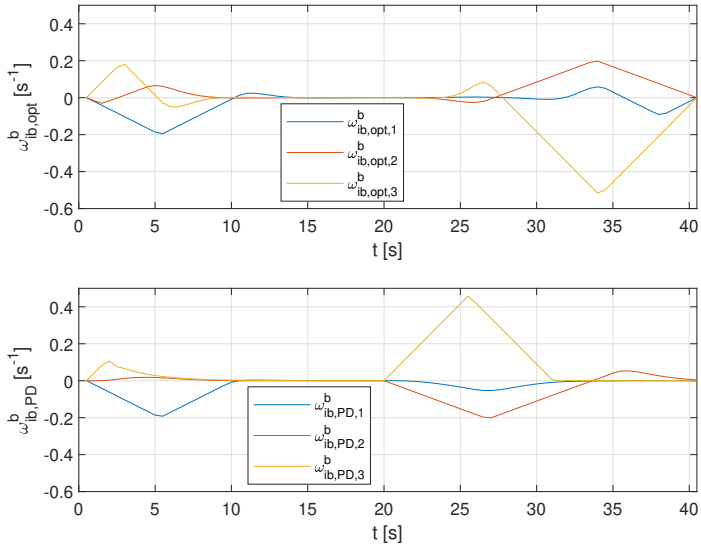

Figure 4.3: $\boldsymbol{\omega}^b_{ib}$ for the optimal plan and for the sun-pointing PD controller.

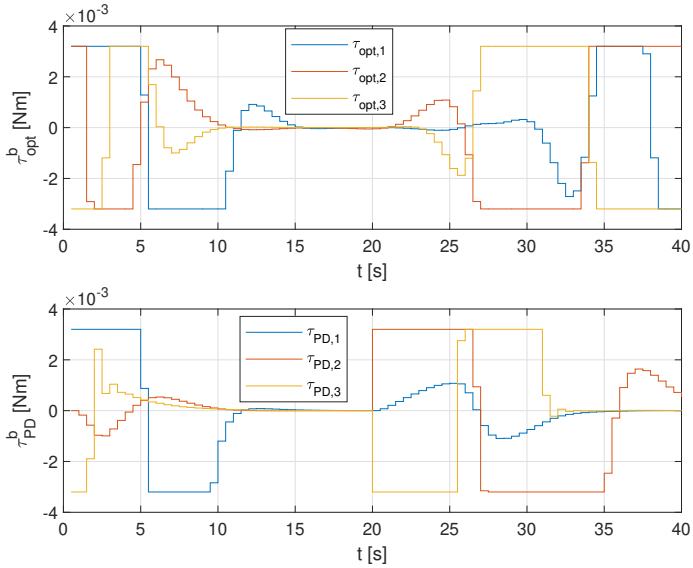

Figure 4.4: $\boldsymbol{\tau}_u^b$ for the optimal plan and for the sun-pointing PD controller.

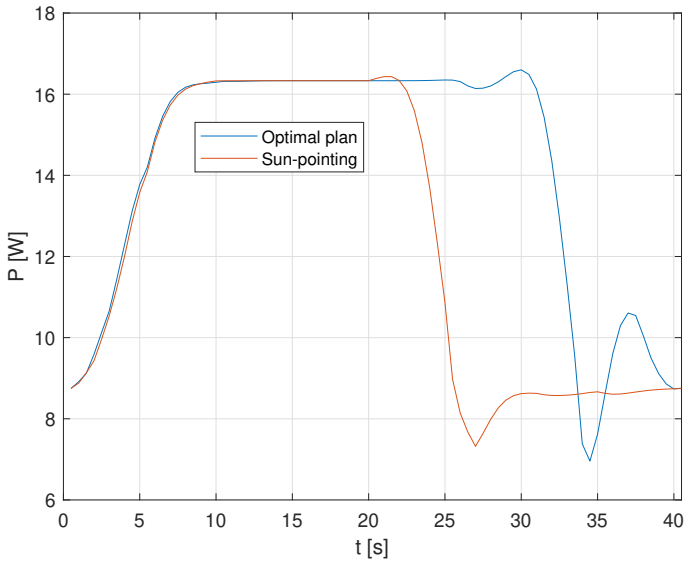

Figure 4.5: Power, $P(\mathbf{x}, \mathbf{u})$, over time for the optimal plan and sun-pointing.

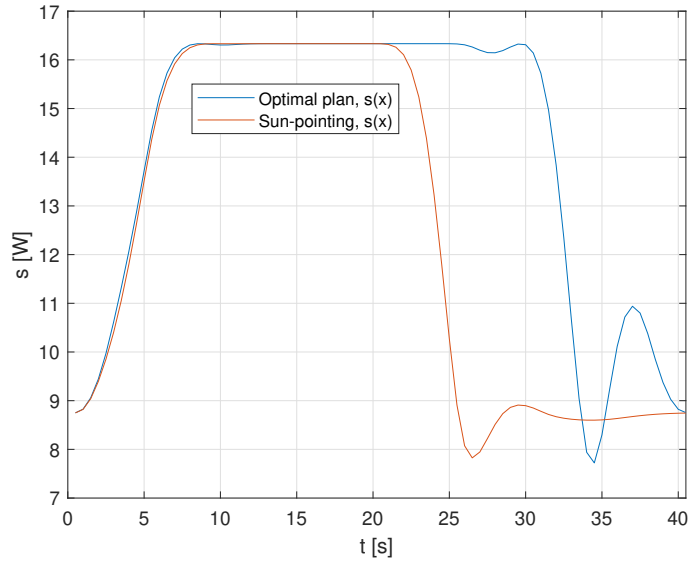

Figure 4.6: Solar power, $s(\mathbf{x})$, over time.

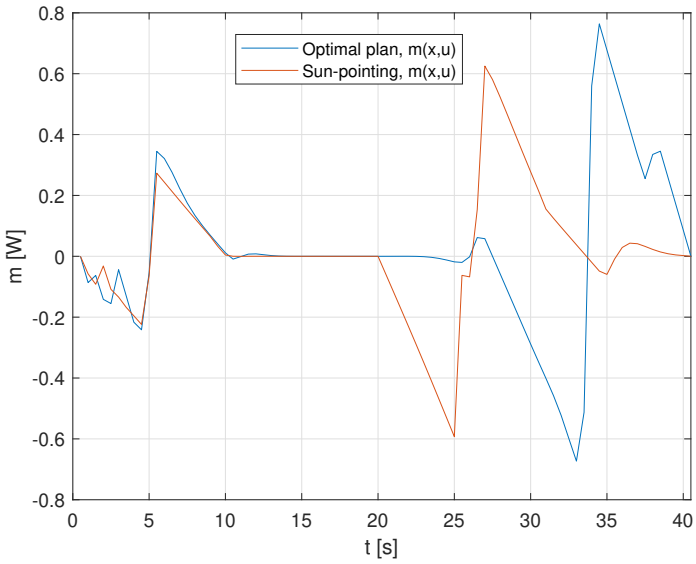

Figure 4.7: Actuation power, $m(\mathbf{x}, \mathbf{u})$, over time.

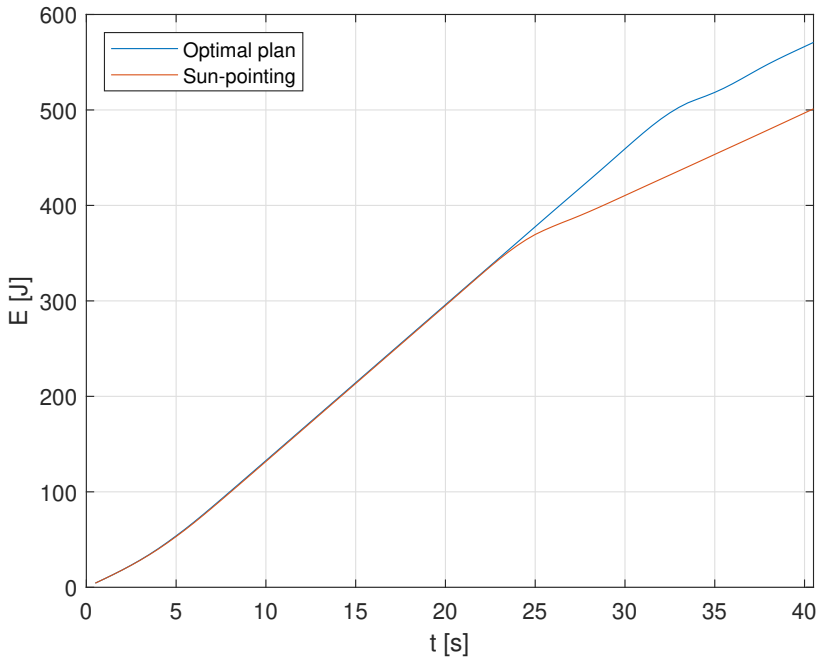

Figure 4.8: Net energy, E, evolution over time.

Table 4.2: Net energy

Control scheme	Energy score
Optimal net energy	566.4 J
Sun-pointing PD controller	501.2 J

Table 4.3: IPOPT output

Output	Value
Number of iterations	48
Total CPU secs in IPOPT (w/o function evaluations)	0.463
Total CPU secs in NLP function evaluations	12.025

4.7 Discussion

From Table 4.2 it is clear that the optimal control problem in (4.9) produces a better net energy score compared to the sun-pointing PD controller. This is illustrated in Figure 4.8, where the net energy of the optimal solution, the blue line, is slightly above the orange sun-pointing line throughout the simulation. The lines diverge after 25 seconds, where the sun-pointing PD has started moving away from the optimal sun-pointing attitude towards the reference quaternion. This divergence is

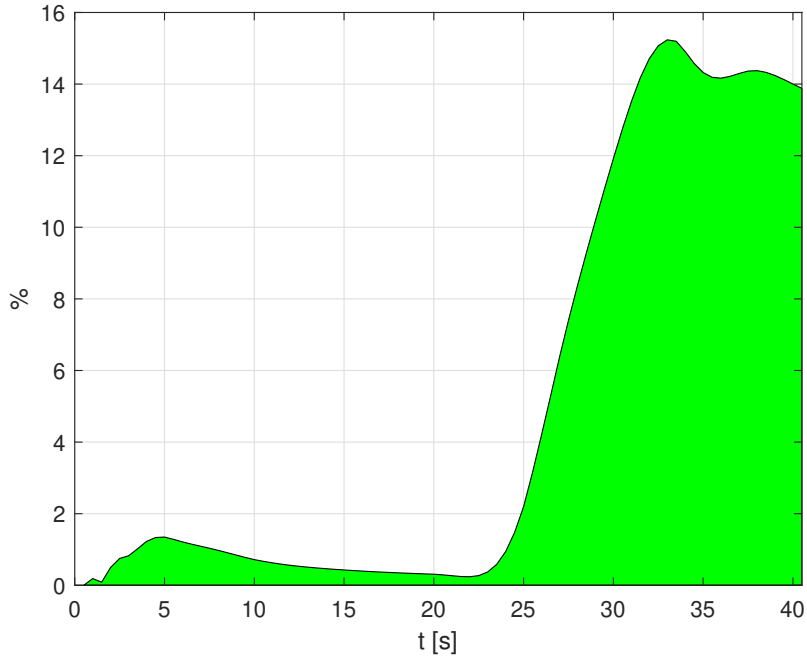

Figure 4.9: Difference in net energy, optimal minus sun-pointing over sun-pointing.

shown better in the plot of the power function (4.1) in Figure 4.5, where it is clear that a large share of the advantage the optimal solution has over the sun-pointing PD comes from the point the PD controller starts moving towards the reference attitude. The PD controller needs this time to control the states sufficiently close to the references. This shows another advantage of the optimal control strategy: the point where the spacecraft turns back does not need to be set explicitly but can instead be specified using the weighting of the costs on the references in (4.13). Note in the same figure that the optimal solution also gains by reaching the top level of the graph faster than the sun-pointing PD controller.

From Figure 4.1 and Figure 4.2, it can be seen that the optimal control solution ends on the negative of the quaternion the PD controller ends on, which is the reference quaternion. This is acceptable behavior due to the positive and negative quaternion representing the same attitude.

The net power function in Figure 4.5, defined in (4.1) as the difference between the solar power and the actuation power, is very similar in both shape and amplitude to the solar power plot in Figure 4.6. Comparing the values of the curves at the various times for solar power in Figure 4.6, which range from just below 6 W to just above 16 W, to the values for actuation power in Figure 4.7, which all fit within ± 0.8 W, it is evident why the total power curve resembles the solar power curve more than the actuation power curve. Note that the actuation power profile

of the optimal controller has more spikes towards the end of the simulation. This is due to the optimal solution's need to stay at the highest value in Figure 4.5 for as long as possible, then making the optimal approach to the reference attitude in a way that returns more energy to the spacecraft than the PD controller, as can be seen from the power curves in Figure 4.5.

The initial difference in net energy, shown in Figure 4.9, is due to the optimal plan reaching the highest values in Figure 4.5 quicker than the PD controller. If the PD controller had been held at the optimal sun-pointing attitude for longer, such as the case would have been for a longer time horizon, the difference between the optimal solution and the PD controller would be smaller percentage-wise, but in absolute terms, it would likely have stayed the same.

4.8 Conclusion

The advantage of the optimal net energy solution is that it finds the optimal trajectory from the initial to the reference attitude. The optimal solution keeps the optimal solar attitude for as long as possible and thus yields more energy to the system than the sun-pointing PD controller it is compared with.

Chapter 5

Energy Optimal Attitude Control and Task Execution for a Solar-Powered Spacecraft

This chapter is based on

[7] **B. A. Kristiansen**, J. T. Gravdahl, S. Gros, and T. A. Johansen, "Energy Optimal Attitude Control and Task Execution for a Solar-Powered Spacecraft", *IEEE Transactions on Control Systems Technology*, 2023, *conditionally accepted for publication.*

5.1 Introduction

The optimal control problem in [31] has similarities to the work in [2] and this chapter. The authors of [31] optimize with respect to what here is referred to as the solar power of the spacecraft only and not the entire net power cost introduced in [2], which this chapter is based on. In addition to this difference, we make efforts to formulate our optimal control problem in a way that makes it possible to solve the problem as a nonlinear program (NLP) through direct multiple shooting, whereas [31] solves their problem as a mixed-integer program.

In [2], the basis for Chapter 4, the net power cost function is introduced and tested through simulations over a short period of time using three orthogonal reaction wheels. The simulations were performed entirely in the sun, and thus the eclipse was not considered. In the present chapter, we expand on the formulation of the optimal control problem in Chapter 4: In addition to the introduction of some known disturbances, or perturbations, we refine the definition of the net power cost function by including a definition of a function labeled $\delta(\cdot,\cdot)$, which returns the amount of solar irradiance the spacecraft experiences based on its position relative to a potentially occluding body. In this chapter, it will be the Earth. The function is defined here so that it describes both the penumbra and umbra regions of the eclipse, thus introducing a physics-based transition between the periods where the spacecraft is exposed to sunlight and when it is in eclipse. Note that [31] also introduces a function where the Earth shadow is defined, but this shadow is defined

as a constant value for the entire eclipse and does, therefore, not include different values for the penumbra and the umbra regions, as we have done in this chapter. The argument for including the penumbra is, among others, made in [32], where the author emphasizes the significance the region has in determining the amount of power available to the spacecraft.

In this chapter, we perform simulations based on a scenario where the spacecraft moves in and out of eclipse during the scenario, an extension of the work presented in Chapter 4. The spacecraft for the studied mission, which has four reaction wheels, has an extra set of actuators in the form of magnetorquers, which are also included in the actuation cost. The magnetorquers are primarily meant to manage momentum, but their power consumption is included in the optimal control problem. Using this expanded model, we explore using the net power cost function for a scenario from the upcoming HYPSO-2 mission.

HYPSO-2 is an Earth observation mission that uses a push-broom hyperspectral imager to achieve its objectives, primarily observing ocean color, water quality, and algal blooms. HYPSO-2 is similar to the HYPSO-1 mission, see [21], but will, due to increased downlink capacity, be more constrained primarily by its solar energy harvesting capacity rather than the amount of data the satellite could downlink as is the case with HYPSO-1. To improve the resolution of the images, the spacecraft, a 6U CubeSat can perform a slewing maneuver at a constant angular rate over the target area. Besides the time spent on image acquisition (slew maneuver), the satellite will spend most of its time harvesting solar energy. While the slewing maneuver can be interesting from a control perspective [1, 33], this chapter focuses on what happens between the slewing (imaging) and communication pointing maneuvers, where the primary objective of the attitude control system is to gather as much energy as possible while executing data processing and communication tasks. HYPSO-2 will be equipped with deployable solar panels, another aspect considered when formulating the optimal control problem.

The contributions of this chapter are the following: we extend the net electric energy cost function introduced in [2] to account for a deployable solar panel. We include a mathematical formulation for the amount of solar irradiance the satellite's solar panels receive and extend the cost function to allow for magnetorquers. The cost function and model are refined to allow more than three reaction wheels. Based on the extended attitude control scenario where a sequence of maneuvers results from a typical sequence of imaging and communication tasks, we argue for the increased benefit of using the proposed method for satellites as the frequency of attitude maneuvers increases.

The remaining sections of this chapter are organized as follows: The novel cost function, defined as the sum of the incoming solar power and the actuation power consumption of the system in [2], is defined and expanded upon in Section 5.2. The optimal control problem itself is stated in Section 5.3, both in a general form and using the frames introduced in Section Section 5.2, using unit quaternions to represent the spacecraft's attitude. Section 5.5 defines the PD controller used for the initial guesses to the optimal solver and as a baseline. It also contains the optimal control problem that defines the references for the sun-pointing PD controller as previously introduced in [2]. Section 5.7 describes the setup for the numerical example using the net energy cost function based on the HYPSO-2 mission. The

results in Section 5.8 show how the optimal net energy solution performs for the given control scenario. The results are discussed in Section 5.9, while the chapter is concluded in Section 5.10.

5.2 Objective function

The cost function based on net power, where the objective is to maximize the net power as proposed in [2], is given as

$$J = J_{\mathrm{F}} - E - E_{\mathrm{other}} = J_{\mathrm{F}} - \int_0^T P(\mathbf{x}, \mathbf{u})\,\mathrm{d}t - E_{\mathrm{other}}(\mathbf{x}, t). \tag{5.1}$$

where E is the net energy of the system, $P(\mathbf{x}, \mathbf{u})$ is the system net power as a function of the system states $\mathbf{x}$ and inputs $\mathbf{u}$, and J_{F} is a cost imposed on the system final state. Note that (5.1) is formulated to fit into a minimization problem, meaning that the objective function is the negative of the desired maximization objective. $E_{\mathrm{other}}(\mathbf{x}, t)$ is the energy used by subsystems other than the control actuators. The purpose of including $E_{\mathrm{other}}(\mathbf{x}, t)$ in the cost function, possibly a function of the state and the time t, is to give the output of the optimization meaning when it comes to the total amount of power flowing in and out of the system. The net power function $P(\mathbf{x}, \mathbf{u})$, in its most general form, is given as

$$P(\mathbf{x}, \mathbf{u}) = s(\mathbf{x}) - m(\mathbf{x}, \mathbf{u}), \tag{5.2}$$

where $s(\mathbf{x})$ represents the solar power harvested by the system at the given state, while $m(\mathbf{x}, \mathbf{u})$ is the power used for actuation. The solar power function $s(\mathbf{x})$, defined as the sum of the power supplied by the solar panels, is given as

$$s(\mathbf{x}) = \eta_{\mathrm{in}} \kappa(\mathbf{R}_b^i, \mathbf{r}_{\mathrm{Sun}}) \delta(\mathbf{r}_{\mathrm{Sun}}, \mathbf{r}_{\mathrm{Earth}}), \tag{5.3}$$

where $\delta(\cdot, \cdot)$ quantifies the fraction of solar radiation that reaches the spacecraft, i.e., $\delta(\cdot, \cdot) = 1$ when the spacecraft is fully exposed to the Sun, and $\delta(\cdot, \cdot) = 0$ when the spacecraft is in the umbra region of the eclipse. Intermediate values correspond to the penumbra region. η_{in} represents the input efficiency of the batteries. The net power objective includes efficiency coefficients to model the cost of storing and using power and assumes that the power continuously cycles through the batteries. This assumption may cause the optimization to miss opportunities for direct consumption, making the results slightly pessimistic. The rotation matrix representation $\mathbf{R}_b^i$ represents the spacecraft's attitude. The indices i and b represent the Earth-centered inertial frame, referred to as the inertial frame, and the body frame, which is a body-fixed frame centered at the center of the spacecraft. $\mathbf{r}_{\mathrm{Sun}}$ and $\mathbf{r}_{\mathrm{Earth}}$ are vectors between the spacecraft and the Sun and the Earth, respectively. For spacecraft where the solar panels are flat, the amount of power the solar panels supply at a given attitude can be calculated as

$$\begin{aligned}\kappa(\mathbf{R}_b^i, \mathbf{r}_{\text{Sun}}) = \left(1 - \max\left(\left(\hat{\mathbf{s}}^b\right)^\intercal \hat{\mathbf{n}}_k^b, 0\right)\right) \cdot \\ \sum_{j=1, j\neq k}^{n_s} \max\left(\left(\hat{\mathbf{s}}^b\right)^\intercal \hat{\mathbf{n}}_j^b, 0\right)\left(\left(\hat{\mathbf{s}}^b\right)^\intercal \hat{\mathbf{n}}_j^b\right) c_{s,j} A_j \\ + \max\left(\left(\hat{\mathbf{s}}^b\right)^\intercal \hat{\mathbf{n}}_k^b, 0\right)\left(\left(\hat{\mathbf{s}}^b\right)^\intercal \hat{\mathbf{n}}_k^b\right) c_{s,k} A_k,\end{aligned} \tag{5.4}$$

where n_s is the number of faces with solar panels, $\hat{\mathbf{s}}^b$ is the unit solar vector represented in the body frame, and $\hat{\mathbf{n}}_j^b$ is the normal vector of the jth solar panel pointing out of the body. $c_{s,j}$ is a constant that is the product of the solar irradiance and the solar panel efficiency, and A_j is the solar panel surface area of the jth face. This equation shows the particular case we are investigating in this chapter, where one of the faces, denoted by index k, is assumed to entirely obscure the spacecraft's other faces when exposed to solar irradiance. The implementation is handled by introducing a term that goes to zero whenever the obscuring face is exposed to solar irradiance, which is accomplished by the $\left(1 - \max\left(\left(\hat{\mathbf{s}}^b\right)^\intercal \hat{\mathbf{n}}_k^b, 0\right)\right)$ factor. The face in question in this chapter is the large face with deployable solar panels that perfectly align with the rest of the satellite body, i.e., they form orthogonal angles with the other faces of the satellite frame. While this formulation is a simplification that only holds when the size of the solar panels goes to infinity or the size of the obscured faces goes to zero, it is assumed to be sufficient for our purposes, given that the deployable solar panels are relatively large compared to the faces they obscure. An example satellite where this is valid is the HYPSO-2 6U CubeSat illustrated in Figure 5.1.

We use an approximation of the $\max(\cdot)$ function, as in Chapter 4, implemented using the function defined in (2.11). Since (2.11) is differentiable, it is possible to take advantage of the automatic differentiation features of CasADi [30], and, more importantly, permits the use of a Newton-type solver like IPOPT.

The $\delta(\cdot, \cdot)$ function, a measure of how much sunlight reaches the spacecraft, can be defined by Algorithm 1. In defining the $\delta(\cdot, \cdot)$ function this way, we assume that the Sun and the Earth are spherical objects. In Algorithm 1, $\mathbf{r}_{\text{Sun}}$ is the vector from the spacecraft to the center of the Sun, $\mathbf{r}_{\text{Earth}}$ is the vector from the spacecraft to the center of the Earth, R_e is the radius of the Earth, and R_s is the radius of the Sun. As is shown in Figure 5.2, the two spherical bodies' external and internal tangents intersect at two different points in space. These points are called external and internal homothetic centers, and their positions are defined by the position of the two spheres and their radii. These intersection points, denoted using the symbol for intersection, $\cap$, in the algorithm, create conic sections together with the Earth, where the $\alpha_{\text{ext,cone}}$ and $\alpha_{\text{int,cone}}$ give the angle between the axes and the generatrix of the cones. These cones, where the internal cone is the cone defined by the intersection that lies between the Earth and the Sun and the Earth itself, and the outer cone, defined by the intersection on the far side of the Earth and the Earth, define the areas of space where the Earth cast a shadow. More precisely, if the spacecraft is inside the internal cone, meaning that the angle defined by α_{int} is smaller than $\alpha_{\text{int,cone}}$, then the spacecraft is in eclipse, but it might be in either

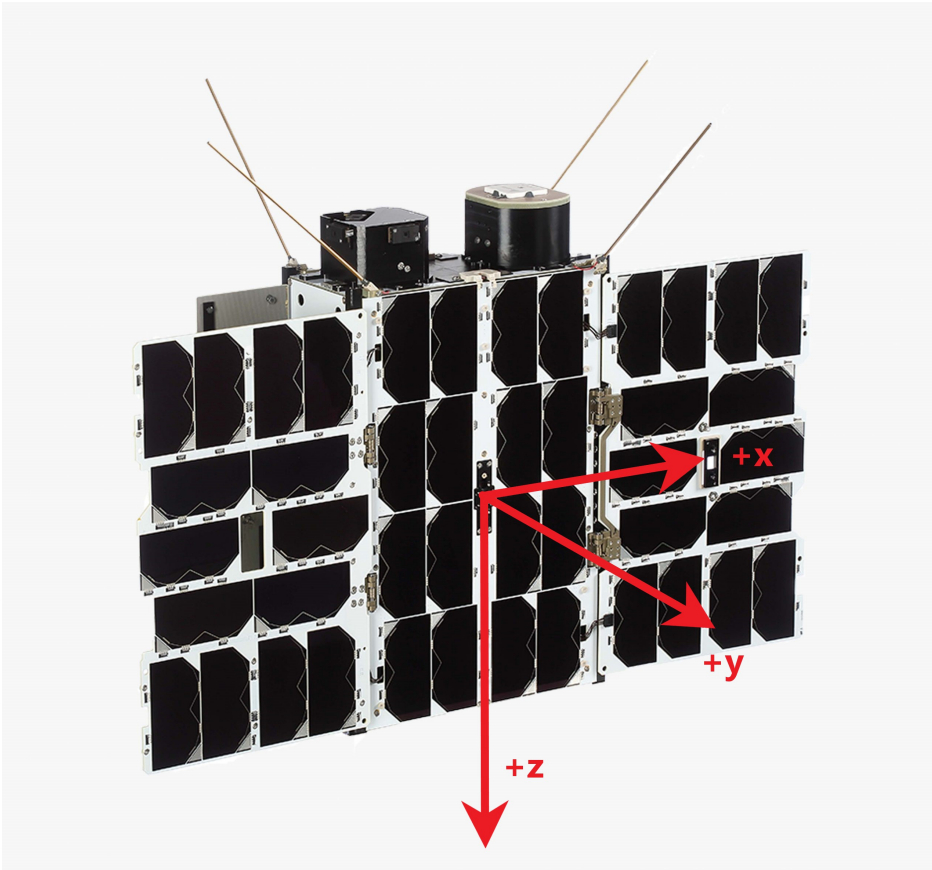

Figure 5.1: Axes over a satellite of the same shape as HYPSO-2, showing the face with the deployable solar panels. The hyperspectral imager is mounted facing down in this image. Image credit: [34].

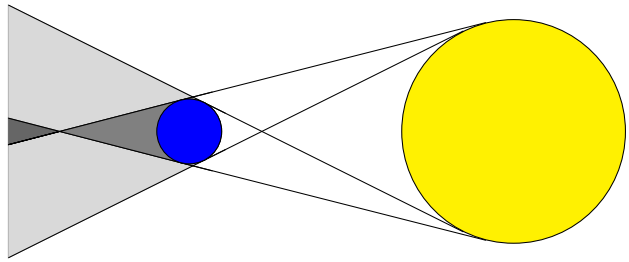

Figure 5.2: Illustration showing the Earth and Sun with the umbra and penumbra regions. The penumbra are the areas in light gray to the left of the Earth (the blue circle), while the umbra region is the darker gray region enclosed by the two penumbra areas and the Earth. The dark gray triangle furthest left in the figure is the antumbra, which is not of interest for this application. Note that the distances in the figure are not to scale.

Algorithm 1 $\delta(\mathbf{r}_{\text{Sun}}, \mathbf{r}_{\text{Earth}})$

$\mathbf{ES} \leftarrow \mathbf{r}_{\text{Sun}} - \mathbf{r}_{\text{Earth}}$
$\widehat{\mathbf{ES}} \leftarrow \frac{\mathbf{ES}}{\|\mathbf{ES}\|}$
$\cap_{\text{int}} \leftarrow \frac{R_e}{R_e + R_s}\mathbf{ES}$
$\cap_{\text{ext}} \leftarrow \frac{R_e}{R_e - R_s}\mathbf{ES}$
$\text{pos}_x \leftarrow \mathbf{r}_{\text{Earth}}^{\intercal}\widehat{\mathbf{ES}}$ ▷ Condition 1
$\alpha_{\text{int,cone}} \leftarrow \arcsin\left(\frac{R_e}{\|\cap_{\text{int}}\|}\right)$
$\text{adj}_{\text{int}} \leftarrow \frac{\mathbf{r}_{\text{Earth}}^{\intercal}\cap_{\text{int}}}{\cap_{\text{int}}^{\intercal}\cap_{\text{int}}}\cap_{\text{int}}$
$\text{hyp}_{\text{int}} \leftarrow \cap_{\text{int}} + \mathbf{r}_{\text{Earth}}$
$\alpha_{\text{int}} \leftarrow \arcsin\left(\frac{\|\text{hyp}_{\text{int}} \times \text{adj}_{\text{int}}\|}{\|\text{hyp}_{\text{int}}\|\|\text{adj}_{\text{int}}\|}\right)$
$\text{in}_{\text{int,cone}} \leftarrow |\alpha_{\text{int,cone}}| - |\alpha_{\text{int}}|$ ▷ Condition 2
$\alpha_{\text{ext,cone}} \leftarrow \arcsin\left(\frac{R_e}{\|\cap_{\text{ext}}\|}\right)$
$\text{adj}_{\text{ext}} \leftarrow \frac{\mathbf{r}_{\text{Earth}}^{\intercal}\cap_{\text{ext}}}{\cap_{\text{ext}}^{\intercal}\cap_{\text{ext}}}\cap_{\text{ext}}$
$\text{hyp}_{\text{ext}} \leftarrow \cap_{\text{ext}} + \mathbf{r}_{\text{Earth}}$
$\alpha_{\text{ext}} \leftarrow \arcsin\left(\frac{\|\text{hyp}_{\text{ext}} \times \text{adj}_{\text{ext}}\|}{\|\text{hyp}_{\text{ext}}\|\|\text{adj}_{\text{ext}}\|}\right)$
$\text{in}_{\text{ext,cone}} \leftarrow |\alpha_{\text{ext,cone}}| - |\alpha_{\text{ext}}|$ ▷ Condition 3
if $\text{pos}_x > 0$ **then**
  if $\text{in}_{\text{int,cone}} > 0$ **then**
    if $\text{in}_{\text{ext,cone}} > 0$ **then**
      $\delta \leftarrow \delta_{\text{umbra}}$ ▷ Umbra
    else if $\text{in}_{\text{ext,cone}} \leq 0$ **then**
      $\delta \leftarrow \delta_{\text{penumbra}}$ ▷ Penumbra
    end if
  else if $\text{in}_{\text{int,cone}} \leq 0$ **then**
    $\delta \leftarrow \delta_{\text{light}}$ ▷ Light
  end if
else if $\text{pos}_x \leq 0$ **then**
  $\delta \leftarrow \delta_{\text{light}}$ ▷ Light
end if
return δ

the penumbra or the umbra regions. Similarly, the spacecraft is inside the external cone if α_{ext} is smaller than $\alpha_{\text{ext,cone}}$. If the spacecraft is in both the outer cone and the internal cone, it is in the umbra region. If it is in only the internal cone but not the outer cone, it is in one of the penumbra regions. These conditions are defined as condition 2 and condition 3 in Algorithm 1, respectively. The position argument, condition 1, is included so that only regions on the far side of the Earth, as seen from the Sun are considered. This is needed since it is possible to be inside both the internal and the external cone while being between the Earth and the Sun, a region of space that obviously will be in the light. The algorithm serves the same purpose as the "Shadow" algorithm in [32].

As no external forces dependent on attitude are included in the orbit calculation, the values for the $\delta(\cdot, \cdot)$ can be calculated beforehand.

The shaded regions of the orbit eclipse, i.e., the penumbra, as seen in Figure 5.2, do not all produce a complete shade. For a satellite orbiting the Earth in low-Earth orbit, there are three regions: the penumbra region, i.e., the semi-dark region enclosing the fully dark region, the umbra, and the sunlit region of the orbit. Figure 5.2 shows the various regions. The scale of some of the elements in the illustration has been exaggerated to show the difference between the penumbra and the umbra regions. Due to the distance between the Sun and the Earth and the relatively short distance between the LEO (Low-Earth Orbit) spacecraft and the Earth, the spacecraft time in the penumbra region is short. Naturally, the time spent in the penumbra regions increases with the orbit's altitude, as can be seen from Figure 5.2. While the penumbra region is distinctly separate from the sunlit and umbra regions [35], the amount of sunlight is not constant in the penumbra region. This could be modeled in Algorithm 1, under condition 2, as a gradual decrease as the spacecraft moves closer to the umbra region. For simplicity, the amount of sunlight in the penumbra region is defined as a fixed number between zero and one.

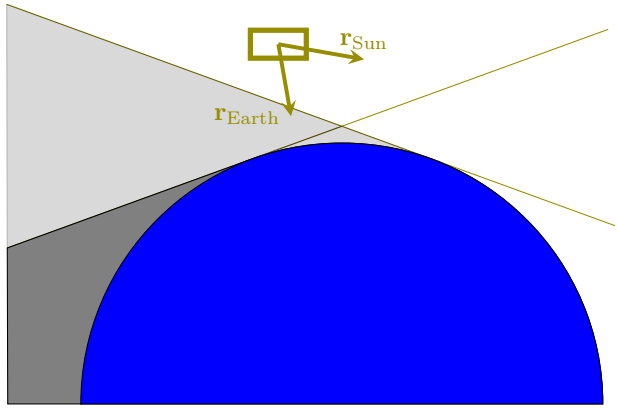

Figure 5.3: Illustration showing a spacecraft in orbit with the umbra and (exaggerated) penumbra regions.

We assume an array of reaction wheels and magnetorquers, where only the reaction wheels are applied for attitude control of the spacecraft, while the mag-

netorquers are used to manage the momentum of the reaction wheels. For a spacecraft actuated by reaction wheels and magnetorquers, the actuation power $m(\mathbf{x}, \mathbf{u})$, where $\mathbf{x}$ is the state and $\mathbf{u}$ is the input, is the sum of the power usage for the reaction wheels $P_{\text{RW}}(\mathbf{x}, \mathbf{u})$ and the magnetorquers $P_{\text{mtq}}(\mathbf{u})$, or

$$\begin{aligned} m(\mathbf{x}, \mathbf{u}) &= P_{\text{RW}}(\mathbf{x}, \mathbf{u}) + P_{\text{mtq}}(\mathbf{u}) \\ &= \frac{1}{\eta_{rw}} \left| (\mathbf{A}\boldsymbol{\tau}_{\text{RW}}^{w})^{\intercal} \mathbf{A}\boldsymbol{\omega}_{\text{RW}}^{w} \right| + \frac{1}{\eta_{\text{out}}} \left(\mathbf{I}_{\text{mtq}}^{b}\right)^{\intercal} \mathbf{V}_{\text{mtq}}^{b}, \end{aligned} \tag{5.5}$$

where η_{rw} is the efficiency of the reaction wheels, and $\boldsymbol{\tau}_{\text{RW}}^{w}$ is the input torque represented in the wheel frame. η_{out} is the output efficiency of the batteries. $\boldsymbol{\omega}_{\text{RW}}^{w}$ is the angular velocity of the reaction wheels in the wheel frame, and $\mathbf{A}$ is the torque distribution matrix. The absolute value is included since energy only flows in one direction, from the batteries to the reaction wheels. In other words, it is assumed that the kinetic energy in the reaction wheels cannot be transformed into electrical energy in the batteries on board the spacecraft. $\mathbf{V}_{\text{mtq}}^{b}$ and $\mathbf{I}_{\text{mtq}}^{b}$ are vectors denoting the voltage over and current through the magnetorquers for each axis in the body frame. The power of the magnetorquers is included as they are part of the control system, even though they are not directly used for attitude control in this chapter. For simplicity, the formula for the power used by magnetorquers is calculated by scaling the magnetic moment by its maximum value and multiplying it by the maximum power drawn by the magnetorquers:

$$P_{\text{mtq}}(\mathbf{u}) = \frac{\sum_{n=1}^{\infty} \left| m_{\text{mtq},i}^{b} \right|}{3 m_{\text{mtq, ub}}} P_{\text{mtq, max}}, \tag{5.6}$$

where $m_{\text{mtq},i}^{b}$ is the i-th channel of the $\mathbf{m}_{\text{mtq}}$ vector, and the divisor the upper bound on the magnetic moment of the magnetorquers, $m_{\text{mtq, ub}}$, multiplied by three as the magnetorquers cover all three body frame axes. $\mathbf{m}_{\text{mtq}}$ is the magnetic moment of the magnetorquer, which is what is calculated by the control algorithm. $P_{\text{mtq, max}}$ is the maximum value for the power drawn by the magnetorquers. Thus, (5.5) in this chapter takes the form

$$\begin{aligned} m(\mathbf{x}, \mathbf{u}) &= P_{\text{RW}}(\mathbf{x}, \mathbf{u}) + P_{\text{mtq}}(\mathbf{u}) \\ &= \frac{1}{\eta_{rw}} \left| (\mathbf{A}\boldsymbol{\tau}_{\text{RW}}^{w})^{\intercal} \mathbf{A}\boldsymbol{\omega}_{\text{RW}}^{w} \right| + \frac{\sum_{n=1}^{\infty} \left| m_{\text{mtq},i}^{b} \right|}{3 m_{\text{mtq, ub}}} P_{\text{mtq, max}}. \end{aligned} \tag{5.7}$$

The output efficiency of the batteries is included in the value given to $P_{\text{mtq, max}}$.

The cost imposed on the problem relating to the final states of the system, J_{F}, can be chosen to be

$$\begin{aligned} J_{\text{F}} &= k_1 J_{\text{path,ref}} + k_2 J_{\text{velocity}} \\ &= k_1 \left(1 - \left| \left(\mathbf{q}_{b}^{i}\right)^{\intercal} \mathbf{q}_{\text{ref}} \right| \right) \\ &\quad + k_2 \left(\boldsymbol{\omega}_{\text{ref}}^{b} - \boldsymbol{\omega}_{ib}^{b} \right)^{\intercal} \left(\boldsymbol{\omega}_{\text{ref}}^{b} - \boldsymbol{\omega}_{ib}^{b} \right), \end{aligned} \tag{5.8}$$

where $J_{\text{path,ref}}$ is a metric on SO(3) [28] that denotes the cost of not reaching the desired attitude, J_{velocity} is the cost of not reaching the desired final angular velocity, and k_1 and k_2 are weights. $\mathbf{q}_{\text{ref}}$ and $\boldsymbol{\omega}^b_{\text{ref}}$ are the reference values for the attitude quaternion and the angular velocity, respectively. $J_{\text{path,ref}}$ is implemented using the smooth max function (4.5),

$$|\left(\mathbf{q}_b^i\right)^\intercal \mathbf{q}_{\text{ref}}| = \max\left(\left(\mathbf{q}_b^i\right)^\intercal \mathbf{q}_{\text{ref}}, -\left(\mathbf{q}_b^i\right)^\intercal \mathbf{q}_{\text{ref}}\right). \tag{5.9}$$

With J_{F} defined this way, the problem becomes multi-objective because the cost function weights energy usage against reference tracking.

5.3 Optimal control problem

The general optimal control problem, based on (5.1), is defined as

$$\begin{aligned}
\min_{\mathbf{x},\mathbf{u}} \quad & J_{\text{F}} - \int_0^T P(\mathbf{x},\mathbf{u})\,\mathrm{d}t - E_{\text{other}}(\mathbf{x},t) && \text{(5.10a)}\\
\text{s.t. } & \dot{\mathbf{x}} = \mathbf{f}(\mathbf{x},\mathbf{u}) && \text{(5.10b)}\\
& \mathbf{g}(\mathbf{x}) \leq 0 && \text{(5.10c)}\\
& \mathbf{u}_{\text{lb}} \leq \mathbf{u} \leq \mathbf{u}_{\text{ub}} && \text{(5.10d)}\\
& \mathbf{x}(0) = \mathbf{x}_0, && \text{(5.10e)}
\end{aligned}$$

where the net energy objective function is constrained by the system dynamics in (5.10b). T is the length of the control horizon. The $\mathbf{g}(\mathbf{x})$ vector constrains the state vector $\mathbf{x}$ to some bounds, such as upper and lower bounds on reaction wheel angular velocities. The control input $\mathbf{u}$ is bounded by both lower bounds, $\mathbf{u}_{\text{lb}}$, and upper bounds, $\mathbf{u}_{\text{ub}}$. We use the J_{F} term to drive the state variables to the desired final states. Note that the problem appears to be singular.

Defining the state $\mathbf{x} = \left[\left(\mathbf{q}_b^i\right)^\intercal, \left(\boldsymbol{\omega}_{ib}^b\right)^\intercal, \left(\boldsymbol{\omega}_{\text{RW}}^w\right)^\intercal\right]^\intercal$ and the input $\mathbf{u} = \left[\left(\boldsymbol{\tau}_{\text{RW}}^w\right)^\intercal, \left(\boldsymbol{\tau}_{\text{mtq}}^b\right)^\intercal\right]^\intercal$, the optimal control problem is defined by [1]

$$\min_{\mathbf{x},\mathbf{u}} \quad J_{\mathrm{F}} - \int_0^T P(\mathbf{x},\mathbf{u})\,\mathrm{d}t - E_{\mathrm{other}}(\mathbf{x},t) \tag{5.11a}$$

$$\text{s.t. } \dot{\mathbf{q}}_b^i = \frac{1}{2}\mathbf{T}(\mathbf{q}_b^i)\boldsymbol{\omega}_{ib}^b + \frac{1}{2}\rho\mathbf{q}_b^i\left(\left(\left(\mathbf{q}_b^i\right)^\intercal \mathbf{q}_b^i\right)^{-1} - 1\right) \tag{5.11b}$$

$$\frac{{}^b d}{dt}\boldsymbol{\omega}_{ib}^b = \mathbf{J}_s^{-1}\left(-\mathbf{S}\left(\boldsymbol{\omega}_{ib}^b\right)\left(\mathbf{J}\boldsymbol{\omega}_{ib}^b + \mathbf{A}\mathbf{J}_w\boldsymbol{\omega}_{\mathrm{RW}}^w\right) - \mathbf{A}\boldsymbol{\tau}_{\mathrm{RW}}^w + \boldsymbol{\tau}_{\mathrm{mtq}}^b + \boldsymbol{\tau}_{\mathrm{ext}}^b\right) \tag{5.11c}$$

$$\frac{{}^w d}{dt}\boldsymbol{\omega}_{\mathrm{RW}}^w = \mathbf{J}_w^{-1}\boldsymbol{\tau}_{\mathrm{RW}}^w - \mathbf{A}^\intercal\frac{{}^b d}{dt}\boldsymbol{\omega}_{ib}^b \tag{5.11d}$$

$$\frac{{}^i d}{dt}\mathbf{r}^i = \mathbf{v}^i \tag{5.11e}$$

$$\frac{{}^i d}{dt}\mathbf{v}^i = -\frac{\mu\mathbf{r}^i}{\|\mathbf{r}^i\|^3} \tag{5.11f}$$

$$\boldsymbol{\tau}_{\mathrm{RW,lb}}^w \leq \boldsymbol{\tau}_{\mathrm{RW}}^w \leq \boldsymbol{\tau}_{\mathrm{RW,ub}}^w \tag{5.11g}$$

$$\mathbf{x}(0) = \mathbf{x}_0, \tag{5.11h}$$

where (5.11b) describes the kinematics of the system, and (5.11c) and (5.11d) describe the dynamics of the spacecraft and the reaction wheels, respectively [1]. The model assumes that the spacecraft is a rigid body, where the translational motion is described in (5.11e) and (5.11f). $\mathbf{q}_b^i = [\eta_b^i,\ \left(\boldsymbol{\epsilon}_b^i\right)^\intercal]^\intercal$ is the attitude unit quaternion, where η_b^i is the scalar and $\boldsymbol{\epsilon}_b^i$ is the vector part of the quaternion. Note that the quaternion $\mathbf{q}_b^i$ defines the rotation matrix in (5.3) and (5.4). In the case study, one reaction wheel exists for each of the body frame axes, in addition to a fourth reaction wheel with equal capacity along each body frame axis. This leads to the torque distribution matrix $\mathbf{A}$ that gives the mapping between the wheel frame and the body frame:

$$\mathbf{A} = \frac{1}{3}\begin{bmatrix} 1 & 0 & 0 & \sqrt{3} \\ 0 & 1 & 0 & \sqrt{3} \\ 0 & 0 & 1 & \sqrt{3} \end{bmatrix}. \tag{5.12}$$

The inertia matrices $\mathbf{J}_s$, $\mathbf{J}_w$, and $\mathbf{J} = \mathbf{J}_s + \mathbf{A}\mathbf{J}_w\mathbf{A}^\intercal$ represent the inertia of the spacecraft only, the reaction wheels, and the total inertia of the complete spacecraft, respectively. μ is the standard gravitational parameter of the Earth, and m is the spacecraft's mass. The external torques that act on the spacecraft are represented by $\boldsymbol{\tau}_{\mathrm{ext}}^b$, and $\boldsymbol{\tau}_{\mathrm{RW,lb}}^b$ and $\boldsymbol{\tau}_{\mathrm{RW,ub}}^b$ are the lower and upper bound on the reaction wheel torques, respectively. The environmental torques are defined in Section 5.11. The limits are defined similarly for the torque from the magnetorquers, $\boldsymbol{\tau}_{\mathrm{mtq}}^b$, but the magnetorquer limits are not included in the optimal control problem since the optimal solver does not determine the magnetic torque. The angular velocity of the reaction wheels is given by $\boldsymbol{\omega}_{\mathrm{RW}}^w$. Note that the angular velocity of the reaction wheels has superscript w. This denotes a wheel frame, which has a channel for each reaction wheel, and thus the vectors in this frame have the same dimension as the number of reaction wheels. Since the reaction wheels only rotate about one axis, the wheel frame does not rotate relative to the body frame. The $\mathbf{T}(\mathbf{q})$ matrix is

given by [18]

$$\mathbf{T}(\mathbf{q}) = \begin{bmatrix} -\boldsymbol{\epsilon}^{\intercal} \\ \eta \mathbf{I}_{3\text{x}3} + \mathbf{S}(\boldsymbol{\epsilon}) \end{bmatrix}, \tag{5.13}$$

where $\mathbf{I}_{3\text{x}3}$ is the three-dimensional identity matrix and $\mathbf{S}(\cdot)$ is a skew-symmetric matrix corresponding to the vector cross product in three dimensions.

The position of the satellite in Earth-centered inertial frame is given as $\mathbf{r}^i$. This vector is denoted $\mathbf{v}^i$ in Figure 5.3. The corresponding velocity is given by $\mathbf{v}^i$, and μ is the standard gravitational parameter of the Earth.

The unit quaternion is not constrained by a normalization constraint other than that the initial attitude should be a unit quaternion. The norm of the unit quaternion is preserved through the accuracy of the numerical integrator and the Baumgarte stabilization term $\frac{1}{2}\rho\mathbf{q}\left((\mathbf{q}^{\intercal}\mathbf{q})^{-1} - 1\right)$, where ρ is a small positive constant [29].

5.4 Magnetorquers control

The magnetorquers are only used for momentum management of the reaction wheels, with the control algorithm given as [36]

$$\boldsymbol{\tau}_{\text{mtq}} = \mathbf{S}(\mathbf{m}^b)\mathbf{B}^b = \mathbf{S}\left(\frac{k_m}{\|\mathbf{B}^b\|_2}\left(\mathbf{S}\left(\mathbf{h}_e^b\right)\mathbf{B}^b\right)\right)\mathbf{B}^b, \tag{5.14}$$

where $\mathbf{m}^b$ is the magnetic moment produced by the magnetorquers. k_m is a positive constant, and $\mathbf{h}_e^b$ is the error in angular momentum for the reaction wheels, given as

$$\mathbf{h}_e^b = \mathbf{A}\mathbf{J}_w(\boldsymbol{\omega}_{\text{RW,ref}}^w - \boldsymbol{\omega}_{\text{RW}}^w), \tag{5.15}$$

where reference angular velocity of the reaction wheels is denoted as $\boldsymbol{\omega}_{\text{RW,ref}}^w$. The commanded torque to the magnetorquers is to produce is calculated directly in this chapter using (5.14) and (5.15).

5.5 Optimization and initial guesses

The optimal control problem is solved using the IPOPT solver [20] in CasADi, where the optimal control problem in (5.11) is discretized as a multiple-shooting problem. The dynamics are discretized and integrated using the CasADi built-in implementation of the Runge-Kutta 4 integrator.

In this chapter, we use a PD controller to produce the initial guesses for the optimal control problem in (5.11) by pointing the spacecraft toward an optimal solar power reference. The details of this scheme can be found in Section 3.2.1.

5.6 Control scenario

The case study is based on the HYPSO satellites' concept of operations, [21, Table VII], where the satellite makes a slewing maneuver during imaging, see Figure 5.4. This is a maneuver with a constant angular velocity, about the satellite's y-axis

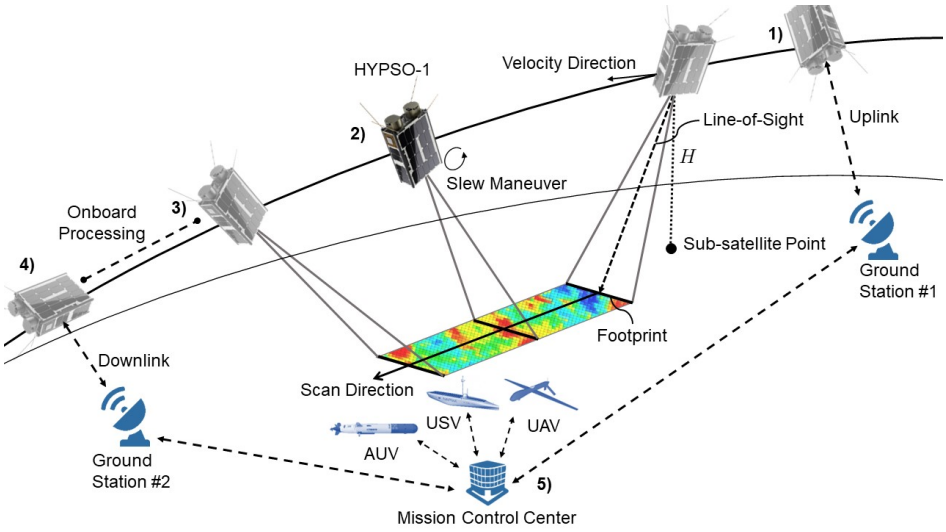

Figure 5.4: Concept of operations (CONOPS) for the HYPSO satellites, from [21].

during image acquisition. The control task will include a sequence of image captures within a single pass. The allocated time for the various parts of the tasks is shown in Table 5.1. In particular, we will study the HYPSO-2 satellite which differs from HYPSO-1 by having deployable solar panels and an X-band radio communication downlink with significantly increased link capacity when compared to HYPSO-1's S-band radio downlink. A typical image taken by the hyperspectral camera is 85 MB, and the X-band is assumed to give a data rate of 10 Mbps, which means that a full hyperspectral image can be downlinked in 68 seconds. The full scenario is modeled as a series of smaller optimizations for each of the tasks as opposed to one large optimization, which it should be noted is not necessarily optimal in a mathematically rigorous sense.

The optimizations described in this chapter occur between image acquisitions or downlinks. The maneuver during image acquisition is not the subject matter of this chapter and is thus omitted. The image acquisition is accomplished in simulation by integrating the translational variables over the stated duration while keeping the other attitude constant. The difference between image capture maneuvers and downlink maneuvers is that the optimization leading up to the image acquisitions should go towards a non-zero angular velocity reference, whereas zero is given as the angular velocity reference for the downlink maneuvers. Additionally, the satellite is rotated differently for the downlink maneuvers, as the antenna and the camera are not placed on the same face. The longest idle phase spans the eclipse from Nigeria to Svalbard (optimization task 7). There are no image acquisitions during the eclipse since the HYPSO-2 imager payload, the hyperspectral camera, requires the target to be lit to produce good data.

The reference quaternions are chosen to coincide with the various targets in Figure 5.5, while the angular velocity references depend on whether their target is

Table 5.1: Optimization scenario for HYPSO-2

Task	Start time (UTC)	End time (UTC)	Duration (s)
Solar energy harvesting, Optimization task 1	09:31:11	09:32:51	100
Communication, Svalbard, Norway	09:32:51	09:34:51	120
Solar energy harvesting, Optimization task 2	09:34:51	09:35:31	40
Image acquisition, Finnmark, Norway	09:35:31	09:36:31	60
Solar energy harvesting, Optimization task 3	09:36:31	09:37:31	60
Image acquisition, Frohavet, Norway	09:37:31	09:38:31	60
Solar energy harvesting, Optimization task 4	09:38:31	09:38:51	20
Image acquisition, Mjøsa, Norway	09:38:51	09:39:51	60
Solar energy harvesting, Optimization task 5	09:39:51	09:45:01	310
Communication, KSAT Spain, Spain	09:45:01	09:46:33	92
Solar energy harvesting, Optimization task 6	09:46:33	09:53:01	388
Image acquisition of coastline, Nigeria	09:53:01	09:54:01	60
Solar energy harvesting, Optimization task 7	09:54:01	11:07:01	4 380
Communication, Svalbard, Norway	11:07:01	11:10:01	180
Solar energy harvesting, Optimization task 8	11:10:01	11:10:41	40
Image acquisition, Finnmark, Norway	11:10:41	11:11:41	60
Solar energy harvesting, Optimization task 9	11:11:41	11:12:41	60
Image acquisition, Trondheim, Norway	11:12:41	11:13:41	60
Solar energy harvesting, Optimization task 10	11:13:41	11:18:45	304
Communication, KSAT Spain, Spain	11:18:45	11:20:47	122

Table 5.2: Control references for the tasks in Table 5.1

Target	$\mathbf{q}_{\text{ref}}$	$\boldsymbol{\omega}^b_{ib,\text{ref}}(^\circ/\text{s})$
Svalbard, Norway (1)	$[0.853, 0.372, -0.019, -0.366]^\intercal$	$[0, 0, 0]^\intercal$
Finnmark, Norway (2)	$[0.084, 0.918, -.329, -0.205]^\intercal$	$[0, -0.754, 0]^\intercal$
Frohavet, Norway (3)	$[0.297, -0.858, 0.407, 0.102]^\intercal$	$[0, -0.754, 0]^\intercal$
Mjøsa, Norway (4)	$[0.275, 0.860, -0.262, -0.343]^\intercal$	$[0, -0.754, 0]^\intercal$
KSAT Spain, Spain (5)	$[0.827, 0.123, 0.333, -0.435]^\intercal$	$[0, 0, 0]^\intercal$
Coastline, Nigeria (6)	$[0.034, 0.710, 0.474, 0.519]^\intercal$	$[0, -0.754, 0]^\intercal$
Svalbard, Norway (7)	$[0.677, 0.642, -0.151, -0.327]^\intercal$	$[0, 0, 0]^\intercal$
Finnmark, Norway (8)	$[0.405, -0.835, 0.372, -0.018]^\intercal$	$[0, -0.754, 0]^\intercal$
Trondheim, Norway (9)	$[0.389, -0.828, 0.402, 0.036]^\intercal$	$[0, -0.754, 0]^\intercal$
KSAT Spain, Spain (10)	$[0.223, 0.906, -0.304, -0.195]^\intercal$	$[0, 0, 0]^\intercal$

for imaging or downlinking data. For downlinking data, the angular velocity reference is set to zero since the radio antennas have a relatively wide beam. In contrast, it is set to a fixed angular velocity about the body frame y-axis for optimizations that transition into an image acquisition: this way, the slewing maneuver the satellite performs during imaging can be prepared directly from the optimization. The targets/tasks coincide with current areas of interest for the HYPSO mission. The map also shows the position and ground track of the HYPSO-1 satellite on the day that is used for this chapter. The references are inferred from the outputs from an internally developed software suite for satellite operations at NTNU. The attitude and angular velocity references are given in Table 5.2.

5.7 Simulation setup

The optimal trajectories are calculated once. The output from the sun-pointing PD controller from Section 5.5 is used as the initial values for the optimization. The PD controller makes the satellite point towards what it perceives as the optimal sun-pointing attitude, given by (3.8), until 20 seconds before the satellite's new target reference is used for the attitude and angular rate. The PD controller is constrained similarly to the optimal control problem in (5.11). The PD controller that provides the initial values and the optimal control problem has a discretization step size h of 2 seconds. The total length of the maneuvers, from start to finish, is 5580 seconds or 93 minutes. During this time, the satellite goes through more than a complete orbit, meaning that the satellite spends some time in the light and some in the shade, and thus $\delta(\cdot, \cdot)$ varies between 0 and 1.

The parameters used in the simulation can be seen in Table 5.3. Note that the constant $c_{s,j}$ from (5.4), given by the solar irradiance multiplied by the given solar panel's efficiency, is equal to c_s in this simulation as all the solar panels are assumed to be identical.

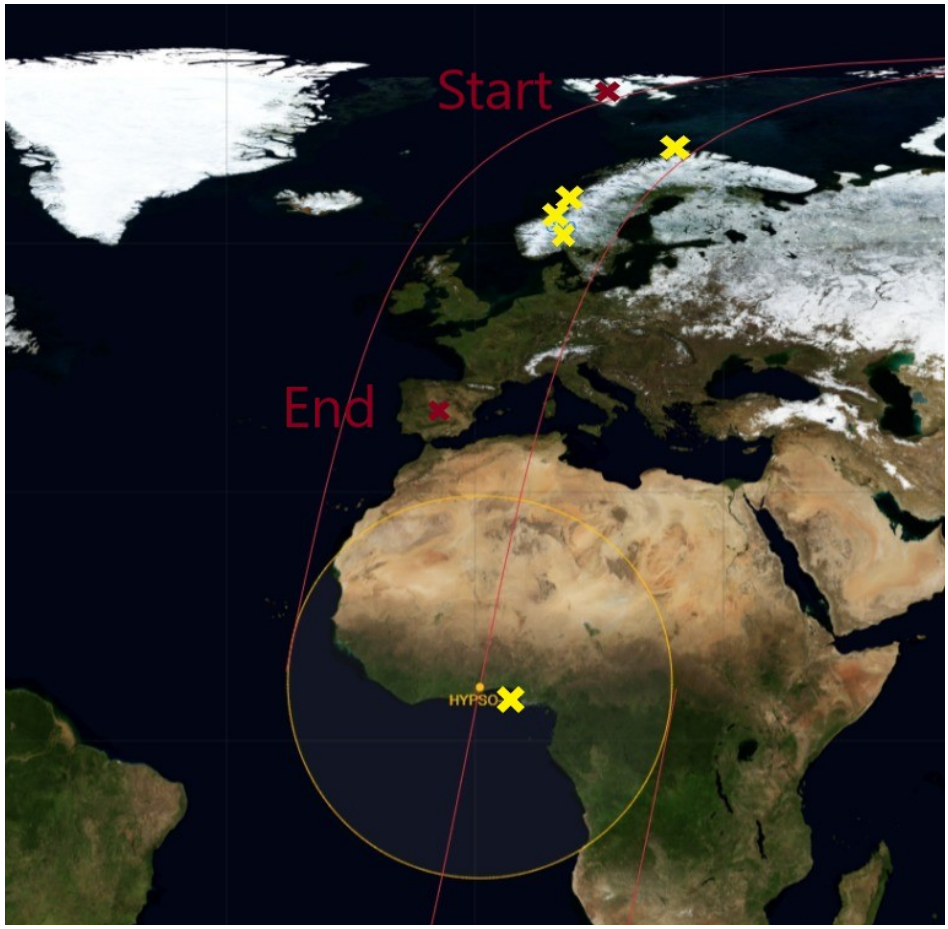

Figure 5.5: Map showing the position and ground track of HYPSO-1 as of March 14, 2023. The satellite is marked by a dark yellow circle, the satellite ground track is marked in red. The initial target, Svalbard, and the final target, KSAT Spain, are marked by dark red crosses. The other targets are marked with yellow crosses following the path of the satellite, going from North to South. Note that the satellite is at the 6th target, the Nigerian coastline, in the figure.

Table 5.3: Optimization constants

Variable	Value	Unit
Step size (h)	2	s
Solar irradiance	1366	$\mathrm{W/m^2}$
Solar panel efficiency	20	%
c_s	272.2	$\mathrm{W/m^2}$
η_{rw}	0.85	-
α	10^{-5}	-
$k_{\max}$	1	$\mathrm{W^2}$
k_1	$T \cdot 1.75 \cdot 10^2$	W
k_2	$T \cdot 10^4$	$\mathrm{W \cdot s^2}$
ρ	$1.1 \cdot 10^{-2}$	-
$\boldsymbol{\tau}^b_{\mathrm{RW,lb}}$	$-3.2 \cdot 10^{-3}$	N·m
$\boldsymbol{\tau}^b_{\mathrm{RW,ub}}$	$3.2 \cdot 10^{-3}$	N·m

The inertia matrices are given by

$$\mathbf{J} = \begin{bmatrix} 0.0950 & 0.0000 & 0.0010 \\ 0.0000 & 0.1370 & 0.0000 \\ 0.0010 & 0.0000 & 0.0570 \end{bmatrix} \mathrm{kg \cdot m^2}, \quad \mathbf{J}_w = I_w \mathbf{I}_{4\mathrm{x}4}, \tag{5.16}$$

where $I_w = 2.1 \cdot 10^{-4}$ kg·m^2. Note that not all the sides of the 6U satellite are covered in solar panels. The areas of the solar cell covered surfaces A_j are then the entries in the vector A in (5.17),

$$A = [0.024, 0.144, 0, 0.024, 0.048, 0]\ \mathrm{m^2}. \tag{5.17}$$

The deployable solar panels are on the positive y-face of the body frame, indicated by the largest entry in the A vector in (5.17).

The position of the Sun relative to the Earth is given in the Earth-centered inertial frame as $\mathbf{r}^i_{\text{Sun-Earth}} = 1.49599870 \cdot 10^{11}\,[0.8944, 0, 0.4472]^\intercal$ m and is constant throughout the simulation. This is assumed to be sufficient due to the simulation's relatively short duration relative to the rotation of the Earth-centered inertial frame around the Sun. $\hat{\mathbf{s}}^b$, which is used for (5.4), is found by transforming $\mathbf{r}^i_{\text{Sun}} = \mathbf{r}^i_{\text{Sun-Earth}} + \mathbf{r}^i$ to the body frame after normalizing the vector.

The initial conditions for the satellite before the first optimization are $\mathbf{x}_0 = \left[\mathbf{q}^i_b(0); \boldsymbol{\omega}^b_{ib}(0); \boldsymbol{\omega}^b_{\mathrm{RW}}(0)\right] = [0, 0, 1, 0, -0.01, 0.02, 0.01, 209.4, 209.4, 209.4, -362.8]^\intercal$, and for optimization 2 through 9, the initial values are taken from the satellite maneuver that leads up to the optimization. The initial values for $\boldsymbol{\omega}^b_{ib}$ are given in rad/s. The reference for the angular velocity of the reaction wheels is the same as the initial value, which means $[209.4, 209.4, 209.4, -362.8]^\intercal$, all in rad/s. The quaternion and angular velocity references are given in Table 5.2.

The torque from the sun-pointing PD controller that is used to find the initial values for the optimization is constrained by the same bounds as the optimal control

torque. The PD controller gains $\mathbf{K}_p$ and $\mathbf{K}_d$ with the constant values $1 \cdot 10^{-2}$ and $3.56 \cdot 10^{-2}$, respectively, are found through tuning.

The magnetic field is modeled using the IGRF model, defined by the potential function [37]. An adaptation of the implementation presented in [38] is used.

The value for the other loads in the cost function, $E_{\text{other}}(\mathbf{x}, t)$, are estimated based on a preliminary mission analysis. When harvesting solar power, the term is set to -13.5 W. The cost during imaging is -29.5 W, and during communication with a ground station it is -40 W.

The external torques, $\boldsymbol{\tau}_{\text{ext}}^b$, that are included are detailed in Section 5.11. Any other effects in the actuators that have not previously been mentioned here, such as handling dead zones in reaction wheels or other nonlinear effects, are not included in the simulations and are then, in effect, assumed to be handled by a lower-level control layer. Depth-of-discharge is not considered in this chapter, so the capacity of the batteries is not modeled.

Table 5.4 gives the initial orbital elements. The other parameters used for the simulation are shown in Table 5.5.

Table 5.4: Orbital elements

Variable	Value	Unit
Semimajor axis	6905.1	km
Eccentricity	0.0007757	-
Inclination	97.439	°
Right ascension of the ascending node	139.3136	°
Argument of perigree	213.7547	°
True anomaly	54	°

5.8 Results

Figure 5.6 shows the optimal attitude quaternion trajectory $\mathbf{q}_b^i$ resulting from IPOPT solving the optimal control problem in (5.11) for all references detailed in Table 5.1 and Table 5.2. All the figures have vertical lines, marking each optimization task's start. The gray-shaded region indicates that the satellite is in eclipse, for a few seconds in the penumbra and then in the umbra. The satellite rotates from in the shadow, a rotation which is owing to the torques from the environment, see Figure 5.16, and a few features of the solution produced by the optimal solver are detailed in the discussion section. Figure 5.7 shows how the net power cost function, (5.1), evolves over the control horizon. The figure shows that the net power is reduced to around zero when entering the umbra. The penumbra region, where the net power supplied to the spacecraft is significantly reduced, but not to zero, is not visible in the figure as the penumbra only spans some seconds with the low altitude orbit of HYPSO-2. This is expected behavior, as only a percentage of the light from the Sun reaches the satellite in the penumbra region, and nothing does while it is in the umbra region. The amount of sunlight that reaches the satellite during the simulation, defined by the $\delta(\cdot, \cdot)$ function, can be seen in

Table 5.5: Simulation parameters

Variable	Value	Unit
δ_{light}	1	-
δ_{penumbra}	0.2	-
δ_{umbra}	0	-
Mass, satellite (m)	7	kg
μ	$3.986 \cdot 10^{14}$	-
Radius, Earth	$6.371 \cdot 10^{6}$	m
Radius, Sun	$6.96340 \cdot 10^{8}$	m
$m^b_{\text{mtq,lb}}$	-0.34	A·m^2
$m^b_{\text{mtq,ub}}$	0.34	A·m^2
Residual magnetic dipole ($\mathbf{m}^b_{\text{res}}$)	$12[1,1,1]^\intercal$	mA·m^2
k_{eddy}	0.01	-
η_{in}	0.92	-
$P_{\text{mtq, max}}$	2.52	W

Figure 5.8. The satellite spends about 20 seconds in the penumbra region in this scenario. The solar power function, (5.4), over time is shown in Figure 5.9. This figure clearly illustrates the need for a $\delta(\cdot,\cdot)$ part in the net power cost function, as there will be no solar power into the satellite while it is in the umbra region. Following this argument, it is intuitive that close to zero net power is optimal during the umbra region, as the optimal control problem reduces to minimizing the actuation power in (5.5). In Figure 5.10, this is accomplished during the umbra region for this control scenario. Figure 5.10 has two peaks for each optimization: one at the beginning and one at the end. These peaks coincide with the net energy cost function Figure 5.7, going from the initial sub-optimal solar power attitude to an optimal one at first and from the optimal attitude to the final attitude. A direct result of these peaks, the angular velocity of the satellite, is shown in Figure 5.12. The cumulative net power over time, giving the total energy accumulated by the system over the control horizon, is given in Figure 5.11. The figure also includes the performance of the PD controller. Figure 5.13 displays the torques from the reaction wheels. This figure is closely related to Figure 5.10, but it is possible to see that some smaller torque is applied to the reaction wheels also inside the umbra region. This behavior is also displayed in the figure showing the satellite's angular velocity, Figure 5.12. The reaction wheels' angular velocity can be seen in Figure 5.14. The torque from the magnetorquers is shown in Figure 5.15, while the perturbing torques are shown in Figure 5.16. The small breaks where the different plots flatline, such as the torque from the reaction wheels in Figure 5.13, often coincide with different imaging slewing maneuvers, and downlink communication pointing maneuvers.

The computation time of the given control scenario is shown in Table 5.6. The optimization was performed with a 2.4 GHz 8-core processor. The power gained over time, or the energy gained, by the different control schemes, evaluated by using the

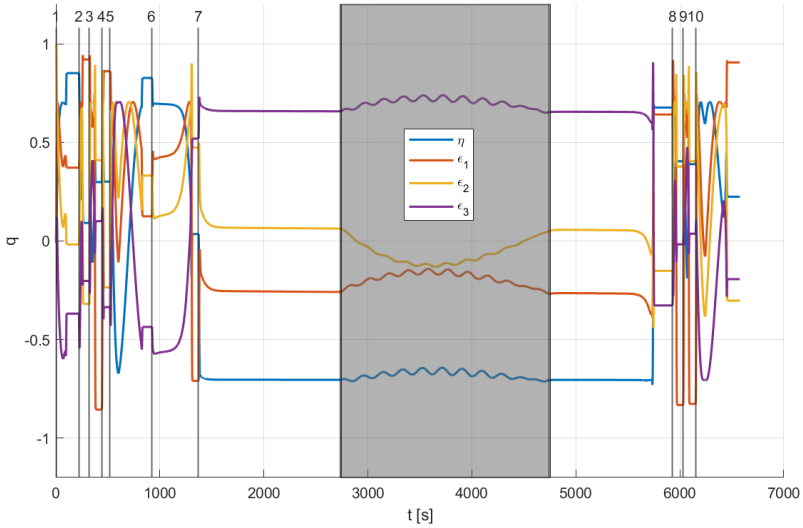

Figure 5.6: The optimal attitude quaternion trajectory, $\mathbf{q}_b^i$.

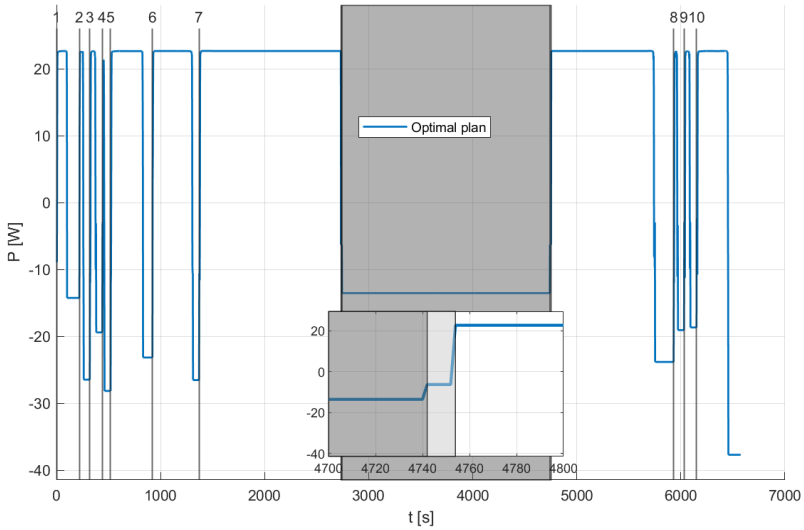

Figure 5.7: Net power, including the loads from the other subsystems, over time. In the lower part of the figure, a zoomed-in area highlights the net power as the satellite exits the umbra and penumbra regions.

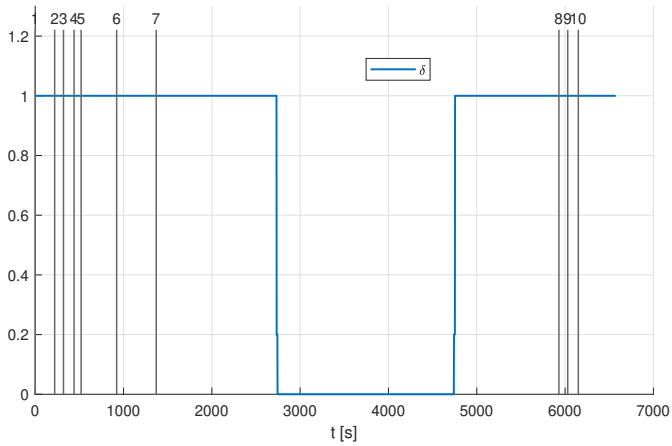

Figure 5.8: Solar magnitude, $\delta(\cdot, \cdot)$, over time.

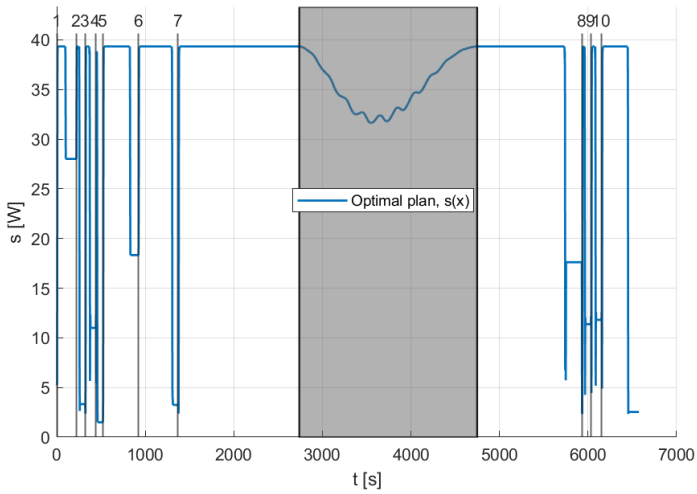

Figure 5.9: Solar power factor $\kappa(\cdot, \cdot)$ of the cost function over time.

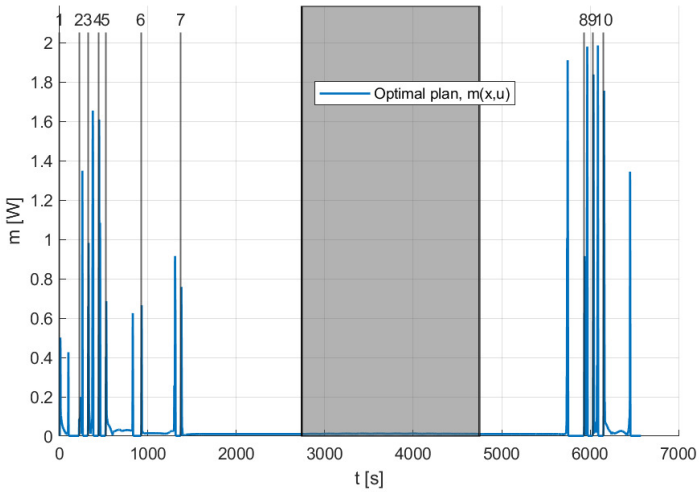

Figure 5.10: Actuation power part of the cost function over time.

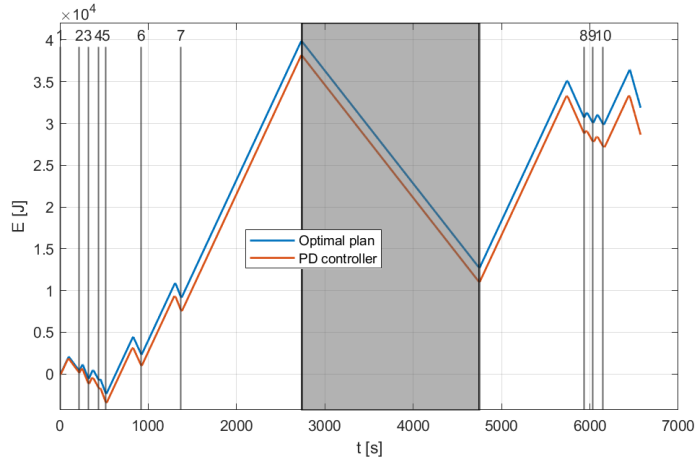

Figure 5.11: Cumulative values for the power terms in the cost function.

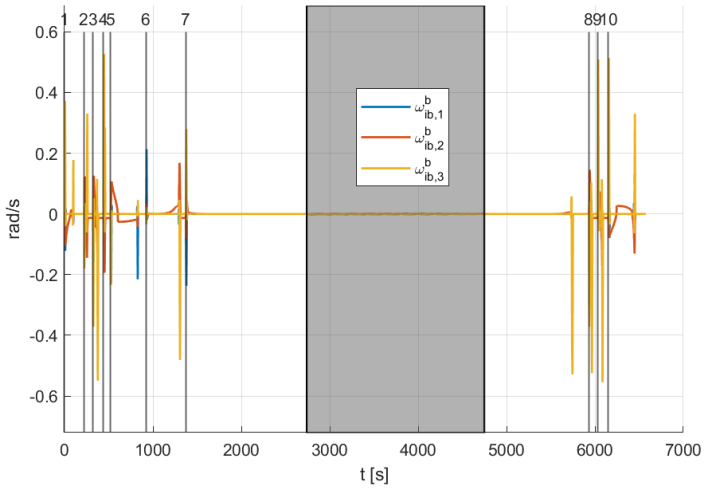

Figure 5.12: Angular velocity, satellite.

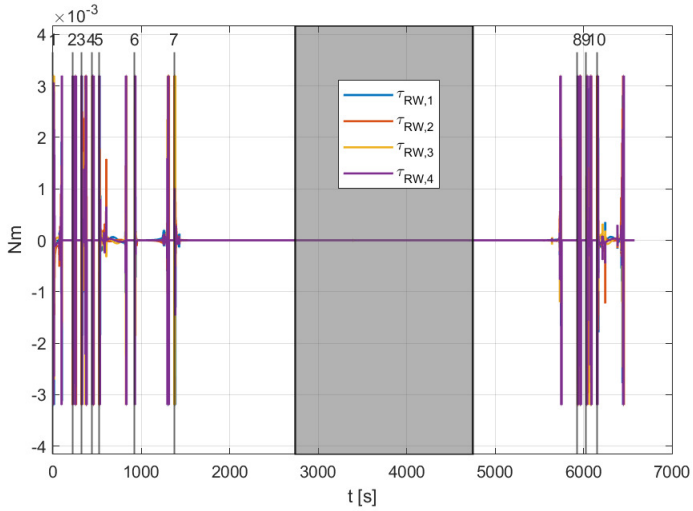

Figure 5.13: Torques from reaction wheels.

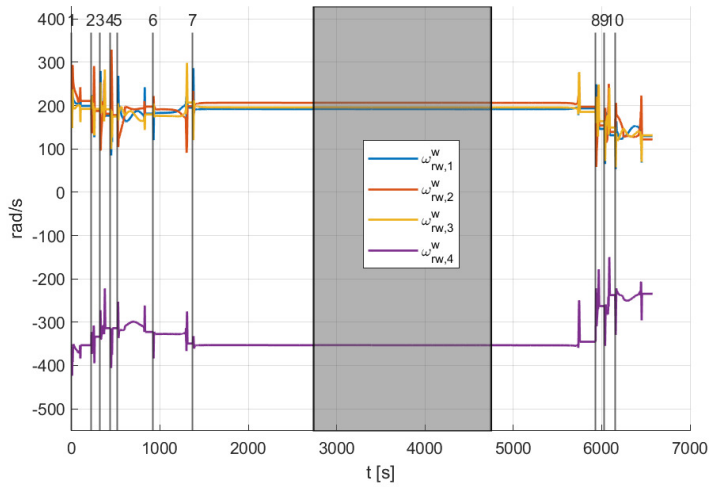

Figure 5.14: Angular velocity, reaction wheels.

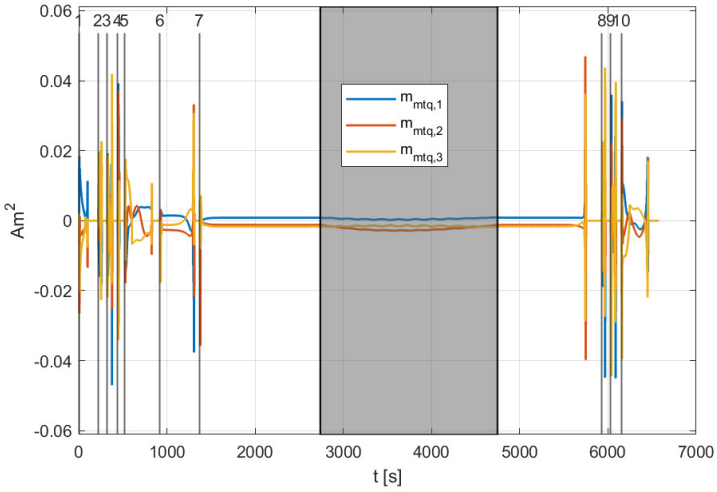

Figure 5.15: Torque from magnetorquers.

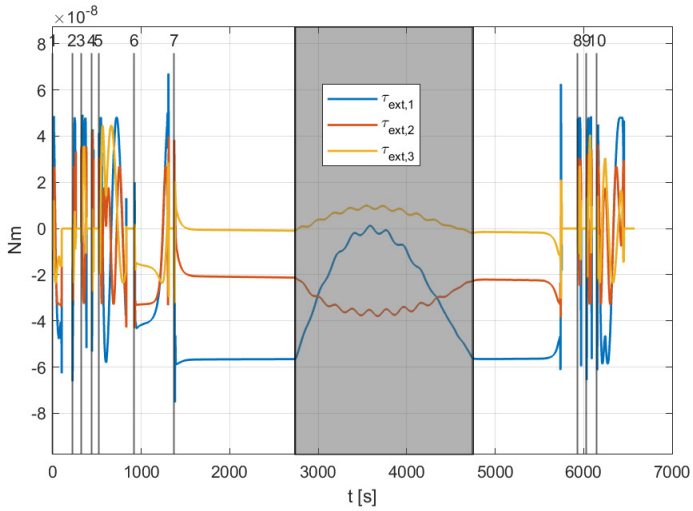

Figure 5.16: Perturbing torques.

cost function in (5.2), is shown in Table 5.7. The optimal solver finds a solution that returns 3229 J more than the PD controller alternative, giving an increase of 11.3%. The table also shows the increase provided by the optimal solution compared to the PD controller when the scenario is reduced, such as without including imaging and communication, without including the energy spent on the other subsystems, and an example where there longest optimization is omitted. The difference that appears in the table between the energy increase which should be identical, such as the total energy compared to the total energy without imaging and communication, is due to rounding errors.

The values for other objectives, the regulation towards the quaternion and angular velocity references, are shown in Table 5.8. The error values are given by the equation shown in (5.8), meaning that the quaternion error is given by $\left(1 - \left|\left(\mathbf{q}_b^i\right)^\intercal \mathbf{q}_{\text{ref}}\right|\right)$, and the angular velocity error is given by $\left(\boldsymbol{\omega}_{\text{ref}}^b - \boldsymbol{\omega}_{ib}^b\right)^\intercal \left(\boldsymbol{\omega}_{\text{ref}}^b - \boldsymbol{\omega}_{ib}^b\right)$. Two of the quaternion error values are negative only due to the change in approximated absolute value function that is used. The table shows that the optimal solver drives values significantly closer to the references than the PD controller.

5.9 Discussion

The attitude quaternion trajectory in Figure 5.6 shows that the satellite manages to reach the reference attitude for each optimization task and with the desired angular velocity required to begin the slew maneuver or downlink, depending on the set reference. An essential property of the eclipse function $\delta(\cdot, \cdot)$ is that it gives the optimal control problem a formulation that defines where the spacecraft can and cannot harvest solar power. More specifically, with the eclipse definition, the

Table 5.6: IPOPT output

Optimization task number	Number of iterations	Total CPU secs in IPOPT (w/o function evaluations)	Total CPU secs in NLP function evaluations
1	106	2.093	38.429
2	81	0.535	12.023
3	119	0.997	26.306
4	27	0.141	2.014
5	402	13.459	457.596
6	198	8.195	289.489
7	253	130.876	4323.100
8	177	1.432	27.125
9	89	0.879	20.079
10	1064	39.577	1226.046

optimal control problem defines an area, the umbra region, where the spacecraft should only consider the actuation cost. Note again that the actuation power in Figure 5.11 is never negative due to the reaction wheels being unable to return electrical energy to the spacecraft. This is a significant change from [2], due to the refined formulation of the actuation power in (5.7).

The main results in Table 5.7 show the amount of energy gained from the optimal control solver and the PD controller for a combination of the smaller control scenarios. There is no difference in energy with and without the imaging and communication tasks since these tasks are set identically for the optimal solution and the PD controller's solution. Removing them decreases the energy gained as a percentage, from 11.3% to 6.51%. Interestingly, the longest optimization, denoted as task 7, only gives a net energy increase of 1.12%. By excluding the longest optimization from the calculations, the increase in energy becomes 39.7%. The reason for this is that the primary benefit of the proposed method comes in the transient phases, in particular, the opportunity to let the optimal solver choose when to let go of the optimal solar attitude. The energy difference values, excluding the shortest optimization, range from about 230 J to about 600 J, no matter how long the optimization becomes. This indicates that the proposed method would be more beneficial the more frequently the imaging and communication tasks happen, or in other words, as the utilization of the satellite is increased.

Note that the one maneuver where the PD controller yields negative energy, task 4, is the shortest task. Given that the task is just 20 seconds, the PD controller does not move to a solar optimal attitude before going towards the reference.

The current scenario shows that the utilization of the satellite could be higher than what is shown in this scenario: The plot in Figure 5.11, which shows the cumulative energy of the satellite, only dips below zero once during the scenario,

Table 5.7: Energy, comparison

Optimization task number	Energy, optimal (J)	Energy, PD (J)	Energy increase (J)	Energy increase (%)
1	2 080.3	1 849.0	+231.3	+12.5
2	726.6	365.0	+361.6	+99.1
3	931.8	567.4	+364.4	+64.2
4	81.3	-18.8	+100.1	-
5	6 788.5	6 507.5	+280.9	+4.32
6	8 490.7	8 241.7	+249.0	+3.02
7	25 825.9	25 539.8	+286.0	+1.12
8	498.5	131.8	+366.7	+278
9	893.2	469.3	+423.9	+90.3
10	6 503.5	5 938.8	+564.7	+9.51
Total energy	31 892	28 663	+3 229	+11.3
Total energy without imaging and comms	52 844	49 615	+3 229	+6.51
Net energy without imaging and comms	129 794	126 565	+3 229	+2.55
Total energy, excluding task 7	10 350	7 407	+2 943	+39.7
Total energy without imaging and comms, excluding task 7	27 019	24 076	+2 943	+12.3
Net energy without imaging and comms, excluding task 7	44 839	41 895	+2 943	+7.02

when the maneuvers are short at the beginning of the scenario. For the rest of the scenario, there is a surplus of energy. Because of this, it can be concluded that the satellite can be utilized more for imaging and downlink than what is presented in this scenario.

The rotations that appear in the umbra region have two causes: they are both due to the existence of external torques and due to the nature of the numerical optimization. With the way the cost function is constructed, owing to the gyroscopic term in the system's dynamics, i.e., (5.11c), finding a solution where the control torque is held at precisely zero, is difficult for the solver, even without other torques affecting the satellite. Efforts can be made to mitigate this effect, such as choosing a set of body frame axes that align with the principal axes of inertia, but the external torques will remain.

A possible limitation of the approach presented in this chapter is the time spent

Table 5.8: Reference comparison

Task number	Quaternion error, optimal	Quaternion error, PD	Angular velocity error, optimal	Angular velocity error, PD
1	$4.2744 \cdot 10^{-6}$	$4.8769 \cdot 10^{-4}$	$8.7045 \cdot 10^{-10}$	$1.3583 \cdot 10^{-3}$
2	$8.1493 \cdot 10^{-5}$	$5.0495 \cdot 10^{-5}$	$5.3019 \cdot 10^{-8}$	$2.6908 \cdot 10^{-4}$
3	$1.1256 \cdot 10^{-5}$	$3.5457 \cdot 10^{-3}$	$1.2866 \cdot 10^{-8}$	$1.5230 \cdot 10^{-3}$
4	$7.2804 \cdot 10^{-4}$	$1.2148 \cdot 10^{-1}$	$3.8977 \cdot 10^{-7}$	$3.9212 \cdot 10^{-2}$
5	$1.3382 \cdot 10^{-6}$	$2.8139 \cdot 10^{-5}$	$5.9935 \cdot 10^{-10}$	$2.9088 \cdot 10^{-6}$
6	$4.8979 \cdot 10^{-7}$	$8.6700 \cdot 10^{-3}$	$1.2434 \cdot 10^{-9}$	$6.6274 \cdot 10^{-3}$
7	$-1.0255 \cdot 10^{-6}$	$8.5661 \cdot 10^{-2}$	$7.8557 \cdot 10^{-13}$	$3.1783 \cdot 10^{-2}$
8	$1.8394 \cdot 10^{-5}$	$2.6905 \cdot 10^{-3}$	$1.5302 \cdot 10^{-8}$	$9.6976 \cdot 10^{-4}$
9	$6.6048 \cdot 10^{-6}$	$4.3345 \cdot 10^{-3}$	$6.5721 \cdot 10^{-9}$	$1.5785 \cdot 10^{-3}$
10	$9.3724 \cdot 10^{-7}$	$1.2350 \cdot 10^{-3}$	$1.0088 \cdot 10^{-9}$	$2.3129 \cdot 10^{-4}$

computing the optimal trajectory, as can be seen in Table 5.6. A spacecraft like HYPSO-2, with the parameters for the orbit presented in Table 5.4, orbits the Earth about once every 90 minutes, and would go into these energy harvesting phases twice during an orbit. In the time it now takes to calculate one single trajectory, the satellite would require several passes if the time needed to construct the problem in CasADi before solving it is included. For this reason, efforts should be made to reduce the time required for calculating the optimal attitude trajectories. A possible avenue towards this goal includes precomputing the position and velocity of the satellite. This is expected to work well, except in a few special cases: Suppose so high accuracy is required that the perturbations in orbital positions dependent on satellite attitude, which were not included in this chapter, must be taken into account. Precomputing the position and velocity will not be an option in that case. Similarly, precomputing the position and velocity of the satellite would not work if the satellite is equipped with thrusters and performs a maneuver during the optimization.

The torque produced by the magnetorquers is calculated by the control algorithm in (5.14). The optimal solver could also calculate this torque. It is possible to include the magnetorquer torque formulation into the optimal control problem and let the solver figure out how much torque the magnetroquers should produce. In this chapter, the formulation given in (5.14) is preferred to limit the computation time for the optimal control trajectory.

5.10 Conclusion

The net power function introduced in [2] has been extended to include the environmental effects the spacecraft experiences in space, a second actuator, and the

$\delta(\cdot,\cdot)$ function that describes the magnitude of the solar irradiance as a function of where the spacecraft is in its orbit. In particular, the net energy optimization performs as desired when the control horizon approaches a complete orbit when the spacecraft traverses both the umbra and penumbra regions of the orbit. The results show that the optimized solution is increasingly beneficial when the time between each maneuver decreases.

5.11 Perturbations

Three types of perturbations are included in the simulations in this chapter to make the simulated environment more realistic: Gravity gradient, magnetic torque, and eddy current torque.

The gravity gradient torque comes from the change in the pull due to different parts of the spacecraft body being in different places in the gravity field and is defined as [39]

$$\boldsymbol{\tau}^b_{\text{grav}} = 3\frac{\mu}{\|\mathbf{r}^i\|^3}\mathbf{S}\left(\frac{\mathbf{r}^\mathbf{i}}{\|\mathbf{r}^i\|}\right)\mathbf{J}\frac{\mathbf{r}^\mathbf{i}}{\|\mathbf{r}^i\|}. \tag{5.18}$$

The magnetic torque is due to the spacecraft carrying electronic equipment that sets up a magnetic field that interacts with Earth's magnetic dipole. The torque is defined as

$$\boldsymbol{\tau}^b_{\text{mag}} = \mathbf{S}(\mathbf{m}^b_{\text{res}})\mathbf{B}^b, \tag{5.19}$$

where $\mathbf{B}^b$ is the magnetic field of the Earth represented in body frame coordinates, and $\mathbf{m}^b_{\text{res}}$ is the residual magnetic dipole vector. Note that while the physical principle used here is the same as is used to control the spacecraft with magnetorquers, the residual magnetic dipole $\mathbf{m}^b_{res}$ is separate from the dipole set up from the magnetorquers.

The eddy current torque is given as [39]

$$\boldsymbol{\tau}^b_{\text{eddy}} = -k_{\text{eddy}}\mathbf{S}(\mathbf{B}^b)\mathbf{S}(\boldsymbol{\omega}^b_{ib})\mathbf{B}^b, \tag{5.20}$$

where k_{eddy} is a positive constant.

We assume the torque from atmospheric drag and solar radiation pressure can be omitted, which is typical e.g., for a CubeSat where the center of mass needs to be in the geometric center of the satellite.

Chapter 6

Energy optimal attitude control of a satellite actuated by magnetorquers in minimum time

This chapter is based on

[5] **B. A. Kristiansen**, J. T. Gravdahl, S. Gros, and T. A. Johansen, "Energy optimal attitude control of a satellite actuated by magnetorquers in minimum time", in *Proceedings of the 7th IEEE Conference on Control Technology and Applications (CCTA)*, Bridgetown, Barbados, Aug. 2023.

6.1 Introduction

Magnetorquers are actuators that use the Earth's magnetic field to control the spacecraft's attitude through magnetic actuation. They commonly produce a very small torque, and thus are primarily used for small satellites. Owing to the physical law the control action of the magnetorquers is bound by, namely that the torque is equal to the vector cross product of the magnetic dipole moment set up by the magnetorquers and the geomagnetic field vector, the system can reach a state where the magnetorquers are unable to supply the desired torque that is required for the system to reach the desired attitude. This occurs when the required magnetic moment parallels the local geomagnetic field vector. This problem, combined with the small torque, makes maneuvers endure for a fraction of an orbit to several orbits, in contrast to maneuvers performed with reaction wheels, which could last from seconds to minutes. While reaction wheels come in sizes that fit into CubeSats, a common structure used for small satellites, magnetorquers as a means of attitude control remain a popular solution, particularly for very small satellites such as 1U and 2U CubeSats.

The concept of using magnetic torque for attitude control has a long history; see for example [40], [41], [42], [43], and [44]. The full control strategy presented in [40] included both a detumbling term, meaning one that uses the magnetic field to dampen the angular velocity, and one that provides attitude feedback. Some of the articles ([40], [41], [42]) discuss global, as opposed to local, attitude stabilization

based on two mathematically different equilibrium points representing the same physical attitude, a concept which is no longer commonly discussed in attitude control literature as global attitude stabilization is not possible with continuous time-invariant feedback [17]. In [43], the authors avoid this problem by looking for almost-global attitude stability. The authors in [45] used hybrid control to show some global stability properties. The survey paper [44] highlights the use of periodic control for magnetic control of satellites, a concept also utilized in [40]. The assumption behind periodic control for magnetic control of satellites is that the magnetic field is periodic, meaning that the magnetic field's values repeat as the satellite makes a full orbit. As the Earth rotates under the satellite as it orbits, in particular for satellites in low-Earth orbit, this does not exactly hold, motivating the stability analysis in [42]. Others have also looked into optimal control strategies: [46], [47], and [48] all studied optimal attitude control with magnetorquers. [46] looked into the linearized model for LQR onboard a satellite. In [47] the authors use a periodic Riccati equation, while [48] uses periodic optimal feedback in discrete-time, both using linearized models.

Time-optimal attitude control has been studied in [10], although the authors did not consider magnetic torque in their problem. In [49], the authors investigated a time-optimal magnetic attitude maneuver using an analytic method for optimization. In this chapter, the optimal control problem is solved using multiple-shooting, a direct numerical optimization method.

The energy optimal aspect of the optimization in this chapter refers to the net power cost function introduced in [50] and extended upon in [7]. The cost function the authors used in [31] is similar to the one used here since the authors optimize based on solar energy, but the net power cost function used here also includes the power spent on actuation.

The contribution of this chapter is demonstrating how an energy optimal numerical control framework can be used to optimize the net energy of a satellite actuated with magnetic torquers, or magnetorquers. The net energy, based on the net power cost function, is the integral of the difference in power that the satellite harvests through its solar cell arrays and the power it spends on actuation. The optimal control problem in this chapter combines the aforementioned cost function with the minimization of maneuvering time. This multi-objective optimization, which is a combination of the four objectives i) maximize net power, ii) reach the desired attitude, iii) reach the desired angular velocity, and iv) minimize time, is formulated to reach objective i)-iii) without having to specify the final time of the optimization.

The remaining sections of the chapter are as follows: in Section 6.2 the optimal control problem for the satellite actuated by magnetorquers is introduced. In addition to this, a brief introduction to the net power cost function and the changes to the optimal control problem that has been made to facilitate the use of magnetorquers for attitude control is included in this section. Section 6.3 introduces the simulation setup. In Section 6.4, the results from the optimization are presented, including the Pareto front, which is commonly used to analyze multi-objective optimization strategies. The penultimate section, Section 6.5, contains the discussion, while the last section, Section 6.6, contains a brief conclusion.

6.2 Problem formulation

6.2.1 Reference frames

Three frames are used in this chapter: the inertial frame is an Earth-centered inertial reference frame with vectors denoted by a superscript i. The satellite itself has a frame attached to it, the body frame, denoted by superscript b. The third frame is a local vertical, local horizontal (LVLH) frame, the orbit frame, is denoted by superscript o. The axes of the orbit frame are defined in (6.1)

$$\hat{\mathbf{z}}^o = -\frac{\mathbf{r}^i}{\|\mathbf{r}^i\|}, \ \hat{\mathbf{x}}^o = \frac{\mathbf{v}^i}{\|\mathbf{v}^i\|}, \ \hat{\mathbf{y}}^o = \frac{\hat{\mathbf{z}}^o \times \hat{\mathbf{x}}^o}{\|\hat{\mathbf{z}}^o \times \hat{\mathbf{x}}^o\|}, \tag{6.1}$$

where $\mathbf{r}^i$ is the position of the satellite in the inertial reference, or ECI, frame, and $\mathbf{v}^i$ is its velocity. $\|\cdot\|$ is the norm of a vector, and $\times$ is the vector cross product. The $\hat{\cdot}$ symbol indicates that it is a unit vector.

6.2.2 Optimal control problem

The optimal control problem we solve in this chapter is given in (6.2),

$$\min_{\mathbf{x},\mathbf{u},T} \quad J_{\mathrm{F}} - \frac{1}{T}\int_0^T P(\mathbf{x},\mathbf{u})\,\mathrm{d}t + k_3 T \tag{6.2a}$$

$$\text{s.t. } \dot{\mathbf{q}}_b^o = \frac{1}{2}\mathbf{T}(\mathbf{q}_b^o)\boldsymbol{\omega}_{ob}^b + \frac{1}{2}\rho\mathbf{q}_b^o\left(((\mathbf{q}_b^o)^\intercal\,\mathbf{q}_b^o)^{-1} - 1\right) \tag{6.2b}$$

$$\frac{{}^b d}{dt}\boldsymbol{\omega}_{ib}^b = \mathbf{J}^{-1}\left(-\mathbf{S}\left(\boldsymbol{\omega}_{ib}^b\right)\left(\mathbf{J}\boldsymbol{\omega}_{ib}^b\right) + \mathbf{S}\left(\mathbf{m}^b\right)\mathbf{B}^b + \boldsymbol{\tau}_{\mathrm{ext}}^b\right) \tag{6.2c}$$

$$\frac{{}^b d}{dt}\boldsymbol{\omega}_{ob}^b = \frac{{}^b d}{dt}\boldsymbol{\omega}_{ib}^b + \left(\mathbf{S}(\boldsymbol{\omega}_{ob}^b)\mathbf{R}_o^b + \mathbf{R}_o^b\mathbf{S}(\mathbf{R}_b^o\boldsymbol{\omega}_{ob}^b)\right)\mathbf{R}_i^o\frac{\mathbf{S}\left(\mathbf{r}^i\right)\mathbf{r}^i}{(\mathbf{r}^i)^\intercal\,\mathbf{r}^i} \tag{6.2d}$$

$$\frac{{}^i d}{dt}\mathbf{r}^i = \mathbf{v}^i \tag{6.2e}$$

$$\frac{{}^i d}{dt}\mathbf{v}^i = -\frac{\mu\mathbf{r}^i}{\|\mathbf{r}^i\|^3} \tag{6.2f}$$

$$\mathbf{m}_{\mathrm{lb}}^b \leq \mathbf{m}^b \leq \mathbf{m}_{\mathrm{ub}}^b \tag{6.2g}$$

$$T > 0 \tag{6.2h}$$

$$\mathbf{x}(0) = \mathbf{x}_0. \tag{6.2i}$$

For details on the dynamical modelling, see Chapter 5, Chapter 11, and [19].

The changes from the optimal control problem in [7] (and [50]) is that the reaction wheels and their dynamics have been removed, and magnetorquers are now used as the main actuator for attitude control. The torque applied to the spacecraft by the magnetorquers is determined by

$$\boldsymbol{\tau}_{\mathrm{mtq}}^b = \left(\mathbf{m}^b\right) \times \mathbf{B}^b = \mathbf{S}\left(\mathbf{m}^b\right)\mathbf{B}^b, \tag{6.3}$$

which can be seen in (6.2c), where $\mathbf{S}(\cdot)$ is a skew-symmetric matrix representing the vector cross product, $\mathbf{B}^b$ is the vector representing the local geomagnetic field in

the body frame, and $\mathbf{m}^b$ is the magnetic moment the magnetorquers can produce, which is what we can control. Because of the cross product in (6.3), the torque has to be perpendicular to the magnetic field vector, which constrains the actuation compared to other actuators. In addition to these changes, an additional term is introduced to the cost function (6.2a), namely $k_3 T$, where k_3 is a weight and T is the final time of the optimization. This term is added to the cost function to minimize this time. The variable $T > 0$ is a free parameter in the optimization.

The rest of the variables in (6.2) describe the attitude control problem: $\mathbf{q}_b^o$ is the unit quaternion representing the attitude of the spacecraft body frame b with respect to the inertial reference frame i. The $\mathbf{T}(\cdot)$ matrix in (6.2b) is given by [18]

$$\mathbf{T}(\mathbf{q}) = \begin{bmatrix} -\boldsymbol{\epsilon}^\intercal \\ \eta \mathbf{I}_{3\text{x}3} + \mathbf{S}(\boldsymbol{\epsilon}) \end{bmatrix}, \tag{6.4}$$

where η and $\boldsymbol{\epsilon}$ are the scalar and vector parts of the unit quaternion, respectively, and $\mathbf{I}_{3\text{x}3}$ is the three-dimensional identity matrix. $\mathbf{R}_o^b$ is the rotation matrix representation of the quaternion. $\mathbf{R}_o^i$ can be constructed using the vectors in the definition of the orbit frame in (6.1). The angular velocity between the body and inertial frame is given by $\boldsymbol{\omega}_{ib}^b$, while the angular velocity between the body frame and the orbit frame is given by $\boldsymbol{\omega}_{ob}^b$. The term $\frac{1}{2}\rho \mathbf{q}_b^o(((\mathbf{q}_b^o)^\intercal \mathbf{q}_b^o)^{-1} - 1)$, where ρ is a small positive constant, is the Baumgarte stabilization term [29]. $\mathbf{J}$ is the spacecraft inertia matrix, and $\mathbf{m}_{\text{lb}}^b$ and $\mathbf{m}_{\text{ub}}^b$ are the lower and upper bounds on the magnetorquers magnetic moment, respectively. The external torques, $\boldsymbol{\tau}_{\text{ext}}$, are in this chapter given by the sum of two torques that commonly affect satellites in low Earth orbit [39]:

$$\boldsymbol{\tau}_{\text{ext}} = \mathbf{S}(\mathbf{m}_{\text{res}}^b)\mathbf{B}^b - k_{\text{eddy}}\mathbf{S}(\mathbf{B}^b)\mathbf{S}(\boldsymbol{\omega}_{ib}^b)\mathbf{B}^b, \tag{6.5}$$

where the first term is the magnetic disturbance torque, and the second is the eddy current torque. μ is the standard gravitational parameter of the Earth. The constraint in (6.2i) is included to ensure that the problem starts at the correct state. The state vector is denoted by $\mathbf{x} = \left[\mathbf{q}_b^o, \boldsymbol{\omega}_{ib}^b, \boldsymbol{\omega}_{ob}^b, \mathbf{r}^i, \mathbf{v}^i\right]^\intercal$, the initial values are denoted by $\mathbf{x}_0$. $\mathbf{u}$ is used as a general symbol for the input to the system.

6.2.3 Cost function

The cost function is given by (6.2a). The first part of the cost function, J_{F}, is

$$\begin{aligned} J_{\text{F}} &= k_1 J_{\text{path,ref}} + k_2 J_{\text{velocity}} \\ &= k_1 \left(1 - |(\mathbf{q}_b^o)^\intercal \mathbf{q}_{\text{ref}}|\right) + k_2 \left(\boldsymbol{\omega}_{\text{e}}^b\right)^\intercal \left(\boldsymbol{\omega}_{\text{e}}^b\right), \end{aligned} \tag{6.6}$$

where $\mathbf{q}_{\text{ref}}$ is the reference for the attitude.The angular velocity error, $\boldsymbol{\omega}_{\text{e}}^b$, is defined as $\boldsymbol{\omega}_{\text{e}}^b = \left(\boldsymbol{\omega}_{\text{ref}}^b - \boldsymbol{\omega}_{ob}^b\right)$, where $\boldsymbol{\omega}_{\text{ref}}^b$ is the angular velocity reference. $\left(1 - \left|\left(\mathbf{q}_b^i\right)^\intercal \mathbf{q}_{\text{ref}}\right|\right)$ is a metric on SO(3) [28]. J_{F} is a terminal cost that applies only at the final state. Including these terms in the cost function is an alternative to including them as hard constraints in the solver.

The middle term of J_{F}, $-\frac{1}{T}\int_0^T P(\mathbf{x}, \mathbf{u})\,\mathrm{d}t$, is the integral of the net power term $P(\mathbf{x}, \mathbf{u})$ [50]. The net power is calculated by subtracting the power spent

on actuation from the incoming power, which is the power the solar cell arrays supply to the system, according to

$$P(\mathbf{x}, \mathbf{u}) = \kappa(\mathbf{R}_b^i, \mathbf{r}_{\text{Sun}})\delta(\mathbf{r}_{\text{Sun}}, \mathbf{r}_{\text{Earth}}) - \left(\mathbf{I}_{\text{mtq}}^b \circ \mathbf{I}_{\text{mtq}}^b\right)^\intercal \mathbf{R}_{\text{mtq}}, \tag{6.7}$$

Here $\kappa(\cdot)$, as a function of the attitude, $\mathbf{R}_b^i$, and the vector from the satellite to the Sun, $\mathbf{r}_{\text{Sun}}$, is the solar power function which is given as

$$\kappa(\mathbf{R}_b^i, \mathbf{r}_{\text{Sun}}) = \sum_{j=1}^{n_s} \max\left(\left(\hat{\mathbf{s}}^b\right)^\intercal \hat{\mathbf{n}}_j^b, 0\right)\left(\left(\hat{\mathbf{s}}^b\right)^\intercal \hat{\mathbf{n}}_j^b\right) c_{s,j} A_j. \tag{6.8}$$

where $\hat{\mathbf{s}}^b$ is the normalized sun vector, $\hat{\mathbf{n}}_j^b, j = 1 \dots n_s$ is the normal vector of each solar panel, which have area A_j. $c_{s,j}$ is the product between solar irradiance and the efficiency of the specific solar panel. The max-function is included so that only the solar power of faces exposed to solar irradiance gets counted. To make the cost function smooth, we use the approximation as defined in Equation (2.11).

The δ-function in (6.7), which is a function of the positions $\mathbf{r}_{\text{Sun}}$ and $\mathbf{r}_{\text{Earth}}$ of the satellite relative to the Sun and to the Earth, respectively, represents the amount of solar irradiance that reaches the satellite. It can be calculated offline when the orbit is set beforehand, such as in the model presented in (6.2e) and (6.2f). In this chapter, the formulation for the $\delta(\cdot)$ function presented in [7] is used. Other representations, such as the ones presented in [32], can also be used.

$\mathbf{I}_{\text{mtq}}^b$ is the vector flow of current through the magnetorquers with resistance $\mathbf{R}_{\text{mtq}}^b$. The operator $\circ$ is the Hadamard, or element-wise, product. The mapping between $\mathbf{m}^b$ and $\mathbf{I}_{\text{mtq}}^b$ is given by

$$\mathbf{m}^b = \left(\mathbf{n}_{\text{mtq}}^b\right) \circ \left(\mathbf{A}_{\text{mtq}}^b\right) \circ \mathbf{I}_{\text{mtq}}^b, \tag{6.9}$$

where $\mathbf{n}_{\text{mtq}}^b$ is the vector with the number of wire turns of the magnetorquer per each axis in the body frame. $\mathbf{A}_{\text{mtq}}^b$ is the vector the cross-sectional areas of the coils.

The weights k_1 and k_2, along with k_3 associated with the minimum time objective, are used to tune the response of the multi-objective optimization. Including the time objective in the cost function this way lets the optimal solver choose the final time based on the chosen weights.

6.3 Simulation setup

The simulation study in this chapter is based on a 6U CubeSat, meaning that the dimensions of the satellite are $10 \times 20 \times 30$ cm^3. The areas covered by solar panels are given by

$$\mathbf{A}_{\text{sca}} = [0.03, 0.06, 0, 0.03, 0.06, 0]^\intercal \text{ m}^2, \tag{6.10}$$

where each value $A_{\text{sca},i}$ corresponds to face number i, $i = 1 \dots 6$, and a value of zero means that no solar panel is present on that face of the spacecraft. The magnetic field is simulated using the IGRF model [37].

The PD controller from [9], which is not constrained by producing a torque perpendicular to the magnetic field, is used to produce the initial guesses for the

solver where the reference for most of the control horizon is held at the energy optimal attitude, as detailed in [50]. The PD controller sampling rate is set to 1 Hz, and the state history and control input are both used as initial guesses for the optimal control problem for each control step N. The initial guess for the time variable T is set to 3000 s.

In this chapter, we want to apply the proposed controller to a point-to-point, sometimes called a rest-to-rest maneuver. The initial values for the states are set to be $\mathbf{q}_b^i(0) = [0, 0, 1, 0]^\intercal$ and $\boldsymbol{\omega}_{ib}^b(0) = [0, 0, 0]^\intercal$, assuming that the satellite is already detumbled, which is a common strategy with magnetorquers, see for example [40]. For $\mathbf{r}^i$ and $\mathbf{v}^i$ the initial values are set by sending the values in Table 6.1 through the RANDV function from [32]. $\boldsymbol{\omega}_{ib}^b$ is uniquely set when the orbit and the orbit frame angular velocity is defined. The references are set to $\mathbf{q}_{\text{ref}} = [0, \frac{1}{\sqrt{2}}, 0, \frac{1}{\sqrt{2}}]$ and $\boldsymbol{\omega}_{ob}^b = [0, 0, 0]$.

The optimal control problem is discretized using multiple shooting, integrated using a Runge-Kutta 4 integrater, and is solved with IPOPT [20] using CasADi [30]. The constraint keeping the time variable positive, (6.2h), is implemented with the lower bound on T set to 100 s instead of zero to promote a physically meaningful solution in the solver. Note that while the time is constrained to be positive, it might be necessary to additionally constrain the final time from above to avoid numerical problems.

Table 6.1: Orbital elements

Variable	Value	Unit
Semimajor axis	6898	km
Eccentricity	0.000713	-
Inclination	97.427	deg (°)
Right ascension of the ascending node	215.365	deg (°)
Argument of perigree	83.564	deg (°)
True anomaly	34.004	deg (°)

The inertia matrix $\mathbf{J}$ is given in (6.11) [1], which is for a 6U CubeSat.

$$\mathbf{J} = \begin{bmatrix} 0.0775 & 0.0002 & -0.0002 \\ 0.0002 & 0.1067 & 0.0005 \\ -0.0002 & 0.0005 & 0.0389 \end{bmatrix} \text{kg} \cdot \text{m}^2, \tag{6.11}$$

Table 6.2 shows the various constants used in the optimal control problem. c_s written only once, as $c_{s,j}$ from (6.8) is identical for all j. The three-dimensional column vector of ones is denoted by $\mathbf{1}$.

Different values of k_3 are tried. The results for $k_3 = 1 \cdot 10^{-8}$ are displayed in the results section. The simulations were performed on a computer with a 2.40 GHz 8-core processor.

Table 6.2: Various constants

Variable	Value	Unit
Control intervals (N)	100	-
Solar irradiance	1366	W/m^2
Solar panel efficiency	20	%
c_s	272.2	W/m^2
η_{rw}	85	%
α	10^{-7}	-
k_1	$2 \cdot 10^3$	W^2
k_2	$2 \cdot 10^5$	J
k_3	$1 \cdot 10^{-8}$	W
ρ	10^{-2}	-
μ	$3.986 \cdot 10^{14}$	-
$\mathbf{m}^b_{\text{des}}$	$12[1,1,1]^\intercal$	$mA{\cdot}m^2$
k_{eddy}	0.01	-
$\mathbf{n}^b_{\text{mtq}}$	$\left(1.1 \cdot 10^5\right)[1,1,1]^\intercal$	-
$\mathbf{A}^b_{\text{mtq}}$	$\left(5 \cdot 10^{-3}\right)^2 \pi[1,1,1]^\intercal$	m^2
$\mathbf{m}^b_{\text{lb}}$	$-0.34\ [1,1,1]^\intercal$	$A{\cdot}m^2$
$\mathbf{m}^b_{\text{ub}}$	$0.34\ [1,1,1]^\intercal$	$A{\cdot}m^2$

6.4 Results

Figure 6.1 shows the attitude trajectory that comes as a result of the optimization when $k_3 = 1 \cdot 10^{-8}$. The shaded area represents the time the satellite is in eclipse. Here, we can see that the attitude optimization reaches the reference value. The accompanying angular velocity, $\boldsymbol{\omega}^b_{ob}$, and magnetic moment, $\mathbf{m}^b$, are shown in Figure 6.2 and Figure 6.3, respectively. The angular velocity is not exactly zero for this optimization, but the state ends relatively close to the reference. Figure 6.1 and Figure 6.2 show that the optimal solution comes close to achieving two of the objectives, namely that the attitude and angular velocity should be close to their references, by the end of the control scenario.

The evolution of the net power part of the cost function over time is shown in Figure 6.4. The maximum power the satellite can receive at any given time with the specified solar panels is 16-17 W, where Figure 6.4 maxes out. The section between 2800 s and 4800 s where the cost function seems zero is where the satellite is in an eclipse, meaning that no solar irradiance reaches the satellite. This coincides with the shaded areas of the plots. The amount of solar irradiance that reaches the satellite, or $\delta(\cdot)$, is shown over time in Figure 6.5.

Table 6.3 shows the time it took for the solver, IPOPT, to find the optimal solution.

Figure 6.6 shows the values of time T plotted against the net energy gained for a range of values of k_3. The values for k_3 are shown in the first column in Table 6.4. Table 6.4 also shows the change in values for the other objectives the optimization tries to accomplish. The points in Figure 6.6 are denoted by the value of the exponent in the value the weight k_3 takes at that point. All the simulations

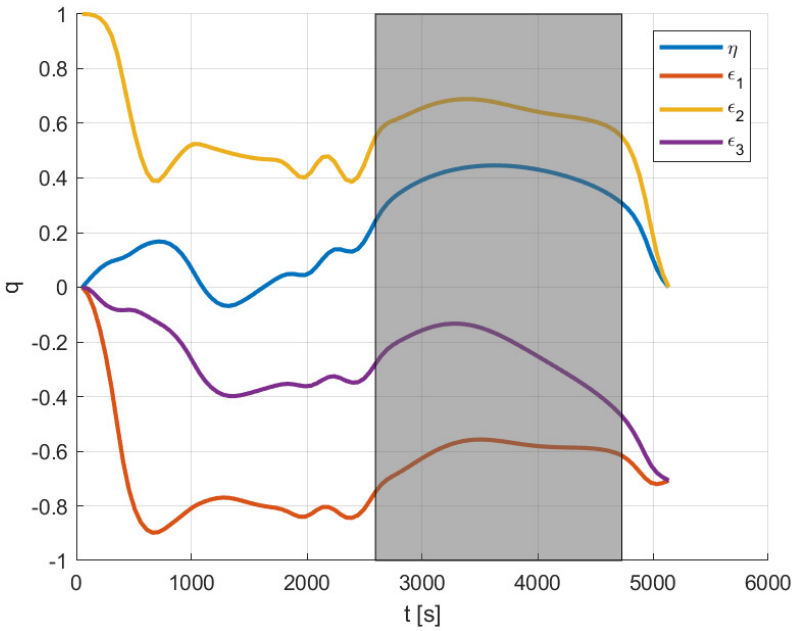

Figure 6.1: Quaternion trajectory.

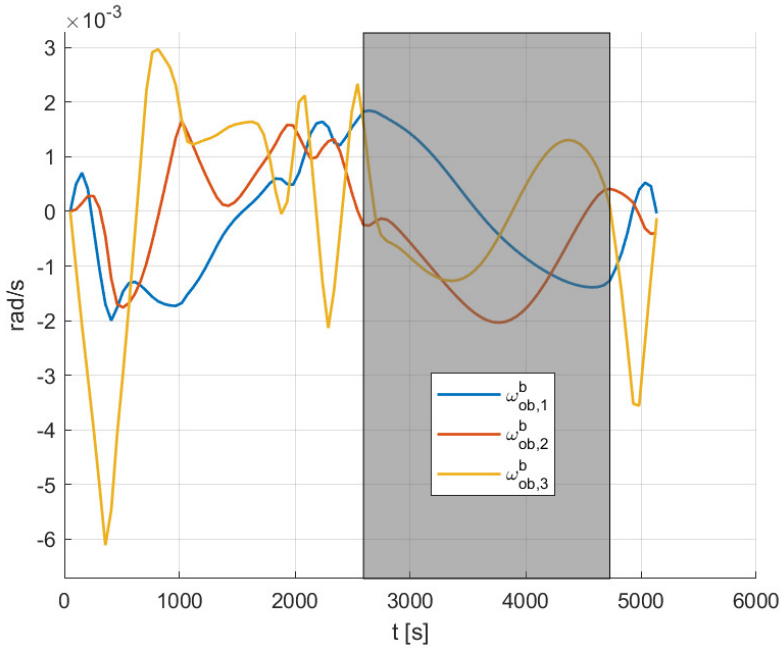

Figure 6.2: Angular velocity, body frame relative to orbit frame.

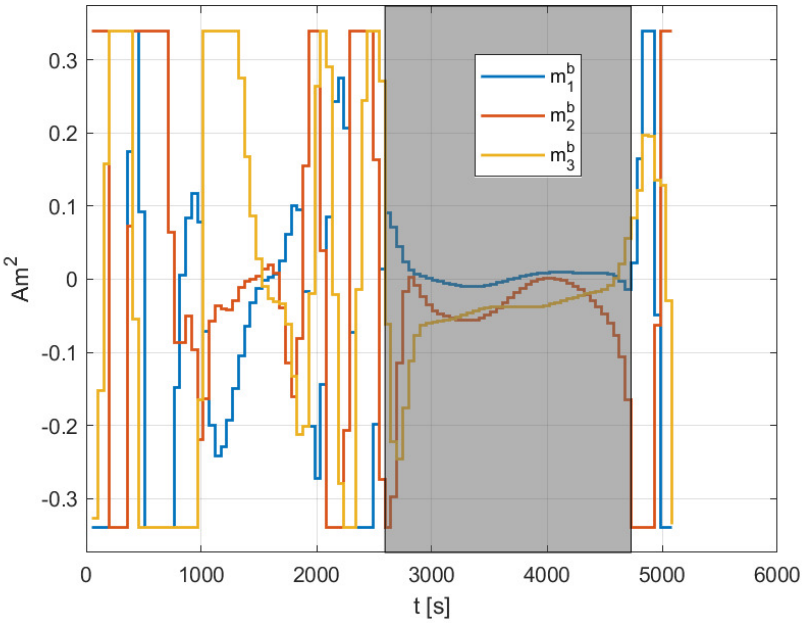

Figure 6.3: Magnetic moment, magnetorquers.

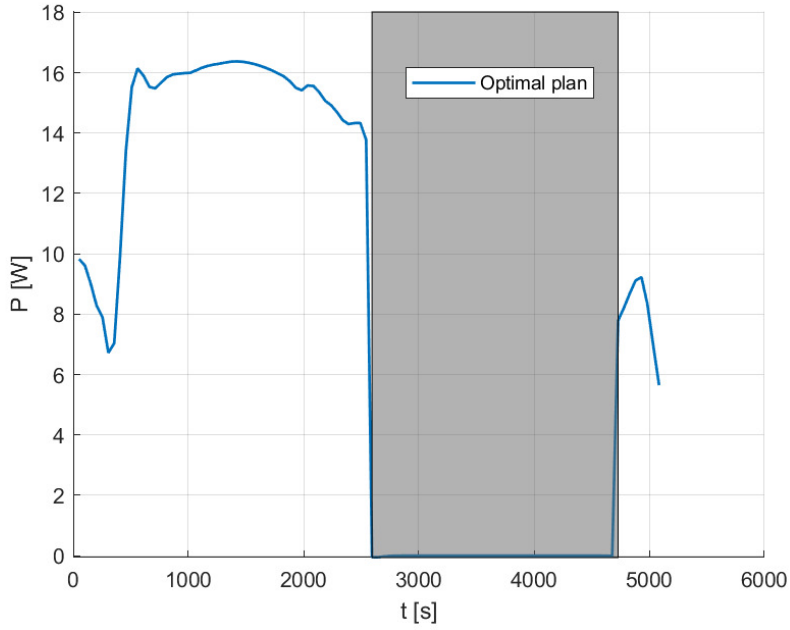

Figure 6.4: Net power evolution over time.

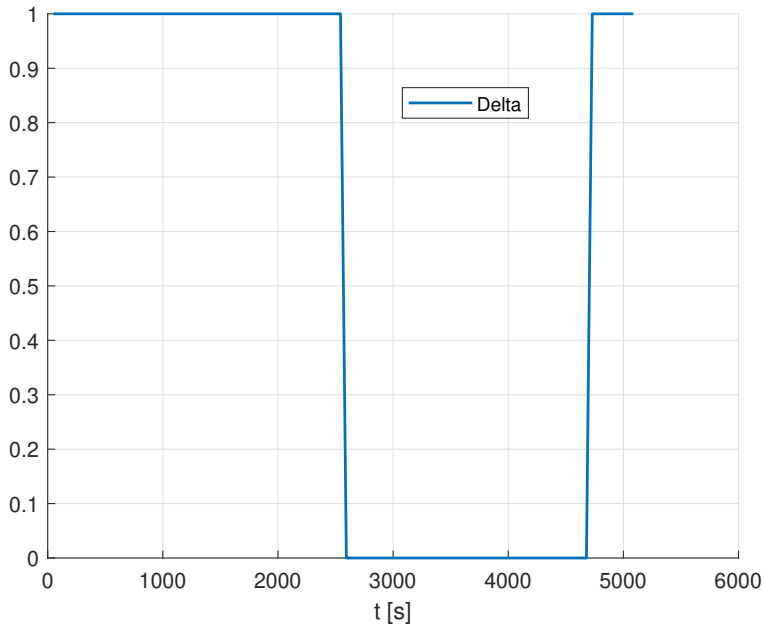

Figure 6.5: Delta function value over time.

Table 6.3: IPOPT output

Output	Value
Number of iterations	524
Total CPU secs in IPOPT (w/o function evaluations)	8.8
Total CPU secs in NLP function evaluations	237.6

for the different values of k_3 are initialized from the same state with the same initial guesses.

6.5 Discussion

The simulation results in Table 6.4 show how well the solver does for a range of values for the weight k_3. In the case where $k_3 = 10^{-8}$ is used, as it is in most figures, a quaternion close to the reference, i.e., the quaternion error in the table close to 1, and a low angular velocity error is obtained. This value for the k_3 weight is the only one of the nine values tried, which results in a large enough final time to gain solar power after the eclipse.

In multi-objective optimization, there is generally a trade-off between the different objectives. All values of k_3 below 10^{-2} yield reasonable terminal error for the quaternion and angular velocity, but when k_3 is set higher (10^{-1} or 10^{0}), the angular velocity at final time is close to its maximum extent, prioritizing the final time over a lower angular velocity error. When k_3 is 10^{0} the terminal quaternion error is also

Table 6.4: Results for range of k_3

Value, k_3	Net energy (J)	Time (T, s)	Quaternion error $1 - \lvert(\mathbf{q}_b^o)^\mathsf{T}\,\mathbf{q}_{\text{ref}}\rvert$	Angular velocity error $\left(\boldsymbol{\omega}_{\text{e}}^b\right)^\mathsf{T}\left(\boldsymbol{\omega}_{\text{e}}^b\right)$
10^{-8}	40068	5086	$4.1068{\cdot}10^{-5}$	$1.7212{\cdot}10^{-7}$
10^{-7}	37109	3346	$4.2665{\cdot}10^{-6}$	$5.0955{\cdot}10^{-8}$
10^{-6}	27136	2109	$2.0705{\cdot}10^{-6}$	$1.6178{\cdot}10^{-7}$
10^{-5}	32514	2882	$1.5036{\cdot}10^{-6}$	$4.9318{\cdot}10^{-8}$
10^{-4}	33909	2660	$2.7902{\cdot}10^{-6}$	$4.2877{\cdot}10^{-7}$
10^{-3}	21509	1690	$1.6428{\cdot}10^{-6}$	$1.3471{\cdot}10^{-7}$
10^{-2}	7487	758	$8.4568{\cdot}10^{-6}$	$4.3484{\cdot}10^{-6}$
10^{-1}	5934	645	$1.9182{\cdot}10^{-4}$	$1.9497{\cdot}10^{-5}$
10^{0}	5100	525	$2.2845{\cdot}10^{-3}$	$7.5625{\cdot}10^{-5}$

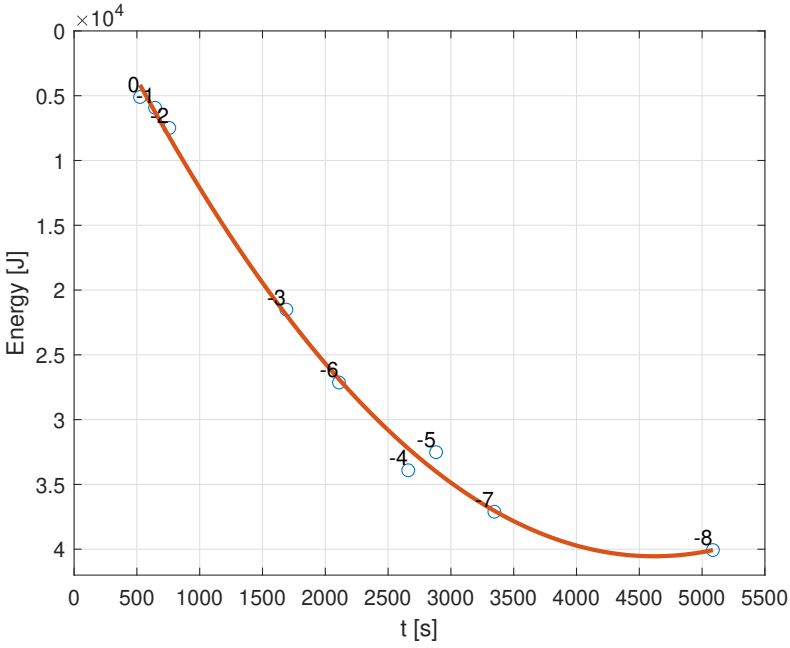

Figure 6.6: Time against net energy for several values of k_3. The number that denotes the point in the figure is connected to the exponent used for k_3, meaning that -3 corresponds to $k_3 = 10^{-3}$.

high. A plausible explanation for this can be suggested from the magnetic moment plot in Figure 6.3. Even with a final time of $T = 5086$ s, the magnetic moment of the magnetorquers saturates for long periods, suggesting that the magnetorquers would struggle to actuate that moment during a shorter period. Thus, the terminal error would naturally degrade. This is without considering the cross-product with the Earth's magnetic field the magnetic moment uses to produce torque, which is a further limiting factor. Also, note that the magnetic moment is not saturated during the eclipse: this comes from the definition of the net power cost, where the objective in the shade becomes an actuation minimization problem.

The values for k_3 from $k_3 = 10^0$ through $k_3 = 10^{-7}$ in Figure 6.6 go through more or less a straight line. This is expected owing to the solar energy, the dominant part of the net energy function when the satellite is not in eclipse, being a linear function of time if the optimal sun-pointing attitude is held, which it will be for the optimal trajectory [50]. The curve in the figure is a second-order polynomial. This can be explained by the eclipse: no energy is gained in the eclipse, only the energy spent is minimized. Thus, the point for $k_3 = 10^{-8}$ is moved further right than it would be if all sections of the orbit were lit.

The order of $k_3 = 10^{-4}$, $k_3 = 10^{-5}$, and $k_3 = 10^{-6}$ are not very intuitive: as minimizing time gets more weight when $k_3 = 10^{-4}$ it is natural to assume that its point would be further left than the point for $k_3 = 10^{-4}$. The weight indicates the importance of minimizing the final time, where a higher number makes time minimization more important to the solver. Reducing the importance of the time minimization objective does not necessarily reduce the time spent on the maneuver in this interval. The behavior displayed in Figure 6.6 may be owing to the solver looking for local optima. Another possibility is that it is an artifact owing to the non-convexity of the problem. Note that the initial guess for time (3000 s) and the beginning of the shadow (around 2800 s) are around the same time as the solution for $k_3 = 10^{-4}$ and $k_3 = 10^{-5}$.

6.6 Conclusion

The optimal control strategy works and gives a set of non-trivial solutions that the user can select based on preferences, weighting time against net energy. Future work will be to reformulate the problem to better account for the artifacts the non-convexity of the problem brings out in the solver to produce optimal trajectories over multiple orbits.

Part II

Maximum Hands-Off Attitude Control

Chapter 7

Introduction

Maximum hands-off control is a form of control where the control signal is as sparse as possible. Where some optimal control problems minimize the first or second norm of the input, meaning the L_1- or the L_2-norms, the objective of maximum hands-off control is to minimize the L_0-norm of the signal. The L_0-norm is the time the control signal takes on a non-negative value. Of course, as the L_0-norm minimization problem is NP-hard, the maximum hands-off control problem is challenging for a computer to solve. It is common to use the L_1 norm as an approximation for the L_0-norm, which in many cases is sufficient. In the publications in this part, we use a different formulation, a relaxation of the L_0-norm, which makes it possible to solve the maximum hands-off control problem with a Newton-type solver.

Chapter 8 is based on

[3] S. K. Schaanning, **B. A. Kristiansen**, and J. T. Gravdahl, "Maximum Hands-Off Attitude Control,", in *2022 American Control Conference (ACC)*, pp. 4003–4010, Atlanta, Georgia, USA, Jun. 2022.

This chapter solves the attitude control problem using a direct multiple-shooting method in the maximum hands-off control formulation. The article the chapter is based on shows that the maximum hands-off control scheme is feasible for the problem we are trying to solve. The simulations are based on the HYPSO-1 satellite, so the actuators in use are reaction wheels.

Chapter 9 is based on

[4] **B. A. Kristiansen** and J. T. Gravdahl, "Maximum Hands-Off Attitude Control of a Spacecraft Actuated by Thrusters," in *Proceedings of the 22nd IFAC World Congress*, July 2023, Yokohama, Japan,

which extends the results from [3] to a satellite with thrusters. Thrusters, by nature, are a more natural choice for maximum hands-off due to their on-off nature. As on-off is not in the Newton-type solver's nature, the formulation of the control problem is extended to facilitate this actuator change. In addition, relative sparsity is introduced as a metric to compare how sparse different controllers are when competing on the same terms.

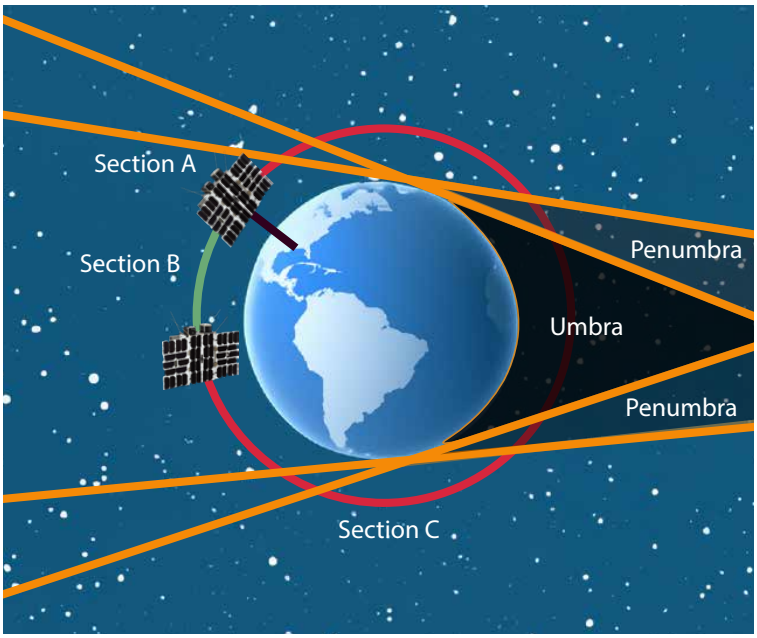

Figure 7.1: Thesis outline.

In the context of Figure 7.1, both articles are maneuvers between two pointing events, placing them in section B of the figure.

The concept of maximum hands-off control, as shown in [51], is an optimal control scheme that aims to minimize the time spent on actuation. The control scheme has a range of applications, including in the control of spacecraft, as was shown for a single-axis attitude control maneuver in [52]. A maximum hands-off controller is an optimal controller with control values which are often zero, i.e., the control values are *sparse*, but still manage to achieve the control objectives [53]. A hands-off controller holds the control values at zero over a time interval, and the *maximum* hands-off controller maximizes the time interval over which the control input is exactly zero [51]. This property is desirable in systems with limited resources, such as in spacecraft (attitude) control. In [54], which is the basis for Chapter 8, we take this concept further by demonstrating how maximum hands-off control would work for a fully nonlinear model for attitude control, using unit quaternions to represent the attitude of a CubeSat actuated by reaction wheels, a case inspired by the HYPSO-1 mission at NTNU [21]. Moreover, in the same chapter, we introduce the concept of moving maximum hands-off control, where the designer can design the cost function such that the control signal can be sparse at specific points during the control horizon.

Maximum hands-off control is a control scheme where the resulting torque is highly discontinuous. While we show in Chapter 8 that reaction wheels, a type of actuator that works well with continuous controllers, can be used with maximum hands-off control to control the attitude of a spacecraft, a more natural choice of

actuators to couple with maximum hands-off control is reaction thrusters. Reaction thrusters, or simply thrusters, are actuators that are either completely on or completely off, giving a discontinuous input to the system. Rather than reaction wheels, thrusters can be used for orbital maneuvers in addition to just attitude control. See for example [55, 56].

There exists thrusters that are not off or on at their maximum magnitude, namely electric thrusters (see for example [57]), which have been suggested for use for the attitude control of a spacecraft [58, 59]. The focus of chapter Chapter 9 is on/off thrusters. However, a brief discussion on generalizing the results in this paper for use with continuous thrust is included.

Chapter 8

Maximum Hands-Off Attitude Control

8.1 Introduction

The main contribution of this chapter is the design of a maximum hands-off controller solving the attitude control problem for a spacecraft actuated by reaction wheels. The maximum hands-off controller is tested through simulations of a 6U CubeSat, which resembles the configuration of HYPSO-1 [21]. HYPSO-1 is a smallsat actuated by reaction wheels and developed at NTNU [21]. We furthermore design and implement the moving maximum hands-off controller as an extension to the maximum hands-off controller. The moving maximum hands-off controller allows the user to specify in which time interval the control inputs should occur and is, to the authors' best knowledge, a novel concept within control. Finally, this chapter compares the responses of the maximum hands-off controller, the moving maximum hands-off controller, and the L_1-optimal controller when solving the spacecraft attitude control problem.

The rest of this chapter is organized as follows: Section 8.2 describes the coordinate frames and presents the spacecraft dynamics. Section 8.3 introduces the theory behind the maximum hands-off controller. Section 8.4 introduces the controller designs, including the design of the novel moving maximum hands-off controller, and Section 8.5 presents the simulation setup. The simulation results are presented in Section 8.6, whereas the findings are discussed in Section 8.7. Section 8.8 provides the conclusion.

8.2 Spacecraft model

In this section, we present the model of a spacecraft orbiting the Earth, actuated by reaction wheels.

8.2.1 Angular velocity

When analyzing the attitude of a spacecraft orbiting the Earth, three different angular velocities are of interest, namely the angular velocities of the body frame $\{b\}$ relative to the orbit frame LVLH $\{o\}$, $\boldsymbol{\omega}_{ob}^{b}$, the angular velocities of $\{o\}$ relative to $\{i\}$, $\boldsymbol{\omega}_{io}^{b}$, and the angular velocities of $\{b\}$ relative to $\{i\}$, $\boldsymbol{\omega}_{ib}^{b}$. The angular velocities relate to one another as follows:

$$\boldsymbol{\omega}_{ob}^{b} = \boldsymbol{\omega}_{ib}^{b} - \boldsymbol{\omega}_{io}^{b} = \boldsymbol{\omega}_{ib}^{b} - \mathbf{R}_{o}^{b}\boldsymbol{\omega}_{io}^{o}, \tag{8.1}$$

where $\boldsymbol{\omega}_{io}^{o}$ is defined as [19]

$$\boldsymbol{\omega}_{io}^{o} = \mathbf{R}_{i}^{o}\frac{\mathbf{S}(\mathbf{r}^{i})\mathbf{v}^{i}}{(\mathbf{r}^{i})^{\intercal}\mathbf{r}^{i}}. \tag{8.2}$$

Moreover, the inertial acceleration of the spacecraft is defined as

$$\dot{\mathbf{v}}^{i} = -\frac{GM}{\|\mathbf{r}^{i}\|_{2}^{3}}\mathbf{r}^{i}, \tag{8.3}$$

where G is the gravitational constant, M is the total mass of the Earth, and $\|\mathbf{r}^{i}\|_{2}$ denotes the 2-norm of $\mathbf{r}^{i}$. The rate of change for $\mathbf{r}^{i}$ is given as

$$\dot{\mathbf{r}}^{i} = \mathbf{v}^{i}. \tag{8.4}$$

8.2.2 Total system dynamics

The total spacecraft dynamics for a spacecraft orbiting the Earth are given as [1, 19, 55, 60]

$$\dot{\mathbf{q}}_{b}^{o} = \frac{1}{2}\mathbf{T}(\mathbf{q}_{b}^{o})\boldsymbol{\omega}_{ob}^{b} \tag{8.5a}$$

$$\frac{{}^{b}d}{dt}\boldsymbol{\omega}_{ib}^{b} = \mathbf{J}_{s}^{-1}(-\mathbf{A}\boldsymbol{\tau}_{u}^{w} - \mathbf{S}(\boldsymbol{\omega}_{ib}^{b})\mathbf{J}\boldsymbol{\omega}_{ib}^{b} + \mathbf{A}\mathbf{J}_{w}\boldsymbol{\omega}_{bw}^{w}) \tag{8.5b}$$

$$\frac{{}^{b}d}{dt}\boldsymbol{\omega}_{ob}^{b} = \frac{{}^{b}d}{dt}\boldsymbol{\omega}_{ib}^{b} + \mathbf{S}(\boldsymbol{\omega}_{ob}^{b})\mathbf{R}_{o}^{b}\boldsymbol{\omega}_{io}^{o} + \mathbf{R}_{o}^{b}\mathbf{S}(\mathbf{R}_{b}^{o}\boldsymbol{\omega}_{ob}^{b})\boldsymbol{\omega}_{io}^{o} \tag{8.5c}$$

$$\frac{{}^{w}d}{dt}\boldsymbol{\omega}_{bw}^{w} = \mathbf{J}_{w}^{-1}\boldsymbol{\tau}_{u}^{w} - \mathbf{A}^{\intercal}\dot{\boldsymbol{\omega}}_{ib}^{b}, \tag{8.5d}$$

where $\mathbf{J} \in \mathbb{R}^{3\times3}$ is the total system inertia of the spacecraft rigid body, defined as $\mathbf{J} = \mathbf{J}_{s} + \mathbf{A}\mathbf{J}_{w}\mathbf{A}^{\intercal}$, where $\mathbf{J}_{s} \in \mathbb{R}^{3\times3}$ denotes the inertia of the spacecraft rigid body excluding the inertia about the spinning axes of the reaction wheels, and $\mathbf{J}_{w} \in \mathbb{R}^{n\times n}$ denotes the inertia matrix of the reaction wheels about the spinning axes.

8.3 Maximum hands-off control

8.3.1 Mathematical preliminaries

The content presented in this section is based on [51], which provides a detailed review of the mathematics behind maximum hands-off control.

The L_1-norm of a vector $\mathbf{x} \in \mathbb{R}^{n_x}$ is defined as

$$\|\mathbf{x}\|_1 \triangleq \sum_{i=1}^{n_x} |x_i|. \tag{8.6}$$

The L_p-norm, with $p \in [1, \infty)$, of a vector of continuous-time signals $\mathbf{u}(t)$ over the time interval $[0, T)$ is defined as

$$\|\mathbf{u}\|_p \triangleq \left(\int_0^T \|\mathbf{u}(t)\|^p dt \right)^{\frac{1}{p}}. \tag{8.7}$$

The norm $\|\cdot\|$ inside the integral in Equation (8.7) can be any p-norm for $p \in [1, \infty)$ [61]. If $p \in (0, 1)$, in Equation (8.7), then $\|\cdot\|_p$ is not a norm as it fails to satisfy the triangle inequality [51].

The support of a function is the set of points where the function takes on nonzero values [62], and the support set of a function $u(t)$, $\text{supp}(u(t))$, is defined by the closure of the set [51]

$$\{t \in [0, T] : u(t) \neq 0\}, \tag{8.8}$$

and by using Equation (8.8), the L_0-norm of a continuous-time signal $u(t)$ can be defined by the length of the support of $u(t)$ accordingly:

$$\|u\|_0 \triangleq \mu(\text{supp}(u(t))), \tag{8.9}$$

where $\mu(\cdot)$ is the Lebesgue measure on $\mathbb{R}$.

8.3.2 Maximum Hands-off Control Problem Formulation

The maximum hands-off control is the control that maximizes the time interval over which the control input is exactly zero. To put it more precisely, the controller minimizes the Lebesgue measure of the support, i.e., the L_0-norm, to find the sparsest of the admissible controls [51]. The L_0-cost function is given as [51]

$$J_0(\mathbf{u}) \triangleq \sum_{i=1}^{m} \lambda_i \|u_i\|_0, \tag{8.10}$$

where m is the number of control inputs, $\mathbf{u}$ is the control input vector, λ_i are positive weights, and u_i denotes each element i in $\mathbf{u}$. The control that minimizes Equation (8.10) is called the *maximum hands-off control*, or the *L_0-optimal control*, and it is the sparsest control among all admissible controls [51].

The L_0-cost function in Equation (8.10) is discontinuous and non-convex [51]. Solving discontinuous and non-convex optimization problems is generally hard [51], and solving the L_0-optimal control problem is NP-hard [63]. Several relaxation methods and reformulations have been suggested to Equation (8.10), for instance, replacing the L_0-norm by the L_1-norm [51].

By defining the L_0-optimal control problem as [63]

$$\underset{\mathbf{x}}{\text{minimize}} \quad f(\mathbf{x}) + \gamma\|\mathbf{x}\|_0 \tag{8.11a}$$
$$\text{subject to} \quad c_i(\mathbf{x}) = 0,\ i \in \mathcal{E} \tag{8.11b}$$
$$c_i(\mathbf{x}) \leq 0,\ i \in \mathcal{I}, \tag{8.11c}$$

the L_0-optimal control problem can be reformulated using a set of complementarity constraints [63] accordingly,

$$\underset{\mathbf{x}}{\text{minimize}} \quad f(\mathbf{x}) + \boldsymbol{\gamma}^\intercal(\mathbf{1}_N - \boldsymbol{\xi}) \tag{8.12a}$$
$$\text{subject to} \quad c_i(\mathbf{x}) = 0,\ i \in \mathcal{E} \tag{8.12b}$$
$$c_i(\mathbf{x}) \leq 0,\ i \in \mathcal{I} \tag{8.12c}$$
$$\boldsymbol{\xi} \leq \mathbf{1}_N \tag{8.12d}$$
$$\pm\boldsymbol{\xi} \circ \mathbf{x} \leq \epsilon\mathbf{1}_N \tag{8.12e}$$
$$\boldsymbol{\xi} \geq \mathbf{0}, \tag{8.12f}$$

where $\mathbf{1}_N$ is the N-vector of ones, N is the number of control intervals, and $\mathbf{1}_N - \boldsymbol{\xi}$ is the support vector of $\mathbf{x}$. The support $1 - \xi_j$ of the state x_j essentially plays the same role as the support, $\text{supp}(\cdot)$, in Equation (8.8). The notation $\mathbf{a} \circ \mathbf{b}$ denotes the componentwise product between the vectors $\mathbf{a}$ and $\mathbf{b}$. $\mathcal{E}$ and $\mathcal{I}$ are two finite index sets, $\boldsymbol{\gamma} > 0$ is a positive vector with components $\gamma_j > 0$, $f(\cdot)$ is the continuously differentiable objective function, and c_i the continuously differentiable constraint functions. $\epsilon > 0$ is a relaxation scalar. It is desirable to investigate the properties of the relaxed problem when ϵ approaches zero because then the complementarity constraints would equal zero.

8.4 Control design

8.4.1 Control objectives

The control objective of the maximum hands-off controller is to find the sparsest control among all admissible control sequences. Note that for the remaining parts of this study, the term *sparsity* is defined in the following way:

Definition 8.4.1 (Sparsity)**.** *A control signal's sparsity refers to the total time the control signal takes on nonzero values.*

Minimizing the number of time intervals in which the control signal takes on nonzero values, a related concept, is called minimum switching control. Minimum switching control has been studied for attitude control in [64].

Although the maximum hands-off controller yields the sparsest control, the control might not occur at the most favorable instants of time, which motivates the design of the moving maximum hands-off controller. The term *moving* refers to the characteristic of the controller, which lets the user move the sparse control according to a desired set of preferences, for instance, environmental conditions.

In some situations, it may be ideal not to have any control input on a satellite, e.g., when a scientific measurement occurs. Using the moving maximum hands-off controller could ensure that no control is applied during the measurement interval.

8.4.2 Maximum hands-off controller

The maximum hands-off controller, or the L_0-optimal controller, aims to minimize the L_0-norm of the control input. The design of the maximum hands-off controller implemented in this chapter is inspired by the relaxed formulation in Equation (8.12) with $\boldsymbol{\gamma} = \mathbf{1}_N$, and is formulated as

$$\underset{\boldsymbol{\tau}_u^b, \boldsymbol{\xi}}{\text{minimize}} \quad k_1 f(\boldsymbol{\omega}_{ob}^b) + k_2 g(\mathbf{q}_b^o) + k_3(\mathbf{1}_N - \boldsymbol{\xi})\mathbf{1}_N^\intercal \tag{8.13a}$$

$$\text{subject to} \quad \dot{\mathbf{x}} = \mathbf{f}(\mathbf{x}, \boldsymbol{\tau}_u^b) \tag{8.13b}$$

$$\pm\boldsymbol{\tau}_u^w \leq \boldsymbol{\tau}_{\text{limit}} \tag{8.13c}$$

$$\mathbf{x}(0) = \mathbf{x}_0 \tag{8.13d}$$

$$\boldsymbol{\xi} \leq \mathbf{1}_N \tag{8.13e}$$

$$\pm\boldsymbol{\xi} \circ \boldsymbol{\tau}_{u,1}^b \leq \epsilon \mathbf{1}_N \tag{8.13f}$$

$$\pm\boldsymbol{\xi} \circ \boldsymbol{\tau}_{u,2}^b \leq \epsilon \mathbf{1}_N \tag{8.13g}$$

$$\pm\boldsymbol{\xi} \circ \boldsymbol{\tau}_{u,3}^b \leq \epsilon \mathbf{1}_N \tag{8.13h}$$

$$\boldsymbol{\xi} \geq \mathbf{0}, \tag{8.13i}$$

where k_1, k_2 and k_3 are positive constants, $\boldsymbol{\xi}$ is the complementarity vector to the control input $\boldsymbol{\tau}_u^b$, and $\mathbf{1}_N - \boldsymbol{\xi}$ is the support vector of $\boldsymbol{\tau}_u^b$. $\boldsymbol{\tau}_{u,1}^b$, $\boldsymbol{\tau}_{u,2}^b$, and $\boldsymbol{\tau}_{u,3}^b$ denotes the components of $\boldsymbol{\tau}_u^b$ about the x, y and z-axis in $\{b\}$, respectively. The state vector $\mathbf{x}$ is defined by $[\mathbf{q}_b^{o\intercal}, \boldsymbol{\omega}_{ib}^{b\intercal}, \boldsymbol{\omega}_{ob}^{b\intercal}, \boldsymbol{\omega}_{bw}^{w\intercal}, \mathbf{v}^{i\intercal}, \mathbf{r}^{i\intercal}]^\intercal$, $\mathbf{x}_0$ denotes the initial state values, and $\mathbf{f}(\mathbf{x}, \boldsymbol{\tau}_u^b)$ is defined by (8.5a), (8.5b), (8.5c), (8.5d), (8.3), and (8.4). The functions $f(\cdot)$ and $g(\cdot)$ are designed to steer $\boldsymbol{\omega}_{ob}^b$ and $\mathbf{q}_b^o$, respectively, to their desired final states. More specifically,

$$\begin{aligned} f(\boldsymbol{\omega}_{ob}^b) &= \sum_{i=1}^{n_\omega} (\omega_{ob,i}^b(T) - \omega_{ob,\text{ref},i}^b)^2 \\ g(\mathbf{q}_b^o) &= 1 - \left| (\mathbf{q}_b^o(T))^\intercal \mathbf{q}_{b,\text{ref}}^o \right|, \end{aligned} \tag{8.14}$$

where T denotes the final time, $\boldsymbol{\omega}_{ob,\text{ref}}^b$ and $\mathbf{q}_{b,\text{ref}}^o$ are the reference angular velocities and reference quaternion, n_ω denotes the number of entries in $\boldsymbol{\omega}_{ob}^b(T)$ and $\boldsymbol{\omega}_{ob,\text{ref}}^b$, and $\omega_{ob,i}^b(T)$ and $\omega_{ob,\text{ref},i}^b$ denotes the ith component of $\boldsymbol{\omega}_{ob}^b(T)$ and $\boldsymbol{\omega}_{ob,\text{ref}}^b$, respectively. The function $g(\cdot)$ is a pseudometric on the unit quaternion but a metric on $SO(3)$ [28]. The absolute value, $|(\mathbf{q}_b^o(T))^\intercal \mathbf{q}_{b,\text{ref}}^o|$, is approximated as $\max\left((\mathbf{q}_b^o(T))^\intercal \mathbf{q}_{b,\text{ref}}^o, -(\mathbf{q}_b^o(T))^\intercal \mathbf{q}_{b,\text{ref}}^o\right)$ [2].

8.4.3 Moving maximum hands-off controller

The design of the moving maximum hands-off controller is similar to that of the maximum hands-off controller in Equation (8.13). The moving maximum hands-off

optimal control problem is formulated as

$$\underset{\boldsymbol{\tau}_u^b, \boldsymbol{\xi}}{\text{minimize}} \quad k_1 f(\boldsymbol{\omega}_{ob}^b) + k_2 g(\mathbf{q}_b^o) + k_3 (\mathbf{1}_N - \boldsymbol{\xi} \circ \mathbf{h}_N) \mathbf{1}_N^\intercal, \tag{8.15}$$

where the constraints on Equation (8.15) are identical to Equations (8.13b) to (8.13i). The vector $\mathbf{h}_N$ specifies where the control torques should occur. By default, the vector $\mathbf{h}_N$ is an N-dimensional vector of all ones. The user might change the values of $\mathbf{h}_N$ to values between 0 and 1, to indicate for which time intervals the control input should occur. For instance, if the value of $\mathbf{h}_N$ is set to 0.1 for $N = 10, \ldots, 20$, it would yield a more optimal solution if the control occurs between these control intervals as sparsity comes at a lower cost in this interval than the rest.

8.4.4 L_1-optimal controller

The design of the L_1-optimal control problem is formulated as

$$\underset{s, \boldsymbol{\tau}_u^b}{\text{minimize}} \quad k_1 f(\boldsymbol{\omega}_{ob}^b) + k_2 g(\mathbf{q}_b^o) + k_3 \sum_{i=0}^{N} s_k \tag{8.16}$$

where Equation (8.16) is constrained by Equations (8.13b) to (8.13d), in addition to $-\mathbf{s}_N \leq \boldsymbol{\tau}_u^b \leq \mathbf{s}_N$. $\sum_{i=0}^{N} s_k$ denotes the L_1-norm of $\boldsymbol{\tau}_u^b$, i.e., $\|\boldsymbol{\tau}_u^b\|_1 = \sum_{i=0}^{n} s_i = \mathbf{1}^\intercal \mathbf{s}$, where $\mathbf{s} \in \mathbb{R}^n$ is a set of slack variables [65].

8.4.5 PD-controller

A standard PD controller is given as [9]

$$\boldsymbol{\tau}_u^b = \mathbf{K}_d \boldsymbol{\omega}_e^b + \mathbf{K}_p \boldsymbol{\epsilon}_e. \tag{8.17}$$

Here, $\boldsymbol{\omega}_e^b$ is the angular velocity error, defined as $\boldsymbol{\omega}_e^b = \boldsymbol{\omega}_{ob}^b - \boldsymbol{\omega}_d^b$, where $\boldsymbol{\omega}_d^b$ is the desired angular velocity. $\boldsymbol{\epsilon}_e$ is the vector part of the error quaternion, defined as $\mathbf{q}_e = \mathbf{q}_d^{-1} \otimes \mathbf{q}_b^o$, where $\mathbf{q}_d = [\eta_d, \boldsymbol{\epsilon}_b^\intercal]^\intercal$ is the desired attitude. $\mathbf{K}_d$ and $\mathbf{K}_p$ are constant and positive definite controller gain matrices. The numerical values of the gain matrices were chosen while tuning the PD controller.

8.5 Simulation setup

The experiments were conducted using CasADi as the optimization tool [30]. The NLP-solver IPOPT was used to solve the optimization problems using the solver's default options. The optimal control problems in Equations (8.13), (8.15) and (8.16) were discretized using direct multiple-shooting, whereas the dynamics of the spacecraft were discretized using Runge-Kutta 4 integration. The output from the PD controller was used as the initial guesses for the L_1-optimal controller, and the output from the L_1-optimal controller was given as initial guesses for the maximum hands-off controller and the moving maximum hands-off controller. The initial guesses were applied to the states $\boldsymbol{q}_b^o$, $\boldsymbol{\omega}_{ib}^b$, and $\boldsymbol{\omega}_{bw}^w$. No initial guesses were applied to the control torque $\boldsymbol{\tau}_u^b$, i.e., the default initial guess of zero used by CasADi was applied.

Some tests were conducted with different initial guesses to see how the controllers responded. The tests revealed that the initial guesses for IPOPT are of significant importance when trying to find the optimal solutions. Different initial guesses cause the optimization to iterate fast or slow towards an optimal solution and affect the quality of the solution [66].

The experiments reported in this chapter were conducted using a 2 GHz Intel Core i7-9700T CPU computer running Windows. The simulation of the experiments was conducted using the parameters for a 6U CubeSat as the spacecraft's rigid body, and it is assumed to orbit in Low-Earth-Orbit (LEO). Four reaction wheels are used to control the attitude of the CubeSat. This is part of the setup used for the HYPSO-1 mission, which motivates the work in this chapter [21]. Three of the reaction wheels are placed orthogonally along the three axes of the body frame. The fourth reaction wheel is placed such that its torque yields equal components in each body frame axis. The torque distribution matrix $\mathbf{A}$ is given as [1]

$$\mathbf{A} = \begin{bmatrix} 1 & 0 & 0 & \frac{1}{\sqrt{3}} \\ 0 & 1 & 0 & \frac{1}{\sqrt{3}} \\ 0 & 0 & 1 & \frac{1}{\sqrt{3}} \end{bmatrix}. \tag{8.18}$$

The total inertia matrix for the spacecraft rigid body and the inertia matrix of the reaction wheels are given as [1]

$$\mathbf{J} = \begin{bmatrix} 0.0775 & 0.0002 & -0.0002 \\ 0.0002 & 0.1067 & 0.0005 \\ -0.0002 & 0.0005 & 0.0389 \end{bmatrix} \text{kg} \cdot \text{m}^2, \ \mathbf{J}_w = J_w \mathbf{I}_{4\times 4}, \tag{8.19}$$

where $J_w = 2.1 \cdot 10^{-4}$ kg·m^2 is the inertia of a single reaction wheel. The controller gains and the parameters required for the optimization are shown in Table 8.1.

After the final optimization procedure finishes, the system is propagated for an additional number of control intervals, denoted N_{prop}, to visualize the post-optimization response of the system. The final state from the optimization serves as the initial state for the propagation, and the control input is set to zero for the whole propagation. The spacecraft's orbit is initialized using the orbital parameters in Table 8.1, which are transformed into ECI coordinates using the RANDV-function from [32]. Two types of simulations were conducted: a single-axis maneuver where the satellite rotates 45° about the x-axis and a multiple-axis maneuver where the satellite rotates about all three axes of the chosen frames.

8.6 Results

Figure 8.1 shows the change in the spacecraft's attitude over time using the Euler angle representation and reveals that all three controllers can steer the spacecraft to the desired orientation of $(\phi, \theta, \psi) = (45°, 0°, 0°)$ and keep the spacecraft at this attitude. The dotted lines ϕ_d, θ_d, and ψ_d denote the angles of the desired attitude, whereas the solid lines ϕ, θ, and ψ correspond to the actual states. The orange area in the moving L_0-section of the figures shows the interval placement where $\mathbf{h}_N$ takes lower values. $\mathbf{h}_N$ is set to 1 for the rest of the interval. The torque vector

Table 8.1: Controller gains, optimization constants, and orbital parameters.

Parameter	Value	Unit
k_1	$1 \cdot 10^6$	s^2
k_2	$1 \cdot 10^2$	-
k_3	$1 \cdot 10^1$	-
$\mathbf{K}_p$	$3\mathbf{J}_s$	N·m
$\mathbf{K}_d$	$2.7\mathbf{J}_s$	N·m·s
Simulation time (T)	70	s
Control intervals (N)	50	-
Step size (h)	1.4	s
Control intervals for propagation (N_{prop})	20	-
ϵ	$1 \cdot 10^{-8}$	-
τ_{limit}	$\pm 3 \cdot 10^{-3}$	N·m
Semi-major axis	6852.2	km
Eccentricity	0.002	-
Inclination	97	°
Right ascension of the ascending node	280	°
Argument of periapsis	0	°
True anomaly	0	°
Standard grav. parameter, Earth (GM)	$3.986 \cdot 10^{14}$	m^3/s^2

$\boldsymbol{\tau}_u^b$ can be seen in Figure 8.2. The torque vector $\boldsymbol{\tau}_u^w$ can be seen in Figure 8.3. The angular velocities $\boldsymbol{\omega}_{ob}^b$ are shown in Figure 8.4 and reveal that the spacecraft stops rotating, i.e., $\{b\}$ stops rotating relative to $\{o\}$, when the desired orientation is reached. The angular velocities $\boldsymbol{\omega}_{bw}^w$ can be seen in Figure 8.5 and illustrate the dynamical response of the reaction wheels. The computation times, the sparsity, and the number of iterations used to find the optimal solution for each of the three controllers are shown in Table 8.2.

Table 8.2: Computation time, sparsity and number of iterations single-axis maneuver.

Controller	CPU time NLP, [s]	CPU time IPOPT, [s]	Sparsity, [s]	Iterations
L_0	3.235	0.253	2.8	25
Moving L_0	46.914	3.828	2.8	371
L_1	2.479	0.204	2.8	19

Figure 8.6 shows the change in the spacecraft's attitude over time from a multiple-axis maneuver from $(\phi, \theta, \psi) = (0°, 0°, 0°)$ to $(90°, 45°, 15°)$. The optimal control torques $\boldsymbol{\tau}_u^b$ and $\boldsymbol{\tau}_u^w$ are shown in Figure 8.7 and Figure 8.8, respectively. The angular velocities $\boldsymbol{\omega}_{ob}^b$ are shown in Figure 8.9. The angular velocities $\boldsymbol{\omega}_{bw}^w$ are shown in Figure 8.10. The computation times, the sparsity, and the number of iterations used to find the optimal solution for each of the three controllers are shown in Table 8.3.

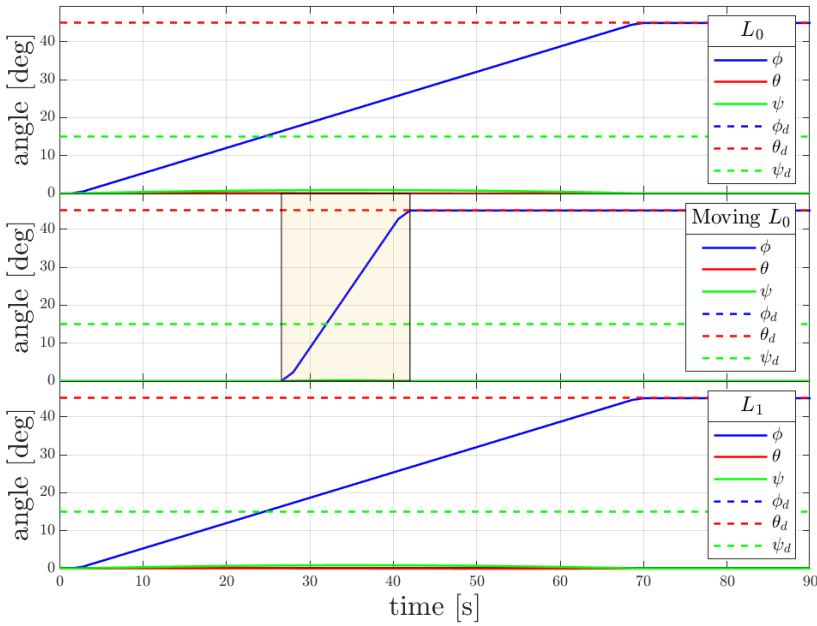

Figure 8.1: Euler angles, single-axis maneuver.

Table 8.3: Computation time, sparsity and number of iterations multiple-axis maneuver.

Controller	CPU time NLP, [s]	CPU time IPOPT, [s]	Sparsity, [s]	Iterations
L_0	66.216	6.106	2.8	497
Moving L_0	90.175	7.706	2.8	699
L_1	5.131	0.360	2.8	39

8.7 Discussion

In this section, the maximum hands-off controller will be referred to as the L_0-optimal controller or the L_0-controller, whereas the moving maximum hands-off controller will be referred to as the moving L_0-optimal controller or the moving L_0-controller. A control signal's *sparsity* is defined in Definition 8.4.1.

8.7.1 Single-axis

Figures 8.1 to 8.4 show that the spacecraft's state space trajectories and the control signals are identical for the L_0-controller and the L_1-controller. These results agree with the findings in [51], and suggest that the L_1-norm may be used as an approximation to the L_0-norm.

As Figures 8.1 to 8.4 show, the spacecraft's state space trajectories and the

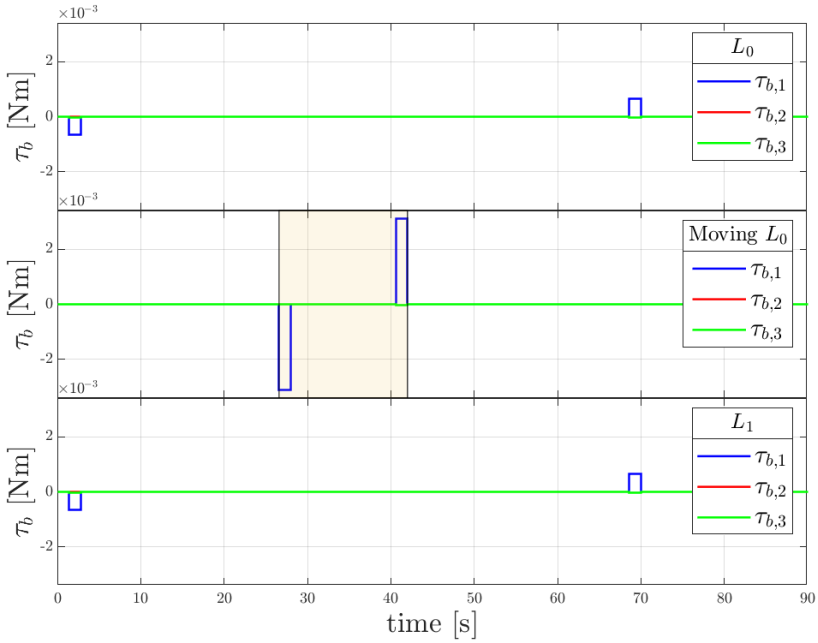

Figure 8.2: Control input in $\{b\}$, single-axis maneuver.

control signals resulting from the moving L_0-controller differ from the two other controllers. The differences can be explained by comparing the cost functions of the three controllers in Equation (8.13a), Equation (8.15), and Equation (8.16). For the moving L_0-controller, the vector $\mathbf{h}_N$ was chosen such that it would cost less for the control inputs to occur between $t = 28$ s and $t = 42$ s. For the two other controllers, it is equally expensive for the control inputs to occur over the whole time interval. Figure 8.2 and Figure 8.3 show that the control inputs produced by the moving L_0-controller occur at $t = 28$ s and $t = 42$ s, and Figure 8.1 and Figure 8.4 show that the spacecraft's states change within this interval.

As can be seen in Figure 8.2 and Figure 8.3, the optimal control signal computed by the moving L_0-controller has a larger amplitude than the control signals produced by the two other controllers. A possible explanation for this is that since the moving L_0-control torques occur closer in time, the torque applied at each of the two time instants has to be larger in order to steer the spacecraft to the desired orientation within a smaller time interval. If the time interval was larger, the control inputs could be smaller as the spacecraft would have more time to rotate towards the desired orientation after the initial control input has been applied.

Figure 8.2 and Figure 8.3 show that the control inputs produced by the moving L_0-controller occur at $t = 28$ s and $t = 42$ s, which means that they occur exactly at the boundaries of the time interval specified by $\mathbf{h}_N$. The saturation limits for the control torque are $\tau_{\text{limit}} = \pm 3 \cdot 10^{-3}$ N·m, and Figure 8.3 shows that the control

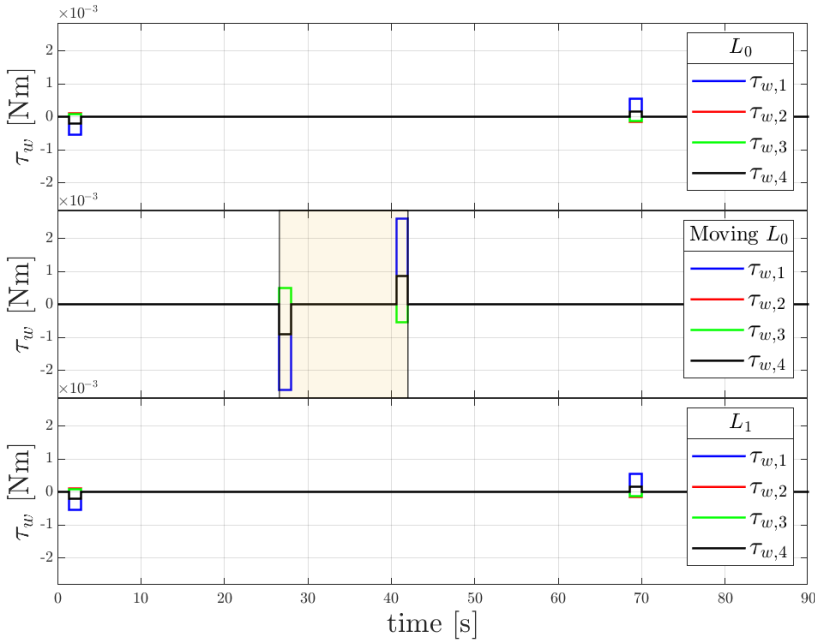

Figure 8.3: Control input in $\{w\}$, single-axis maneuver.

torques produced by the moving L_0-controller are close to the saturation limits. If the control torques had occurred at other time instants in the interval specified by $\mathbf{h}_N$, they would occur closer in time, and the torques would therefore have larger values. The control torques are already close to the saturation limits when they occur at $t = 28$ s and $t = 42$ s, and if the torque values were to increase, the reaction wheels may saturate. If the reaction wheels saturate, an additional control torque may be required to perform the spacecraft maneuver, and an additional control torque would yield a less sparse control signal. It is cheaper for the control input to occur between $t = 28$ s and $t = 42$ s, but if the control torques are too close in time, they may saturate. Then, the controller would have to apply an additional control torque, which would result in a less sparse control signal. Therefore, it makes sense that the control torques occur at the borders of the time interval specified by $\mathbf{h}_N$, i.e., at $t = 28$ s and $t = 42$ s.

Table 8.2 shows that all three controllers yield optimal control signals that have the same sparsity. This finding confirms that all three controllers are able to find the sparsest solution. For this type of spacecraft single-axis maneuver, it is not possible to find a control signal sparser than two time steps, which means a total signal length of 2.8 s, as one control torque has to push the spacecraft towards the desired attitude and one control input has to stop the spacecraft rotation. For the conditions in this chapter, a control signal in which torques occur at two different time instants provides the sparsest optimal control signal for the spacecraft's single-

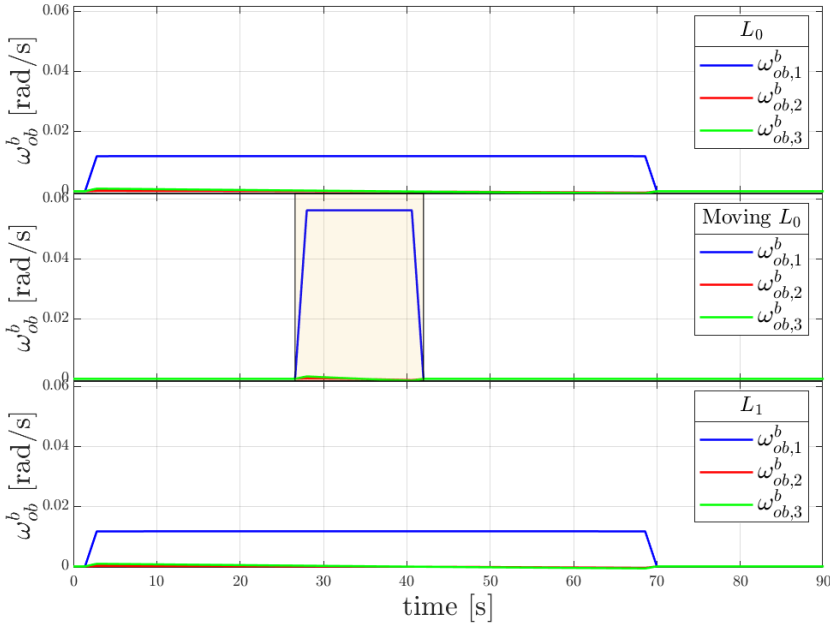

Figure 8.4: Angular velocities, $\boldsymbol{\omega}^b_{ob}$, single-axis maneuver.

axis maneuver.

When maneuvering the spacecraft an angle $\phi = 45°$ about the x-axis, one might expect an optimal controller to yield control torque simply about the body-frame x-axis. Figure 8.2 shows that control torques are applied about all three axes, although the control torque about the x-axis is the most prominent. The optimal control algorithms yield torque about all three axes because the spacecraft rotates relative to its orbit at the same time as it orbits the Earth. A spacecraft in orbit, such as the one used in this work, would rotate relative to its orbit, which results in the angular velocity dynamics in Equation (8.5c). Because of the spacecraft's rotation around the Earth, there will be rotation about the y- and z-axis throughout the optimization horizon, in addition to the control effort made about the x-axis. Therefore, the reaction wheels' torque must be applied to compensate for the drift about the y- and z-axis.

The total inertia matrix for the spacecraft rigid body, $\mathbf{J}$, in Equation (8.19) also contributes to rotation about multiple axes. Due to the nonlinearity of the spacecraft dynamics, the terms are coupled, which results in a torque about all three axes, even though motion is only needed about one axis. The total system inertia matrix given in Equation (8.19) is not diagonal. If a diagonal $\mathbf{J}$-matrix were used instead of the one in Equation (8.19), the states would be less coupled, which is clear from Equation (8.5b). Less coupling of the dynamics would yield less torque about the y- and z-axis, when a maneuver is performed about the x-axis.

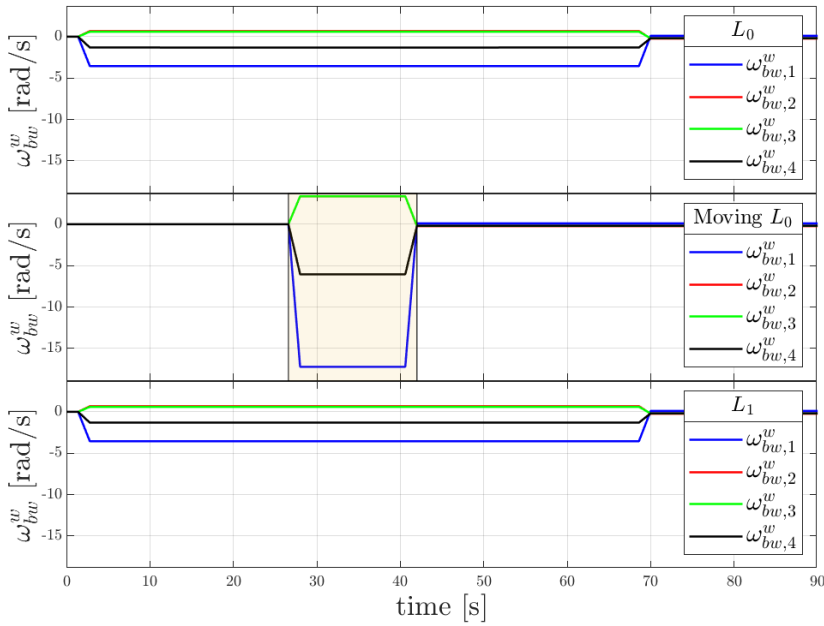

Figure 8.5: Angular velocities, $\boldsymbol{\omega}_{bw}^{w}$, single-axis maneuver.

8.7.2 Multiple-axis maneuver

Figure 8.7 and Figure 8.8 show that the first control torque from the moving L_0-controller occurs after about $t = 5$ s, and the second control torque occurs close to $t = 40$ s. The second control torque occurs within the interval specified by $\mathbf{h}_N$. The vector $\mathbf{h}_N$ was chosen such that it would cost less for the control inputs to occur between $t = 28$ s and $t = 42$ s. One might have expected all control inputs to occur within this time interval. However, one control input occurs outside this interval. This is because there are no constraints on where the control input should not occur; it only costs less between $t = 28$ s and $t = 42$ s. The optimization procedure aims to satisfy the constraints and to minimize the cost function, which is also a function of the final state values. If it is impossible to reach this goal by applying control input within the cheap interval specified by $\mathbf{h}_N$, some or all control input will occur outside this interval. Therefore, control inputs may occur outside the interval defined by $\mathbf{h}_N$. Should it be desirable to force control inputs at any point to zero, adding a constraint on the input would be a possible solution.

The L_1-optimal control signal and L_0-optimal control signal are not identical, which can be seen in Figure 8.7 and Figure 8.8. The first control input produced by the L_1-controller occurs before the first control input produced by the L_0-controller, whereas the two last control inputs coincide. The amplitude of the control torques from the L_1 controller are smaller than those from the L_0 controller. A possible explanation for the difference in amplitudes is that since there is more time between

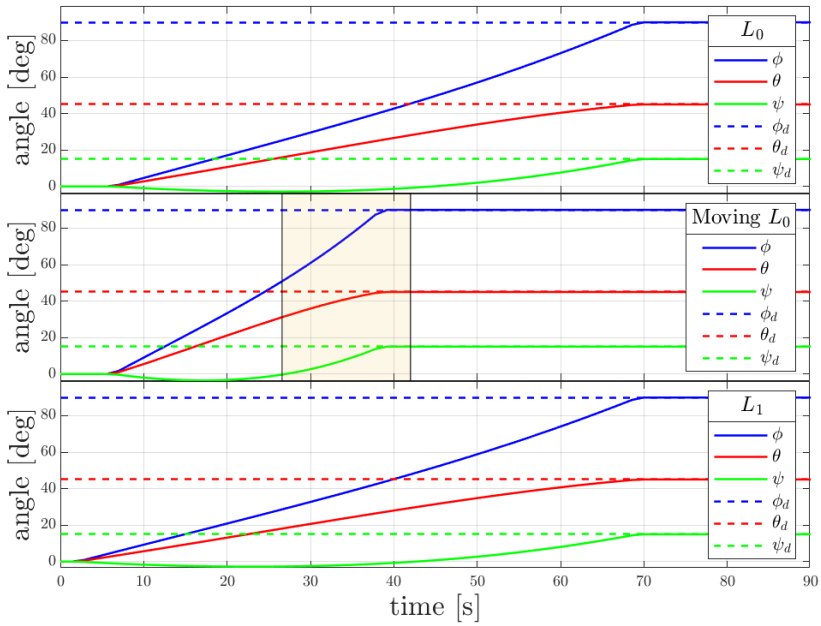

Figure 8.6: Euler angles, multiple-axis maneuver.

the two L_1-control inputs, the spacecraft will have more time to rotate to the desired orientation, and thus, less torque would need to be applied. Therefore, it makes sense that the control torque produced by the L_1 controller is smaller than the control torque produced by the L_0 controller. These results suggest that the L_1-optimal solution does not always equal the L_0-optimal solution. On the other hand, they suggest that the L_1-optimal control problem could be an acceptable approximation to the L_0-optimal control problem.

8.8 Conclusion

The main goal of this chapter has been to explore the use of maximum hands-off control, also called L_0-optimal control, for the spacecraft attitude control problem. Our work has shown that the maximum hands-off controller can steer the spacecraft to the desired attitude and final state. Thus, our work confirms that the maximum hands-off controller works for the spacecraft attitude control problem. The moving maximum hands-off controller has also been explored for the spacecraft attitude control problem. Our findings suggest that the controller works as intended, producing a control signal that can be moved to a predefined interval specified by the vector $\mathbf{h}_N$. While the cost in certain intervals might be lowered with the choice of $\mathbf{h}_N$, control torque may still occur outside this interval as the optimization procedure aims to satisfy the constraints while minimizing the cost

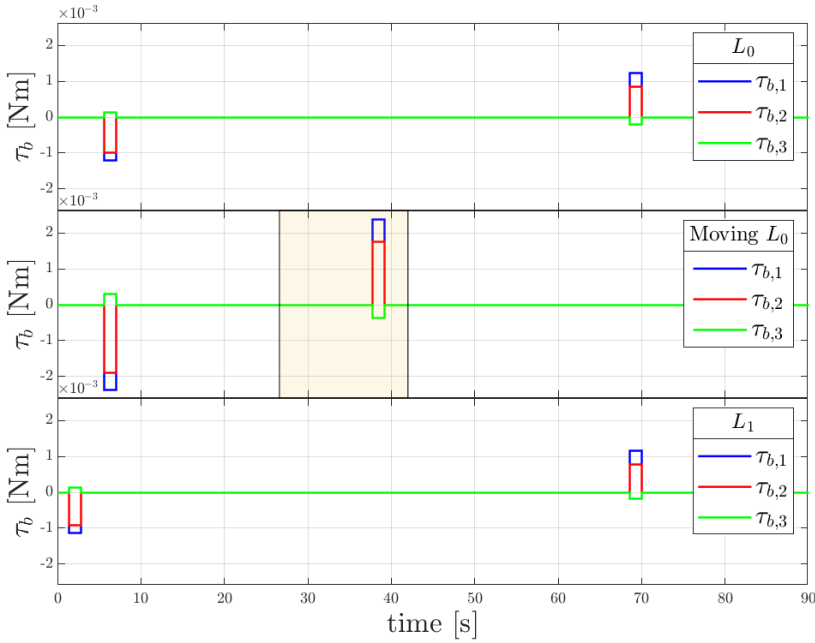

Figure 8.7: Control input in $\{b\}$, multiple-axis maneuver.

function.

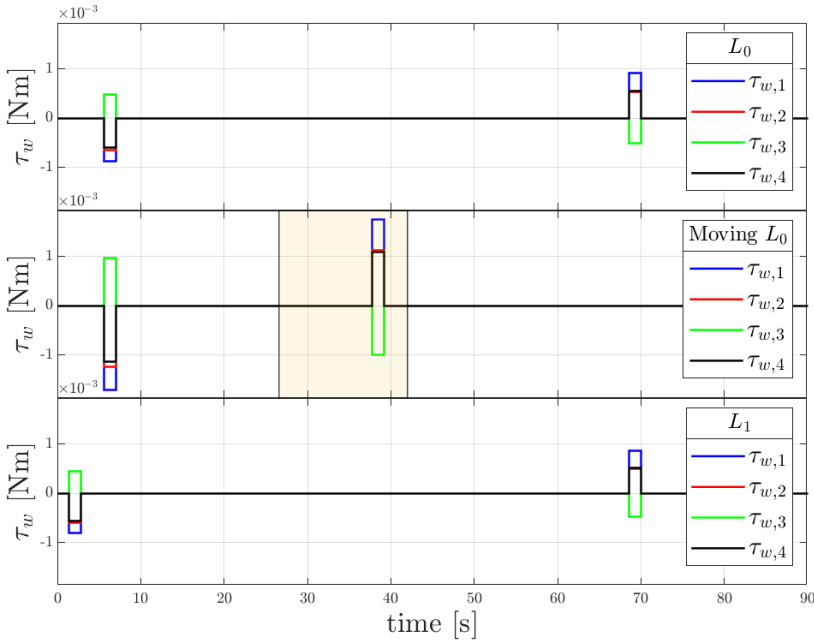

Figure 8.8: Control input in $\{w\}$, multiple-axis maneuver.

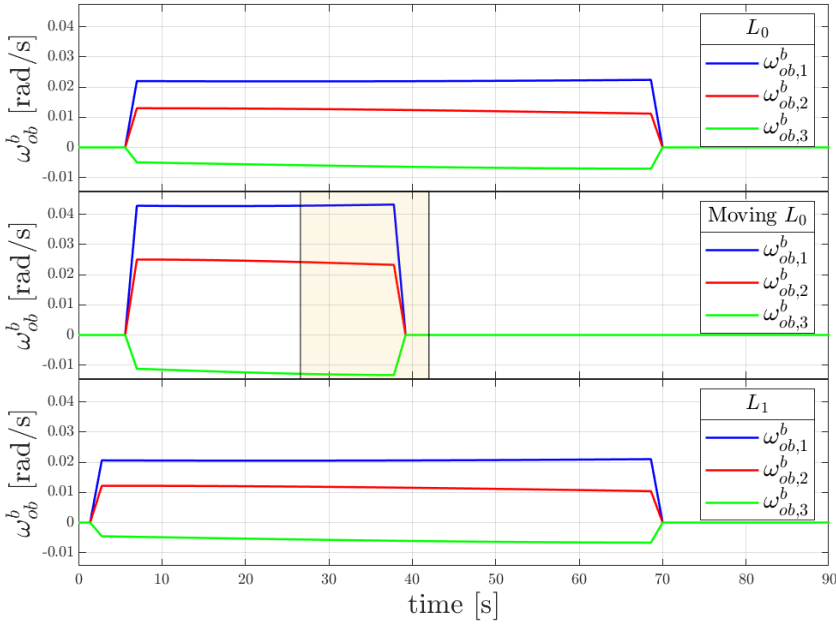

Figure 8.9: Angular velocities, $\boldsymbol{\omega}^b_{ob}$, multiple-axis maneuver.

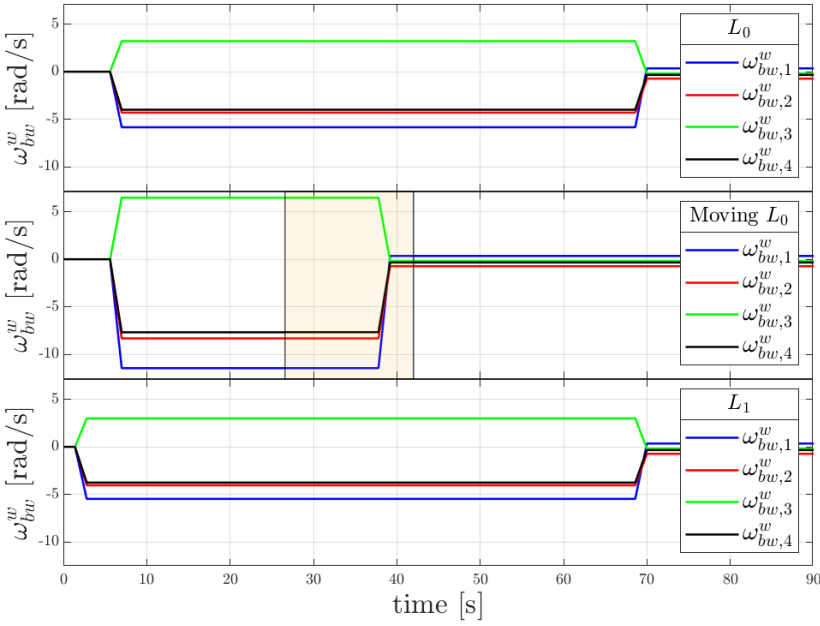

Figure 8.10: Angular velocities, $\boldsymbol{\omega}^w_{bw}$, multiple-axis maneuver.

Chapter 9

Maximum Hands-Off Attitude Control of a Spacecraft Actuated by Thrusters

9.1 Introduction

Maximum hands-off control is a control scheme where the resulting torque is highly discontinuous. While [54] showed that reaction wheels, a type of actuator that works well with continuous controllers, can be used with maximum hands-off control to control the attitude of a spacecraft, a more natural choice of actuators to couple with maximum hands-off control is reaction thrusters. Reaction thrusters, or simply thrusters, are actuators that are either completely on or completely off, giving a discontinuous input to the system. As opposed to reaction wheels, thrusters can be used for orbital maneuvers in addition to for attitude control. See for example [55, 56].

There exists thrusters that are not off or on at their maximum magnitude, namely electric thrusters (see for example [57]), which have been suggested for use for the attitude control of a spacecraft [58, 59]. The focus of this chapter will be on/off thrusters. However, a brief discussion on generalizing the results in this chapter for use with continuous thrust is included.

The contributions in this chapter are the following: we show that the maximum hands-off control formulation demonstrated for a satellite with reaction wheels also works with attitude maneuvers for a satellite actuated with reaction thrusters. The formulation used in this chapter differs from the previous one, as the cost function is extended with an additional term. Furthermore, we justify using the union operator for optimizing based on the L_0-norm for a problem with multiple inputs. Finally, we defined the term relative sparsity as a way to compare the sparsity of different control strategies. The impact of the sampling rate and saturation limits on the inputs on the relative sparsity is discussed in some detail.

The remaining part of the chapter is structured as follows: the max hands-off control is defined in Section 9.2, both in general terms and with the relaxed formulation used for direct optimization in [54]. In the same section, we introduce the

union operator and define relative sparsity. The optimal control problem, including the cost function based on the maximum hands-off formulation from Section 9.2, is presented in Section 9.3. The simulation setup is described in Section 9.4, which is made up of three scenarios: a simple maneuver showing that the control strategy can accomplish the desired objectives and two different scenarios designed to show how the system parameters impact relative sparsity. The results are presented in Section 9.5 and discussed in Section 9.6, while the chapter is concluded in Section 9.7.

9.2 Max hands-off control

This section will introduce the theory behind the maximum hands-off formulation, as defined by [51]. The support of a function of time $u(t)$, a continuous-time signal, is defined by the closure of the set

$$\{t \in [0, T] : u(t) \neq 0\}, \tag{9.1}$$

which is the set of points where the function takes on non-zero values.

The authors of [51] use (9.1) to define the L_0-norm of $u(t)$ as the length of the support using the Lebesgue measure on $\mathbb{R}$, This yields the definition of the L_0-norm

$$\|u\|_0 \triangleq \mu(\text{supp}(u(t))). \tag{9.2}$$

where $\mu(\cdot)$ is the mentioned Lebesque measure. In defining their optimal control problem, [51] define a cost function based on the continuous time-signal $u(t)$ as

$$J_0(u(t)) \triangleq \sum_{i=1}^{m} \lambda_i \|u_i\|_0, \tag{9.3}$$

where m is the number of control inputs in the time domain, λ_i are positive weights for each control signal, and the L_0-norm is the one that was defined in (9.2).

As the formulation in (9.3) is only for a single continuous-time signal, the cost function should be changed to facilitate several continuous-time signals in a vector. With the maximum hands-off control scheme, we want to minimize the total time any input is applied to the system. In other words, if one of the channels of the vector has support at a given time step, it should not cost anything for the other channels to have a non-zero signal at that time step. To achieve this, we reformulate the L_0 cost function in (9.3) as,

$$J_0(\mathbf{u}(t)) \triangleq \sum_{i=1}^{m} \bigcup_{j=1}^{n} \lambda_{j,i} \|\mathbf{u}_{j,i}\|_0, \tag{9.4}$$

where n is the number of channels in the input vectors, which in this chapter will be the number of thrusters.

A longer discussion on different implementations of the maximum hands-off control and how the choices affect the amount of input signals the system receives can be found in [66].

The relative sparsity of a discrete signal can be defined as

$$\text{Relative sparsity} = \frac{\text{Time steps with actuation}}{\text{Total time steps}} \cdot 100\%. \tag{9.5}$$

The relative sparsity, defined this way, makes sense as a comparison measure between different control signals regarding how sparse the signal is as it measures how much of the available control horizon the control signal uses for actuation. This measure could give a better view of how sparse the actuation is compared to the view provided directly by the values from the L_0-norm, which will directly result from the simulation's point resolution or the experiment.

The maximum hands-off control problem is discontinuous, so to use IPOPT we need to relax the problem. In this chapter, we use the same relaxation for the maximum hands-off control problem as in [54]. Formally, by defining the L_0-optimal control problem as

$$\begin{aligned} \min_{\mathbf{x}} \quad & f(\mathbf{x}) + \gamma \|\mathbf{x}\|_0 && \text{(9.6a)} \\ \text{s.t.} \quad & c_i(\mathbf{x}) = 0,\ j \in \mathcal{E} && \text{(9.6b)} \\ & c_j(\mathbf{x}) \leq 0,\ j \in \mathcal{I}, && \text{(9.6c)} \end{aligned}$$

where $c_i(\mathbf{x})$ and $c_j(\mathbf{x})$ are constraints in the set of equality constraints, $\mathcal{E}$, and inequality constraints, $\mathcal{I}$, respectively. γ is an arbitrary, positive constant. the L_0-optimal control problem can be relaxed using a set of complementarity constraints [63]

$$\begin{aligned} \min_{\mathbf{x}} \quad & f(\mathbf{x}) + \boldsymbol{\gamma}^\top (\mathbf{1}_N - \boldsymbol{\xi}) && \text{(9.7a)} \\ \text{s.t.} \quad & c_i(\mathbf{x}) = 0,\ i \in \mathcal{E} && \text{(9.7b)} \\ & c_i(\mathbf{x}) \leq 0,\ i \in \mathcal{I} && \text{(9.7c)} \\ & -\epsilon \mathbf{1} \leq \boldsymbol{\xi} \circ \mathbf{x} \leq \epsilon \mathbf{1} && \text{(9.7d)} \\ & \mathbf{0} \leq \boldsymbol{\xi} \leq \mathbf{1}, && \text{(9.7e)} \end{aligned}$$

where the vector $\boldsymbol{\xi}$ is a vector of the same size as the number of control intervals that indicates whether or not any control signal is spent at a given time step. The operator $\circ$ is the Hadamard product, which is the element-wise product of the two factors. ϵ is a small, positive number multiplied by a vector of ones, $\mathbf{1}$, of the same size as $\boldsymbol{\xi}$. The vector $\mathbf{0}$ is a vector of zeros of the same size as $\boldsymbol{\xi}$, similar to $\mathbf{1}$.

9.3 Optimal Control Problem

The optimal control problem, using a relaxed formulation of the maximum hands-off control problem using the cost as it is defined in (9.4) for the attitude of a

satellite actuated by thrusters, is given by

$$\min \quad k_1 f(\boldsymbol{\omega}_{ib}^b) + k_2 g(\mathbf{q}_b^i) + k_3(\mathbf{1} - \boldsymbol{\xi})\mathbf{1}^\top \tag{9.8a}$$

$$\text{s.t.} \quad \dot{\mathbf{q}}_b^i = \frac{1}{2}\mathbf{T}(\mathbf{q}_b^i)\boldsymbol{\omega}_{ib}^b \tag{9.8b}$$

$$\dot{\boldsymbol{\omega}}_{ib}^b = \mathbf{J}^{-1}(-\mathbf{S}(\boldsymbol{\omega}_{ib}^b)\mathbf{J}\boldsymbol{\omega}_{ib}^b + \mathbf{B}\boldsymbol{\tau}_u) \tag{9.8c}$$

$$\mathbf{0} \leq \boldsymbol{\tau}_u \leq \boldsymbol{\tau}_{\text{limit}} \tag{9.8d}$$

$$\mathbf{x}(0) = \mathbf{x}_0 \tag{9.8e}$$

$$-\epsilon\mathbf{1} \leq \boldsymbol{\xi} \circ \boldsymbol{\tau}_{u,j}(t) \leq \epsilon\mathbf{1} \tag{9.8f}$$

$$\mathbf{0} \leq \boldsymbol{\xi} \leq \mathbf{1}, \tag{9.8g}$$

where $f(\cdot)$ and $g(\cdot)$ are costs imposed on the error in the angular velocity, $\boldsymbol{\omega}_{ib}^b$, and the quaternion, $\mathbf{q}_b^i$, with respect to the reference quaternion, respectively, given as

$$\begin{aligned} f(\boldsymbol{\omega}_{ib}^b) &= (\boldsymbol{\omega}_e^b)^\intercal \boldsymbol{\omega}_e^b, \quad \boldsymbol{\omega}_e^b = \boldsymbol{\omega}_{ib,\text{ref}}^b - \boldsymbol{\omega}_{ib}^b(T), \\ g(\mathbf{q}_b^i) &= 1 - \left|(\mathbf{q}_b^i(T))^\top \mathbf{q}_{b,\text{ref}}^i\right|, \end{aligned} \tag{9.9}$$

where T is the length of the control horizon, making an arbitrary vector $\mathbf{x}$ take the value $\mathbf{x}(T)$ at the final time. The function $g(\cdot)$ in (9.9) is chosen due to it being a metric on SO(3) [28]. The sub- and superscripts i and b denote the inertial and body frame, respectively. Note that the rigid body model is assumed to be sufficient for the studied problem, i.e., the change in the inertia matrix is assumed to be either symmetric or small enough to be disregarded. $\mathbf{T}(\cdot)$ is given as [18]

$$\mathbf{T}(\mathbf{q}) = \begin{bmatrix} -\boldsymbol{\epsilon}^\intercal \\ \eta\mathbf{I}_{3\text{x}3} + \mathbf{S}(\boldsymbol{\epsilon}) \end{bmatrix}, \tag{9.10}$$

where η is the scalar part, and $\boldsymbol{\epsilon}$ is the vector part of the quaternion. The $\mathbf{S}(\cdot)$ matrix is a matrix that works like the three-dimensional cross product. k_1, k_2, and k_3 are positive constants that determine how much weight the optimization should put into getting closer to the reference in attitude or angular velocity or to keep the L_0-norm small, respectively. $\mathbf{J}$ is the satellite inertia matrix. $\mathbf{B}$ is the torque distribution matrix, mapping the torques from the thrusters, $\boldsymbol{\tau}_u$, into the body frame. $\boldsymbol{\tau}_u$ is a vector with one element for each thruster, showing only the sign and the magnitude of the torque the thruster provides. The torque from each separate thruster is accessed separately through $\boldsymbol{\tau}_{u,j}(t)$. The state, given by $\mathbf{x}$, is defined by $\mathbf{x} = [\mathbf{q}_b^i; \boldsymbol{\omega}_{ib}^b]$. The initial state variable, $\mathbf{x}(0)$, is given by $\mathbf{x}_0$. Note that the term $\boldsymbol{\tau}_{u,i}(t)$ in (9.8f) indicates that each element of the torque vector should be multiplied with the torque vector for a given time step, which satisfies the definition of the L_0-cost we want to use in this chapter, as defined in (9.4).

We assume that the thrusters are either on at maximum thrust or completely shut off. For such discontinuous thrust, an extra term must be appended to the cost function (9.8a), yielding

$$\min \; k_1 f(\boldsymbol{\omega}_{ib}^b) + k_2 g(\mathbf{q}_b^i) + k_3(\mathbf{1} - \boldsymbol{\xi})\mathbf{1}^\intercal + k_4 \sum_{i=1}^{N} \boldsymbol{\xi}(i) \sum_{j=1}^{n_u} \tau_{u,(j,i)}(\tau_{\text{limit}} - \tau_{u,(j,i)}), \tag{9.11}$$

where N is the number of control intervals, n_u is the number of thrusters, k_4 is a positive constant, and $\tau_{u,(j,i)}$ is the element of the torque vector $\boldsymbol{\tau}_u$ specified for thruster j at time step i. The added term provides the on/off behavior from the optimization: as $\boldsymbol{\xi}$ is a measurement for when a control signal is applied, this term should be close to zero when there is no control action at a given time step and one when control is applied. Thus, using $\boldsymbol{\xi}$ will only be an extra cost based on control signals where at least one of the channels in the control vector, signifying that one of the thrusters is active. The difference term $(\tau_{\text{limit}} - \tau_{u,(j,i)})$ is included to force the torque from each thruster to its maximum value, τ_{limit}. As we do not want to force all thrusters to fire when one of the thrusters is active, the maximizing terms need to be multiplied by the torque value from the given thruster, $\tau_{u,(j,i)}$. This term is necessary due to $\boldsymbol{\xi}$ having only one element shared between all torques, an artifact of the L_0-formulation as shown in (9.4).

For continuous thrust actuators, it seems reasonable to assume that the formulation in (9.8) is sufficient, making the extra term introduced in (9.11) redundant when the actuation can take a continuous range of values.

9.4 Simulation setup

The simulations in this chapter are based on the ESEO satellite, [55]. The inertia of the satellite is given by

$$\mathbf{J} = \begin{bmatrix} 4.350 & 0 & 0 \\ 0 & 4.3370 & 0 \\ 0 & 0 & 3.6640 \end{bmatrix} \text{kg} \cdot \text{m}^2. \tag{9.12}$$

The optimal control problem (9.8) is solved using IPOPT in CasADi. Runge-Kutta 4 is used as the numerical solver. Six thrusters actuate the satellite, each set to only give torque along one body frame axis. This gives the torque distribution matrix $\mathbf{B}$,

$$\mathbf{B} = \begin{bmatrix} 1 & 0 & 0 & -1 & 0 & 0 \\ 0 & 1 & 0 & 0 & -1 & 0 \\ 0 & 0 & 1 & 0 & 0 & -1 \end{bmatrix}, \tag{9.13}$$

with the negative signs signifying that all elements in $\boldsymbol{\tau}_u$ contain positive torque values.

Three simulation scenarios are run: one to show that the attitude control system can provide satisfactory results with maximum hands-off control with thrusters, and two scenarios where the relative sparsity metric's properties are explained. In the attitude control example, the satellite is given the initial conditions $\mathbf{x}(0) = [\mathbf{q}_b^i; \boldsymbol{\omega}_{ib}^b](0) = [0, 1, 0, 0, 0, 0, 0]^\intercal$, where the first four elements are the quaternion and the latter three are the angular velocity. The references, $\mathbf{q}_{b,\text{ref}}^i$ and $\boldsymbol{\omega}_{ib,\text{ref}}^b$, are given as $[0.5774, 0, -0.5774, -0.5774]^\intercal$ and $[0, 0, 0]^\intercal$. The control horizon T is set to be 30, and the number of steps is set as $N = 90$, yielding a time step of $h = \frac{T}{N} = \frac{30}{90}\text{s} = \frac{1}{3}$ s. The limit on the torques from the thrusters is set to be $\tau_{\text{limit}} = 0.195$ N$\cdot$m, consistent with the thrusters in [55], where $\boldsymbol{\tau}_{\text{limit}} = \tau_{\text{limit}} \mathbf{1}_{n_u \text{x} 1}$. The torque limit, as well as the torque from the trusters themselves, take the distance between the place the force from the truster is applied, as well as the

magnitude of the force from the trusters into account, and thus, the torque is expressed directly in this chapter for simplicity. As discussed in [54], the maximum hands-off attitude control problem is very sensitive to the choice of initial values. In this chapter, the initial values are chosen to be the trajectory resulting from a PD controller modulated with a simple Schmitt trigger.

For the scenarios showcasing the properties of the relative sparsity metric, the initial conditions and references are identical to those for the attitude demonstration example. In both of the scenarios, the thrusters are made less effective by reducing the torque limit by 50%, essentially weakening the actuators or moving them further from the center of rotation. At the same time, the number of control intervals has been decreased by 50% in the latter scenario.

The values for k_1, k_2, k_3, and k_4 for the different scenarios, enumerated 1, 2, and 3, as introduced in this chapter, can be found in Table 9.1.

Table 9.1: Cost function constants

k_i	Scenario 1	Scenario 2	Scenario 3
k_1	18.4	18.4	18.4
k_2	$3.92 \cdot 10^3$	$3.92 \cdot 10^3$	$3.92 \cdot 10^3$
k_3	$(N)^{-1} \cdot 4.5 \cdot 10^4$	$(N)^{-1} \cdot 4.5 \cdot 10^4$	$(N)^{-1} \cdot 1.35 \cdot 10^5$
k_4	$\frac{2.295 \cdot 10^5}{N \cdot n_u}$	$\frac{2.295 \cdot 10^5}{N \cdot n_u}$	$\frac{6.885 \cdot 10^5}{N \cdot n_u}$

9.5 Results

9.5.1 Attitude control maneuver

Figure 9.1 shows the attitude response of the system with the trajectory based on the maximum hands-off control formulation solved using IPOPT. As can be seen from the figure, at the end of the simulation, the optimal trajectory reaches the reference attitude, as the quaternion covers SO(3) twice, making $\mathbf{q}$ and $-\mathbf{q}$ represent the same attitude. The corresponding angular velocities are shown in Figure 9.3. The torques from the thrusters are plotted in Figure 9.2. Note that thruster one is fixed in the opposite direction of thruster four, thruster two in the opposite direction of thruster five, and thruster three in the opposite direction of thruster six, as indicated by the distribution matrix in (9.13). The output from the optimal solver IPOPT, showing the time it takes to solve the problem and the number of iterations, is shown in Table 9.2. The relative sparsity for this scenario, calculated using the definition in (9.5), is 11.11% for this scenario.

9.5.2 Relative sparsity simulations

Figure 9.6 shows the torque with stricter torque limits than in Section 9.5.1. As seen from the quaternion trajectory in Figure 9.4 and the angular velocity trajectories in Figure 9.5, the satellite still manages to reach the reference values.

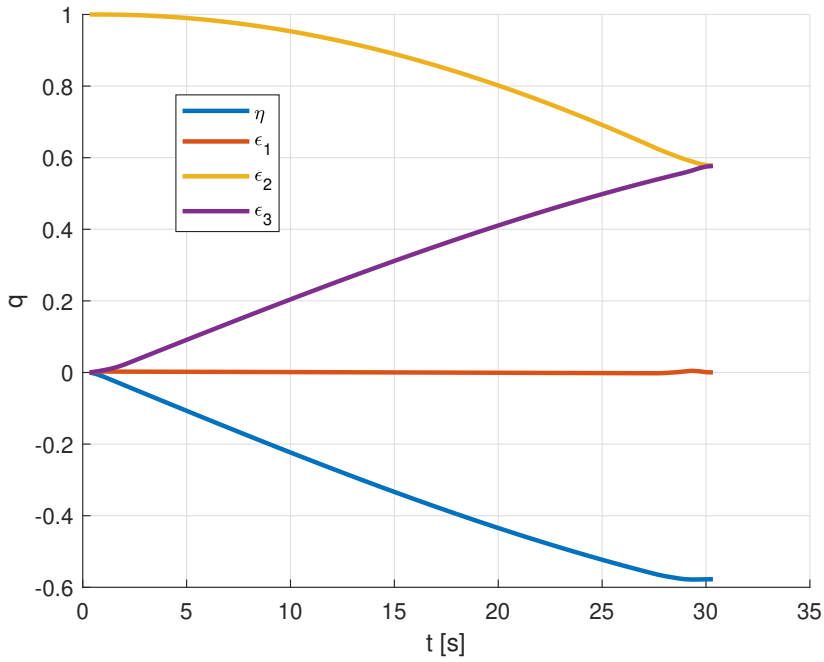

Figure 9.1: Quaternion response with maximum hands-off control.

Table 9.2: IPOPT output

Output	Value
Number of iterations	5635
Total CPU secs in IPOPT (w/o function evaluations)	58.893
Total CPU secs in NLP function evaluations	929.226

Keeping the torque limit low and reducing the time step gives the quaternion and angular velocity trajectories, as shown in Figure 9.7 and Figure 9.8, respectively. The torques this scenario requires are shown in Figure 9.9. The relative sparsity of the two simulations are shown in Table 9.3.

Table 9.3: Relative sparsity comparison

Controller	Relative sparsity (%)
With stricter torque limit	16.6667
With lower N	20.000

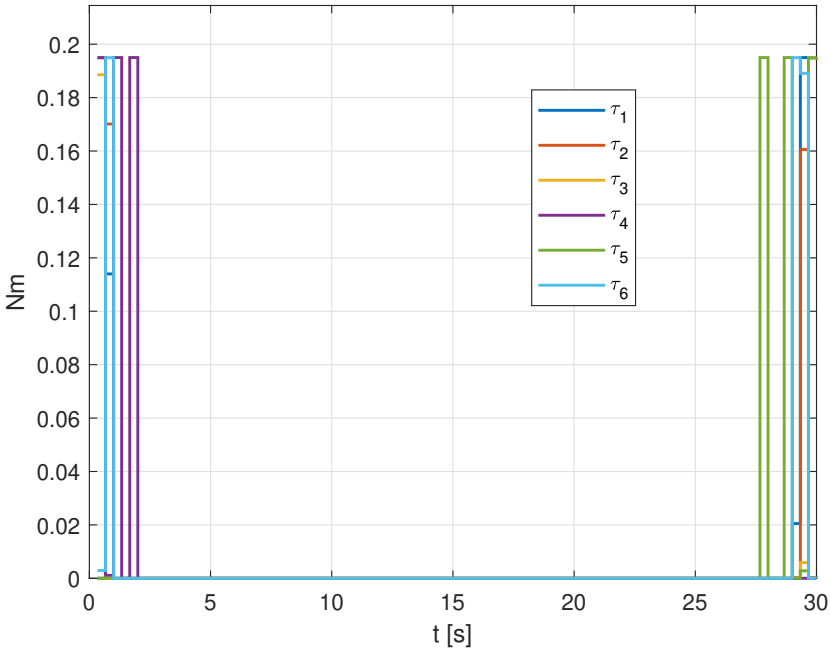

Figure 9.2: Torque from the trusters with maximum hands-off control.

9.6 Discussion

9.6.1 Attitude control maneuver

The results in Section 9.5.1 show that the maximum hands-off control algorithm, as described in this chapter, works for controlling the attitude of a satellite towards a desired attitude and angular velocity.

The main issue with the direct optimization approach to the maximum hands-off control problem using a solver based on derivatives like IPOPT is that the problem is discontinuous. This would be an issue for the maximum hands-off control problem even if the reaction thrusters with their on/off actuation were not in use, as the L_0-norm is not differentiable and motivates the approximation given in (9.7). With the relaxation parameter ϵ set above zero, some of the values in the optimized trajectory will be slightly above zero, which is where they would be if the solver managed to find the "true" optimal solution without the relaxed formulation. Furthermore, there are four different objectives the optimization should accomplish: the attitude quaternion and the angular velocity should reach their references, the torque should be applied for as little time as possible, and the torque should always be on/off. The first three are not opposing criteria for optimization: by defining a region around the references, there will be a minimum number of (discrete) torque signals required to reach this region. Most control signals will be as high as possible, probably reaching the saturation limits for all or all but one control

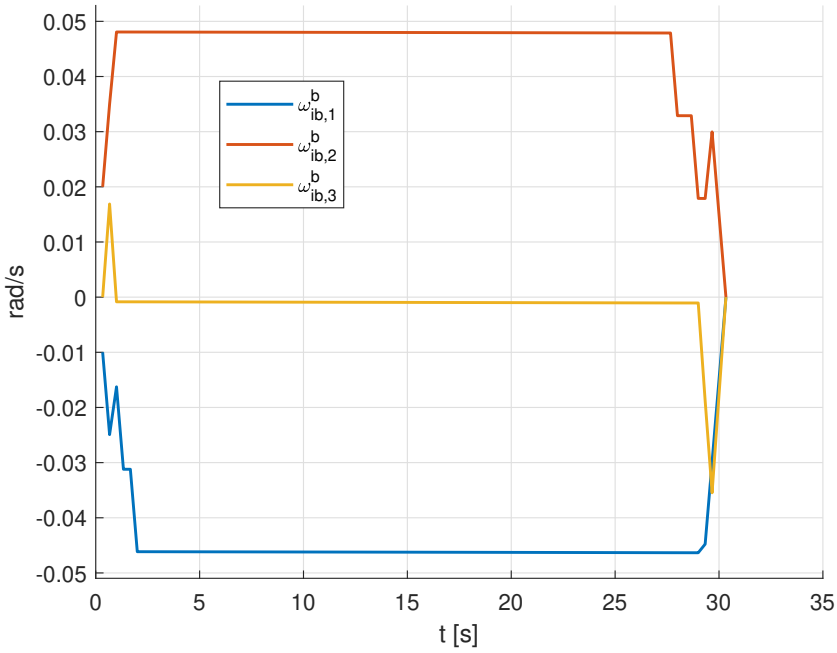

Figure 9.3: Angular velocity response with maximum hands-off control.

signal to minimize the control signals in the optimal scenario. The problem with the fourth criterion arises if the control horizon is too coarse relative to the desired region around the references, i.e., N is large relative to T, so it might be hard for the solver to find a good trajectory without careful tuning. This explains why even the optimal solution here has some non-maximized values, as the solver prioritizes reaching the end attitude and angular velocities. Saturating the values from this optimization based on a threshold would give the true on/off behavior the actuators require, but the values for the other objectives, particularly the quaternion and the angular velocity, will naturally end up further from the references than they are in Figure 9.1 and Figure 9.3.

A point was made in Section 9.4 about the importance of initial guesses for the maximum hands-off control problem. The last term in the cost function, which was introduced in (9.11), $k_4 \sum_{i=1}^{N} \boldsymbol{\xi}(i) \sum_{j=1}^{n_u} \tau_{u,(j,i)}(\tau_{\text{limit}} - \tau_{u,(j,i)})$, is introduced to penalize the solver if the control signal is not on or off, as required by the actuators. Optimizing without this term, using a trajectory generated by a regular PD controller, does not yield satisfactory results as the resulting control signal is significantly less sparse than what is shown in Section 9.5.1. This suggests that the term would help create the maximum hands-off control in situations where the torque does not have to reach its maximum magnitude each time the actuators are used, as it seems to improve the solver's resilience against poor initial guesses. The term could, however, if the maximum control torque is not called for at any point,

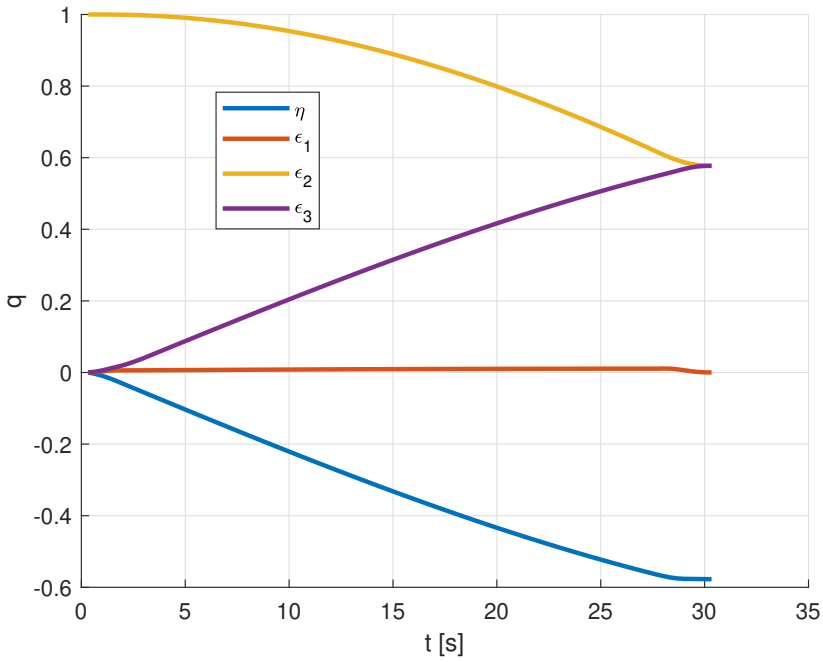

Figure 9.4: Quaternion response with maximum hands-off control with lower torque saturation limits.

lead to a less sparse solution than the maximum hands-off control scheme calls for, as it will force the control signal at a given point toward the maximum value, requiring more torque to counteract the motion when moving towards the reference value. Additionally, the added term and the maximum hands-off term work in the opposite direction: the maximum hands-off term drags the values toward zero, while the added term drags the terms toward the maximum value. This could introduce an extra error into the system since the vector $\boldsymbol{\xi}$ cannot be exactly zero, meaning that the added term will often be in effect when it should not be.

9.6.2 Relative sparsity simulations

The relative sparsity metric for the two scenarios with stricter torque limits and longer time steps, given in Table 9.3, shows a significant increase compared to the 11.11% relative sparsity in the nominal case in Section 9.5.1. For the stricter torque limit case, this consequence is always to be expected when lowering the torque limit as long as the maximum hands-off torque naturally reaches the saturation limit before it is lowered, which is what is shown in the figures here. For the decrease in control intervals, i.e., the decrease in N, the case is the opposite: if the control signal is naturally saturated before N is decreased, the relative sparsity will not necessarily increase. An example that illustrates this is a control signal with four

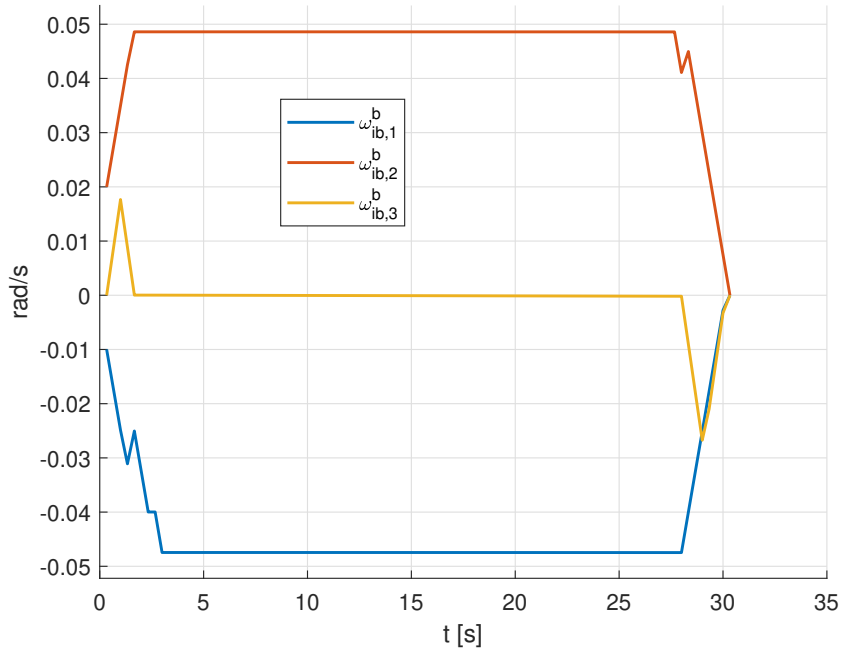

Figure 9.5: Angular velocity response with maximum hands-off control with lower torque saturation limits.

saturated control signal points before the decrease in N. If N is divided by four, there will be one saturated control signal point, thus preserving the relative sparsity. If N, for some reason, is divided by three, two new signal points will be required to represent the same control signal, which in turn will span a more extended area on $\mathbb{R}$, thus increasing the relative sparsity. Due to these concerns, it is important only to compare two different control schemes with respect to relative sparsity if the underlying conditions, such as the control limits, the control horizon, and the number of control signals, differ between the schemes.

9.7 Conclusion

Maximum hands-off control, as formulated in [54], also works with thrusters, although the on/off nature of the actuators makes the problem harder to solve. Using the union operator is reasonable for the L_0 norm, and relative sparsity can be used to distinguish between sparse control signals, provided the sampling rate, saturation limits, and control horizon stay identical.

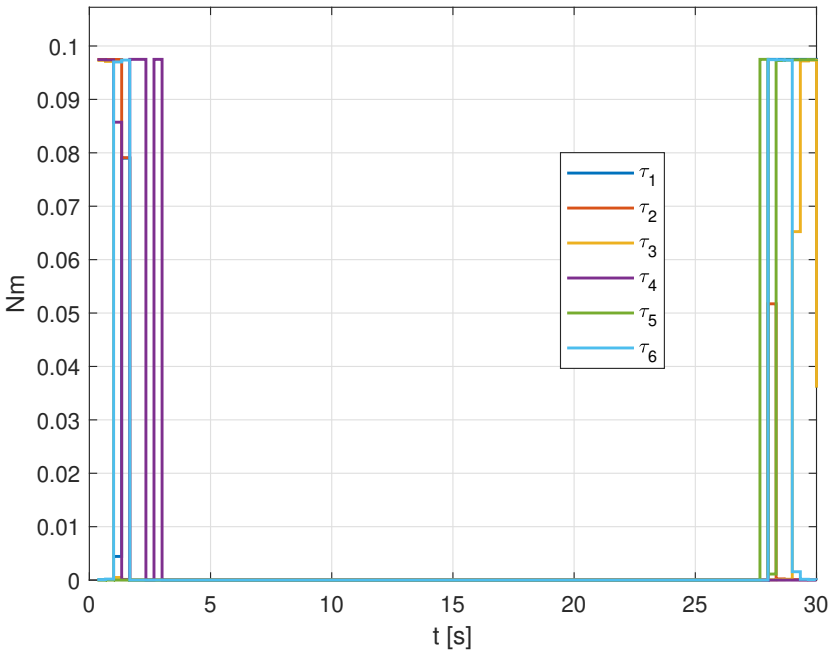

Figure 9.6: Torque from the trusters with maximum hands-off control with lower torque saturation limits.

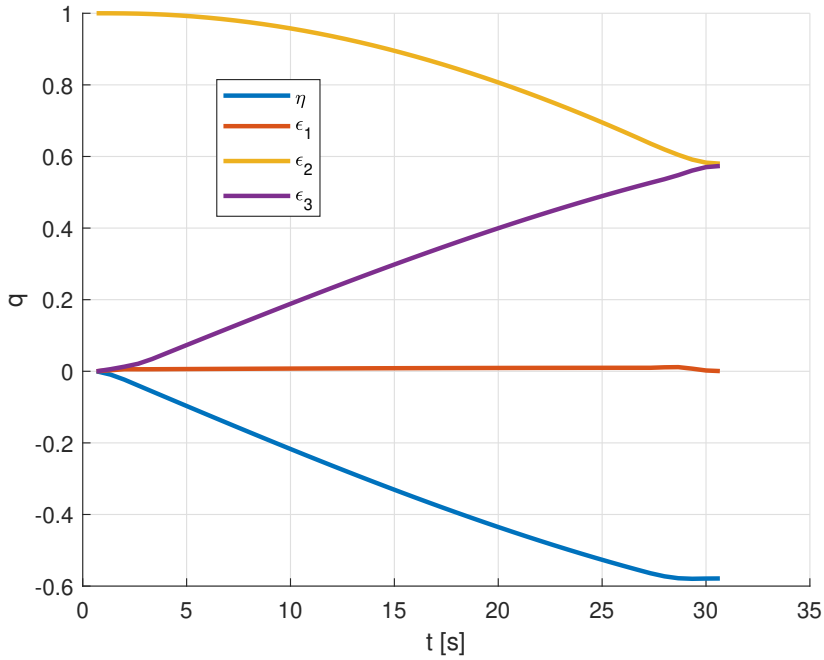

Figure 9.7: Quaternion response with maximum hands-off control with fewer control intervals.

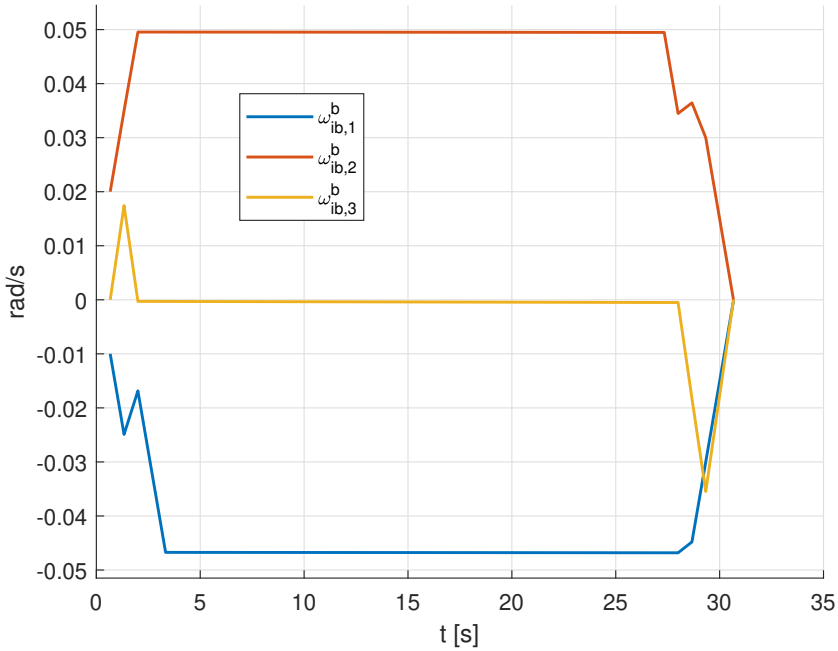

Figure 9.8: Angular velocity response with maximum hands-off control with fewer control intervals.

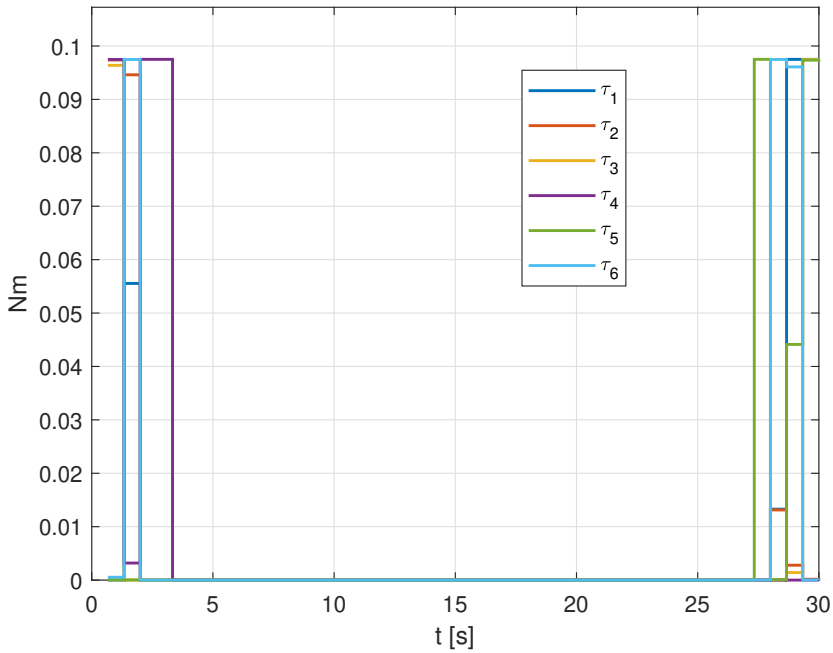

Figure 9.9: Torque from the thrusters with maximum hands-off control with fewer control intervals.

Part III

Slewing Maneuver Results

Chapter 10

Introduction

This part of the thesis concerns the control maneuver the HYPSO-1 satellite performs during its science, which is a slew maneuver. In the context of Figure 10.1, this part is in section C, the short period where the satellite takes images.

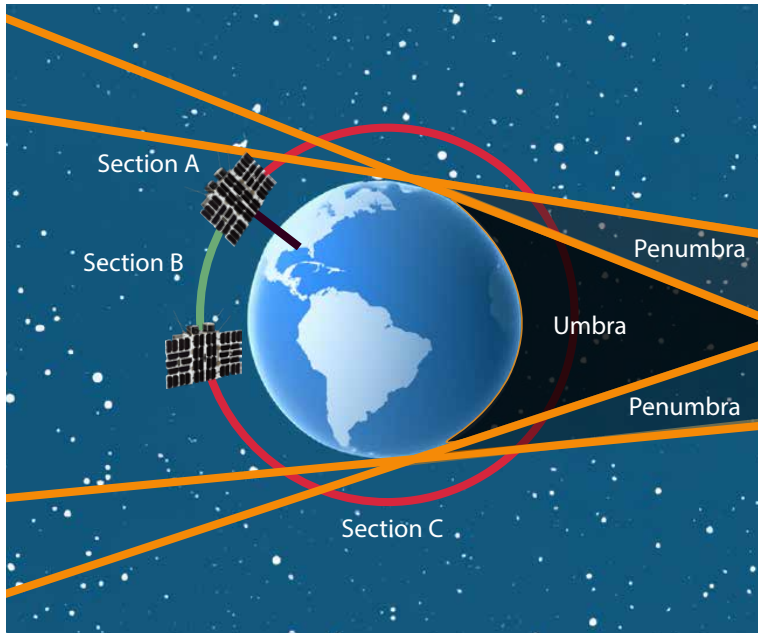

Figure 10.1: Thesis outline.

Figure 10.2 illustrates the slew maneuver with the various frames used in the two chapters.

Chapter 9 is based on

[1] **B. A. Kristiansen**, M. E. Grøtte, and J. T. Gravdahl, "Quaternion-Based Generalized Super-Twisting Algorithm for Spacecraft Attitude Control", in

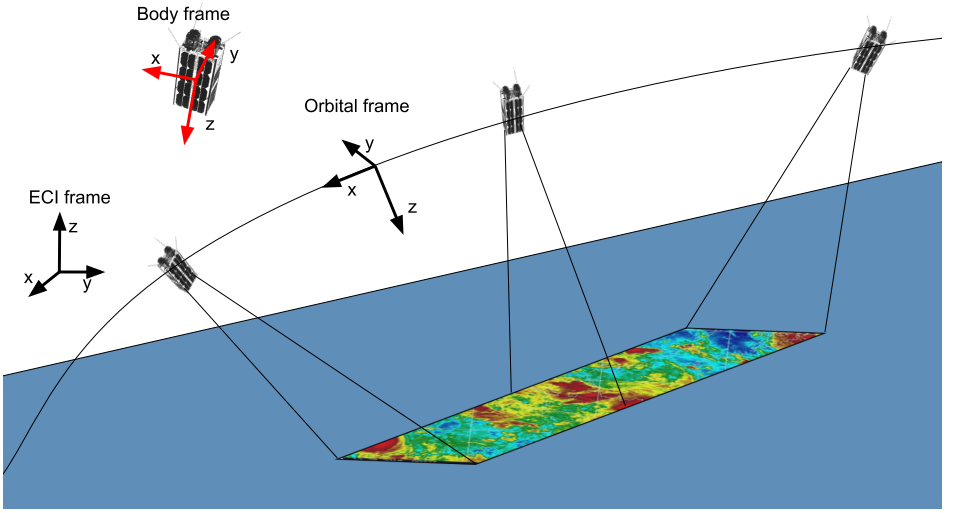

Figure 10.2: The HYPSO-1 slew maneuver. Three coordinate frames are depicted: the body frame, the orbital frame (the LVLH frame), and the inertial (ECI) frame. The satellite moves from right to left in the figure as it images the area of interest. The image is from [6], which is part of this thesis.

Proceedings of the 21st IFAC World Congress, Berlin (Virtual), Germany, July 2020,

where the authors demonstrate through simulations that a second-order sliding mode controller named generalized super-twisting algorithm could be a feasible choice for pointing and the HYPSO-1 slew maneuver.

Chapter 12 is based on

[6] **B. A. Kristiansen**, D. D. Langer, J. L. Garrett, S. Berg, J. T. Gravdahl, and T. A. Johansen, "Accuracy of a slew maneuver for the HYPSO-1 satellite — in-orbit results," in *13th Workshop on Hyperspectral Image and Signal Processing Evolution in Remote Sensing (IEEE-WHISPERS)*, Athens, Greece, Oct. 2023,

which is a paper evaluating the performance of the slew maneuver for the HYPSO-1 satellite on experimental results, investigating if the slew maneuver increases the data quality as the mission analysis originally assumed.

Chapter 11

Quaternion-Based Generalized Super-Twisting Algorithm for Spacecraft Attitude Control

11.1 Introduction

The spacecraft attitude control problem is a well-studied topic ([9], [67], [55]). Various control laws for attitude control have been proposed such as the sliding mode control (SMC) [68], [69], which has robustness towards modeling uncertainties and disturbances. However, an issue with SMC is chattering, which is an effect due to the signum term of the control algorithm, causing a zig-zag effect in the controlled channels. A method for attenuating this effect is to hide the discontinuous signum function behind an integrator [70]. An example is the super-twisting algorithm [71], a second-order sliding mode algorithm. The super-twisting algorithm was studied for attitude control of a spacecraft actuated by magnetorquers in [72]. This algorithm was further developed into the generalized super-twisting algorithm (GSTA), which is robust to bounded time-varying disturbances [73]. In practice, the GSTA has successfully been applied for attitude control of other vehicles, such as articulated intervention AUVs [74].

In this chapter we present a nonlinear spacecraft model with a control law based on GSTA. Simulation results are shown for two attitude maneuvers, pointing and slewing, of a spacecraft actuated by reaction wheels using the GSTA. These extend to the case studies presented in [33]. While [33] investigates time-varying attitude control strategies using an augmented proportional-derivative controller with feedforward terms and requirements for magnetorquer control law, the contributions of this chapter are to compare SMC and PD with GSTA for a slewing and pointing spacecraft using state feedback.

This chapter is organized as follows: In Section 11.2 describes the model of the dynamics used for the simulations. The model includes attitude parameterized by unit quaternions, a dynamical model for the reaction wheels, and a model of perturbations. Section 11.3 introduces the momentum dumping control law used on the magnetorquers, the GSTA and the SMC we use for attitude control with

the reaction wheels. We present the simulation results using parameters for a 6U CubeSat in Section 11.4, while conclusions are provided in Section 11.5.

11.2 Spacecraft Model

In this section, we present the model of an internally actuated spacecraft.

11.2.1 Coordinate frames

Earth-centered inertial (ECI)

The earth-centered inertial frame $\{i\}$ has origin at the Earth's center of mass, with the z-axis pointing through the North Pole, the x-axis pointing towards vernal equinox, and the y-axis completing the right-handed system. Vectors and derivatives with respect to the ECI frame are denoted with superscript i.

Orbit frame

The Local Vertical, Local Horizontal (LVLH) frame, or the orbit frame $\{o\}$, has superscript o for vectors represented in the frame. The orbit frame is centered in the center of mass of the spacecraft. The z-, x-, and y-axis point in the direction of the Earth's center of mass, the orbit velocity vector, and in a direction that completes the right-handed coordinate system, respectively. The unit vectors of the frame are given by

$$\hat{\mathbf{z}}^o = -\frac{\mathbf{r}^i}{\|\mathbf{r}^i\|_2},\ \hat{\mathbf{x}}^o = \frac{\mathbf{v}^i}{\|\mathbf{v}^i\|_2},\ \hat{\mathbf{y}}^o = \frac{\hat{\mathbf{z}}^o \times \hat{\mathbf{x}}^o}{\|\hat{\mathbf{z}}^o \times \hat{\mathbf{x}}^o\|_2}, \tag{11.1}$$

where $\mathbf{r}^i$ is the distance between the spacecraft and the center of the Earth, and $\mathbf{v}^i$ is the spacecraft's inertial velocity.

Body frame

The axes of the body frame $\{b\}$ follow the spacecraft structure, and its origin is centered in the spacecraft's center of mass. Vectors represented in this frame have superscript b.

Wheel frame

The wheel frame $\{w\}$ specifies vectors directly related to the reaction wheels. The two vectors represented in this frame are the wheel angular velocity, $\boldsymbol{\omega}_{bw}^w$, and the torque applied to each wheel, $\boldsymbol{\tau}_u^w$. The dimension of these vectors equals the number of reaction wheels, where each channel of the vectors specifies the angular velocity or torque applied about each wheel's axis of rotation. The mapping of the wheel frames to the body frame is represented by the matrix $\mathbf{A} \in \mathbb{R}^{3\text{x}n}$, as

$$\boldsymbol{\tau}_u^b = \mathbf{A}\boldsymbol{\tau}_u^w \Rightarrow \boldsymbol{\tau}_u^w = \mathbf{A}^+\boldsymbol{\tau}_u^b, \tag{11.2}$$

where $\mathbf{A}^+$ is the pseudo-inverse of $\mathbf{A}$. Note that $\mathbf{A}$ is a constant mapping between the wheel and body frames due to a fixed reaction wheel configuration.

11.2.2 Attitude representation

Unit quaternions, represented as $\mathbf{q} = \begin{bmatrix}\eta & \boldsymbol{\epsilon}\end{bmatrix}^\intercal = \begin{bmatrix}\eta & \epsilon_1 & \epsilon_2 & \epsilon_3\end{bmatrix}^\intercal$, are used to describe the attitude of the spacecraft, where η is the scalar part of the quaternion, $\boldsymbol{\epsilon}$ is the vector part of the quaternion and satisfies the condition $\eta^2 + \boldsymbol{\epsilon}^\intercal\boldsymbol{\epsilon} = 1$. $\mathbf{q}_{ob}$ is denoted as the attitude of the body frame relative to the orbit frame. Similarly, the rotation matrix between the two frames is given as [18]

$$\mathbf{R}_b^o = \mathbf{I}_{3\times 3} + 2\eta_{ob}\mathbf{S}(\boldsymbol{\epsilon}_{ob}) + 2\mathbf{S}^2(\boldsymbol{\epsilon}_{ob}), \tag{11.3}$$

where $\mathbf{I}_{3\times 3}$ is the three-dimensional identity matrix, and $\mathbf{S}(\cdot)$ is a skew-symmetric matrix. The time derivative of a rotation matrix $\mathbf{R}_o^b$ is $\dot{\mathbf{R}}_o^b = -\mathbf{S}(\boldsymbol{\omega}_{ob}^b)\mathbf{R}_o^b$, where $\boldsymbol{\omega}_{ob}^b$ denotes the angular velocity of $\{b\}$ relative to $\{o\}$.

The kinematic differential equation for $\mathbf{q}_{ob}$ is given by

$$\dot{\mathbf{q}}_{ob} = \begin{bmatrix}\dot{\eta}_{ob}\\ \dot{\boldsymbol{\epsilon}}_{ob}\end{bmatrix} = \frac{1}{2}\begin{bmatrix}-\boldsymbol{\epsilon}_{ob}^\intercal\\ \eta_{ob}\mathbf{I}_{3x3} + \mathbf{S}(\boldsymbol{\epsilon}_{ob})\end{bmatrix}\boldsymbol{\omega}_{ob}^b = \frac{1}{2}\mathbf{T}(\mathbf{q_{ob}})\boldsymbol{\omega}_{ob}^b. \tag{11.4}$$

where $\mathbf{T}(\cdot)$ is the angular velocity transformation matrix.

11.2.3 Angular velocity

The angular velocity of the spacecraft's body frame relative to the orbit frame is given as

$$\boldsymbol{\omega}_{ob}^b = \boldsymbol{\omega}_{ib}^b - \boldsymbol{\omega}_{io}^b = \boldsymbol{\omega}_{ib}^b - \mathbf{R}_o^b\boldsymbol{\omega}_{io}^o, \tag{11.5}$$

where $\boldsymbol{\omega}_{io}^b$ is the angular velocity of the $\{o\}$ relative to the $\{i\}$, and $\boldsymbol{\omega}_{ib}^b$ is the angular velocity of the $\{b\}$ relative to the $\{i\}$.

The angular velocity of the $\{o\}$ frame relative to $\{i\}$, denoted $\boldsymbol{\omega}_{io}^o$, is defined in [19] as

$$\boldsymbol{\omega}_{io}^o = \mathbf{R}_i^o\frac{\mathbf{S}(\mathbf{r}^i)\mathbf{v}^i}{(\mathbf{r}^i)^\intercal\mathbf{r}^i}. \tag{11.6}$$

11.2.4 Attitude dynamics

The total system inertia of the spacecraft's rigid body is given by $\mathbf{J} \in \mathbb{R}^{3\text{x}3}$, such that

$$\mathbf{J} = \mathbf{J}_s + \mathbf{A}\mathbf{J}_w\mathbf{A}^\intercal, \tag{11.7}$$

where the inertia of the rigid body excluding the inertia about the spinning axis of the reaction wheels is $\mathbf{J}_s \in \mathbb{R}^{3\text{x}3}$, and the inertia matrix of the reaction wheels about the spinning axes is $\mathbf{J}_w \in \mathbb{R}^{n\text{x}n}$.

The total angular momentum of the spacecraft is given as [60]

$$\mathbf{H}_s^b = \mathbf{J}\boldsymbol{\omega}_{ib}^b + \mathbf{A}\mathbf{J}_w\boldsymbol{\omega}_{bw}^w. \tag{11.8}$$

Using Euler's second axiom, the rigid body dynamics is

$$\mathbf{J}\overset{b}{\frac{d}{dt}}\boldsymbol{\omega}_{ib}^b + \mathbf{A}\mathbf{J}_w\overset{w}{\frac{d}{dt}}\boldsymbol{\omega}_{bw}^w + \mathbf{S}(\boldsymbol{\omega}_{ib}^b)\mathbf{H}_s^b = \boldsymbol{\tau}_{\text{mtq}}^b + \boldsymbol{\tau}_{\text{ext}}^b, \tag{11.9}$$

where $\boldsymbol{\tau}_{\text{mtq}}^b$ is the torque produced by the magnetorquers and $\boldsymbol{\tau}_{\text{ext}}$ is the external perturbation torque acting on the spacecraft.

11.2.5 Perturbations

The total perturbing torque is given by

$$\boldsymbol{\tau}^b_{\text{ext}} = \boldsymbol{\tau}^b_{\text{drag}} + \boldsymbol{\tau}^b_{\text{srp}} + \boldsymbol{\tau}^b_{\text{grav}} + \boldsymbol{\tau}^b_{\text{mag}}, \tag{11.10}$$

where $\boldsymbol{\tau}^b_{\text{drag}}$ is the torque due to aerodynamic drag, $\boldsymbol{\tau}^b_{\text{srp}}$ is the torque due to solar radiation pressure, $\boldsymbol{\tau}^b_{\text{grav}}$ is the torque due to the gravity gradient, and $\boldsymbol{\tau}^b_{\text{mag}}$ is the torque due to the interaction between internal spacecraft electronics and the Earth's magnetic field.

Aerodynamic drag

Aerodynamic drag is given by

$$\mathbf{F}^b_{\text{drag}} = -\frac{1}{2}\rho A_{\text{drag}} \|\mathbf{v}^b\|^2 C_D \frac{\mathbf{v}^b}{\|\mathbf{v}^b\|}, \tag{11.11}$$

where ρ is the atmosphere's density at a given altitude, C_D is the drag coefficient, and A_{drag} is the surface area the contact force affects. For simplicity, the surface area of the largest face of the spacecraft is chosen.

We use a simplified version of the torque produced by the aerodynamic drag

$$\boldsymbol{\tau}^b_{\text{drag}} = (\mathbf{x}^b_{CP} - \mathbf{x}^b_{CG}) \times \mathbf{F}^b_{\text{drag}}, \tag{11.12}$$

where $\mathbf{x}^b_{CP}$ is the center of pressure and $\mathbf{x}^b_{CG}$ is the center of gravity. The vectors are chosen such that the distance between the centers is as large as possible but limited by the spacecraft structure size.

Gravity gradient

The gravity gradient torque is due to the spacecraft not being a point mass when modeling the rigid body dynamics. It is given in [39] as

$$\boldsymbol{\tau}^b_{\text{grav}} = 3\frac{\mu}{\|\mathbf{r}^i\|^3}\mathbf{S}(\mathbf{c}_3)\mathbf{J}\mathbf{c}_3, \tag{11.13}$$

where $\mathbf{c}_3$ is the third column vector of $\mathbf{R}^b_o$.

Solar radiation pressure

We use a simplified model for the solar radiation pressure, where the sun's position is constant in the inertial frame, and the surface area affected by the sunlight is assumed to be the largest face of the spacecraft. Another simplification made is that the solar radiation pressure is constantly applied. Together, these eliminate the need to model the sun's actual position. These simplifications do not represent an accurate model of the sun's effect on the system. Still, they are sufficient to simulate the worst-case impact of solar radiation with respect to attitude control in a relatively brief time. The force is given by [42]

$$\mathbf{F}^b_{\text{srp}} = \mathbf{R}^b_i \frac{F_{\text{srp}}}{c} A_{\text{srp}}(1+l)cos(\alpha) \begin{bmatrix} 0 & 1 & 0 \end{bmatrix}^\intercal, \tag{11.14}$$

where F_{srp} is the solar constant, c is the speed of light in vacuum, A_{srp} represents the maximum exposed surface area, l is the reflectance, and α is the incidence angle of the incoming light. The values for A_{srp}, α, and the direction vector are chosen to maximize the absolute value of the force.

The corresponding torque is given as

$$\boldsymbol{\tau}^b_{\text{srp}} = (\mathbf{x}^b_{CP} - \mathbf{x}^b_{CG}) \times \mathbf{F}^b_{\text{srp}}. \tag{11.15}$$

The center of pressure and the center of gravity are chosen in the same manner as they were for the aerodynamic drag torque.

Magnetic torque

The magnetic torque is created due to the spacecraft's electronics setting up a dipole that interacts with the Earth's magnetic field. The magnetic torque is given by

$$\boldsymbol{\tau}^b_{\text{mag}} = \left(D\sqrt{\frac{1}{3}} \cdot [1,1,1]^\intercal \right) \times \mathbf{B}^b, \tag{11.16}$$

where D is a constant representing the size of the residual magnetic dipole, and $\mathbf{B}^b$ is the body frame vector of the Earth's magnetic field. The IGRF (International Geomagnetic Reference Field) model in the simulations represents the latter.

11.2.6 Reaction wheel dynamics

The angular momentum of the reaction wheels is given as [60]

$$\mathbf{H}^b_w = \mathbf{A}\mathbf{J}_w\mathbf{A}^\intercal(\boldsymbol{\omega}^b_{ib} + \mathbf{A}\boldsymbol{\omega}^w_{bw}) = \mathbf{A}\mathbf{J}_w\boldsymbol{\omega}^w_{iw} = \mathbf{A}\mathbf{J}_w\mathbf{A}^\intercal\boldsymbol{\omega}^b_{iw}. \tag{11.17}$$

We find the reaction wheel dynamics by applying Euler's second axiom,

$$\begin{aligned}
&\frac{{}^i d}{dt}\mathbf{H}^b_w = \frac{{}^b d}{dt}(\mathbf{A}\mathbf{J}_w\mathbf{A}^\intercal\boldsymbol{\omega}^b_{iw}) + \mathbf{S}(\boldsymbol{\omega}^b_{iw})\mathbf{H}^b_w \\
&= \mathbf{A}\mathbf{J}_w\mathbf{A}^\intercal\frac{{}^b d}{dt}\boldsymbol{\omega}^b_{iw} + \mathbf{S}(\mathbf{A}\boldsymbol{\omega}^w_{iw})(\mathbf{A}\mathbf{J}_w\boldsymbol{\omega}^w_{iw}) = \mathbf{A}\mathbf{J}_w\mathbf{A}^\intercal\frac{{}^b d}{dt}\boldsymbol{\omega}^b_{iw} \\
&= \mathbf{A}\mathbf{J}_w\mathbf{A}^\intercal(\frac{{}^b d}{dt}\boldsymbol{\omega}^b_{ib} + \mathbf{A}\frac{{}^w d}{dt}\boldsymbol{\omega}^w_{bw}) = \boldsymbol{\tau}^b_u = \mathbf{A}\boldsymbol{\tau}^w_u,
\end{aligned} \tag{11.18}$$

where we have used that

$$\mathbf{S}(\mathbf{A}\boldsymbol{\omega}^w_{iw})(\mathbf{A}\mathbf{J}_w\boldsymbol{\omega}^w_{iw}) = 0 \tag{11.19}$$

when the inertia of the reaction wheels are equal.

11.2.7 Attitude error dynamics

The attitude error variables are defined as

$$\mathbf{q}_e = \mathbf{q}_d^{-1} \otimes \mathbf{q}_{ob} = \begin{bmatrix} \eta_d & \boldsymbol{\epsilon}_d^\intercal \\ -\boldsymbol{\epsilon}_d & \eta_d\mathbf{I}_{3x3} - \mathbf{S}(\boldsymbol{\epsilon}_d) \end{bmatrix} \mathbf{q}_{ob} \tag{11.20}$$

where η_d and $\boldsymbol{\epsilon}_d$ are the scalar and vector part of the desired quaternion $\mathbf{q}_d$, respectively, and

$$\boldsymbol{\omega}_e^b = \boldsymbol{\omega}_{ob}^b - \boldsymbol{\omega}_d^b = \boldsymbol{\omega}_{ib}^b - \mathbf{R}_o^b \boldsymbol{\omega}_{io}^o - \boldsymbol{\omega}_d^b, \tag{11.21}$$

where $\boldsymbol{\omega}_d^b$ represents the desired angular velocity. We find the angular velocity error dynamics by differentiating Equation (11.21) with respect to time. Specifically,

$$\begin{aligned} \frac{{}^b d}{dt}(\mathbf{R}_o^b \boldsymbol{\omega}_{ib}^o) &= \frac{{}^b d}{dt}(\mathbf{R}_o^b)\boldsymbol{\omega}_{io}^o + \mathbf{R}_o^b \frac{{}^b d}{dt}(\boldsymbol{\omega}_{io}^o) \\ &= -\mathbf{S}(\boldsymbol{\omega}_{ob}^b)\mathbf{R}_o^b \boldsymbol{\omega}_{io}^o - \mathbf{R}_o^b \mathbf{S}(\mathbf{R}_b^o \boldsymbol{\omega}_{ob}^b)\boldsymbol{\omega}_{io}^o, \end{aligned} \tag{11.22}$$

where we have used that the orbit is constant over time. Equation (11.18) can be used to rewrite (11.9) by taking advantage of (11.7),

$$\begin{aligned} \mathbf{J}_s \frac{{}^b d}{dt}\boldsymbol{\omega}_{ob}^b &= -(\mathbf{A}\mathbf{J}_s\mathbf{A}^\intercal \frac{{}^b d}{dt}\boldsymbol{\omega}_{ib}^b + \mathbf{A}\mathbf{J}_w \frac{{}^w d}{dt}\boldsymbol{\omega}_{bw}^w) - \mathbf{S}(\boldsymbol{\omega}_{ib}^b)\mathbf{H}_s^b \\ &+\boldsymbol{\tau}_{\text{mtq}}^b + \boldsymbol{\tau}_{\text{ext}}^b = -\mathbf{A}\boldsymbol{\tau}_u^w - \mathbf{S}(\boldsymbol{\omega}_{ib}^b)\mathbf{H}_s^b + \boldsymbol{\tau}_{\text{mtq}}^b + \boldsymbol{\tau}_{\text{ext}}^b \end{aligned} \tag{11.23}$$

From (11.20), (11.21), (11.22), and (11.23), the error dynamics become

$$\dot{\mathbf{q}}_e = \frac{1}{2}\mathbf{T}(\mathbf{q}_e)\boldsymbol{\omega}_e^b, \tag{11.24}$$

$$\begin{aligned} \mathbf{J}_s \frac{{}^b d}{dt}\boldsymbol{\omega}_e^b &= -\mathbf{S}(\boldsymbol{\omega}_{ib}^b)\mathbf{H}_s^b - \mathbf{A}\boldsymbol{\tau}_u^w + \boldsymbol{\tau}_{\text{mtq}}^b + \boldsymbol{\tau}_{\text{ext}}^b \\ &+\mathbf{J}_s \mathbf{S}(\boldsymbol{\omega}_{ob}^b)\mathbf{R}_o^b \boldsymbol{\omega}_{io}^o + \mathbf{J}_s \mathbf{R}_o^b \mathbf{S}(\mathbf{R}_o^b \boldsymbol{\omega}_{ob}^o)\boldsymbol{\omega}_{io}^o - \mathbf{J}_s \frac{{}^b d}{dt}\boldsymbol{\omega}_d^b. \end{aligned} \tag{11.25}$$

11.3 Control design

This section presents the control algorithms we use on the spacecraft's actuators. The primary actuator for attitude control will, in this chapter, be the reaction wheels. A momentum dumping controller counteracts momentum building up in the reaction wheels. We use the magnetorquers to provide the external torque required for the momentum dumping.

11.3.1 Momentum dumping controller

The momentum dumping control law is given as [36]

$$\boldsymbol{\tau}_{\text{mtq}} = \mathbf{m}^b \times \mathbf{B}^b = \left(\frac{k_m}{\|\mathbf{B}^b\|_2} \left(\mathbf{h}_e^b \times \mathbf{B}^b \right) \right) \times \mathbf{B}^b, \tag{11.26}$$

where $\mathbf{m}^b$ is the magnetic moment, k_m is a positive constant, and $\mathbf{h}_e^b$ is the error in angular momentum for the reaction wheels, given as

$$\mathbf{h}_e^b = \mathbf{A}\mathbf{J}_w(\boldsymbol{\omega}_{bw}^w - \boldsymbol{\omega}_{bw,\text{ref}}^w), \tag{11.27}$$

where $\boldsymbol{\omega}_{bw,\text{ref}}^w$ is the reference speed of the reaction wheels.

11.3.2 Generalized super-twisting algorithm (GSTA)

The generalized super-twisting algorithm is proposed here to control the attitude with the reaction wheels. The GSTA is a second-order sliding mode control algorithm robust to bounded time-varying disturbances, such as the environmental torques $\boldsymbol{\tau}_{\text{ext}}^b$. The GSTA is given as

$$\begin{aligned} \boldsymbol{\tau}_u^b &= (-1)\cdot(-\mathbf{k}_1\boldsymbol{\phi}(\boldsymbol{\sigma})_1 + \mathbf{z}), \\ \dot{\mathbf{z}} &= -\mathbf{k}_2\boldsymbol{\phi}(\boldsymbol{\sigma})_2, \\ \boldsymbol{\phi}_1(\boldsymbol{\sigma}) &= \lfloor\boldsymbol{\sigma}\rceil^{\frac{1}{2}} + \boldsymbol{\beta}\boldsymbol{\sigma}, \\ \boldsymbol{\phi}_2(\boldsymbol{\sigma}) &= \frac{1}{2}\lfloor\boldsymbol{\sigma}\rceil^0 + \frac{3}{2}\boldsymbol{\beta}\lfloor\boldsymbol{\sigma}\rceil^{\frac{1}{2}} + \boldsymbol{\beta}^2\boldsymbol{\sigma}, \end{aligned} \tag{11.28}$$

where $\mathbf{k}_1, \mathbf{k}_2$, and $\boldsymbol{\beta}$ are positive and constant positive controller gain vectors that are applied element-wise, $\boldsymbol{\sigma}$ is the sliding surface, and the function $\lfloor\cdot\rceil^x$ is defined as $\lfloor a\rceil^b = |a|^b sign(a)$, which is used element-wise when the argument a is a vector.

Surface for pointing

For pointing, we propose the sliding surface

$$\boldsymbol{\sigma}_p = \dot{\boldsymbol{\epsilon}}_e^b + \mathbf{K}\boldsymbol{\epsilon}_e^b, \mathbf{K} > 0, \tag{11.29}$$

where $\boldsymbol{\epsilon}_e^b$ is the vector part of the error quaternion. On the sliding surface, $\boldsymbol{\sigma}_p = \mathbf{0}$, such that $\dot{\boldsymbol{\epsilon}}_e^b = -\mathbf{K}\boldsymbol{\epsilon}_e^b$, and thus the origin $\boldsymbol{\epsilon}_e^b = \mathbf{0}$ is asymptotically stable. As the unit quaternion is defined to have a length equal to one, the surface will have two asymptotically stable equilibrium points in $\boldsymbol{\epsilon}_e = \mathbf{0}, \eta_e = \pm 1$.

Surface for slewing

We use a sliding surface based on [75] for slewing, given as

$$\boldsymbol{\sigma}_s = \boldsymbol{\omega}_e^b - 2c_1\frac{\partial W}{\partial \eta_e}\boldsymbol{\epsilon}_e, \tag{11.30}$$

where c_1 is a positive constant, and W is a Lyapunov function candidate (LFC) chosen to be $W = 1 - |\eta_e|$. From this choice, the surface becomes

$$\boldsymbol{\sigma}_s = \boldsymbol{\omega}_e^b + 2c_1\ sgn(\eta_e)\boldsymbol{\epsilon}_e. \tag{11.31}$$

Note that the signum function is defined to be positive when evaluated at zero. Based on the proof in [75], a sketch of the proof showing asymptotic stability for the chosen sliding surface is as follows:

Differentiating the general LFC $\mathrm{W}(\eta_e)$ yields

$$\frac{d}{dt}W(\eta_e) = \frac{\partial W}{\partial \eta_e}\frac{\partial \eta_e}{\partial t} = \frac{\partial W}{\partial \eta_e}(-\frac{1}{2}\boldsymbol{\epsilon}_e^\intercal\boldsymbol{\omega}_e^b) = -c_1(\frac{\partial W}{\partial \eta_e})^2\boldsymbol{\epsilon}_e^\intercal\boldsymbol{\epsilon}_e, \tag{11.32}$$

where Equation (11.30) set to zero has been used to define $\boldsymbol{\omega}_e^b$. The time derivative of the LFC is negative definite for all $\boldsymbol{\epsilon}_e \neq \mathbf{0}$ as long as $\mathrm{W}(\eta_e)$ is chosen such that $\frac{\partial W}{\partial \eta_e}$ is always non-zero. The LFC

$$W(\eta_e) = 1 - |\eta_e|, \tag{11.33}$$

satisfies this constraint since $\frac{\partial W}{\partial \eta_e} = -sgn(\eta_e)$. The LFC is positive definite, and the time derivative

$$\frac{d}{dt}W(\eta_e) = -c_1(\frac{\partial W}{\partial \eta_e})^2 \boldsymbol{\epsilon}_e^\intercal \boldsymbol{\epsilon}_e = -c_1 \boldsymbol{\epsilon}_e^\intercal \boldsymbol{\epsilon}_e, \tag{11.34}$$

is negative definite, and from this, we can use Lyapunov's second method to conclude that the two equilibrium points of the quaternion representation ($\eta_e = \pm 1, \boldsymbol{\epsilon}_e = 0$) are asymptotically stable. This conclusion only holds when the signum function is defined as non-zero.

11.3.3 Sliding mode control (SMC)

Sliding mode control (SMC) is given as

$$\boldsymbol{\tau}_u^b = \mathbf{k}\ sgn(\boldsymbol{\sigma}), \tag{11.35}$$

where $\boldsymbol{\sigma}$ is the sliding surface, defined as for the GSTA, and $\mathbf{k}$ is a constant (positive) controller gain vector that is applied element-wise.

11.3.4 Proportional–derivative controller (PD)

The PD controller is given as [9]

$$\boldsymbol{\tau}_u^b = \mathbf{K}_d \boldsymbol{\omega}_e^b + \mathbf{K}_p \boldsymbol{\epsilon}_e \tag{11.36}$$

where $\mathbf{K}_d$ and $\mathbf{K}_p$ are constant (positive definite) controller gain matrices, with numerical values to be chosen when tuning the controller.

11.4 Simulation

This section presents the numerical simulations based on spacecraft attitude control scenarios with two maneuvers: pointing and slewing. We compare the response of the controlled variables with the GSTA, SMC, and PD controller.

11.4.1 Setup

A 6U CubeSat model is chosen as the spacecraft's rigid body in this simulation. It has magnetorquers on all three body axes and four reaction wheels. Three reaction wheels are fixed separately on each of the three body axes, and a fourth is tilted such that the resulting torque has equal components in each axis in the body frame. The torque distribution matrix is given as

$$\mathbf{A} = \frac{1}{3}\begin{bmatrix} 3 & 0 & 0 & \sqrt{3} \\ 0 & 3 & 0 & \sqrt{3} \\ 0 & 0 & 3 & \sqrt{3} \end{bmatrix}. \tag{11.37}$$

The total inertia matrix and the reaction wheel inertia matrix are given as

$$\mathbf{J} = \begin{bmatrix} 0.0775 & 0.0002 & -0.0002 \\ 0.0002 & 0.1067 & 0.0005 \\ -0.0002 & 0.0005 & 0.0389 \end{bmatrix} \text{kg} \cdot \text{m}^2, \quad \mathbf{J}_w = I_w \mathbf{I}_{4\text{x}4}, \tag{11.38}$$

where $I_w = 2.1 \cdot 10^{-4}$ kg m^2 is the inertia of a single reaction wheel, which are all set to be identical. $\mathbf{J}_s$ is found by combining (11.37) and (11.38) with (11.7).

Parameters used in simulations are shown in Tables 11.1-11.5.

Table 11.1: Orbital elements of initial orbit

Orbital element	Value
Semimajor axis	6852.2 km
Eccentricity	0.002
Inclination	97°
Right ascension of the ascending node	280°
Argument of perigree	0°
True anomaly	90°

Table 11.2: Physical parameters

Physical parameter	Value
CubeSat mass	7 kg
CubeSat surface area ($A_{\text{srp}}, A_{\text{drag}}$)	0.06 m^2
Earth Radius	$6.371 \cdot 10^6$ m
Standard grav. parameter, Earth (μ)	$3.986 \cdot 10^{14}$ m^3/s^2
Atmospheric density (ρ)	$1.7741 \cdot 10^{-12}$ kg/m^3
Drag coefficient (C_D)	2.1
Solar constant (F_{srp})	1367 W/m^2
Speed of light in vacuum (c)	$3{\cdot}10^8$ m/s
Reflectance, satellite (l)	0.2
Angle of sunlight on the satellite (α)	0°
Residual magnetic dipole (D)	$1{\cdot}10^{-2}$

Table 11.3: Saturation bounds

Saturation bounds	Value
Reaction wheel angular velocity	$\pm$ 5000 RPM
Reaction wheel angular velocity, rate	$\pm$ $4.5 \cdot 10^3$ rad/s^2
Reaction wheel input torque	$\pm$ $3 \cdot 10^{-3}$ N·m
Magnetorquer magnetic moment	$\pm$ $5 \cdot 10^{-1}$ A·m^2

The orbit represented by the parameters in Table 11.1 is a commonly chosen Low-Earth-Orbit (LEO) for remote sensing. In Table 11.4, the reaction wheel jittering is modeled based on friction and speed resolution in the reaction wheels, while the $\boldsymbol{\omega}_{ib}^b$ noise is due to unwanted thermal and structural effects. Perfect attitude knowledge is assumed.

Table 11.4: Noise

Noise	Value
Reaction wheel jittering	3 RPM
$\boldsymbol{\omega}_{ib}^{b}$ noise	$6.9813{\cdot}10^{-8}$ rad/s

Table 11.5: Controller gains

Controller gain	Value
k_m (mtq)	$1.5{\cdot}10^{-2}$
$\mathbf{K}$ (surface)	$0.15 \cdot \mathbf{I}_{3x3}$
$\mathbf{k}_1$ (GSTA)	$\frac{2.5}{1000}\mathbf{J}_s \cdot \mathbf{1}_{3x1}$
$\mathbf{k}_2$ (GSTA)	$(2 \cdot 10^{-8})\mathbf{1}_{3x1}$
$\boldsymbol{\beta}$ (GSTA)	$15 \cdot \mathbf{1}_{3x1}$
$\mathbf{K}_p$ (PD, point)	$\mathbf{J}_s$
$\mathbf{K}_p$ (PD, slew)	$0.01\mathbf{J}_s$
$\mathbf{K}_d$ (PD)	$2.7\mathbf{J}_s$
$\mathbf{k}$ (SMC, point)	$0.01\mathbf{J}_s \cdot \mathbf{1}_{3x1}$
$\mathbf{k}$ (SMC, slew)	$\frac{2}{1250}\mathbf{J}_s \cdot \mathbf{1}_{3x1}$
c_1 (GSTA, slew)	2
c_1 (SMC, slew)	$2 \cdot 10^{-3}$

For the momentum dumping controller, the reference reaction wheel speed $\boldsymbol{\omega}_{bw,\text{ref}}^{w}$ is set to $2000 \cdot \begin{bmatrix}1 & 1 & 1 & -\sqrt{3}\end{bmatrix}^\intercal$ RPM. At this point, the angular momentum the reaction wheels creates will be net zero about the axes in $\{b\}$.

11.4.2 Performance measures

The performance is measured using stationary signals' root-mean-square error (RMSE). We define the signal as stationary when it has settled, meaning it stays inside a given error band around the target value. The error band is defined to be $\pm 0.5^\circ$ for pointing, and $\pm 4 \cdot 10^{-4}$ rad/s for slewing. The settling time is the time it takes from applying the desired reference value to the error band being reached, provided that it stays within the error band. Each channel's steady-state error (SSE) is measured at the end of each simulation.

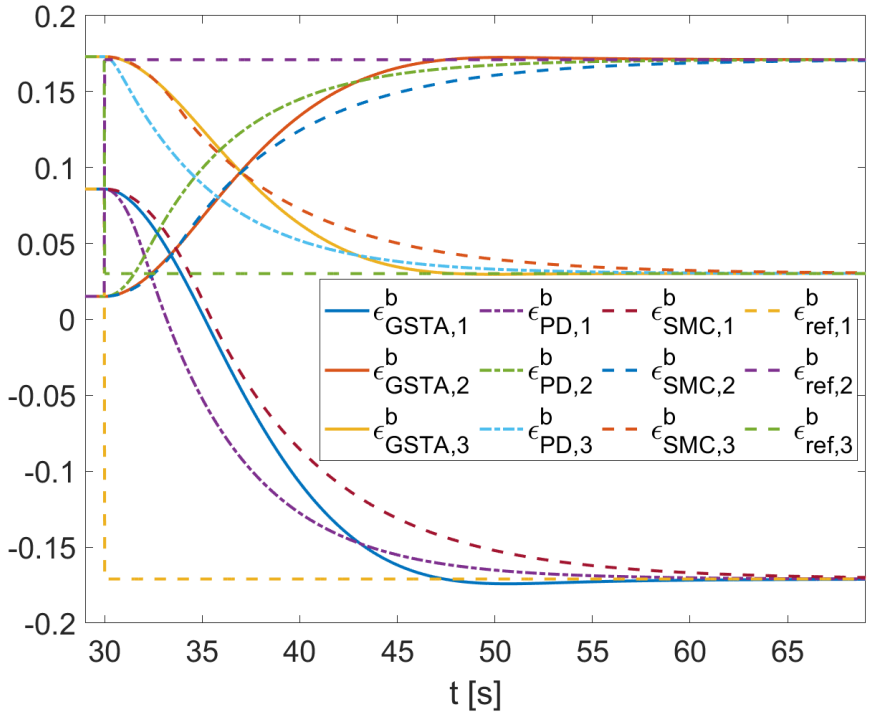

Figure 11.1: Pointing: Plot of the vector part of $\mathbf{q}$ and $\mathbf{q}_d$.

11.4.3 Pointing

Pointing is a fixed-vector orientation towards a desired attitude. Both the GSTA and the SMC use the surface defined in Equation (11.29).

Table 11.6: Pointing performance

	Settling time	RMSE	SSE
GSTA	[15.9, 15.7, 15.2]s	[4.80, 3.14, 2.43]*	[0.5, 0.0, 0.0]*
PD	[21, 20, 18.4]s	[4.24, 4.22, 4.24]*	[0.5, 0.0, 0.1]*
SMC	[29.1, 27.2, 25.8]s	[4.93, 4.91, 4.88]*	[0.6, 0.0, 0.1]*

The star (*) in Table 11.6 denotes 10^{-2} angular degrees (°). Figures 11.1, 11.2, and 11.3 are centered around the transient period of the control. Figures 11.4, 11.5, and 11.6 are plotted over a longer time to show the effects of attitude control and momentum dumping controller on the reaction wheel speed. For pointing, the objective is illustrated in Figure 11.1, where a slight overshoot can be seen in the GSTA response. In the error variables shown in Figure 11.2, it can be seen that this overshoot does not result in the signal escaping the error band, indicating that the performance of GSTA is better than that of PD controller and SMC. It is also

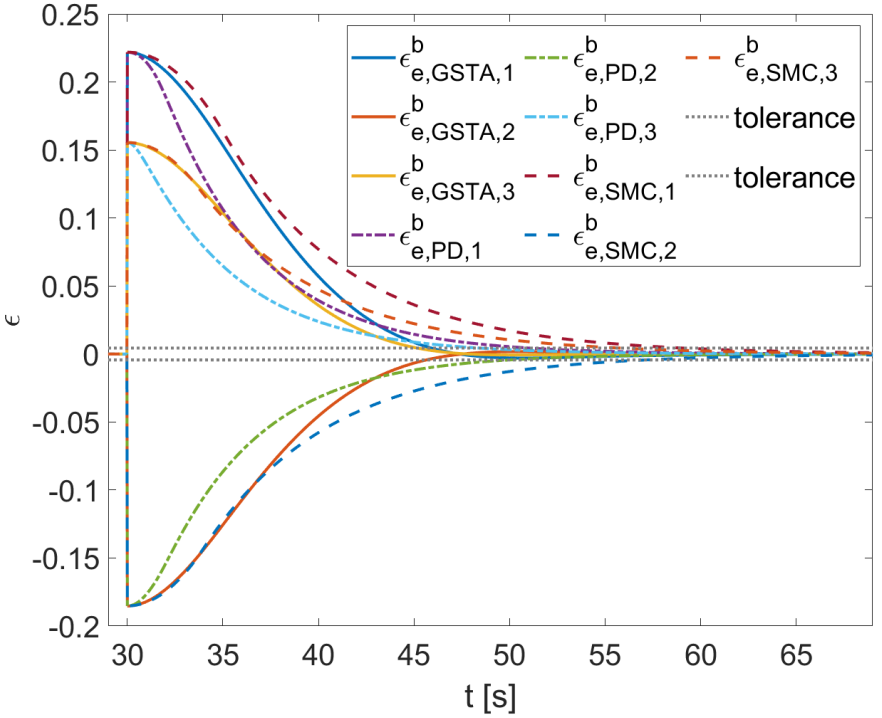

Figure 11.2: Pointing: Plot of the vector part of $\mathbf{q}_e$.

performing better with respect to settling time across all channels: between four and five seconds for the PD controller and over 10 seconds for the SMC.

As seen in Figure 11.2, the PD controller converges fastest initially, but the GSTA tracks the desired attitude better when the signals approach the desired state. The RMSE values are slightly better for GSTA than PD and SMC along the second and third channels, while the PD is the best along the first. The SSE values are similar for all three controllers.

The angular velocity response shown in Figure 11.3 also highlights the performance difference between the PD controller and GSTA, where the curve of the latter follows a gentler slope. The angular velocity of the reaction wheels, as shown in Figure 11.4, are returned to their initial values after the reference changes at 30 seconds, except when using the PD controller. The magnetorquer response is similar for all three control laws, as seen in figure 11.6. The torque applied by the GSTA has a sharper slope than the SMC, as seen in Figure 11.5, causing a lot more torque to be applied to the reaction wheels after the system has settled. The PD controller has a higher peak and varies more than GSTA before and after the transient period.

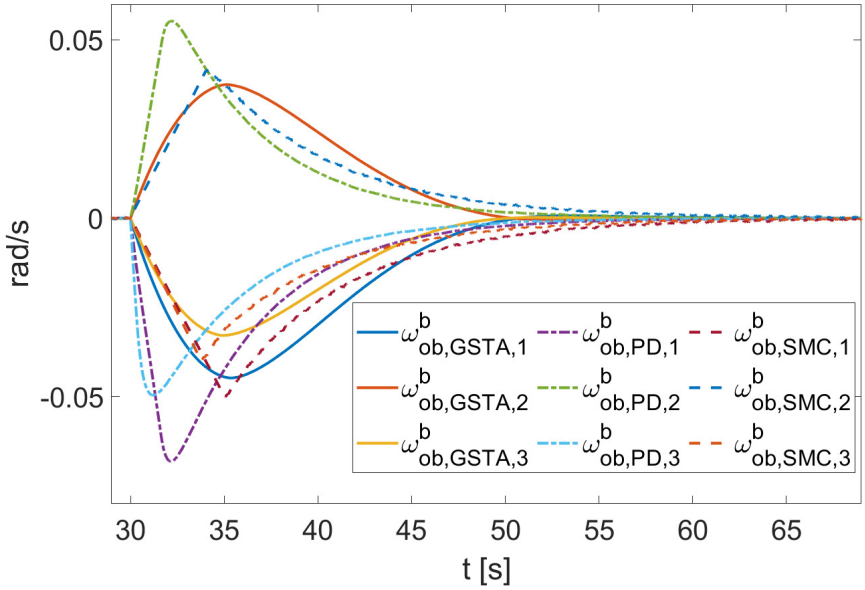

Figure 11.3: Pointing: Plot of $\boldsymbol{\omega}^b_{ob}$.

11.4.4 Slewing

When the spacecraft performs a slew maneuver, the angular velocity of the $\{b\}$ relative to $\{o\}$ is non-zero and constant. We choose a desired angular velocity about the y-axis in this simulation. The GSTA and the SMC use the surface defined in Equation (11.31) for slewing.

Table 11.7: Slewing performance

	Settling time	RMSE	SSE
GSTA	[-1, 3.63, -1]s	[3.91, 4.93, 4.95]*	[5.05, 0.30, 4.40]*
PD	[-1, 1.3, -1]s	[4.78, 5.32, 5.33]*	[3.73, 0.66, 5.08]*
SMC	[-1, 7.28, -1]s	[7.88, 11.1, 8.21]*	[5.99, 5.30, 11.7]*

The star (*) in Table 11.7 denotes 10^{-5} rad/s, and -1 indicates channels that start inside the error band and never leave and therefore are permanently settled.

Figure 11.7 shows the slew maneuver objective. In general, the GSTA outperforms the SMC when considering settling time. However, the PD controller performs better, as shown clearly in Figure 11.7 and Table 11.7. The GSTA uses 3.63 seconds, while the SMC uses 7.28 seconds to settle about the y-axis. For comparison, the PD controller uses just 1.3 seconds. Note that the inclination of the sliding surface used for slewing, the positive definite constant c_1 from Equation (11.31), is different for the GSTA and the SMC algorithm, as specified in Table 11.5. This is due to the SMC algorithm overshooting the reference if the chosen value is too

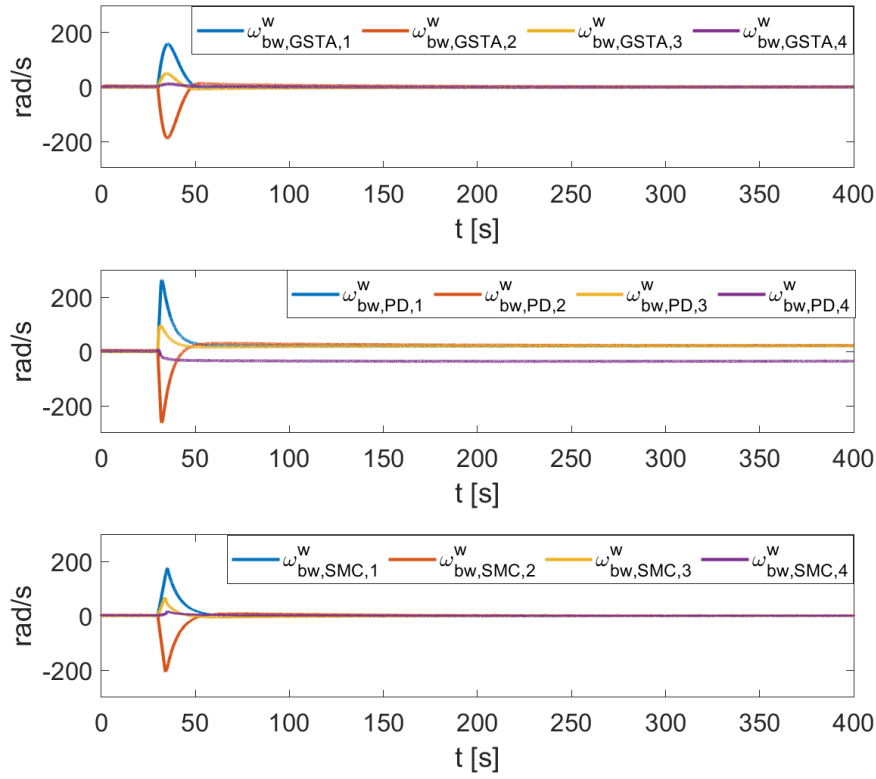

Figure 11.4: Pointing: Plot of $\boldsymbol{\omega}^{w}_{bw} - \boldsymbol{\omega}^{w}_{bw,\mathrm{ref}}$.

high. By decreasing c_1 from the value set for GSTA, the SMC manages to control the system. Furthermore, the GSTA performs well with the given c_1 values.

It is possible to increase the SMC gain to lower the settling time, but this would increase the RMSE values, and the SMC might be unable to settle within the error band in a chosen period. Even with the current values, the SMC has a significantly higher RMSE than the GSTA and PD controller for slewing.

Increasing the gain for the GSTA to lower the settling time would also increase the RMSE value, which is slightly better than the values of the PD controller with the current parameters.

For reaction wheel speed, it can be seen in Figure 11.8 that the momentum dumping controller uses a longer time to reach the initial speed values compared to pointing, as seen in Figure 11.4. To improve this, the reference angular momentum must be updated in a slew maneuver, as shown in [33]. Figure 11.10 shows that the magnetorquers produce high-frequency signals as in pointing, but of a different shape than those in Figure 11.6 as it counteracts a distinct change in the wheel

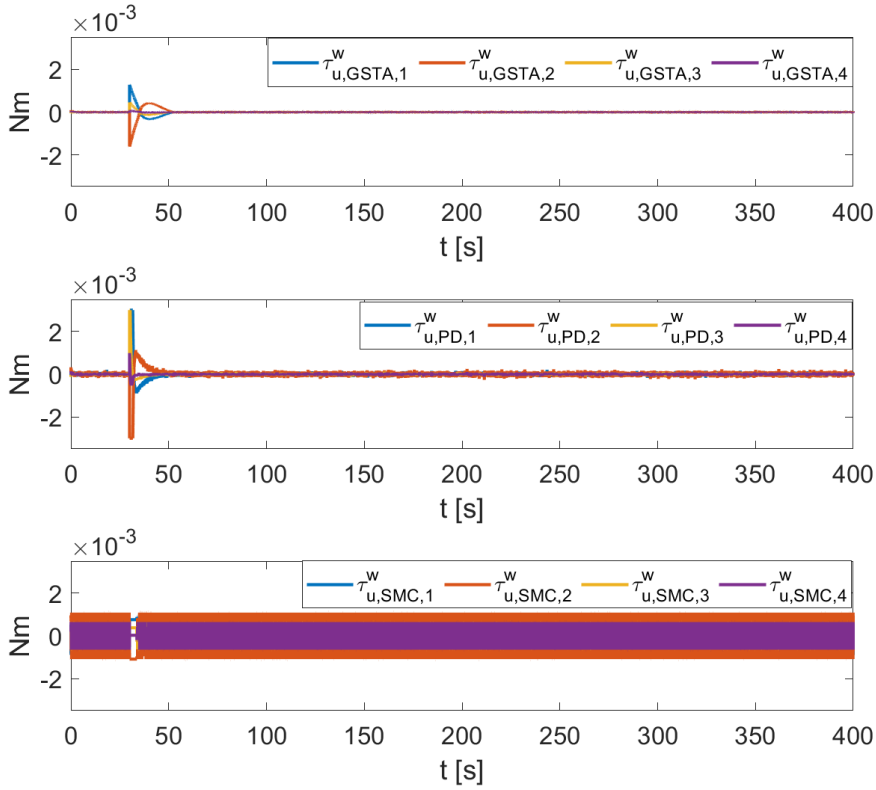

Figure 11.5: Pointing: Plot of $\boldsymbol{\tau}_u^w$.

speed. The torque plot for the attitude control algorithms, Figure 11.9, shows that the GSTA has a spike around the change in reference at 60 seconds, while the amplitude of the SMC signal has a fixed maximum value. Note that the peak value of the PD controller is significantly higher than the peak of the GSTA, and the signal is more contaminated by noise for the PD controller, as shown in Figure 11.5.

11.5 Conclusion

In this chapter, we have studied the performance of three different control algorithms applied to the attitude control of a spacecraft actuated with reaction wheels: the GSTA, SMC, and PD controller. The simulation results show that the GSTA control chatter is significantly reduced compared to SMC. Overall attitude control performance is improved when comparing GSTA to SMC in a slew maneuver. GSTA displays similar accuracy as the PD controller under the given conditions

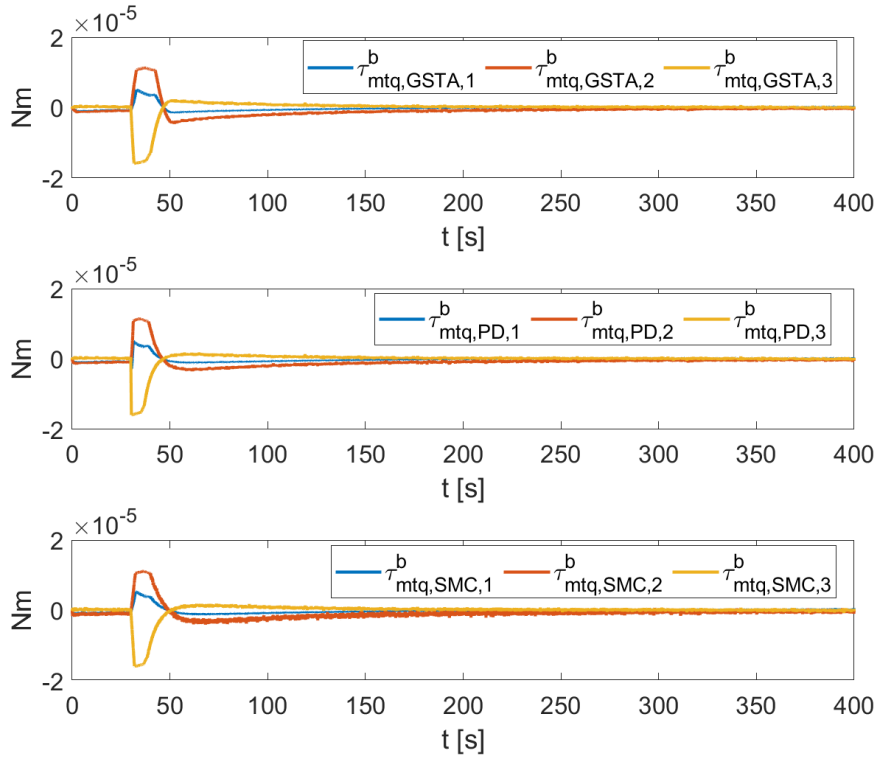

Figure 11.6: Pointing: Plot of $\boldsymbol{\tau}^b_{\text{mtq}}$.

but with lower spikes and less chatter in the torque applied to the reaction wheels. The settling time for the GSTA is shorter for pointing but longer for slewing when compared to a well-tuned PD controller.

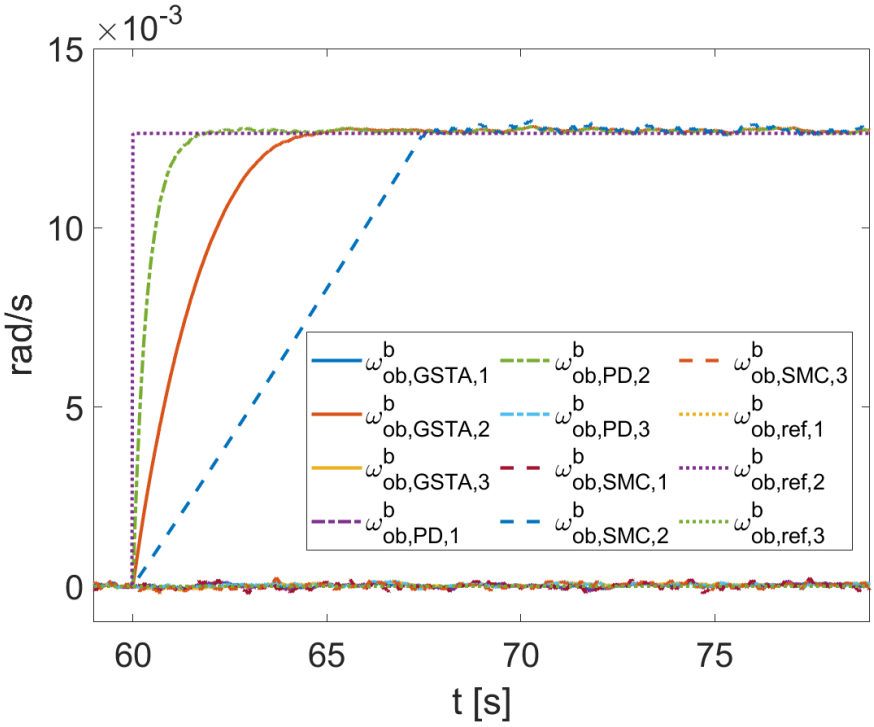

Figure 11.7: Slewing: Plot of $\boldsymbol{\omega}_{ob}^{b}$.

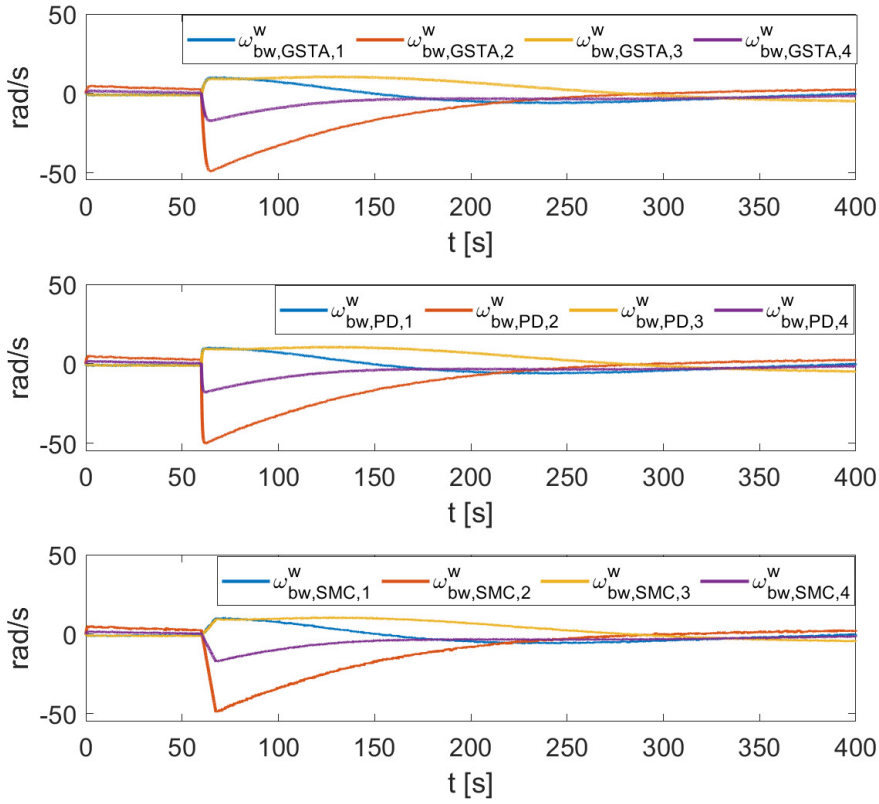

Figure 11.8: Slewing: Plot of $\boldsymbol{\omega}^{w}_{bw} - \boldsymbol{\omega}^{w}_{bw,\mathrm{ref}}$.

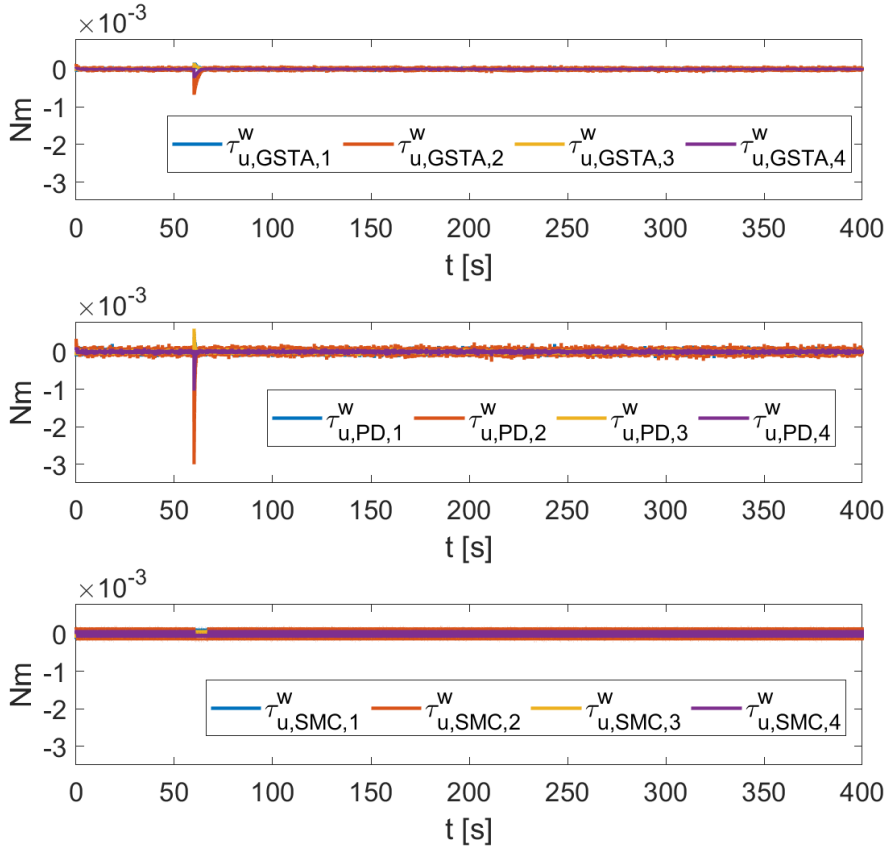

Figure 11.9: Slewing: Plot of $\boldsymbol{\tau}_u^w$.

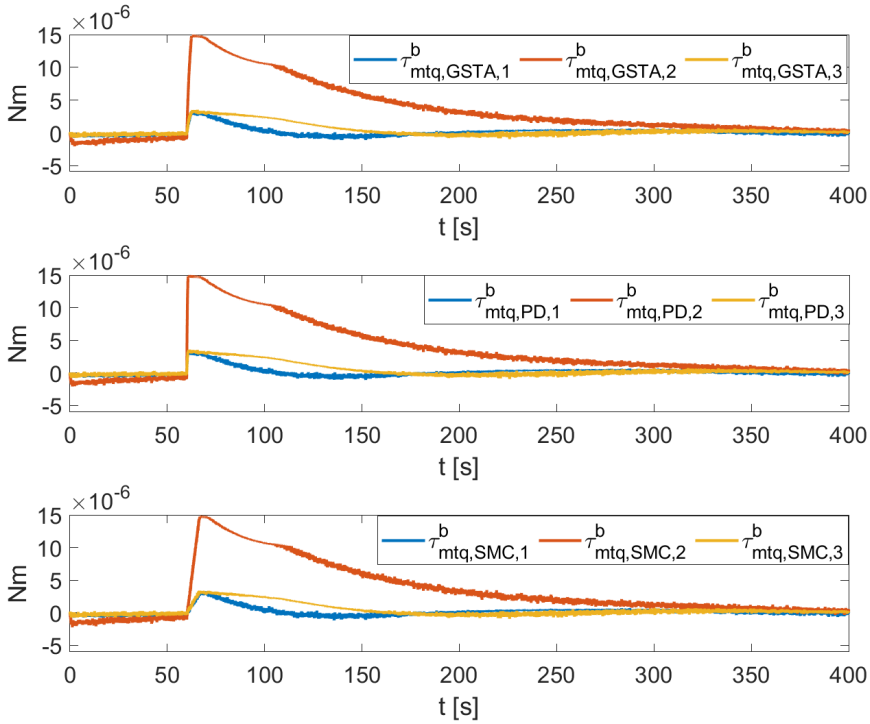

Figure 11.10: Slewing: Plot of $\boldsymbol{\tau}^b_{\text{mtq}}$.

Chapter 12

Accuracy of a slew maneuver for the HYPSO-1 satellite – in-orbit results

12.1 Introduction

During a slew maneuver, the body, in this chapter a satellite, rotates with a constant angular velocity relative to some frame. This is in contrast to point-to-point maneuvers, otherwise called pointing maneuvers or set-point regulation. Various papers discuss the slew maneuver in theory, see for example [33], [13], [76], [77], and Chapter 11. Possible benefits of using a slew maneuver have been discussed for imaging satellites; see for example [78]. Slew maneuvers for satellites are usually deployed for a specific reason, such as the need for a particular sensor, often a camera, to track an area of interest. The method can also compensate for the Earth's rotation, essentially pointing the satellite towards a fixed point on the ground. The latter control scheme is also known as "spotlight mode" [79].

The mission design for the HYPSO-1 [21] stipulates a single-axis slew maneuver to improve the data gathered by its payload. The HYPSO-1 CubeSat carries a push-broom hyperspectral imager as its main payload, which produces hyperspectral data cubes. The slew maneuver is intended to let subsets of the resulting image, henceforth called scan-lines, overlap with each other along track, so that techniques such as super-resolution can increase the utility of the downlinked data [80, 81].

This chapter contributes to the analysis of data collected during a slew maneuver performed by the HYPSO-1 satellite. The accuracy of the selected slew maneuver is evaluated in the context of images taken by the satellite in the first months of operation. The performance is measured by looking at raw data from the hyperspectral camera for two different images of the same location, showing how the HYPSO-1 slew maneuver can be used to decrease the ground sampling distance (GSD) and, consequently, increase the number of samples per area within the target region.

Section 12.2 describes the theory and methods used: the slew maneuver, including the coordinate frames, and the performance metrics are defined. Section 12.3 describes the hyperspectral imager of the HYPSO-1 mission and the observation campaign conducted to obtain the data used in this chapter. Section 12.4 presents

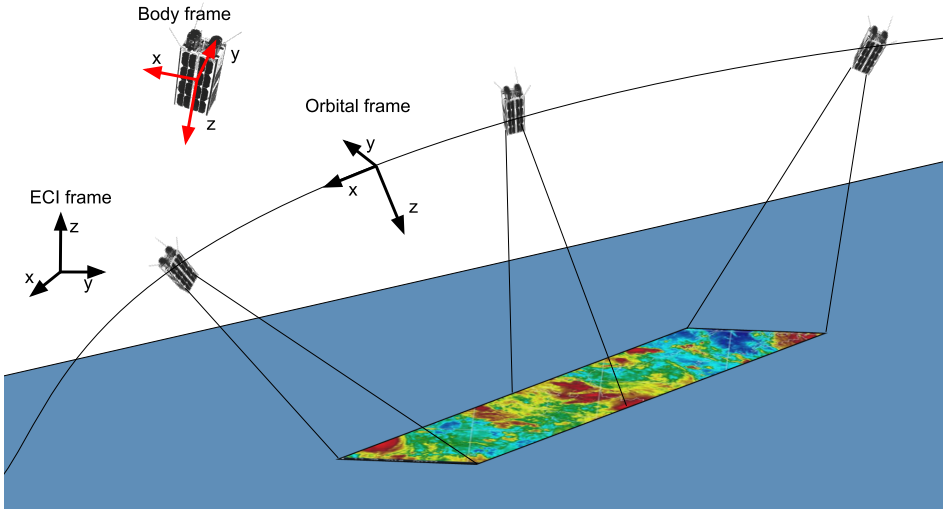

Figure 12.1: The HYPSO-1 slew maneuver. Three coordinate frames are depicted: the body frame, the orbital frame (the LVLH frame), and the inertial (ECI) frame. The satellite moves from right to left in the figure as it images the area of interest.

the data from the campaign, with accompanying calculations and the evaluation based on the methods introduced in Section 12.2. The results are discussed in Section 12.5, and Section 12.6 concludes the chapter.

12.2 Theory

Three coordinate frames are relevant to the slew maneuver: the inertial reference frame, i, the orbital reference frame, o, and the satellite body frame, b, see Figure 12.1. For the satellite body frame, the axes coincide with the main axes of inertia of the satellite, with, most notably, the z-axis pointing out through the side where the hyperspectral imager is pointing. The orbital reference frame is a local vertical, local horizontal (LVLH) reference frame with the z-axis pointed towards nadir. The x-axis of the orbital reference frame points in the velocity direction, and the y-axis completes the right-handed coordinate system. The LVLH frame can then be expressed as

$$\hat{\mathbf{x}}_o^i = \frac{\mathbf{v}^i}{||\mathbf{v}^i||}, \quad \hat{\mathbf{z}}_o^i = -\frac{\mathbf{r}^i}{||\mathbf{r}^i||}, \quad \hat{\mathbf{y}}_o^i = \frac{\hat{\mathbf{z}}_o^i \times \hat{\mathbf{x}}_o^i}{||\hat{\mathbf{z}}_o^i \times \hat{\mathbf{x}}_o^i||}, \tag{12.1}$$

where $\hat{\mathbf{x}}_o^i$, $\hat{\mathbf{y}}_o^i$, and $\hat{\mathbf{z}}_o^i$ denote the orthogonal unit vectors for the LVLH reference frame, $\mathbf{r}^i$ and $\mathbf{v}^i$ are the position and velocity vectors represented in the inertial

frame, respectively, and $\times$ is the vector cross product, required for completing the right-handed coordinate system.

During the slew maneuver, the satellite's angular velocity relative to the orbit frame is controlled. This angular velocity can be calculated as [18]

$$\boldsymbol{\omega}_{ob}^{b} = \boldsymbol{\omega}_{ib}^{b} - \boldsymbol{\omega}_{io}^{b} = \boldsymbol{\omega}_{ib}^{b} - \mathbf{R}_{i}^{b}\boldsymbol{\omega}_{io}^{i}, \tag{12.2}$$

where $\boldsymbol{\omega}_{io}^{b}$ is the angular velocity of the orbit frame relative to the inertial frame, $\boldsymbol{\omega}_{ib}^{b}$ is the angular velocity of the body frame relative to the inertial frame, both represented in body frame and $\mathbf{R}_{i}^{b}$ is the rotation matrix from orbit frame to body frame. The angular velocity of the orbit frame relative to the inertial frame, represented in the intertial frame, $\boldsymbol{\omega}_{io}^{i}$, is defined in [19] as

$$\boldsymbol{\omega}_{io}^{i} = \frac{\mathbf{r}^{i} \times \mathbf{v}^{i}}{(\mathbf{r}^{i})^{\intercal}\mathbf{r}^{i}}. \tag{12.3}$$

Equation (12.3) is changed slightly compared to [19] because the quaternion between the inertial and the body frame is available in the telemetry, making it possible to compute $\mathbf{R}_{i}^{b}$ directly.

Note that (12.2) is necessary since $\boldsymbol{\omega}_{ob}^{b}$ is not directly measured, as the IMU will measure $\boldsymbol{\omega}_{ib}^{b}$. Using the estimated position and velocity, $\mathbf{r}^{i}$ and $\mathbf{v}^{i}$, in addition to the estimated values for $\boldsymbol{\omega}_{ib}^{b}$ based on sensor measurements, we can find an estimate for $\boldsymbol{\omega}_{ob}^{b}$ through the relationships in (12.2) and (12.3). Maneuvers on the HYPSO-1 satellite are implemented using PD controllers, see e.g., [9].

For the accuracy measurements, we use a root-mean-square deviation (RMSD) measure, for convenience, given here as

$$RMSD = \sqrt{\frac{1}{T}\sum_{t=1}^{T}(x_{\mathrm{ref},t} - x_{t})^{2}}, \tag{12.4}$$

where T is the number of time steps, x_t is the reference value at the given time step and $x_{\mathrm{ref},t}$ is the corresponding reference value. For attitude accuracy, the "root square deviation" part of (12.4) is replaced, resulting in

$$\mathrm{Accuracy}_{\mathrm{quaternion}} = \frac{1}{T}\sum_{t=1}^{T}\arccos\left(|\mathbf{q}_{t}^{\intercal}\mathbf{q}_{\mathrm{ref},t}|\right), \tag{12.5}$$

where $\arccos\left(|\mathbf{q}_{t}^{\intercal}\mathbf{q}_{\mathrm{ref},t}|\right)$ is a distance metric on SO(3) [28], and $\mathbf{q}_t$ and $\mathbf{q}_{\mathrm{ref},t}$ are the quaternion and quaternion reference for a given time step, respectively.

There exist several spatial resolution metrics to characterize imagery [82]. Among them is the ground sampling distance (GSD), which is expected to be decreased by the slewing maneuver. [82] describes GSD as *pixel pitch projected onto ground plane*. Pixel pitch is the distance from the pixel center to the pixel center of two consecutive pixels in an image. For a push broom scanning system, GSD can be drastically different in the two dimensions of an image, along-track and across-track. This chapter focuses on along-track GSD.

12.3 Experimental setup

The the attitude control system of the HYPSO-1 satellite, based on the NanoAvionics M6P satellite bus, is equipped with reaction wheels and magnetorquers. HYPSO-1 is a 6U CubeSat ($10 \times 20 \times 30$ cm) with about 7 kg mass. The reaction wheels are the main actuators used for attitude control, meaning they produce the torque required to perform the pointing of the hyper-spectral imager towards targets on the ground, and to perform the slewing maneuver. The magnetorquers are used to de-saturate the reaction wheels. For more info on the imager itself, see [83].

There are several ways to change the GSD, for example, by changing the framerate. Here, the framerate is kept constant to inspect the impact of the slewing maneuver itself.

Two images targeting the same location are taken. Both images are captured when HYPSO-1 passes over the location of interest close to zenith. One image is captured using a nadir pointing maneuver, and the other using a slewing maneuver. For the nadir pointing maneuver, the reference was given in terms of a unit quaternion as $\mathbf{q}_b^o = [0.99871, -0.036528, 0.035297, 0]^\intercal$, specifying body frame orientation relative to the orbit frame. Note that the unit quaternion is denoted with the scalar part first, followed by the three components that make up the vector part. Also note that the pointing is not precisely nadir, but offset by about 5.8°. For brevity, the maneuver will still be referred to as the nadir pointing maneuver for the remainder of this chapter.

The angular velocity about the orbit frame y-axis, the reference for the slew maneuver, is given in terms of initial and final nadir angle of 10° and −10°. A slew duration of 43.45 seconds yields an angular velocity reference of $\boldsymbol{\omega}_{ob,\text{ref}}^b = [0, -0.0080329, 0]^\intercal$rad/s. Note that the reference differs from the nominal slew maneuver [21]. The start and end attitude of the slewing maneuver minimally affect the slew as the current implementation moves the transient periods of the angular velocity response outside the specified slew duration.

The nadir pointing image was taken on Saturday July 16 at 08:29:00 UTC, and the slewing maneuver image was taken on Sunday July 24 at 08:30:33 UTC. The target area for both of the maneuvers on the ground was a part of the coastal area where Romania meets the Black Sea. The full hyperspectral cubes are downlinked together with the Attitude Determination and Control System (ADCS) telemetry, containing the pose information of the satellite.

12.4 Results

Figure 12.2 shows the two RGB representations of the hyperspectral data cubes manually georeferenced over a topographic map, with the image taken by the nadir pointing maneuver to the left and the image taken during slew maneuver to the right. Note the difference in the area covered by the two maneuvers. A zoom-in of a common section of both images is shown in Figure 12.3, again with the nadir image on the left and the slewing maneuver on the right. The images have

been bilinearly resampled to the same scale. The contrast has been enhanced to differentiate between the details in each picture.

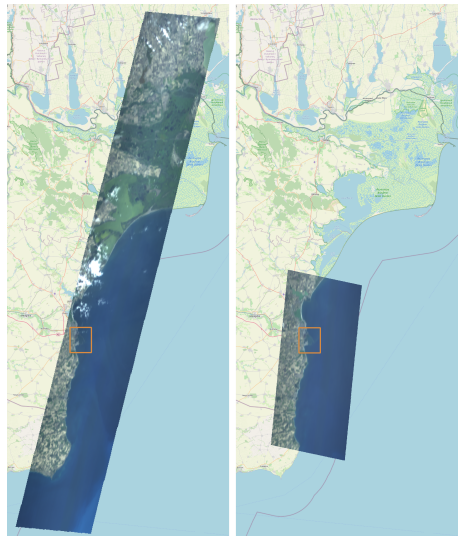

Figure 12.2: Nadir pointing (left) and slew (right) RGB images overlayed on topographical map (OpenStreetMap).

Figure 12.3: Nadir pointing (left) and slew (right) RGB images over the port of Constanța, Romania. Zoom-in on the images in Figure 12.2, bilinearly resampled to the same scale with the contrast enhanced.

Figure 12.4 shows the ADCS telemetry derived satellite pose in 3D space. The figure also shows a latitude-longitude grid representing the Earth with coordinates labels, the satellite orbital and ground track, the footprint of the images captured during the maneuver, and lines indicating the pointing direction during image capture. Note the difference in pointing direction between the two captures.

The telemetry includes the attitude represented as a unit quaternion $\mathbf{q}_b^i$, the angular velocity $\boldsymbol{\omega}_{ib}^b$, the position $\mathbf{r}^i$, and the velocity $\mathbf{v}^i$, all estimated onboard. For the nadir pointing capture, they are shown in Figure 12.5. The accuracy for the nadir pointing maneuver, using (12.5) is taken during the maneuver itself, as marked with the shaded area starting at time zero in the figures. The accuracy of

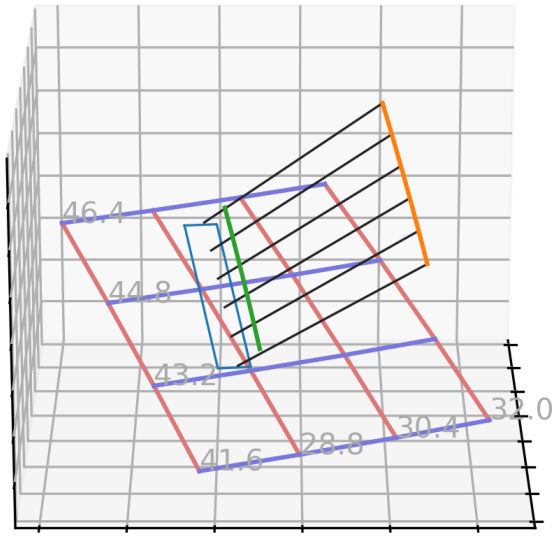

(a) Pointing geometry of nadir capture.

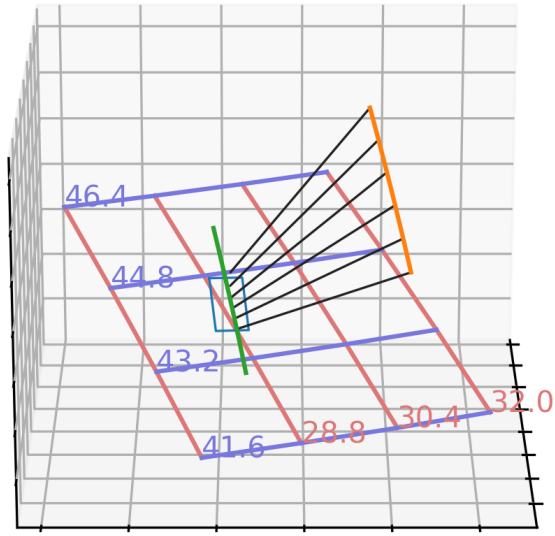

(b) Pointing geometry of slew capture.

Figure 12.4: Capture pointing geometry inferred from ADCS telemetry. Orange: Satellite track in ECI. Green: Satellite ground track. Blue rectangle: Image ground footprint. Black lines: z-axis direction at six uniformly spaced points in time during image capture. Light red: lines of constant longitude. Light blue: Lines of constant latitude.

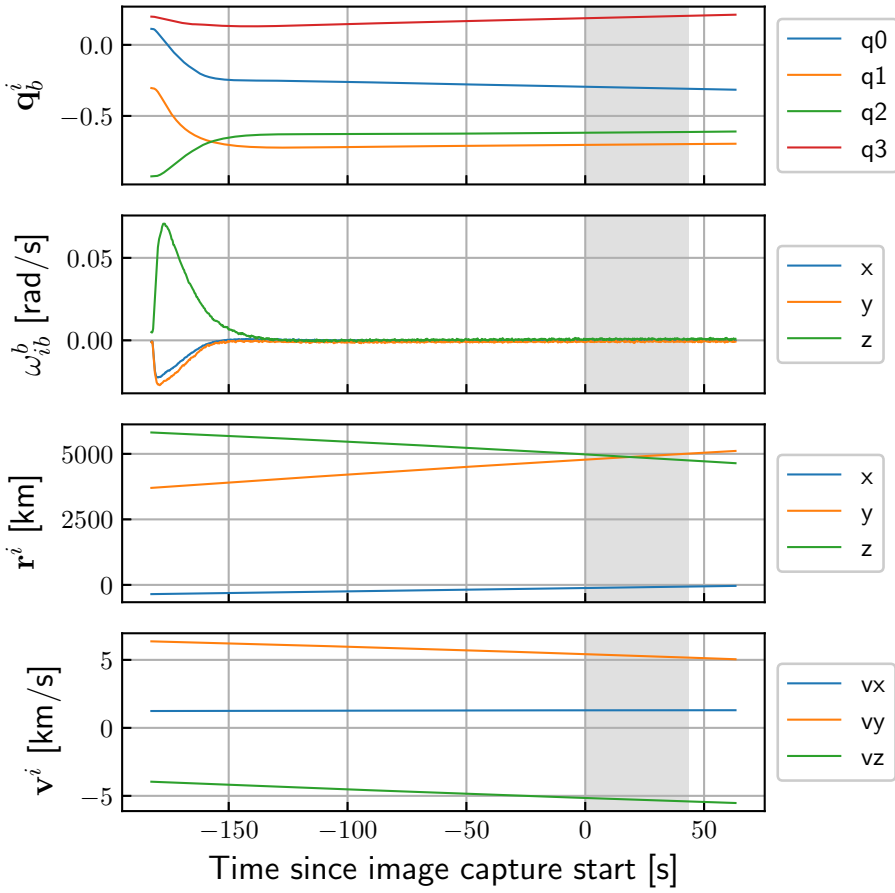

Figure 12.5: Telemetry from the spacecraft when pointing nadir. From top to bottom: $\boldsymbol{\omega}_{ib}^b$, $\mathbf{q}_b^i$, $\mathbf{r}^i$ and $\mathbf{v}^i$. Gray area indicates the time period when HYPSO-1 was recording data.

the nadir pointing maneuver is 0.00114 rad = 0.0653°, computed using (12.5), see Table 12.1.

Figure 12.6 shows the LVLH quaternion $\mathbf{q}_b^o$ during the image capture. To construct $\mathbf{q}_b^o$, $\mathbf{q}_o^i$ is inferred from the attitude information for $\mathbf{q}_b^i$, shown in Figure 12.5, and the definition of the LVLH coordinate system in (12.1).

The telemetry is displayed in Figure 12.7 for the slew maneuver. Note that the satellite prepares the slew maneuver by spinning up to a constant angular rate ahead of the defined start, thus moving the transient outside of the image capture period. $\boldsymbol{\omega}_{ob}^b$, the angular velocity of the body relative to the orbit frame, is computed based on the telemetry calculated by (12.2) and shown in Figure 12.8. Figure 12.8 also displays $\boldsymbol{\omega}_{io}^b$, albeit given in a different frame than in (12.3) for easier comparison to the other measurements in the figure. Note that $\boldsymbol{\omega}_{ib}^b$ and $\boldsymbol{\omega}_{ob}^b$

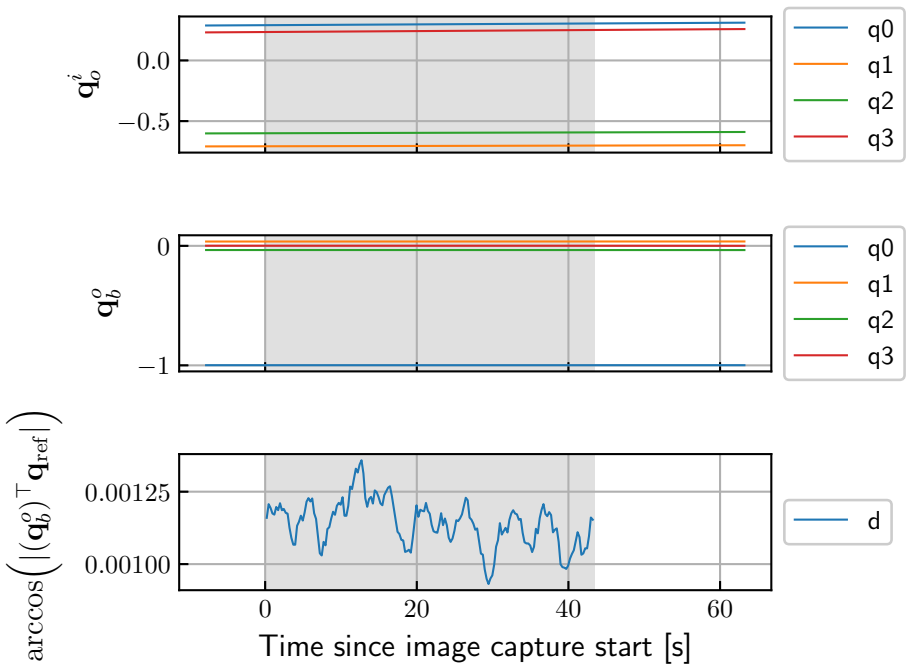

Figure 12.6: Attitude information from the nadir pointing maneuver during image capture. Quaternion representing the attitude of the axes of the LVLH frame relative to the inertial frame $\mathbf{q}_o^i$, the attitude of the body axes relative to the LVLH frame $\mathbf{q}_b^o$, and the distance from the reference quaternion used in (12.5), given in radians.

Table 12.1: Accuracy measurements for the two maneuvers.

Capture	**Accuracy**
Pointing	1.14 mrad
Slew	$[0.6347, 0.6752, 0.4551]^\intercal$ mrad/s

are very similar in Figure 12.8 due to the magnitude of $\boldsymbol{\omega}_{ib}^b$ being larger than that of $\boldsymbol{\omega}_{io}^b$. The last part of the figure shows the control error during the image capture period. The accuracy of the slew maneuver in terms of RMSD between the signal and the reference for the angular velocity during capture is shown in Table 12.1. It has three components, one for each component of the $\boldsymbol{\omega}_{ob}^b$ vector. The y-component is the axis around which the slew rotation takes place. That all three components are approximately the same magnitude signifies that the satellite manages to hold the reference in all three axes equally well.

Figure 12.9 shows the GSD along track in the center of the swath for the pointing and slewing captures. Noise in the telemetry translates into noise of the GSD estimation. Table 12.2 shows that the area covered by the image taken during the nadir pointing maneuver covers over twice as large an area as the image taken

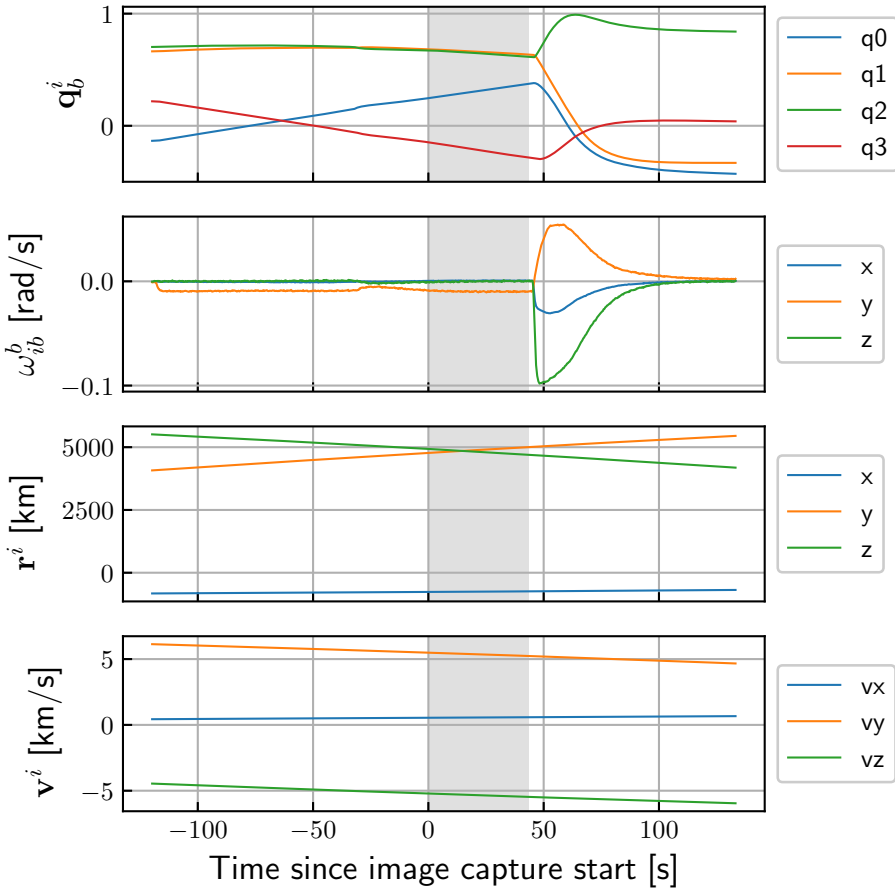

Figure 12.7: Telemetry from the ADCS before, during, and after the slew maneuver. From top to bottom: $\boldsymbol{\omega}_{ib}^b$, $\mathbf{q}_b^o$, $\mathbf{r}^i$, and $\mathbf{v}^i$. The gray area indicates the time period when HYPSO-1 was recording data.

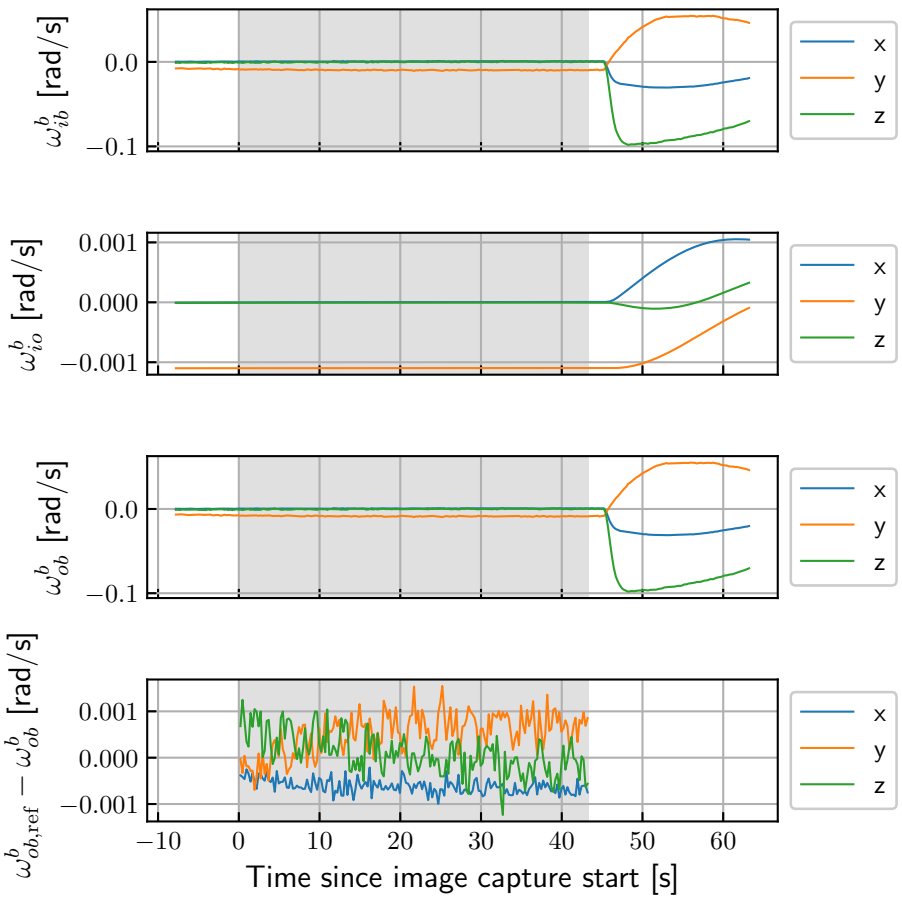

Figure 12.8: From top to bottom: $\boldsymbol{\omega}_{ib}^b$ from telemetry, $\boldsymbol{\omega}_{io}^b$ from (12.2) and (12.3), $\boldsymbol{\omega}_{ob}^b$ from (12.3), and the control error $\boldsymbol{\omega}_{ob,\mathrm{ref}}^b - \boldsymbol{\omega}_{ob}^b$. The gray area indicates the time period when HYPSO-1 was recording data.

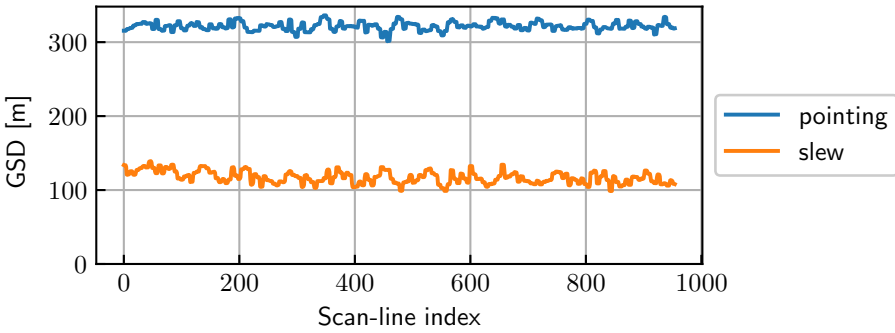

Figure 12.9: Ground-sampling-distance along the scanning direction for nadir pointing and slew maneuver.

Table 12.2: Figures of interest for the two captures.

Capture	**mean GSD**	**ca. Area [km^2]**	**Pixels in region**
Pointing	321.6 m	13726	1825
Slew	117.0 m	4959	5117

during the slewing maneuver. Table 12.2 also shows the mean GSD over all scan lines. The decrease from 321.6 m to 117.0 m signifies a 63.6% reduction. The fourth column in Table 12.2 shows how many pixel samples are contained in the region bounded by the orange rectangle shown in Figure 12.2, containing an area of 192 km^2. The region contains 64.3% less samples for the image taken during pointing compared to slewing. The increased density of pixels correlates with an increase in the signal, or the amount of light collected, per unit area.

12.5 Discussion

Several steps are used to acquire the data presented in this chapter, giving us four possible error sources. The four stages are 1) generating a reference, 2) estimating the attitude, 3) controlling the attitude towards the reference, and 4) possible error sources related to the hyperspectral imager. The first error source, generating a reference, might be slightly offset compared to our desired reference if the model we use to calculate where we want to point is not accurate enough. In addition, the time where the maneuver starts has to be specified: while a small error here might give a significant deviation in the image, it would not change the accuracy results we got using the performance metrics introduced in Section 12.2, as they are indifferent to what the imager captures. The control system will not be able to control the satellite towards the reference attitude exactly but with an error required to within a small bound, see [21]. The same can be said for the estimated variables. There is a possibility that error source 4), errors with the imager, also influence the final images. However, these errors should be static, meaning they should be identical between the various images. Error source 1) can possibly vary

depending on location.

Using the results from the telemetry, we can see from the accuracy of the pointing and slewing maneuver that the ADCS manages to control the satellite towards its references, making error source three small. As the images show what we expect to see, we may conclude that the compound errors from the four mentioned sources are small.

The basic idea behind the concept of operations for the HYPSO-1 satellite is that it performs a slew maneuver, such as the one performed in this chapter, to acquire push-broom hyperspectral images. From the results in this chapter, we can see that the attitude control objectives are met with some accuracy during the duration of the image captures. The distance from the reference attitude for nadir pointing is, as shown in Figure 12.6, very low, making it a good comparison for the slew maneuver when looking at the science results. As Table 12.2 shows, the mean GSD of the slew maneuver is decreased by 2/3 relative to the image taken during the pointing maneuver. This measure sets a limit for how much post-processing algorithms can improve the image, and thus it can be argued that using this slewing maneuver helps increase the limit for how much information can be gathered.

12.6 Conclusion

The slew maneuver of the HYPSO-1 satellite performs well according to the accuracy measures used in this chapter. Moreover, the slew maneuver increases the number of photons detected per area of the hyperspectral image by decreasing the GSD. This suggests that the slew maneuver produces images that can be exploited through image restoration, deconvolution, and super-resolution image processing algorithms (e.g., [84]) to increase the utility of the HYPSO-1 data products.

Chapter 13

Conclusion

This section contains the conclusion of the full thesis, a short discussion on the limitations of the results, and how the previously discussed results relate to the research questions presented in Section 1.2. This thesis presents three parts: an energy optimal attitude control part, a maximum hands-off attitude control part, and a part focusing on the slew maneuver used by the HYPSO-1 satellite.

Part I primarily concerns research question 1: "How can attitude control maneuvers be more time and energy-efficient?". Through the three papers on which this part is based, we redefined what it means to be energy optimal when it comes to attitude control, presented a framework for formulating such problems as optimal control problems, and showed how the framework improves upon the current method. The part also answers research question 3, "How can the results in research questions 1 and 2 be taken advantage of in agile and holistic satellite operations?" when the formulation for the attitude control system is expanded to take other parts of the system into account. Through this extension and the case study of HYPSO-2, it is possible to see the benefit the energy optimal control formulation would have on the operations of a satellite system over time. In the final part of part I, the formulation is investigated in relation to a minimum-time objective when the satellite is actuated by magnetorquers, which leads back to the time-efficiency aspect in research question 1.

Research question 2, "How can alternative approaches for attitude control be used for satellites with payloads that are not continuously operated?" is answered in parts II and III. In part II, the focus is on maximum hands-off control, which is a less-used norm formulation. The idea with maximum hands-off control is to make the control signal as sparse as possible, which can be an asset for the operations of a satellite where the control signals have to be at specific points in time to be observable by the operator, for example. In Chapter 11, we looked into the possibility of increasing the performance of the slew maneuver, which we analyzed in Chapter 12. The latter example is, of course, another case where research question three is answered, as the final part of part III looks into the impact of the attitude control system of HYPSO-1 on its operations.

Implementing the energy optimal attitude control methods in part I on an actual satellite could potentially result in some issues. The primary issue would

be the computation time required for the optimizer to find an optimal trajectory, even on a standard computer. Owing to this heavy computational load, using the optimal control problem formulations introduced in part I directly as part of a nonlinear model predictive control (NMPC) scheme onboard the satellite would not be feasible. However, the trajectory can easily be found through optimization on the ground and then sent to the satellite, where it would be fed to a trajectory tracking controller.

The maximum hands-off concept in part II is essentially an open loop concept: the assumption that everything is known about the system is required for the satellite to move as desired. This is not necessarily the case, and the satellite would potentially miss slightly if this control strategy were used. Recalculating the required torque towards the end of the maneuver could solve this problem: it would reduce the uncertainty and, potentially, let the system compensate for any modeling errors. However, the issue with this procedure is that the maximum hands-off optimization requires long computations like the energy optimal optimizations in part I, making such a computation during the maneuver infeasible with the current setup. Furthermore, there are some extra aspects to consider about the maximum hands-off concept for a satellite actuated by thrusters in Chapter 9. The assumption that was made about the on-off behavior of the thrusters, meaning that they work perfectly as a discontinuous on-off actuator, needs to be taken into consideration before implementation on an actual system as thrusters commonly need some time to warm up. This, together with the aforementioned issue that the method cannot produce perfectly on-off signals due to the structure of the problem, is left as future work.

References

[1] B. A. Kristiansen, M. E. Grøtte, and J. T. Gravdahl, "Quaternion-based generalized super-twisting algorithm for spacecraft attitude control," *IFAC-PapersOnLine*, vol. 53, no. 2, pp. 14 811–14 818, 2020, 21st IFAC World Congress.

[2] B. A. Kristiansen, J. T. Gravdahl, and T. A. Johansen, "Energy optimal attitude control for a solar-powered spacecraft," *European Journal of Control*, 2021 European Control Conference Special Issue, vol. 62, pp. 192–197, Nov. 2021.

[3] S. K. Schaanning, B. A. Kristiansen, and J. T. Gravdahl, "Maximum Hands-Off Attitude Control," in *2022 American Control Conference (ACC)*, Jun. 2022, pp. 4003–4010.

[4] B. A. Kristiansen and J. T. Gravdahl, "Maximum Hands-Off Attitude Control of a Spacecraft Actuated by Thrusters," in *22nd IFAC World Congress 2023*, Yokohama, Japan, Jul. 2023.

[5] B. A. Kristiansen, J. T. Gravdahl, S. Gros, and T. A. Johansen, "Energy optimal attitude control of a satellite actuated by magnetorquers in minimum time," in *7th IEEE Conference on Control Technology and Applications (CCTA)*, Bridgetown, Barbados, 2023.

[6] B. A. Kristiansen, D. D. Langer, J. L. Garrett, S. Berg, J. T. Gravdahl, and T. A. Johansen, "Accuracy of a slew maneuver for the HYPSO-1 satellite – in-orbit results," in *13th Workshop on Hyperspectral Image and Signal Processing Evolution in Remote Sensing (IEEE-WHISPERS)*, Athens, Greece, Oct. 2023.

[7] B. A. Kristiansen, J. T. Gravdahl, S. Gros, and T. A. Johansen, "Energy Optimal Attitude Control and Task Execution for a Solar-Powered Spacecraft," *IEEE Transactions on Control Systems Technology*, 2023, conditionally accepted for publication.

[8] S. Bakken, M. B. Henriksen, R. Birkeland, D. D. Langer, A. E. Oudijk, S. Berg, Y. Pursley, J. L. Garrett, F. Gran-Jansen, E. Honoré-Livermore, M. E. Grøtte, B. A. Kristiansen, M. Orlandic, P. Gader, A. J. Sørensen, F. Sigernes, G. Johnsen, and T. A. Johansen, "HYPSO-1 CubeSat: First Images and In-Orbit Characterization," *Remote Sensing*, vol. 15, no. 3, p. 755, Jan. 2023.

[9] J.-Y. Wen and K. Kreutz-Delgado, "The attitude control problem," *IEEE Transactions on Automatic Control*, vol. 36, no. 10, pp. 1148–1162, Oct. 1991.

[10] T. Lee, M. Leok, and N. H. McClamroch, "Time optimal attitude control for a rigid body," in *Proceedings of the 2008 American Control Conference*, Jun. 2008, pp. 5210–5215.

[11] H. Shen and P. Tsiotras, "Time-Optimal Control of Axisymmetric Rigid Spacecraft Using Two Controls," *Journal of Guidance, Control, and Dynamics*, vol. 22, no. 5, pp. 682–694, 1999.

[12] A. Olivares and E. Staffetti, "Time-Optimal Attitude Scheduling of a Spacecraft Equipped with Reaction Wheels," *International Journal of Aerospace Engineering*, vol. 2018, Apr. 2018.

[13] E. Sin, M. Arcak, S. Nag, V. Ravindra, A. Li, and R. Levinson, "Attitude Trajectory Optimization for Agile Satellites in Autonomous Remote Sensing Constellation," in *AIAA Scitech 2021 Forum*, AIAA, Jan. 2021.

[14] I. Ioslovich, "Arbitrary fuel-optimal attitude maneuvering of a non-symmetric space vehicle in a vehicle-fixed coordinate frame," *Automatica*, vol. 39, no. 3, pp. 557–562, Mar. 2003. (visited on 08/30/2023).

[15] C. Wu and X. Han, "Energy-optimal spacecraft attitude maneuver path-planning under complex constraints," *Acta Astronautica*, vol. 157, pp. 415–424, Apr. 2019.

[16] H. C. Marsh, M. Karpenko, and Q. Gong, "Relationships Between Maneuver Time and Energy for Reaction Wheel Attitude Control," *Journal of Guidance, Control, and Dynamics*, vol. 41, no. 2, pp. 335–348, 2018.

[17] N. A. Chaturvedi, A. K. Sanyal, and N. H. McClamroch, "Rigid-body attitude control," *IEEE Control Systems Magazine*, vol. 31, no. 3, pp. 30–51, Jun. 2011.

[18] O. Egeland and J. T. Gravdahl, *Modeling and simulation for automatic control*. Marine Cybernetics Trondheim, Norway, 2002.

[19] E. Oland and R. Schlanbusch, "Reaction wheel design for cubesats," in *2009 4th International Conference on Recent Advances in Space Technologies*, IEEE, 2009, pp. 778–783.

[20] A. Wächter and L. T. Biegler, "On the implementation of an interior-point filter line-search algorithm for large-scale nonlinear programming," *Mathematical Programming*, vol. 106, no. 1, pp. 25–57, Mar. 2006.

[21] M. E. Grøtte, R. Birkeland, E. Honoré-Livermore, S. Bakken, J. L. Garrett, E. F. Prentice, F. Sigernes, M. Orlandić, J. T. Gravdahl, and T. A. Johansen, "Ocean color hyperspectral remote sensing with high resolution and low latency—the HYPSO-1 CubeSat mission," *IEEE Transactions on Geoscience and Remote Sensing*, vol. 60, pp. 1–19, 2022.

[22] M. Krstic and P. Tsiotras, "Inverse optimal stabilization of a rigid spacecraft," *IEEE Transactions on Automatic Control*, vol. 44, no. 5, pp. 1042–1049, May 1999.

[23] W. Luo, Y.-C. Chu, and K.-V. Ling, "Inverse optimal adaptive control for attitude tracking of spacecraft," *IEEE Transactions on Automatic Control*, vol. 50, no. 11, pp. 1639–1654, Nov. 2005.

[24] J. D. Biggs and L. Colley, "Geometric Attitude Motion Planning for Spacecraft with Pointing and Actuator Constraints," *Journal of Guidance, Control, and Dynamics*, vol. 39, no. 7, pp. 1672–1677, 2016.

[25] D. P. Lubey and H. Schaub, "Instantaneous Quadratic Power-Optimal Attitude Tracking with N Control Moment Gyroscopes," *Journal of Guidance, Control, and Dynamics*, vol. 40, no. 3, pp. 702–709, 2017.

[26] C. Pukdeboon and A. S. I. Zinober, "Control Lyapunov function optimal sliding mode controllers for attitude tracking of spacecraft," *Journal of the Franklin Institute*, Advances in Guidance and Control of Aerospace Vehicles using Sliding Mode Control and Observation Techniques, vol. 349, no. 2, pp. 456–475, Mar. 2012.

[27] H. Schaub and V. J. Lappas, "Redundant Reaction Wheel Torque Distribution Yielding Instantaneous L2 Power-Optimal Spacecraft Attitude Control," *Journal of Guidance, Control, and Dynamics*, vol. 32, no. 4, pp. 1269–1276, 2009.

[28] D. Huynh, "Metrics for 3d rotations: Comparison and analysis," *Journal of Mathematical Imaging and Vision*, vol. 35, pp. 155–164, Oct. 2009.

[29] S. Gros, M. Zanon, and M. Diehl, "Baumgarte stabilisation over the SO(3) rotation group for control," in *Proceedings of the 54th IEEE Conference on Decision and Control*, IEEE, Dec. 2015, pp. 620–625.

[30] J. A. E. Andersson, J. Gillis, G. Horn, J. B. Rawlings, and M. Diehl, "CasADi – A software framework for nonlinear optimization and optimal control," *Mathematical Programming Computation*, vol. 11, no. 1, pp. 1–36, 2019.

[31] C. A. Rigo, L. O. Seman, E. Camponogara, E. Morsch Filho, and E. A. Bezerra, "Task scheduling for optimal power management and quality-of-service assurance in CubeSats," *Acta Astronautica*, vol. 179, pp. 550–560, Feb. 2021.

[32] D. A. Vallado, *Fundamentals of astrodynamics and applications*, 2nd ed. El Segundo, California, USA and Dordrecht, The Netherlands: Microcosm Press and Kluwer Academic Publishers, 2001.

[33] M. E. Grøtte, J. T. Gravdahl, T. A. Johansen, J. A. Larsen, E. M. Vidal, and E. Surma, "Spacecraft Attitude and Angular Rate Tracking using Reaction Wheels and Magnetorquers," in *Proc. of the 2020 IFAC World Congress*, 2020.

[34] "6U Nanosatellite Bus M6P," NanoAvionics. (), [Online]. Available: https://nanoavionics.com/small-satellite-buses/6u-nanosatellite-bus-m6p/.

[35] B. Neta and D. Vallado, "On satellite umbra/penumbra entry and exit positions," *The Journal of the Astronautical Sciences*, vol. 46, no. 1, pp. 91–103, Mar. 1, 1998.

[36] F. L. Markley and J. L. Crassidis, *Fundamentals of spacecraft attitude determination and control*. Springer, 2014.

[37] P. Alken, E. Thébault, C. D. Beggan, H. Amit, J. Aubert, J. Baerenzung, T. N. Bondar, W. J. Brown, S. Califf, A. Chambodut, A. Chulliat, G. A. Cox, C. C. Finlay, A. Fournier, N. Gillet, A. Grayver, M. D. Hammer, M. Holschneider, L. Huder, G. Hulot, T. Jager, C. Kloss, M. Korte, W. Kuang, A. Kuvshinov, B. Langlais, J.-M. Léger, V. Lesur, P. W. Livermore, F. J. Lowes, S. Macmillan, W. Magnes, M. Mandea, S. Marsal, J. Matzka, M. C. Metman, T. Minami, A. Morschhauser, J. E. Mound, M. Nair, S. Nakano, N. Olsen, F. J. Pavón-Carrasco, V. G. Petrov, G. Ropp, M. Rother, T. J. Sabaka, S. Sanchez, D. Saturnino, N. R. Schnepf, X. Shen, C. Stolle, A. Tangborn, L. Tøffner-Clausen, H. Toh, J. M. Torta, J. Varner, F. Vervelidou, P. Vigneron, I. Wardinski, J. Wicht, A. Woods, Y. Yang, Z. Zeren, and B. Zhou, "International geomagnetic reference field: The thirteenth generation," *Earth, Planets and Space*, vol. 73, no. 1, p. 49, Feb. 11, 2021.

[38] J. Davis, *Mathematical Modeling of Earth's Magnetic Field*, Technical report, Blacksburg, VA 24061, May 12, 2004.

[39] P. C. Hughes, *Spacecraft Attitude Dynamics*. Mineola, New York, USA: Dover Publications, 2004.

[40] R. Wiśniewski and M. Blanke, "Fully magnetic attitude control for spacecraft subject to gravity gradient," *Automatica*, vol. 35, no. 7, pp. 1201–1214, Jul. 1, 1999.

[41] A. Astolfi and M. Lovera, "Global spacecraft attitude control using magnetic actuators," in *Proceedings of the 2002 American Control Conference*, vol. 2, May 2002, 1331–1335 vol.2.

[42] J. T. Gravdahl, E. Eide, A. Skavhaug, K. M. Fauske, K. Svartveit, and F. M. Indergaard, "Three axis attitude determination and control system for a picosatellite: Design and implementation," in *54th International Astronautical Congress of the International Astronautical Federation, the International Academy of Astronautics, and the International Institute of Space Law*, Bremen, Germany: American Institute of Aeronautics and Astronautics, Sep. 29, 2003.

[43] M. Lovera and A. Astolfi, "Spacecraft attitude control using magnetic actuators," *Automatica*, vol. 40, no. 8, pp. 1405–1414, Aug. 1, 2004.

[44] E. Silani and M. Lovera, "Magnetic spacecraft attitude control: A survey and some new results," *Control Engineering Practice*, Aerospace IFAC 2002, vol. 13, no. 3, pp. 357–371, Mar. 1, 2005.

[45] E. Sharifi and C. J. Damaren, "Nonlinear optimal approach to spacecraft attitude control using magnetic and impulsive actuations," *Journal of Guidance, Control, and Dynamics*, vol. 43, no. 6, pp. 1154–1163, 2020, American Institute of Aeronautics and Astronautics.

[46] K. L. Musser and W. L. Ebert, "Autonomous spacecraft attitude control using magnetic torquing only," in *Flight Mechanics/Estimation Theory Symposium*, Oct. 1, 1989.

[47] R. Wisniewski and F. Landis Markley, "Optimal magnetic attitude control," *IFAC Proceedings Volumes*, 14th IFAC World Congress 1999, Beijing, Chia, 5-9 July, vol. 32, no. 2, pp. 7991–7996, Jul. 1, 1999.

[48] T. Pulecchi, M. Lovera, and A. Varga, "Optimal discrete-time design of three-axis magnetic attitude control laws," *IEEE Transactions on Control Systems Technology*, vol. 18, no. 3, pp. 714–722, May 2010.

[49] J. Liang, R. Fullmer, and Y. Q. Chen, "Time-optimal magnetic attitude control for small spacecraft," in *2004 43rd IEEE Conference on Decision and Control (CDC)*, vol. 1, Dec. 2004, 255–260 Vol.1.

[50] B. A. Kristiansen, J. T. Gravdahl, and T. A. Johansen, "Energy optimal attitude control for a solar-powered spacecraft," *European Journal of Control*, 2021.

[51] M. Nagahara, D. E. Quevedo, and D. Nešić, "Maximum hands-off control: A paradigm of control effort minimization," *IEEE Trans. Automat. Contr.*, vol. 61, no. 3, pp. 735–747, 2015.

[52] T. Ikeda and M. Nagahara, "Time-optimal hands-off control for linear time-invariant systems," *Automatica*, vol. 99, pp. 54–58, 2019.

[53] D. Chatterjee, M. Nagahara, D. E. Quevedo, and K. M. Rao, "Characterization of maximum hands-off control," *Syst. Control. Lett.*, vol. 94, pp. 31–36, 2016.

[54] S. K. Schaanning, B. A. Kristiansen, and J. T. Gravdahl, "Maximum hands-off attitude control," in *2022 American Control Conference (ACC)*, 2022, pp. 4003–4010.

[55] R. Kristiansen, P. J. Nicklasson, and J. T. Gravdahl, "Satellite attitude control by quaternion-based backstepping," *IEEE Transactions on Control Systems Technology*, vol. 17, no. 1, pp. 227–232, 2009.

[56] J. Jin, B. Park, Y. Park, and M.-J. Tahk, "Attitude control of a satellite with redundant thrusters," *Aerospace Science and Technology*, vol. 10, no. 7, pp. 644–651, Oct. 2006.

[57] D. Rafalskyi, J. M. Martínez, L. Habl, E. Zorzoli Rossi, P. Proynov, A. Boré, T. Baret, A. Poyet, T. Lafleur, S. Dudin, and A. Aanesland, "In-orbit demonstration of an iodine electric propulsion system," *Nature*, vol. 599, no. 7885, pp. 411–415, Nov. 2021.

[58] F. Mier-Hicks and P. C. Lozano, "Electrospray Thrusters as Precise Attitude Control Actuators for Small Satellites," *Journal of Guidance, Control, and Dynamics*, vol. 40, no. 3, pp. 642–649, 2017.

[59] J. T. King, J. Kolbeck, J. S. Kang, M. Sanders, and M. Keidar, "Performance analysis of nano-sat scale μCAT electric propulsion for 3U CubeSat attitude control," *Acta Astronautica*, vol. 178, pp. 722–732, Jan. 2021.

[60] T. R. Krogstad and J. T. Gravdahl, "6-DOF mutual synchronization of formation flying spacecraft," in *Proc. 45th IEEE Conf. Decis. Control*, IEEE, 2006, pp. 5706–5711.

[61] H. K. Khalil, *Nonlinear systems*. Saddle River, New Jersey, USA: Prentice Hall, 2002.

[62] H. L. Royden and P. Fitzpatrick, *Real analysis*. Macmillan, New York, USA, 1988, vol. 32.

[63] M. Feng, J. E. Mitchell, J.-S. Pang, X. Shen, and A. Wächter, "Complementarity formulations of l0-norm optimization problems," *Industrial Engineering and Management Sciences. Technical Report. Northwestern University, Evanston, IL, USA*, 2016.

[64] A. Garulli, A. Giannitrapani, and M. Leomanni, "Minimum switching control for systems of coupled double integrators," *Automatica*, vol. 60, pp. 115–121, 2015.

[65] S. Gros and M. Diehl, *Numerical Optimal Control (Draft)*. 2019.

[66] S. K. Schaanning, "Maximum hands-off control for attitude control of a spacecraft," M.Sc. thesis, Norwegian University of Science and Technology, 2021.

[67] S. K. Shrivastava and V. J. Modi, "Satellite attitude dynamics and control in the presence of environmental torques-A brief survey," *J. Guid. Control Dyn.*, vol. 6, no. 6, pp. 461–471, 1983.

[68] J. L. Crassidis and F. L. Markley, "Sliding mode control using modified Rodrigues parameters," *J. Guid. Control Dyn.*, vol. 19, no. 6, pp. 1381–1383, 1996.

[69] J. McDuffie and Y. Shtessel, "A de-coupled sliding mode controller and observer for satellite attitude control," in *Proc. The Twenty-Ninth Southeastern Symposium on System Theory*, Mar. 1997, pp. 92–97.

[70] Y. Shtessel, C. Edwards, L. Fridman, and A. Levant, *Sliding mode control and observation*. Springer, 2014.

[71] A. Levant, "Sliding order and sliding accuracy in sliding mode control," *Int. J. Control*, vol. 58, no. 6, pp. 1247–1263, Dec. 1993.

[72] S. Janardhanan, M. un Nabi, and P. M. Tiwari, "Attitude control of magnetic actuated spacecraft using super-twisting algorithm with nonlinear sliding surface," in *2012 12th Int. Workshop on Variable Structure Systems*, Jan. 2012, pp. 46–51.

[73] I. Castillo, L. Fridman, and J. A. Moreno, "Super-Twisting Algorithm in presence of time and state dependent perturbations," *Int. J. Control*, vol. 91, no. 11, pp. 2535–2548, Nov. 2018.

[74] I.-L. G. Borlaug, K. Y. Pettersen, and J. T. Gravdahl, "Tracking control of an articulated intervention AUV in 6DOF using the generalized super-twisting algorithm," in *2019 American Control Conference (ACC)*, Jul. 2019, pp. 5705–5712.

[75] O.-E. Fjellstad and T. Fossen, "Singularity-free tracking of unmanned underwater vehicles in 6 DOF," in *Proc. of 1994 33rd IEEE Conference on Decision and Control*, vol. 2, Dec. 1994, 1128–1133 vol.2.

[76] K.-S. Kim and Y. Kim, "Robust backstepping control for slew maneuver using nonlinear tracking function," *IEEE Transactions on Control Systems Technology*, vol. 11, no. 6, pp. 822–829, Nov. 2003.

[77] J. Li, M. Post, and R. Lee, "Real-Time Nonlinear Attitude Control System for Nanosatellite Applications," *Journal of Guidance, Control, and Dynamics*, vol. 36, no. 6, pp. 1661–1671, Nov. 2013.

[78] M. A. Cutter, D. R. Lobb, and R. A. Cockshott, "Compact High Resolution Imaging Spectrometer (CHRIS)," *Acta Astronautica*, 2nd IAA International Symposium on Small Satellites for Earth Observation, vol. 46, no. 2, pp. 263–268, Jan. 2000.

[79] H. Kim and Y. K. Chang, "Mission scheduling optimization of SAR satellite constellation for minimizing system response time," *Aerospace Science and Technology*, vol. 40, pp. 17–32, Jan. 2015.

[80] J. L. Garrett, D. Langer, K. Avagian, and A. Stahl, "Accuracy of super-resolution for hyperspectral ocean observations," in *IEEE/MTS OCEANS, Marseille*, 2019.

[81] J. L. Garrett, S. Bakken, E. F. Prentice, D. Langer, F. S. Leira, E. Honoré-Livermore, R. Birkeland, M. E. Grøtte, T. A. Johansen, and M. Orlandić, "Hyperspectral image processing pipelines on multiple platforms for coordinated oceanographic observation," in *11th Workshop on Hyperspectral Imaging and Signal Processing: Evolution in Remote Sensing (WHISPERS)*, 2021.

[82] Á. Q. Valenzuela and J. C. G. Reyes, "Basic spatial resolution metrics for satellite imagers," *IEEE Sensors Journal*, vol. 19, no. 13, pp. 4914–4922, 2019.

[83] E. F. Prentice, M. E. Grøtte, F. Sigernes, and T. A. Johansen, "Design of a hyperspectral imager using COTS optics for small satellite applications," in *International Conference on Space Optics — ICSO 2020*, vol. 11852, SPIE, Jun. 2021, pp. 2154–2171.

[84] R. C. Gonzalez and R. E. Woods, *Digital image processing*, 4th ed. London, UK: Pearson, 2018.

ISBN 978-82-326-7580-7 (printed ver.)
ISBN 978-82-326-7579-1 (electronic ver.)
ISSN 1503-8181 (printed ver.)
ISSN 2703-8084 (online ver.)

NTNU

Norwegian University of
Science and Technology